Geological Processes on Mercury and the Mapping of the Derain (H-10) Quadrangle.

Thesis

Geological Processes on Mercury and the Mapping of the Derain (H-10) Quadrangle.

Christopher Charles Malliband
MSci (Hons)

A thesis submitted to The Open University for the degree of Doctor of Philosophy

School of Physical Sciences

October 2020

ABSTRACT

I present the results from the first geological map of the Derain (H-10) quadrangle of Mercury and in-depth studies of features identified in the map.

I used ArcGIS software to produce the geological map by integrating and analysing data from the MESSENGER (MErcury Surface, Space ENvironment, GEochemistry, and Ranging) spacecraft. My results show that the Derain quadrangle has a similar geological history to other quadrangles investigated on Mercury. My mapping showed that two plains classifications are insufficient to represent the diversity of plains material within the Derain quadrangle. Intermediate plains remain enigmatic, but I conclude that at least some are likely to be thin coverings of lava, insufficient to hide underlying craters, that are younger than most smooth plains.

My work to characterise plains units within the Derain quadrangle led to an investigation of previously unstudied small patches (<15,000 km^2) of smooth plains, both within and outside the Derain quadrangle. Several of these are found abutting (ponded against) lobate scarps. Therefore, these smooth patches must post-date the onset of global contraction and so the end of widespread effusive volcanism. The mechanism of emplacement is not clear, but smooth patches are most likely formed by either late-stage volcanism or impact-related processes. In most cases, I argue for a volcanic origin.

While investigating the Derain quadrangle, I identified a previously unknown mass-wasting process on Mercury: down-slope streaks that I refer to as 'slope lineae'. I surveyed the Hokusai quadrangle for these features and show that slope lineae are found predominantly on equator-facing slopes. The preference for equator-facing slopes, common association with 'hollows', and the morphology of some examples may indicate that volatile loss contributes to their formation.

ACKNOWLEDGMENTS

Great thanks are due to my supervisors Dave, Susan, and Matt. Thank you for all the support, encouragement, and putting up with the endless stream of spelling and grammar mistakes. I don't think I could have had a better team onside.

I also owe thanks to my fellow Mercury students, Pegg, Jack, and Ben, who have helped enormously with both science discussions and understanding when Arc does something inexplicable. Particular thanks to Pegg who was always just over the monitors for a discussion on the finer points of crater degradation or the EWR alignments.

I am grateful for all my colleagues in the office, and room 101 for the ever-entertaining conversations and levity through the PhD. It's helped so much. I owe a lot to Andrew and David who had to put up with me writing up from home through lockdown but have helped so much with keeping me sane throughout.

I'm not sure how I'd have made through the whole process without the support of my family. You've all helped so, so, much. While I'm sorry not everyone is here to see the result, I know they'd be proud that it's done.

CONTENTS

CHAPTER 1
INTRODUCTION AND OVERVIEW

1.1 Thesis Overview

In this thesis I present the results of my geological survey and mapping of the Derain (H-10) quadrangle of Mercury, and the results of detailed studies that arose from my quadrangle survey. The map is the first of this area of Mercury and mapping at large scale was able to reveal previously undocumented or unknown features that became the subject of further study. I have examined these features both inside and outside the mapped quadrangle as well as examining potential analogues on other planetary bodies.

The map was completed in co-ordination with other mappers across Europe as part of an effort to complete a global set of geological maps in preparation for the arrival of the ESA-JAXA BepiColombo mission.

1.2 Structure

This thesis has seven further chapters.

Chapter 2 provides a history of the exploration of Mercury and a summary of Mercury's geology.

Chapter 3 and Chapter 4 both describe my geological mapping of the Derain quadrangle. This is shown in the included map sheet. Chapter 3 describes how I created the map and the unit definitions I used. Chapter 4 gives my interpretation of the geological history of the quadrangle, with key localities described in more depth.

Chapter 5 is a study of previously undescribed small patches of smooth plains found during my mapping. I describe localities both inside and outside the quadrangle and evaluate different formation mechanisms.

Chapter 6 is a study of slope lineae, a previously undocumented mass-wasting processes on Mercury. This arose from an example found during mapping and was expanded to a systematic survey outside the quadrangle. I describe localities of slope lineae and discuss potential formation mechanisms.

The final chapters, Chapter 7 and Chapter 8, suggest future work and summarise my conclusions.

The research in each chapter has been completed and driven by myself in collaboration with my supervisors. I have based my mapping methodology on those of Valentina Galluzzi and Jack Wright to enable integration into the global geological basemap. However, I have shaped the strategy to best reflect the geology of the quadrangle.

CHAPTER 2
THE GEOLOGICAL EXPLORATION OF MERCURY

2.1 History of Mercury Exploration

2.1.1 Early Days

Mercury has been known to humanity since, at least, classical antiquity. Its fast movement across the sky led it to be named for the messenger gods in several cultural groups. Early observation records showed Mercury has an orbital period of approximately 88 days.

Transits observed through the 18th century by Halley and others were used in determining the absolute size of the planets and Earth-Sun distance. The clear outline of transiting Mercury compared the more diffuse outline transiting Venus was used to suggest the absence of an atmosphere at Mercury.

Telescopic studies of the surface of Mercury are not easy due to Mercury's diminutive size, and position close to the Sun. 20th century telescope observations were able though to distinguish albedo features (Antoniadi et al., 1934). Such surface features were mapped and eventually used to estimate the rotational period of Mercury as 58.64 days (Chapman, 1967). This corroborated with radar observations (Pettengill and Dyce, 1965). Given this was 2/3 the orbital period of 88 days, it became clear that Mercury had a 3:2 orbital resonance (Colombo, 1965). This means for every 3 rotations of Mercury, the planet orbits twice around the sun. Given this resonance, a solar day on Mercury lasts exactly two Mercury years. Another consequence of Mercury's spin resonance and the eccentricity of Mercury's orbit are the so called 'hot poles' (Soter and Ulrichs, 1967). These are the points on the

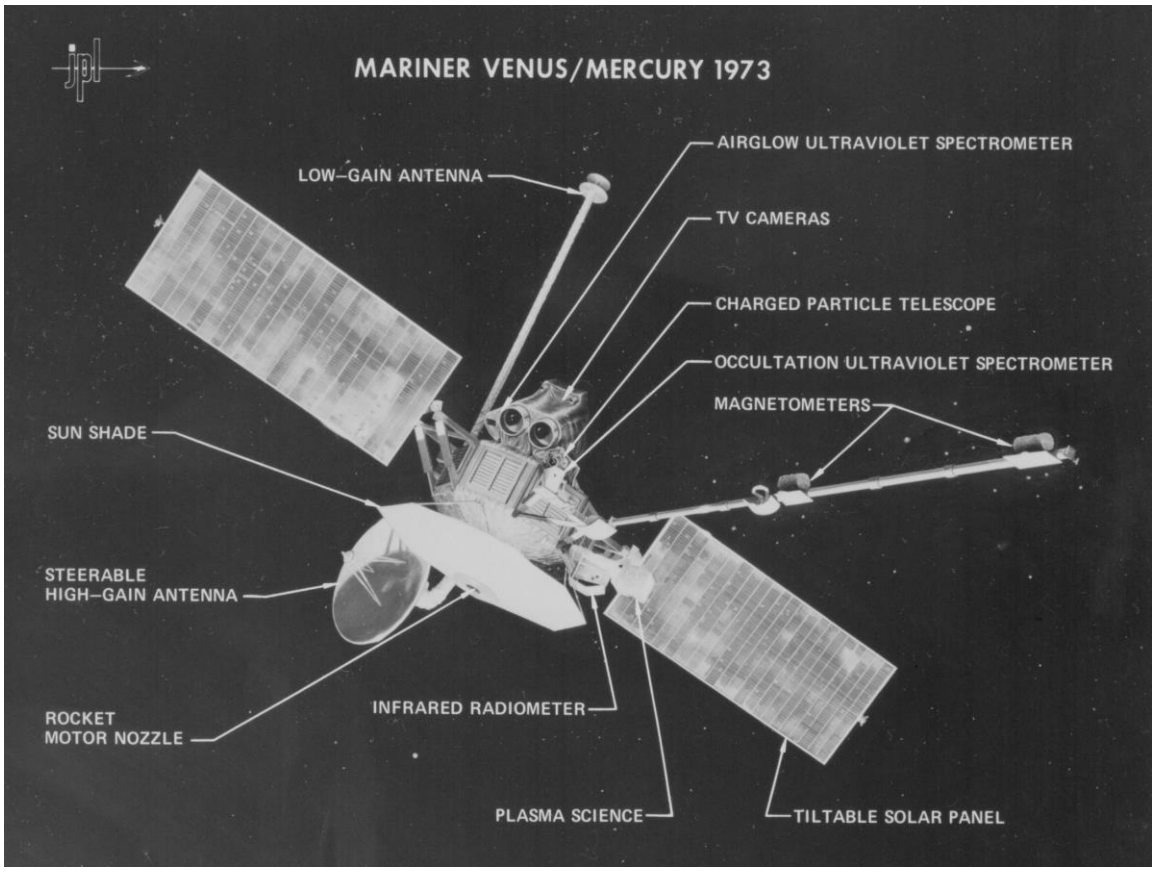

Figure 2.1: Mariner 10 instrumentation. Image: NASA/JPL

equator at 0° and 180° longitude where solar noon occurs at alternate perihelia, and so have the highest average temperatures (~700°K) on the planet.

Mercury's mass had been determined to be large compared it its size prior to Mariner 10 (Hill, 1898). This led to the conclusion that Mercury must have a large iron core (Lyttleton, 1969).

2.1.2 Mariner 10

Mercury remained an intriguing target for exploration by spacecraft, and was the target, alongside Venus for Mariner 10, the final flight of NASA's Mariner program. Mariner 10 was well equipped by the standards of the day and carried a wide range of instruments (Figure 2.1), including a TV science experiment, magnetometers, and a UV spectrometer.

Mariner 10 completed three flybys of Mercury between 1974 and 1975 (Dunne and Burgess, 1978). Unfortunately, due to the orbital resonance of Mariner 10 with Mercury, the same hemisphere was illuminated during all three flybys, so approximately 45% of the globe was imaged (Davies et al., 1978). These flybys returned the first images of the surface, from the television science experiments, as well as observations from the other instruments such as the magnetometers. Images were obtained in a variety of lighting conditions.

2.1.2.1 Magnetic Field

One of the most unexpected results of the Mariner 10 mission was the discovery of Mercury's large, internally-generated, magnetic field (Connerney and Ness, 1988; Ness et al., 1975). This suggested a liquid, convecting core at the present day (Connerney and Ness, 1988). A liquid core was unexpected as, given Mercury's small size, thermal models suggested the core would have solidified (Solomon, 1976). Later observations in the MESSENGER era have demonstrated the field is generated by the geo-dynamo in the core (Anderson et al., 2010, 2008; Uno et al., 2009).

2.1.2.2 Geology

Mariner 10 provided the first images of the surface of Mercury. Images revealed a dynamic world with the large Caloris Basin (McCauley et al., 1981), tectonism (Strom et al., 1975), and varied surface geology (Trask and Guest, 1975). The images from Mariner 10 covered ~45% of the surface, and have low-spatial resolution (~1km per pixel) (Head et al., 2007). This is comparable to telescope observations of the Moon prior to the launch of spacecraft (Head et al., 2007).

From these images, the first geological maps of Mercury were made (De Hon et al., 1981; Grolier and Boyce, 1984; Guest and Greeley, 1983; King and Scott, 1990; McGill and King, 1983; Schaber and McCauley, 1980; Spudis and

Prosser, 1984; Strom et al., 1990; Trask and Dzurisin, 1984). This work found the presence of two widespread geological plains units: smooth and intercrater plains. Smooth plains are smooth in texture and relatively un-cratered (Trask and Guest, 1975). Given the similar crater densities of each example they were thought to be of similar age. Interpretations of the geology were guided by the recent (1969 - 1972) Apollo missions. Given the misinterpretation of the impact-derived (Apollo Field Geology Investigation Team, 1973; Oberbeck et al., 1973) lunar Cayley plains as volcanic based on their smooth morphology (Kain et al., 1971), workers were careful not to assume a volcanic origin based on smooth morphology alone (Trask and Strom, 1976; Wilhelms, 1976).

Intercrater plains were described as being distinguished by their high density of small (5-10 km) superimposing craters (Trask and Guest, 1975). Notably, intercrater plains were not described as crater saturated (Malin, 1976), and so were not thought to completely predate the late heavy bombardment. The late heavy bombardment is a hypothesised stage at around 4.0 Ga of particularly high impact flux across the inner solar system (Gomes et al., 2005; Wetherill, 1975). Mappers included a third, intermediate plains unit (Trask and Guest, 1975). This was less areally expansive than the smooth or intercrater plains and was thought to be intermediate in age (Trask and Guest, 1975).

A full review of our understanding of Mercury's geology at the end of the Mariner 10 era of Mercury exploration was produced by Head et al. (2007).

2.2 The MESSENGER Era

The next significant change in our understanding of Mercury was brought about by the launch of NASA's MESSENGER (MErcury Surface, Space ENvironment, GEochemistry, and Ranging) spacecraft in 2004 (Solomon et al., 2001). MESSENGER made three flybys of Mercury (January, October 2008;

September 2009), and became the first spacecraft to orbit Mercury in March 2011. A review of the mission and its payload is in Solomon and Anderson (2018) and references therein. MESSENGER remained in orbit until April 2015. Its orbit was eccentric to allow the spacecraft to cool. As periherm was always over the northern hemisphere, data quality for surface datasets is usually best towards the north (e.g. Denevi et al., 2016).

2.2.1 Instrumentation

MESSENGER provided the first global coverage of data for Mercury and carried a suite of instrumentation (Figure 2.2). The eccentric orbit of MESSENGER constrained instrumentation.

2.2.1.1 MDIS: Mercury Dual Imaging System

MDIS was the imaging system on MESSENGER (Hawkins et al., 2007). It was comprised of the wide angle (WAC) and narrow angle (NAC) cameras. Ground resolution for both cameras varied with MESSENGER's orbit, therefore was generally better at high northern latitudes. As MESSENGERS orbit degraded over the mission lifespan later images in the mission can have higher surface resolution. The cameras could not operate in stereo.

The WAC had a 10.5° by 10.5° field of view and was able to image in monochrome or using 11 colour filters over the range 395 to 1040 nm. WAC images have good global coverage and make up a large proportion of the images used in global photomosaic basemaps. Resolution was generally no better than 250 mpp. Reflectance values from the various filters for the WAC have been used to attempt to infer geochemistry (e.g. Denevi et al., 2013; Klima et al., 2018; Namur and Charlier, 2017).

The NAC had a 1.5° by 1.5° field of view and could image only in monochrome. Coverage of NAC images is biased toward the northern latitudes due to MESSENGER's orbit. It provides the highest resolution images

available of Mercury with images from the end-of-life low altitude campaign below 20 mpp. NAC images include both targeted images of features of interest as well as many untargeted general images.

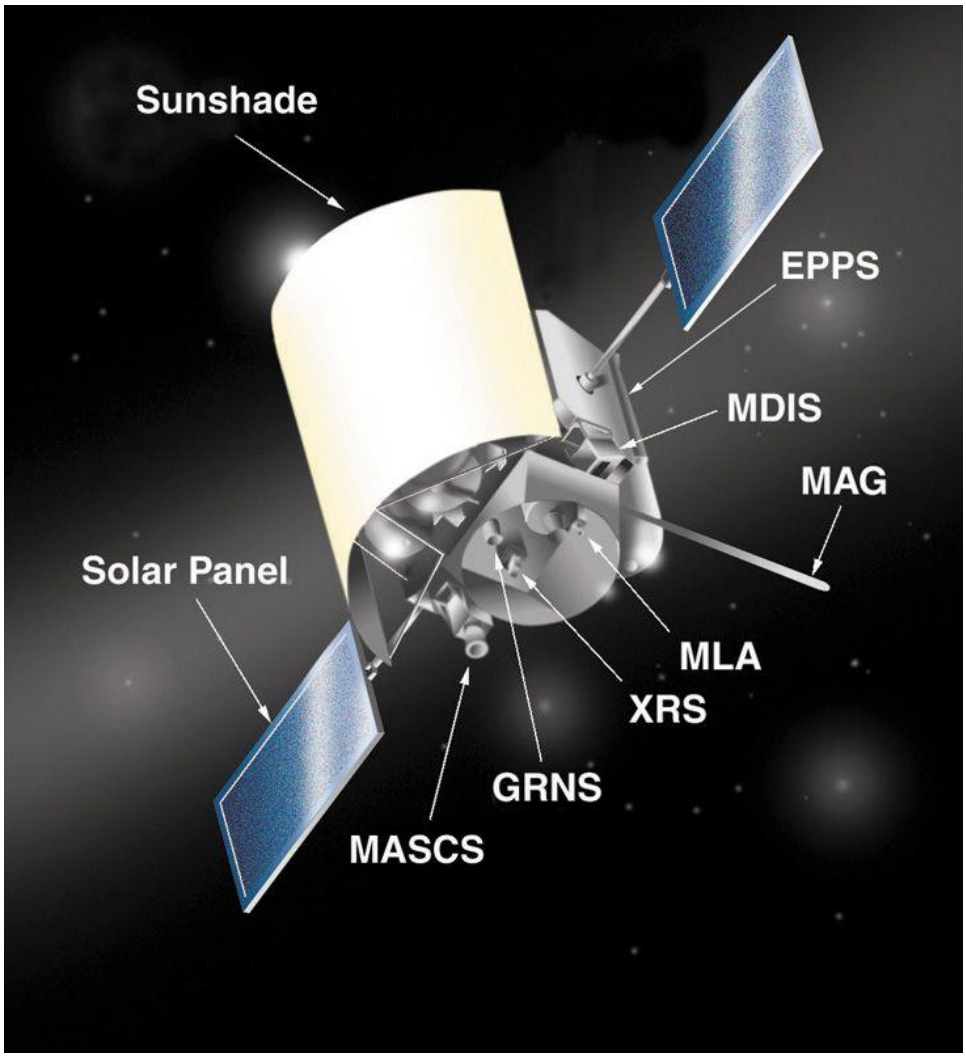

Figure 2.2: MESSENGER Instrumentation. EPPS: Energetic Particle and Plasma Spectrometer; MDIS: Mercury Dual Imaging System; MAG: Magnetometer; MLA: Mercury Laser Altimeter; XRS: X-Ray Spectrometer; GRNS: Gamma-Ray and Neutron Spectrometer; MASCS: Mercury Atmospheric and Surface Composition Spectrometer. Image: NASA/GSFC.

2.2.1.2 MLA: Mercury Laser Altimeter

MLA was a laser altimeter with a maximum range of ~1500 km and precision of ~30 cm (Cavanaugh et al., 2007). It provided a large number of accurate topographic profiles. Again, due to MESSENGER's orbit, there is a higher

density of tracks in the northern latitudes, and very few tracks cross the equator.

2.2.1.3 XRS: X-ray Spectrometer

The XRS measured X-ray fluorescence from the surface of Mercury induced by incident solar X-rays (Schlemm et al., 2007). This gives elemental abundance data from the top mm of Mercury's surface. It detected emissions from elements in the 1-10 keV range. This included detection of magnesium, aluminium, silicon, sulphur, calcium, titanium and iron. The instrument has a 12° by 12° field of view, and a ground spatial resolution of between 42 km per pixel at periherm (in the northern hemisphere) to 3200 km per pixel at apoherm. Therefore, while the XRS gives important compositional information, it is usually on a very coarse scale compared to visual image data.

2.2.1.4 MASCS: Mercury Atmospheric and Surface Composition Spectrometer

The MASCS instrument combines an ultraviolet spectrometer and infrared spectrograph (McClintock and Lankton, 2007). Ultraviolet coverage was over far-ultraviolet (115-180 nm), middle ultraviolet (160-320 nm) and visible (250-600nm) bands. Infrared coverage was obtained using detectors in 300-1050 nm and 850–1450 nm ranges (McClintock and Lankton, 2007). The instrument was used, as the name implies, for both observations of exosphere composition, and Mercury's surface. The ultraviolet spectrometer was used particularly for observations of the exosphere and Mercury's polar deposits and had a ground resolution of up to 25 km per pixel at periherm. The near-infrared spectrograph was able to determine wavelengths diagnostic of iron and titanium-rich minerals. It had a resolution of up to 3 km per pixel at periherm. Coverage by these instruments is not globally complete and is poor in the southern hemisphere.

2.2.1.5 GRNS: Gamma-Ray and Neutron Spectrometer

The GRNS instrument package included both a gamma-ray spectrometer and neutron spectrometer (Goldsten et al., 2007). Both used emissions generated from incident cosmic rays. The gamma-ray spectrometer used the characteristic gamma emissions of elements in the 0.1-10 MeV range. This allowed detection of elements including hydrogen, magnesium, silicon, iron, titanium, sodium and calcium. The neutron spectrometer detected thermal and epithermal neutrons whose ratio could be used to estimate hydrogen distribution.

2.2.1.6 Magnetometer

The magnetometer was used to characterise the magnetic field of Mercury. It had a three-axis detector and so was able to determine strength and position with altitude (Anderson et al., 2007). The instrument was mounted on a boom to reduce signals from the spacecraft. Mercury's magnetosphere is generally outside the scope of the thesis.

2.2.1.7 EPPS: Energetic Particle and Plasma Spectrometer

The EPPS measured composition, energies, and distribution of the charged particles in Mercury's exosphere and magnetosphere with two sensors (Andrews et al., 2007). Mercury's exosphere is beyond the scope of this thesis.

2.2.2 Stratigraphy

As discussed in section 2.1.2.2, after Mariner 10 three global plains units were recognised, smooth, intermediate, and intercrater plains (Figure 2.3). MESSENGER datasets were able to give a much higher resolution and global perspectives on these units and the geological history of the innermost planet. In this section I use the term flooded in relation to effusive volcanism.

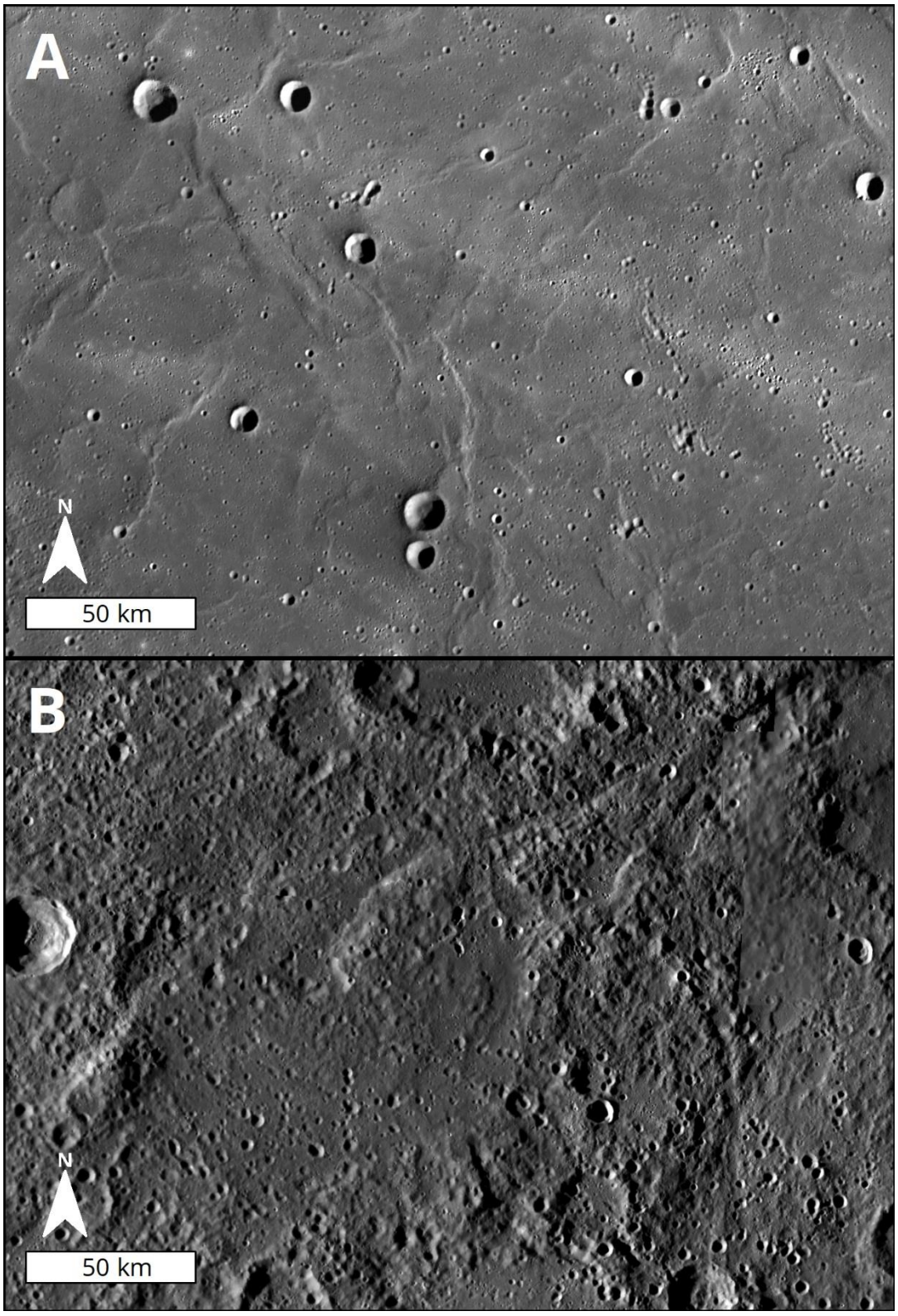

Figure 2.3: Comparison of smooth plains (A) and intercrater plains (B) in a MDIS mosaic. Note the smooth texture with few, fresh superimposing craters in the smooth plains, whereas intercrater plains are more textured with many superimposing craters of various states of degradation. A is centred at 45°E, 55°N. B is centred at 43°E, 8°S.

It is the accepted term in the literature for the cover of a superimposing unit that appears to have been emplaced with no clear internal divisions. The use of flooded does not imply any particular emplacement style.

2.2.2.1 Smooth Plains

The genesis of smooth plains units on Mercury was unclear during the Mariner 10 era. Smooth plains were first thought to be analogous to lunar maria and thus likely to be volcanic (Strom et al., 1975). This was based on the smooth morphology, the vast areas that were filled over a short geological time scale as well as the distinct spectral contrast with surrounding areas. However, no evidence of vents or other unambiguously volcanic landforms was observed. A volcanic origin for smooth plains was questioned by Wilhelms (1976), who found the arguments made similar to those made for a volcanic origin for the Caley formation (Kain et al., 1971), but was found by Apollo 16 to be fluidised ejecta deposits (Apollo Field Geology Investigation Team, 1973).

MESSENGER's first flyby in 2008 returned evidence of impact features and surrounding areas that have been 'flooded' (Head et al., 2008). Effusive volcanism in these degraded impacts was inferred from the shallow flooding of craters and embayment of crater ejecta (Head et al., 2008; Murchie et al., 2008). Spectral evidence using the MDIS-WAC found distinctive colour properties of these areas of effusive volcanism (Blewett et al., 2009; Denevi et al., 2009; Murchie et al., 2008; Robinson et al., 2008). I describe the difference between impact and volcanic driven smooth features in detail in Chapter 5.

As MESSENGER gave a global perspective on Mercury, large previously unseen areas of smooth plains were revealed for the first time (Figure 2.5) including the extensive northern smooth plains (Head et al., 2011), covering over 7% of the planet's surface (Ostrach et al., 2015). The northern smooth

plains (NSP), now formally named as 'Borealis Planitia', have many 'ghost' craters, where a resurfacing unit has covered a crater, so only the rim trace is visible. The NSP has a clear colour signature and appears homogeneous, although a greater proportion of small, ghosted or partially flooded craters appear at some margins (Head et al., 2011). Depth of volcanic fill has been estimated, using estimates of original rim heights of partially flooded craters to between 700 and 1800 m. This leads to volume estimates of between 4×10^6 and 4×10^7 km^3 (Ostrach et al., 2015). This is comparable to estimates for the volume of all lunar maria (1×10^7 km) (Head and Wilson, 1992). No regions of differing crater density nor evidence of individual flow units have been found (Ostrach et al., 2015). This lack of differing crater densities and flow units has led to the conclusion that the NSP seen at the surface today represent a phase of large scale 'flood' volcanism emplaced over a short period of time (Ostrach et al., 2015), based on estimated crater counts this may be 100 MYr or less (Ostrach et al., 2015).

Further morphological evidence of volcanism was found in smooth plains close to the NSP. Byrne et al. (2013) found a series of flow features, particularly broad channels with streamlined islands (Figure 2.4), and sharp contacts to surrounding intercrater plains. This demonstrates that Mercury's effusive volcanism has, at least in places, acted erosively. It also suggests high temperature, low viscosity lavas, potentially growing through overland flow, rather than growth principally through inflation (Byrne et al., 2013).

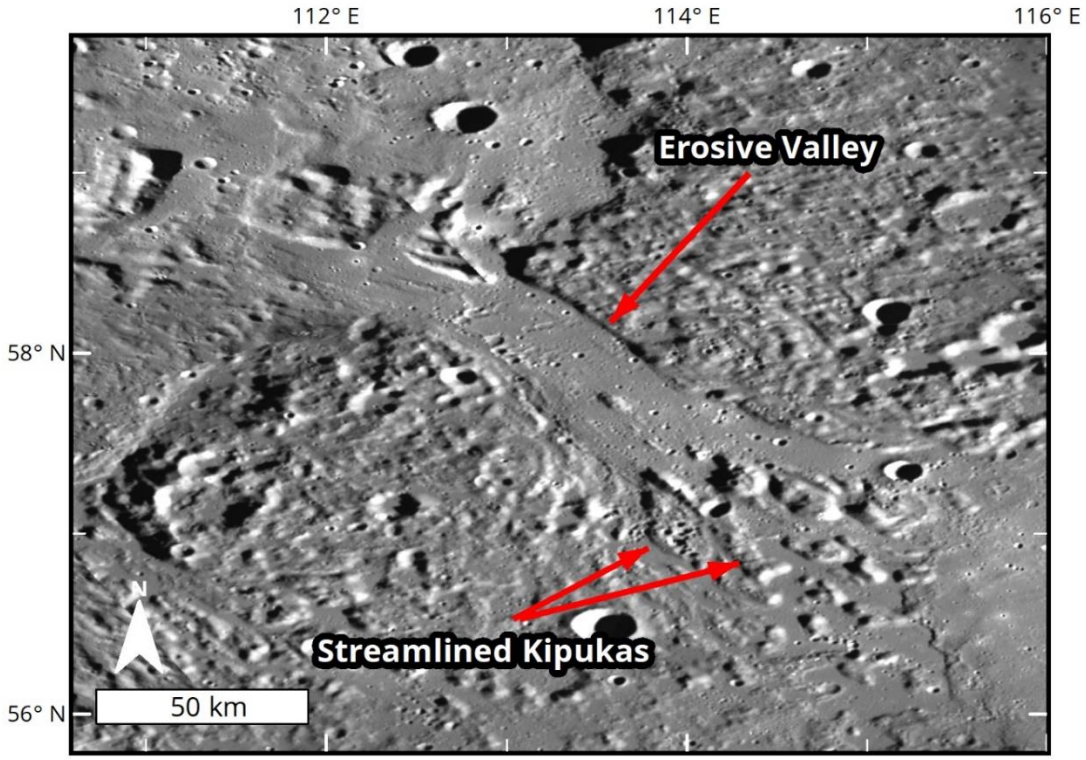

Figure 2.4: Lava flow features in Angkor Vallis in the MDIS 166 mpp basemap. Note the incised, erosive valley, with sharp morphological and topographic boundary with the surrounding intercrater plains. In the channel are streamlined kipukas, areas of pre-existing terrain surrounded by erosive flow. The volume of material and length of time required for erosive flow suggests volcanic rather than impact process.

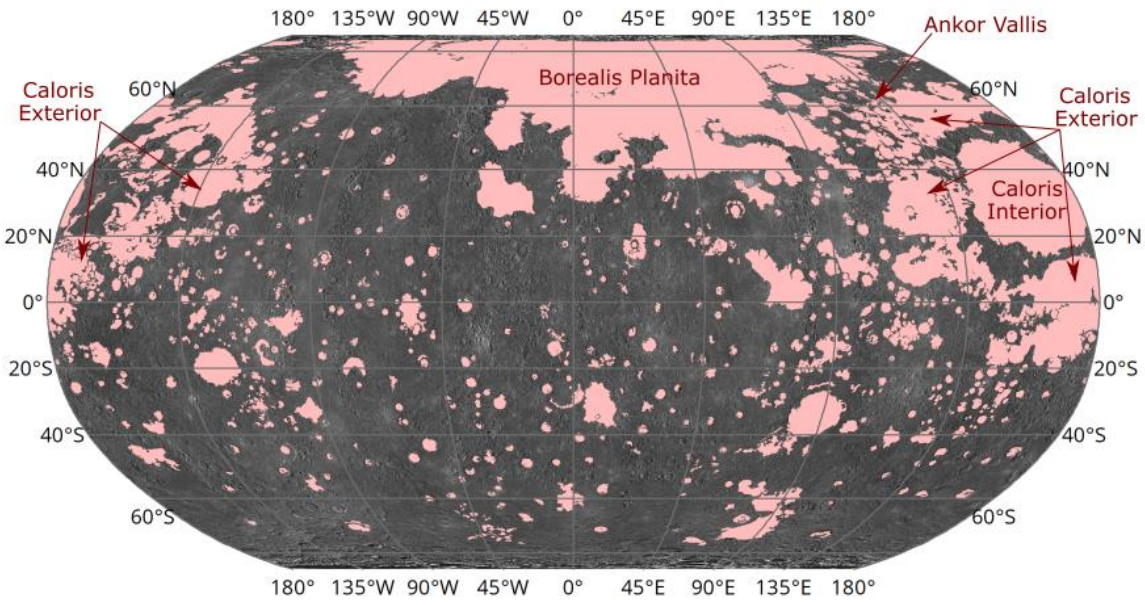

Figure 2.5: Global distribution of smooth plains (pink) from mapping by Denevi et. al. (2013)*. Note the large area of smooth plains at high northern latitudes (Borealis Planitia). Major smooth plains and Ankor Vallis (Fig 2.4) labelled. Robinson projection.*

The NSP are the best-studied area of smooth plains compositionally. Mg/SI, Ca/Si and Al/Si values obtained from MESSENGER X-ray spectrometer observations (Nittler et al., 2011; Weider et al., 2012) and petrological modelling (Stockstill-Cahill et al., 2012) suggest a magnesian basalt composition, with a relatively high K abundance (Peplowski et al., 2012). Similar compositions, albeit with lower K abundance have also been found in the Caloris basin interior smooth plains (Peplowski et al., 2012). The geochemical compositions are clearly different from typical terrestrial basalts. The differing degrees of partial melt from a chondritic mantle to satisfy these constraints suggests Mercury's mantle has evolved differently to that of the Earth. Due to the small areal extents and limited spatial resolution of MESSENGER geochemical data, this work cannot be replicated on smaller areas of smooth plains. However, many mapped areas of smooth plains have WAC spectral properties similar to the NSP, and so a magnesian basalt composition is plausible (Denevi et al., 2013). Magnesian basalt would have been erupted at high temperature and have low viscosity under modelled Mercury conditions (Stockstill-Cahill et al., 2012). This fits well with the observations of lava flow features (Byrne et al., 2013).

Denevi et al. (2013) defined and mapped (Figure 2.5) the global extent of the smooth plains on the basis of MESSENGER data. Smooth plains were defined as 'smooth, relatively sparsely cratered terrain that displays sharp boundaries with adjacent regions and is level to gently sloped over a baseline of ~100–200 km' (Denevi et al., 2013). This mapping showed ~27% of Mercury is covered with smooth plains, compared with 17% of the Moon covered by mare basalts (Head and Wilson, 1992). Mapping showed that smooth plains are concentrated in the northern hemisphere (Denevi et al., 2013). This observation has not been explained.

Crater counts completed in areas of smooth plains suggest large scale smooth plains were emplaced by 3.5 Ga (Byrne et al., 2016). This is around

the onset of global contraction (Byrne et al., 2016). This is consistent with early predictions that large scale effusive volcanism would be inhibited by global contraction (Wilson and Head, 2008).

While the majority of smooth plains have features that clearly indicate a volcanic origin (e.g. 'flooded' craters, embayed ejecta, flow features, sharp colour boundaries), many smaller areas do not (Denevi et al., 2013). These areas may still be volcanic, and just lack diagnostic features in current datasets, or may be emplaced by impact processes (Malliband et al., 2018; Whitten and Head, 2015).

2.2.2.2 Intercrater Plains

Intercrater plains are the background and most widespread plains unit on Mercury. They were, as discussed in section 2.1.2.2, first mapped in Mariner 10 studies. The main characteristic of the intercrater plains is the abundance of small craters (Trask and Guest, 1975). The intercrater plains were re-evaluated with MESSENGER data by Whitten et al. (2014), who defined them as 'characterized by an extremely textured surface, caused by the high density of craters <10 km in diameter', and noted that 'locally the Intercrater plains are nearly level deposits, but regionally the plains are a more gently rolling or undulating unit' (see Figure 2.3).

New datasets from MESSENGER showed intercrater plains to be less reflective than the smooth plains (Denevi et al., 2009). However, data from the gamma-ray (Peplowski et al., 2015b) and X-ray (Nittler et al., 2011; Weider et al., 2015, 2012) spectrometers on MESSENGER showed considerable overlap in composition with the smooth plains. For this reason, and difficulties reconciling the number of large impacts to produce enough ejecta for an impact source (Fassett et al., 2012), a volcanic origin for the smooth plains is currently preferred (Denevi et al., 2018).

2.2.2.3 Intermediate Plains

The intermediate plains were mapped in Mariner 10 era maps (Grolier and Boyce, 1984; Guest and Greeley, 1983; King and Scott, 1990; McGill and King, 1983; Schaber and McCauley, 1980; Spudis and Prosser, 1984; Strom et al., 1990; Trask and Dzurisin, 1984). They were defined as 'planar to undulating surfaces that have higher crater density than smooth plains material, but are less heavily cratered than intercrater plains material' (Spudis and Prosser, 1984).

Mapping of type localities identified as intermediate plains in Mariner 10 mapping was completed by Whitten et al. (2014). They concluded that MESSENGER images showed no distinct morphological characteristics of these areas, and mapping as separate units was probably due to unfavourable lighting and resolution. Although they recognised that there is a 'spectrum' of plains types and morphologies across Mercury, Whitten et al. (2014) proposed that all units should be classified as either smooth plains or as intercrater plains, the two end members of this 'spectrum', and intermediate plains were not a mappable unit.

In contrast, quadrangle mapping completed by others (Galluzzi et al., 2016; Guzzetta et al., 2017; Wright et al., 2019) found it necessary to map an intermediate plains unit to adequately display the diversity of plains units present (Galluzzi et al., 2017). Other workers have mapped a similar unit as a subdivision of the intercrater plains (Ostrach et al., 2019).

It is not therefore clear if the intermediate plains are a mappable unit. When looking at a general global stratigraphy, the intermediate plains do not appear to be a globally defined unit (Whitten et al., 2014). However, morphologically intermediate plains are visible and mappable at the quadrangle level. These regional intermediate plains have not been fully defined, and geological interpretations of mapped intermediate units differ.

For example, Wright (2019) suggests some intermediate plains may be younger than smooth plains, whereas Galluzzi et al. (2016), interprets intermediate plains in the Victoria quadrangle to be younger than the intercrater plains only. This supports the idea that while the intermediate plains are not necessarily a widespread global unit, they are mappable on the regional or local scale.

2.2.2.4 Time Series

A time-stratigraphic series, to split geological time into defined systems, for Mercury was first proposed in the Mariner 10 era (Spudis and Guest, 1988). It was based on the equivalent lunar system (Shoemaker and Hackman, 1962; Wilhelms, 1987), with five systems named for impact events that defined the base, or exemplar for each. Estimates of absolute ages were based on the assumption that areas of similar crater densities on the Moon and Mercury were similar in absolute age (Spudis and Guest, 1988).

The absolute ages of boundaries were re-evaluated in the MESSENGER era. The base of the Calorian and Tolstojan systems are defined by the Caloris and Tolstoj impact events respectively. The absolute ages of these impacts were evaluated and revised on the basis of crater counts (Ernst et al., 2017). The younger Mansurian and Kuiperian systems were defined by the level of crater degradation exemplified by namesake craters (Figure 2.6) (Spudis and Guest, 1988). This was re-evaluated by Banks et al. (2017), who used the global population of similarly fresh craters to estimate absolute ages. These revisions have radically changed the age estimates of the end of the Calorian in particular.

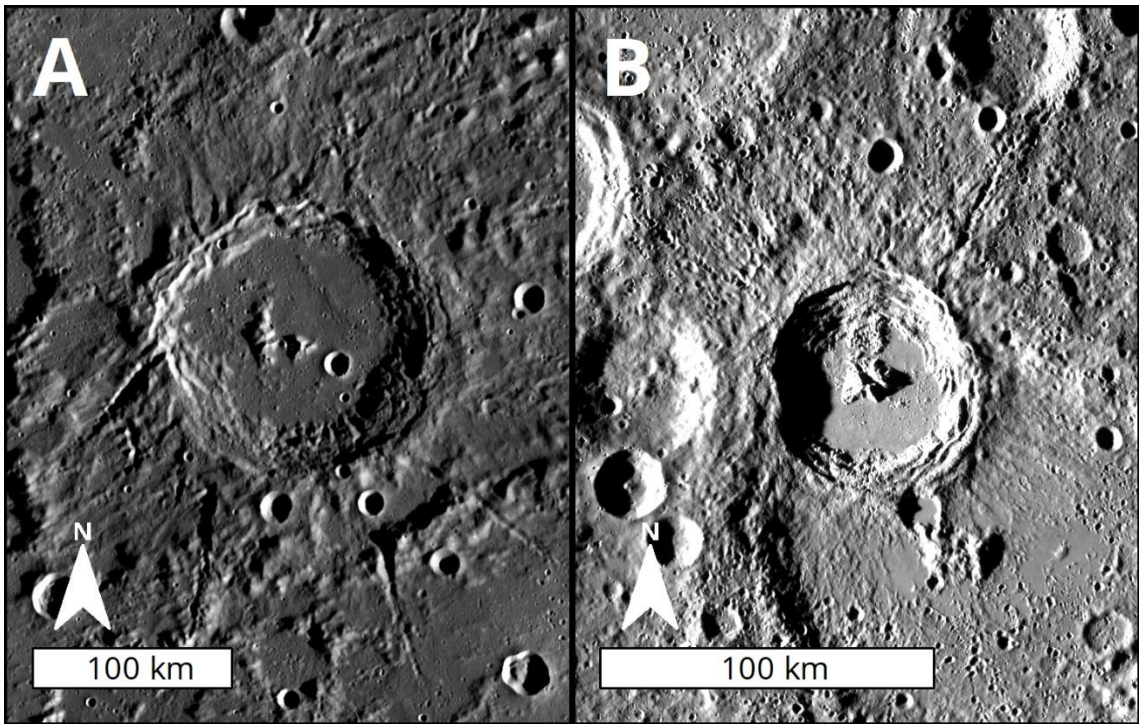

Figure 2.6: A: Mansur (224°E, 47°N) and B: Kuiper (349°E, 11°S), the namesake craters for the Mansurian and Kuiperian. Note how Mansur (A) has slight slumping of crater terracing and more craters overprinting the continuous ejecta blanket than Kuiper. Not visible in this moderate angle monochrome mosaic of the 'crater rays' that are diagnostic of the most recent (Kuiperian) craters, these are better visible in enhanced colour and low incidence angle products.

As absolute ages are dated using crater counts, the absolute age estimates will depend on the crater production functions used. A crater production function provides an estimate or average rates of cratering by size. The two functions currently favoured are those of Marchi et al. (2009), and Le Feuvre and Wieczorek (2011). As can be seen in Figure 2.7, these give differing age estimates, particularly for the Calorian/Mansurian boundary. For simplicity for the rest of this thesis I use the boundaries from the Marchi et al. (2009) crater production function.

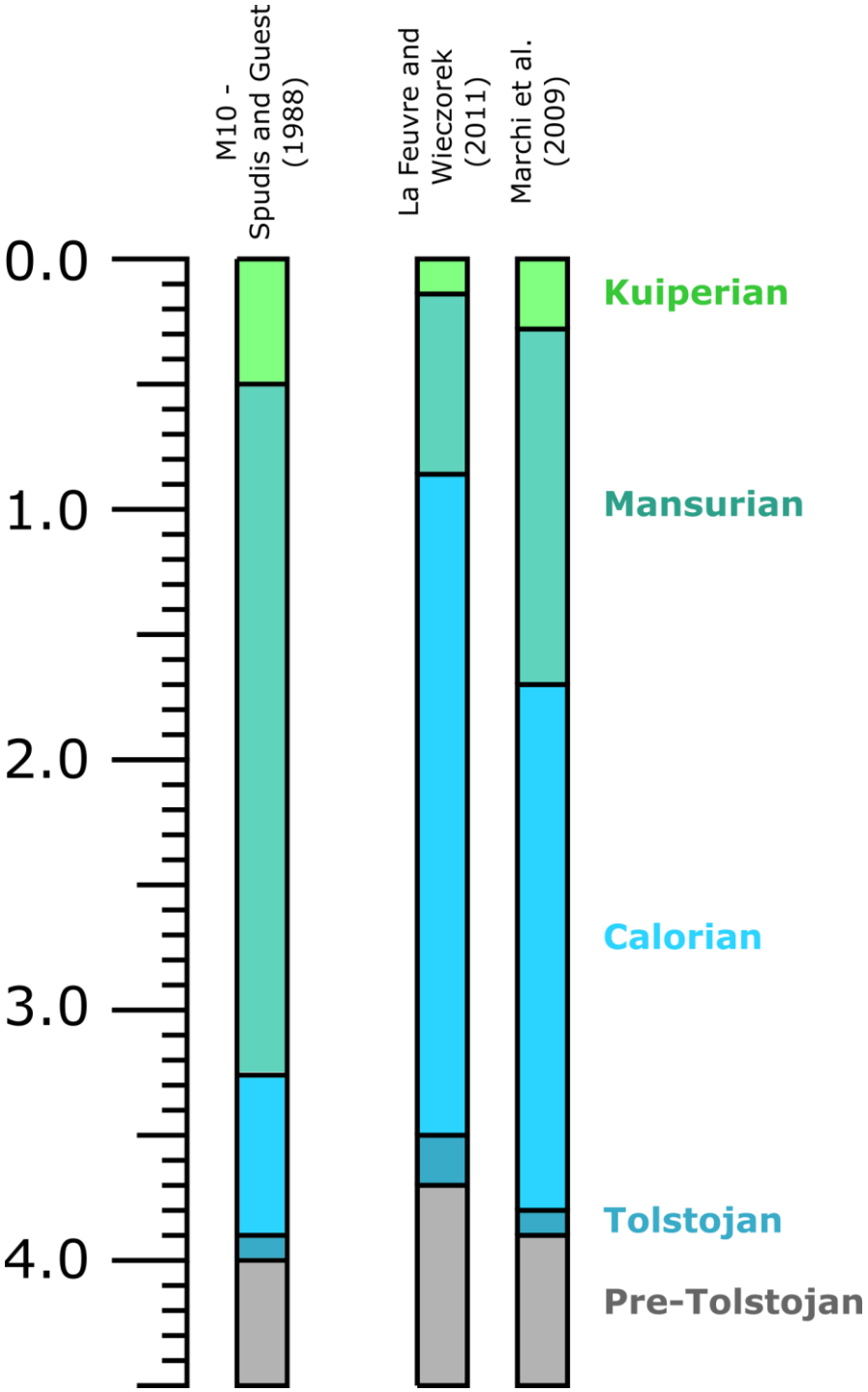

Figure 2.7: Mercury time-stratigraphic series, as devised by Spudis and Guest (1988)*, and revised in the MESSENGER era by Banks et al.* (2017) *and Ernst et al.* (2017) *with the crater production functions of Le Feuvre and Wieczorek* (2011) *and Marchi et al.* (2009)*.*

2.2.2.5 Early crust

The current surface of Mercury is dominated by volcanic, and impact derived units (Section 2.2.2). The global population of large (D>300 km) basins

(Fassett et al., 2011; Orgel et al., 2020) suggests global resurfacing at around 4.0-4.1 Ga (Marchi et al., 2013). Therefore, there will be no in-situ primary crust at Mercury's surface at the present day.

As Mercury is a differentiated body, it will very likely have had a magma ocean during its formation (Brown and Elkins-Tanton, 2009). Therefore, conventionally it would have formed a flotation crust. The surface composition of Mercury at the present day is dominated by forsterite, plagioclase (both more anorthitic and albitic), and enstatite (Namur and Charlier, 2017). This precludes the presence of an anorthitic flotation crust similar to the Moon (Nittler et al., 2011). Geochemical results from MESSENGER show Mercury's surface to be Fe-poor (Nittler et al., 2011). Given, as well, that the NSPs are Fe-poor and thought to represent magmas derived from a high degree of partial melting (Weider et al., 2012), it follows that Mercury's mantle is also Fe-poor (Nittler et al., 2011). Therefore, Mercury's silicate portion and so magma ocean would be low density. This would be unlike the magma ocean of the Moon (Riner et al., 2009), with anorthite not being buoyant enough to float.

Experimental petrological modelling of melts simulating Mercury's magma ocean showed the only mineral to remain buoyant was graphite (Vander Kaaden and McCubbin, 2015). The thickness estimate of a graphite flotation crust is 1- 100m, although this is highly speculative (Vander Kaaden and McCubbin, 2015). This process is shown in Figure 2.8. The experimental result is consistent with detections of higher concentrations of carbon (<5 wt.%) in low reflectance material at Mercury's surface (Peplowski et al., 2016). As some impacts excavate low reflectance material, it is possible that portions of the primary crust are still being excavated (Peplowski et al., 2016). A graphite primary crust is supported by Mercury appearing rich in carbon compared to terrestrial planets (Murchie et al., 2015a; Peplowski et al., 2015a).

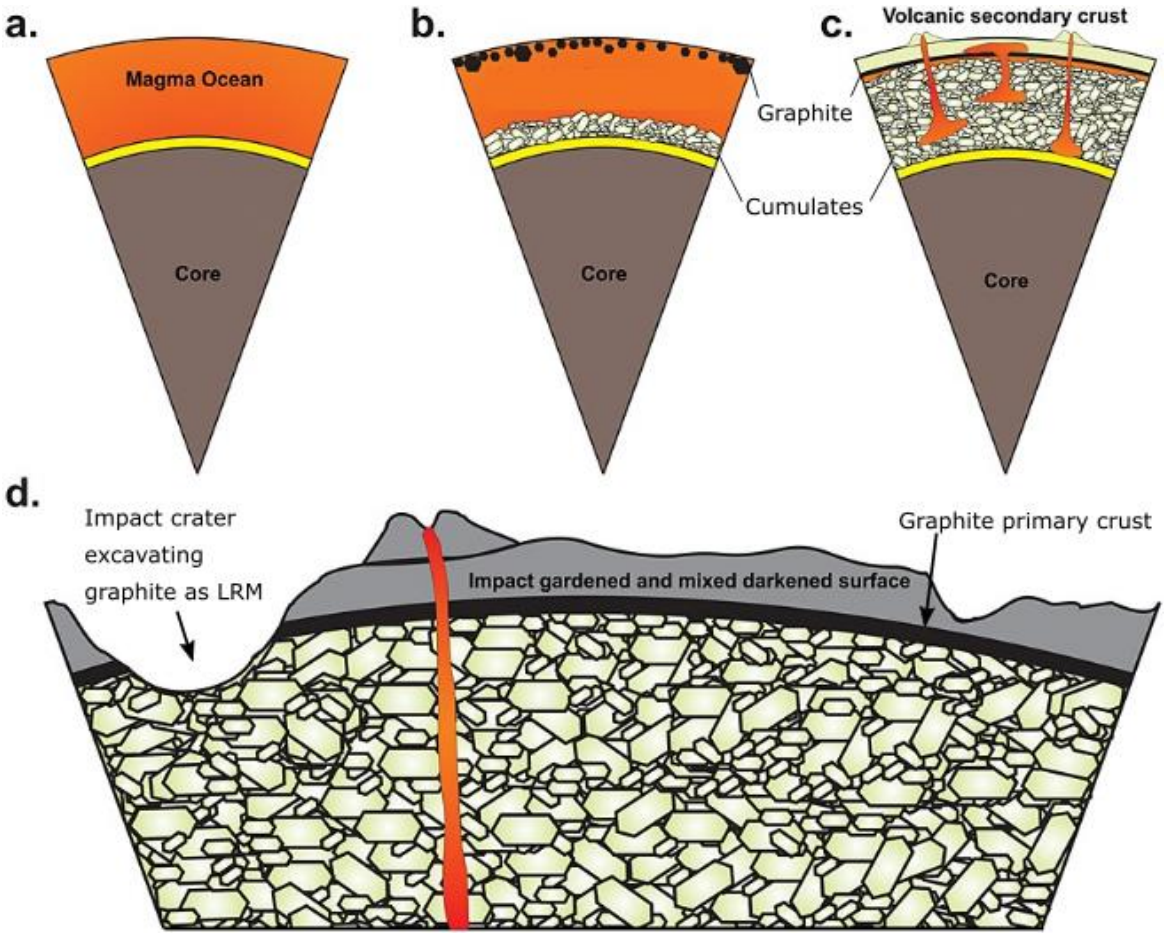

Figure 2.8: Cartoon illustration of the formation of a graphite primary crust on Mercury from Vander Kaaden and McCubbin (2015). A: Mercury's low-density magma ocean. B: phases begin to crystalise out of the ocean; most are denser and so sink and form cumulates; only graphite is able to float and form Mercury's primary crust. C: Crystallization of the magma ocean continues, with partial melts and volcanism forming Mercury's secondary crust, burying the graphite layer. D: Later impacts can excavate the graphite layer as LRM. Image adapted from Vander Kaaden and McCubbin (2015).

2.2.3 Unexpected Volatiles

One of the unexpected discoveries of the MESSENGER mission was multiple lines of evidence of volatile species on Mercury.

2.2.3.1 Hollows

Hollows are pristine, flat-floored, irregular depressions (Blewett et al., 2011), typically up a few km across and tens of metres deep (Blewett et al., 2016, 2011; Thomas et al., 2014a). The floors are flat and uncratered (Figure 2.9A).

Their pristine appearance and uncratered floors suggest they are geologically young. Hollows have a distinctive bright aqua blue colour in the MESSENGER enhanced colour image product (see section 3.2.1.6 for more information (Blewett et al., 2011). Hollows often appear in clusters, and large hollows appear to be the result of multiple hollows coalescing (Blewett et al., 2011).

Hollows are found globally (Thomas et al., 2014a), however due to their small size and MESSENGER's eccentric orbit, relatively few have been found in the low southern latitudes (14 locations south of 50°S) (Thomas et al., 2014a). Thomas (2014a) found a very weak correlation between hollows and proximity to Mercury's hot poles (see section 2.1.1), but this does not appear to be the dominant factor in hollow location. Hollows appear to be found more often on equator (and thus sun) facing slopes in a subset of known exemplar locations, (Blewett et al., 2013, 2011). This has not been tested on the global population. Geologically, hollows are found predominantly in and close to impact craters and basins, on crater floors, walls, and ejecta (Blewett et al., 2013, 2011; Thomas et al., 2014a). There a few sites of hollows away from impact structures (Thomas et al., 2014a). Some of these isolated patches are found with low-reflectance halos (Xiao et al., 2013a). Almost all hollows are found near low reflectance material (LRM) (Blewett et al., 2013; Denevi et al., 2009; Thomas et al., 2014a).

The location of hollows often on crater ejecta or walls is unlikely for volcanic features, nor do hollows resemble explosive volcanism found on Mercury (Section 2.2.3.2). The most likely formation mechanism is loss of volatile species when exposed to Mercury surface conditions (Blewett et al., 2011). This would help explain the present-day distribution near craters, as impact cratering will excavate material from depth allowing new volatiles to be exposed at the surface. As hollows are almost always co-located with LRM, this has been used to suggest that LRM hosts the volatile species (Thomas et al., 2016). The exact method of volatile loss is not agreed. Evidence for a

preference for hollows to form at hot poles or on equator-facing slopes has been used to suggest insolation may drive volatile release (Blewett et al., 2013; Thomas et al., 2014a). These observations cannot be explained by alternative formation mechanisms such as micro-meteorite bombardment (Blewett et al., 2011), which would be equally efficient at all longitudes and slope faces. Insolation driven volatile loss can account for the floors of hollows appearing flat, with similar depths globally (Blewett et al., 2016). This indicates depths after which hollows cannot deepen. As volatiles must make up a proportion of the hollow forming layers, non-volatile material will be left and create a growing lag layer as volatiles are lost. Depending on the concentration of volatiles at a certain depth this lag would be too thick for volatile loss via solar processes.

The volatile species responsible for hollows is unknown and a key question for future research (Rothery et al., 2020). Current evidence from absorption values from MDIS-WAC images shows that sulphides are present at locations of hollows (Lucchetti et al., 2018; Vilas et al., 2016). Experimental work shows CaS and MgS decompose at Mercury surface-like conditions (Helbert et al., 2013). At present, these are the favoured candidates to be the volatile species involved in hollow formation (Blewett et al., 2018).

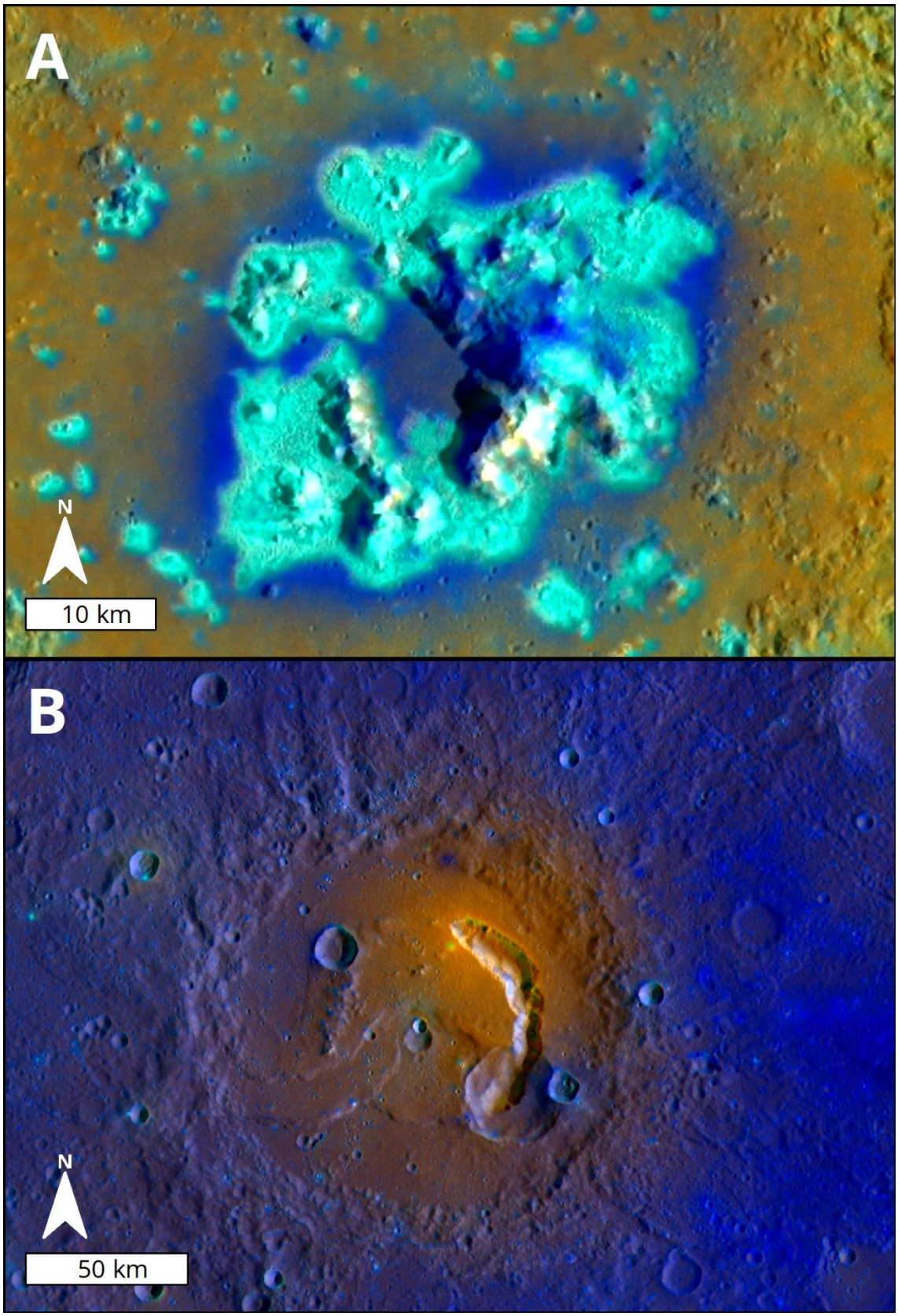

Figure 2.9: Volatile driven landforms on Mercury seen in the enhanced colour mosaic. A: Hollows in Eminescu crater (114°E, 10°N). B: Explosive volcanic vent, with bright diffuse 'halo' (facula) in Picasso crater (50°E, 3°N).

2.2.3.2 Explosive Volcanism

While explosive volcanism was considered prior to MESSENGER (Rava and Hapke, 1987; Robinson and Lucey, 1997), the number (Thomas et al., 2014b) and size (Kerber et al., 2009) of examples of explosive volcanism was unexpected and is further evidence that Mercury's crust or mantle contains abundant volatiles. Sites of explosive volcanism on Mercury have been identified by a diffuse, spectrally red, halo (facula) surrounding rimless irregular depressions (Head et al., 2009; Kerber et al., 2009). An example is shown in Figure 2.9B. The irregular depressions are clearly different in shape and morphology to observed impact craters on Mercury.

The bright halos surrounding irregular pits are spectrally and texturally distinct. The halos have higher reflectance than typical plains units and red trending spectral slopes (Goudge et al., 2014; Kerber et al., 2011, 2009). The diffuse deposits also clearly mantle, and so must postdate, the surrounding plains units (Thomas et al., 2014b). Together this has been used to suggest that diffuse deposits are unconsolidated pyroclastic material. There is no evidence of any effusive deposits linked to these explosive vents, and activity is thought to be exclusively explosive.

Sites of explosive volcanism are widely distributed across the planet with Thomas et al. (2014b) identifying 124 sites. They are found on all major plains units of Mercury, and so are likely relatively young features (Thomas, 2015; Thomas et al., 2014b). To date, there is no clear single factor that explains the distribution of explosive volcanism (Klimczak et al., 2018), although clusters have been noted around the edges of large basins (Head et al., 2008). Favourable stress conditions for magma ascent are thus likely to influence the location of explosive volcanic sites.

There is a notable cluster around the edge of the Caloris basin (Head et al., 2009; Murchie et al., 2008), and this area has some of the best-studied vents.

Work by Kerber et al. (2009) on one of the vents on the Caloris basin margin suggested a minimum explosive velocity of 300 m/s. This suggested a volatile content of between 0.36 – 1.35 % (Kerber et al., 2009), a considerably higher proportion than had been thought possible on Mercury due to its thin silicate layer. Work by Rothery et al. (2014) demonstrated evidence that an explosive vent near the edge of the Caloris basin had erupted multiple times. Recent work has shown that multiple eruptions are common across known sites of explosive volcanism (Pegg et al., 2019a).

2.2.3.3 Polar volatiles

Radar observations between the Mariner 10 and MESSENGER eras found evidence of highly reflective deposits in the north polar region of Mercury (Slade et al., 1992). This was similar to results from other water ice deposits in the solar system and taken as tentative evidence for polar water ice on Mercury. MESSENGER was equipped with instrumentation, such as the MLA and GNRS, to investigate this further.

MESSENGER was able to determine that permanently shadowed regions in craters at both the north and south poles hosted reflective material (Chabot et al., 2012). Reflectance values are consistent with the deposits being predominantly thermally stable water ice (Neumann et al., 2013a; Paige et al., 2013). Direct imaging of the polar deposits showed morphology and revealed the deposits are covered by a thin layer of less reflective volatile material (Chabot et al., 2014). Observations have shown that although the Moon also has polar ice deposits in cold traps, these are quantitatively different from those on Mercury (Lawrence, 2017).

The origin of the polar ices is still an area of active research; however, some work favours delivery of water through a recent large impact, such as the Hokusai impact (Ernst et al., 2018).

2.2.4 Tectonics

Mariner 10 showed that Mercury was a tectonic planet, with many shortening structures (Murray et al., 1975; Strom et al., 1975). MESSENGER's global imaging has greatly increased our understanding of tectonism on Mercury. A global view of tectonics on Mercury has found evidence of extensive shortening in the form of lobate scarps and wrinkle ridges (Byrne et al., 2014; Watters et al., 2015), long-wavelength topographic variations (James et al., 2015; Klimczak et al., 2013), and limited local extension (Murchie et al., 2008; Ruiz et al., 2012).

Global contraction from secular cooling was considered as an origin for the shortening lobate scarps seen on Mariner 10 images (Strom et al., 1975). As a planetary interior of a one-plate planet cools, it will contract, and the surface will shorten. A global survey of lobate scarps and other shortening structures calculated a ~7 km decrease in Mercury's radius accounted for by faulting (Byrne et al., 2014).

Contractional structures from global contraction would be expected to be random in direction, as the contractional stresses would be homogeneous across the planet's surface. However, mapping of all landforms showed a non-uniform distribution, with predominantly north-south trending structures at low to mid-latitudes, and east-west trending structures in the high latitudes (Watters et al., 2015). It is not clear though how illumination bias may affect observed populations of linear features such as lobate scarps on Mercury (Fegan et al., 2017). This non-uniform distribution is consistent with patterns predicted if tidal despinning was also an important process in driving Mercury's tectonism (Figure 2.10). Tidal despinning is the relaxation of a larger equatorial bulge as a planet's rotational period slows (Melosh, 1977). A combination of tidal despinning forming contractional features early in Mercury's history and these features being reactivated, alongside new

features, with the onset of global contraction, is currently favoured. Distributions of tectonic features on Mercury also suggest influence from mantle dynamics (King, 2008; Watters et al., 2015).

Faulting on Mercury appears to have occurred early in Mercury's history as a result of tidal despinning (Watters et al., 2015). Buffered crater counts along a large lobate-scarp system suggested no significant movement on the system since 3.5 Ga (Giacomini et al., 2015). However, cross-cutting relationships of lobate scarps across different units and craters of differing degradation states appears to show that fault movement has happened to a greater or lesser extent over much of the past 3 to 4 Ga (Banks et al., 2015). Together these results suggest the majority of movement on lobate scarps happened before 3.5 Ga but has continued as global contraction slows. High-resolution images from MESSENGER's low-altitude campaign show small thrust fault scarps tens of metres high (Watters et al., 2016). These features appear pristine, and cross-cut small fresh impact craters indicating they are geologically recent. Given the rate of landscape evolution on Mercury (Fassett et al., 2017), and the small size of the scarp, these faults are estimated to have an age of less than 50 Ma. This suggests that Mercury may still be tectonically active today (Watters et al., 2016).

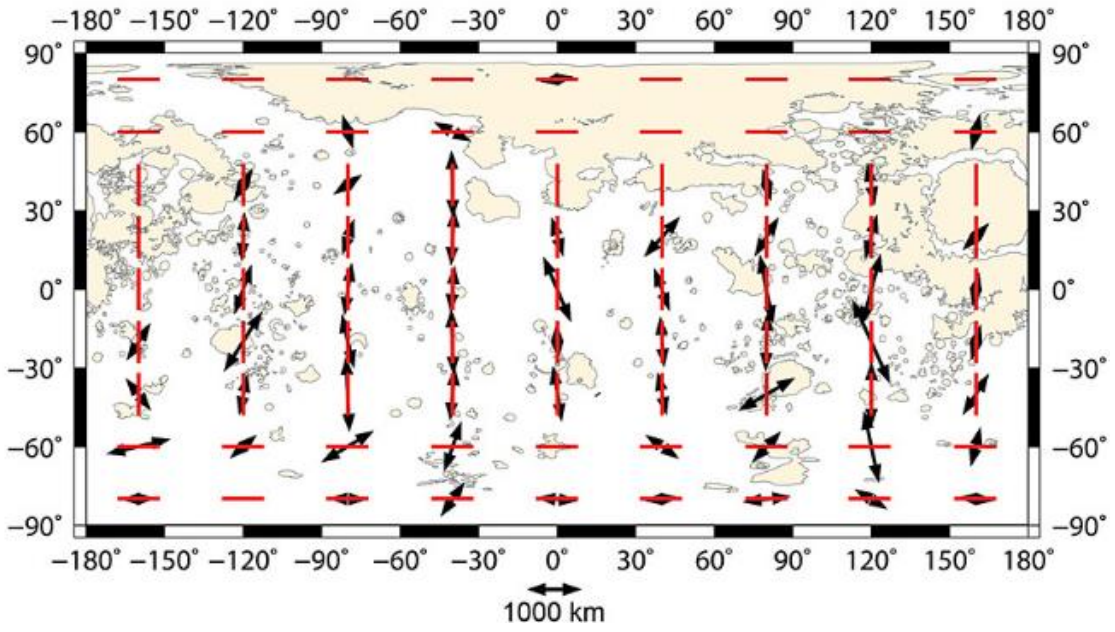

Figure 2.10: Distribution of contractional tectonic features compared to modelled distributions from Watters et al. (2015). Black arrows show the length weighted orientation means of features in 40° by 20° boxes. This is compared to modelled orientations of tectonic features formed by a combination of global contraction and tidal despinning (red lines).

2.2.5 Mercury's Origin

Mercury's origin has been difficult to account for with accretion from purely chondritic material. Mariner 10's discovery of Mercury's large iron core means that credible models must account for the loss of a large part of the silicate portion. MESSENGER's discovery that Mercury is enriched in volatiles, through hollows, and explosive volcanism (Section 2.2.3) has meant models for the formation of the planet must account for this too.

The discovery of the high proportion of volatiles at Mercury has cast doubt on collision-based models, such as a single large impact (Benz et al., 1988) or a 'hit and run' impactor (Asphaug and Reufer, 2014). These models explain the large ratio of metal to silicate, as such impacts would only re-accrete a small portion of the outer silicate layer. Given lighter elements will preferentially be lost, as well as causing a period of intense heating that can

cause loss of volatiles, this would leave the planet depleted in volatiles (Peplowski et al., 2011). Formation involving partial vaporization or stripping of the silicate mantle by the solar wind (Cameron, 1985), would also preferentially strip away Mercury's volatile component.

Currently favoured models prefer accretion from more than just ordinary chondritic material in the protoplanetary disk, such as iron-rich accretion (Weidenschilling, 1978), aided by the early solar magnetic field promoting the concentration of iron-rich aggregates at around Mercury's orbit (Kruss and Wurm, 2018); or gradients of materials in the protoplanetary disk (Ebel and Alexander, 2011).

2.3 BepiColombo

The next spacecraft mission to Mercury is the joint European Space Agency (ESA) and Japanese Aerospace Exploration Agency (JAXA) BepiColombo mission (Benkhoff et al., 2020 (in press), 2010) currently in flight. It comprises 3 spacecraft, an ESA-led Mercury Planetary Orbiter (MPO), a JAXA-led Mercury Magnetospheric Orbiter (MMO) (Murakami et al., 2020), and a transfer module without scientific payload (MTM) (Figure 2.11). BepiColombo is scheduled to complete Mercury orbital insertion on 5th December 2025, and science operations underway by May 2026.

BepiColombo's exploration of Mercury's surface will be led by the instrumentation on the MPO (Figure 2.11). Thanks to a different cooling strategy to MESSENGER the MPO will have a far less eccentric orbit, with much lower orbital height over the southern hemisphere. This will greatly improve our understanding of the geology of the southern hemisphere (Rothery et al., 2020). The key instruments for understanding the surface geology are the SIMBYO-SYS imaging system (Cremonese et al., 2020); BELA laser altimeter (Steinbrügge et al., 2018), MERTIS thermal imaging spectrometer (Hiesinger et al., 2020), MGNS neutron and gamma-ray

spectrometers (Mitrofanov et al., 2010), and MIXS X-ray spectrometer (Bunce et al., 2020 (in press); Fraser et al., 2010). All these instruments will provide wider coverage and more precise, or higher-resolution data than their equivalents on MESSENGER.

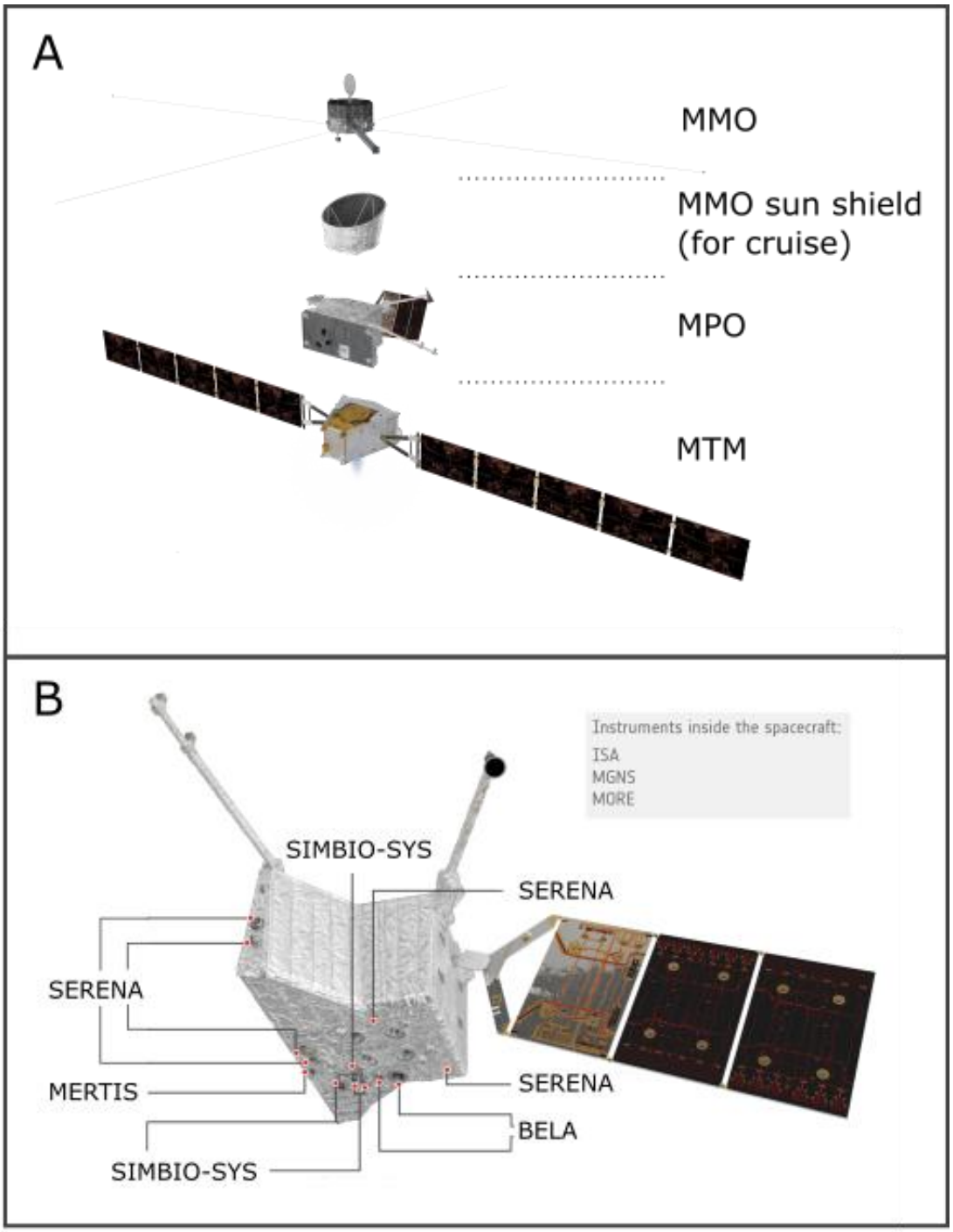

Figure 2.11: BepiColombo. A: Exploded BepiColombo spacecraft stack in cruise configuration. B: Instrumentation on the MPO. Images adapted from ESA.

The MESSENGER mission has revolutionised our understanding of Mercury. However, there remain many unanswered questions (Rothery et al., 2020). To fully understand what questions need to be addressed by BepiColombo, we must review the available data from MESSENGER. An effective way to systematically review the data available for an area, and characterise the geology is through geological mapping. Mapping was not a MESSENGER deliverable, and no quadrangle level mapping was planned, although the MESSENGER team have produced a low resolution global geological map (Prockter et al., 2016). To prepare for BepiColombo, and identify science targets, there has been a coordinated effort to produce a series of coherent quadrangle level maps (Galluzzi et al., 2017). These will be merged to form a global basemap (Galluzzi et al., 2016, 2017). It was as part of the program that I have mapped the Derain (H-10) quadrangle of Mercury.

2.4 This thesis in the context of Mercury exploration.

To make best use of BepiColombo, it is essential to interrogate MESSENGER data to determine what can be answered before BepiColombo's arrival. This will help to determine targets for data acquisition and better refine the science goals of the mission (Rothery et al., 2020). I have already indicated the scope of this thesis in Chapter 1. Here I make a few further remarks in context.

As part of this thesis, I constructed a geological map of the Derain (H10) quadrangle of Mercury (Chapter 4 and Chapter 5) as part of an effort to produce a coherent geological map in advance of BepiColombo (Galluzzi et al., 2016, 2017). This mapping then led on to further, more detailed studies on features of interest (Chapter 6 and Chapter 7). When I started the map, my research questions were:

- What is the geological history of the Derain quadrangle, and how does this link to the global history of Mercury? (Addressed in Chapter 3 and Chapter 4)
- Are there mappable plains units visible in morphological data beyond intercrater and smooth plains? (addressed in Chapter 4). After an initial survey of the quadrangle, I also decided to consider how have pre-existing structures affected small areas of volcanic resurfacing? (Addressed in Chapter 5)

Observations of a previously unreported type of feature (slope lineae) that I made during my mapping led me to pursue an additional question about the nature and distribution of downslope mass movements on Mercury (addressed in Chapter 6). I aimed to find how widespread slope lineae and other downslope mass-movement features are, and how they may have formed.

CHAPTER 3
MAKING A GEOLOGICAL MAP OF THE DERAIN (H-10) QUADRANGLE.

3.1 Previous Geological Mapping of Mercury

For mapping purposes, Mercury is divided into 15 quadrangles of similar size. The first quadrangle level mapping of Mercury was compiled using Mariner 10 'fly-by' images. Given that Mariner 10 imaged only approximately 50% of Mercury's surface (Figure 3.1) the mapping series had near-complete coverage of six quadrangles (H-02, H-03, H-06, H-07, H-11 and H-12), and a further three quadrangles (H-01, H-08, and H-15) had partial mapping coverage due to poorly lit images (with the majority of the frame in shadow) over a significant proportion of the quadrangle.

Unlike Mariner 10, MESSENGER was able to orbit Mercury, so obtained global image coverage, allowing mapping of all quadrangles. A 1:25 million scale map is being produced by members of the MESSENGER team (Prockter et al., 2016). This will be the first global geological map. While the Prockter et al. (2016) global map will give an overview of Mercury's geology, it will not be at a sufficiently large scale for target identification and mission planning for the ESA-JAXA BepiColombo mission. Therefore, a coordinated European mapping programme is underway to produce new maps of every quadrangle at 1:3 000 000. Mapping in co-operation avoids duplication of work and means quadrangle boundaries are seamless, ensuring a coherent global product. At time of writing, there are four published maps (Galluzzi et al., 2016; Guzzetta et al., 2017; Mancinelli et al., 2016; Wright et al., 2019) with the

work described here, and shown in the accompanying map sheet, being the fifth. Mapping of most of the remaining quadrangles is in progress.

Two quadrangles, Borealis and Derain, are also undergoing mapping under the United States Geological Survey (USGS) mapping program (Ostrach et al., 2019; Whitten et al., 2018), but these maps are being completed with little liaison with the European quadrangle mapping and will exist as stand-alone products.

3.1.1 Why Derain?

The first task in this project was to decide upon a quadrangle to begin mapping. At the start of the project, there were three published maps (Galluzzi et al., 2016; Guzzetta et al., 2017; Mancinelli et al., 2016), and two other quadrangles where mapping had started. While I was making my selection, three other quadrangles had not been started but already had mappers allocated. This left seven possible quadrangles: H-09, and H-10 in the equatorial region; H-11, H-12, and H-13 in the southern mid-latitudes; and H-15 in the South Polar region. The state of mapping when I was selecting a quadrangle is shown in Figure 3.2.

MESSENGER had an elliptical orbit around Mercury to avoid overheating. Periapsis occurred over the northern hemisphere; therefore, the resolution of the imagery is considerably better for the northern hemisphere. The elliptical orbit means the laser altimeter tracks have poor spatial coverage outside the high northern latitudes, and no coverage in the southern hemisphere as the instrument was out of range. Given the better data quality in the northern hemisphere, it seemed logical to select an equatorial, rather than a southern hemisphere quadrangle. It also seemed logical to map a quadrangle where at least one adjoining quadrangle had either been mapped or was undergoing active mapping, to allow my mapping to be more easily integrated into the global map.

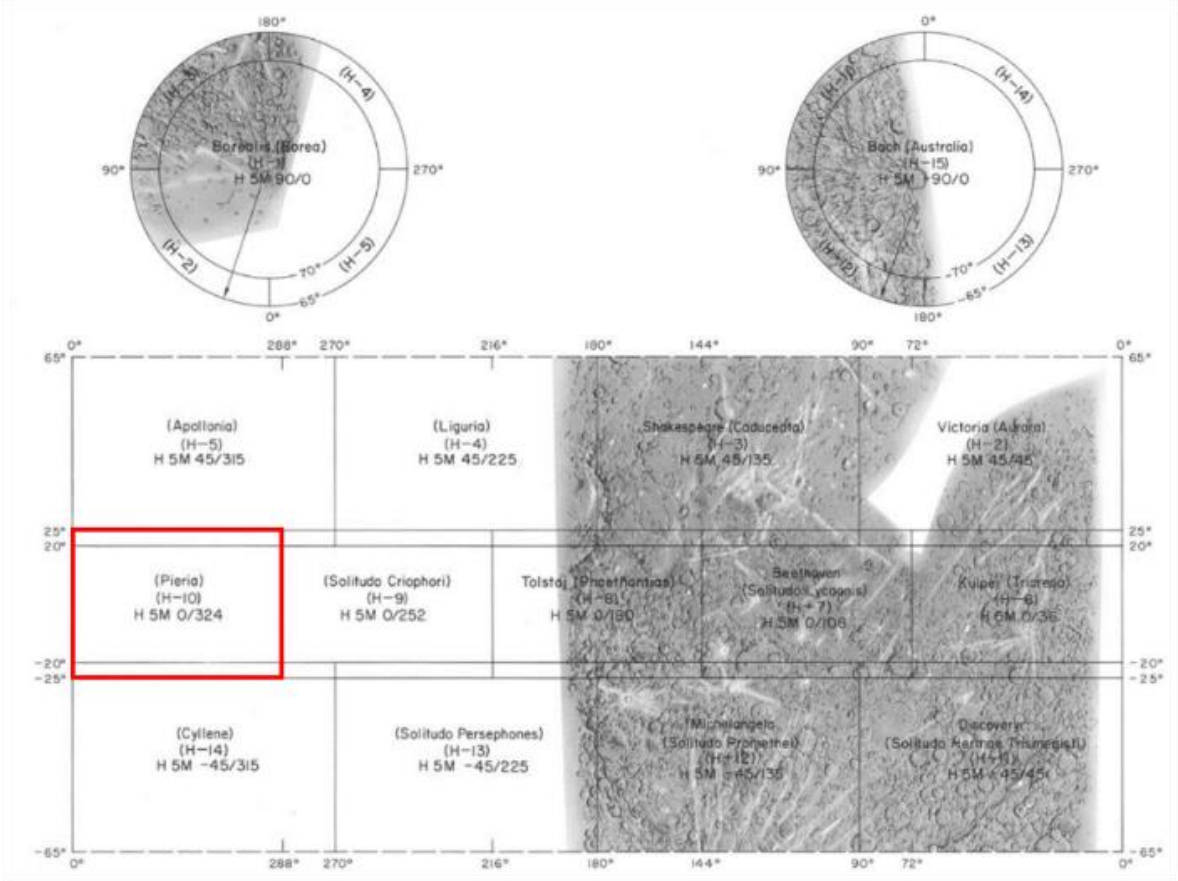

Figure 3.1: Mariner 10 Image coverage (from Davies et al., 1978). The Derain quadrangle (highlighted) was referred to as Pieria in the Mariner 10 era.

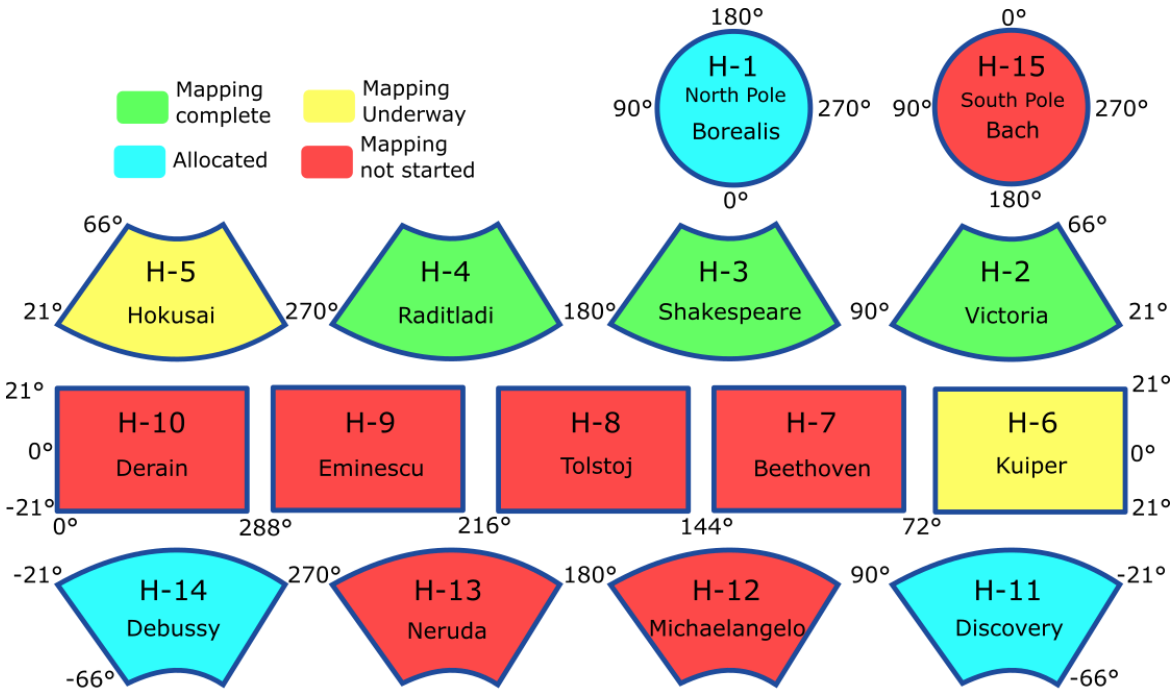

Figure 3.2: Quadrangle mapping status in 2016 at the start of the project

I spent the first six weeks of my project looking at the available quadrangles and evaluating some of the key geological features. All quadrangles contain a variety of diverse and engaging geology. Consequently, there will be many promising areas of further research, including features and topics which may not become apparent until studied in detail. When evaluating scientific interest, I primarily looked for evidence of tectonic and volcanic activity as this was one of my key areas of scientific interest. When examined from a volcanic and tectonic perspective, I found Tolstoj (H-8), Derain (H-10) and Neruda (H-13) to be particularly interesting. All available quadrangles contained examples of faulting and documented explosive volcanism, but Tolstoj and Derain contained more examples of volcanic smooth plains units, as well as basins filled with smooth plains units. As Tolstoj and Derain are equatorial quadrangles with interesting geological features, they were my preferred quadrangles.

As well as being equatorial, the Derain quadrangle is located in the hemisphere of Mercury not imaged by Mariner 10. It also had the logistical advantage of having two adjoining quadrangles currently being mapped, making it easier to merge with other quadrangle maps as part of the European mapping program. This logistical advantage, along with Derain appearing as a quadrangle that fitted my scientific interests, led to my choice of the Derain (H-10) quadrangle to map. Various views of the Derain quadrangle can be seen in Figure 3.3, Figure 3.4, Figure 3.5.

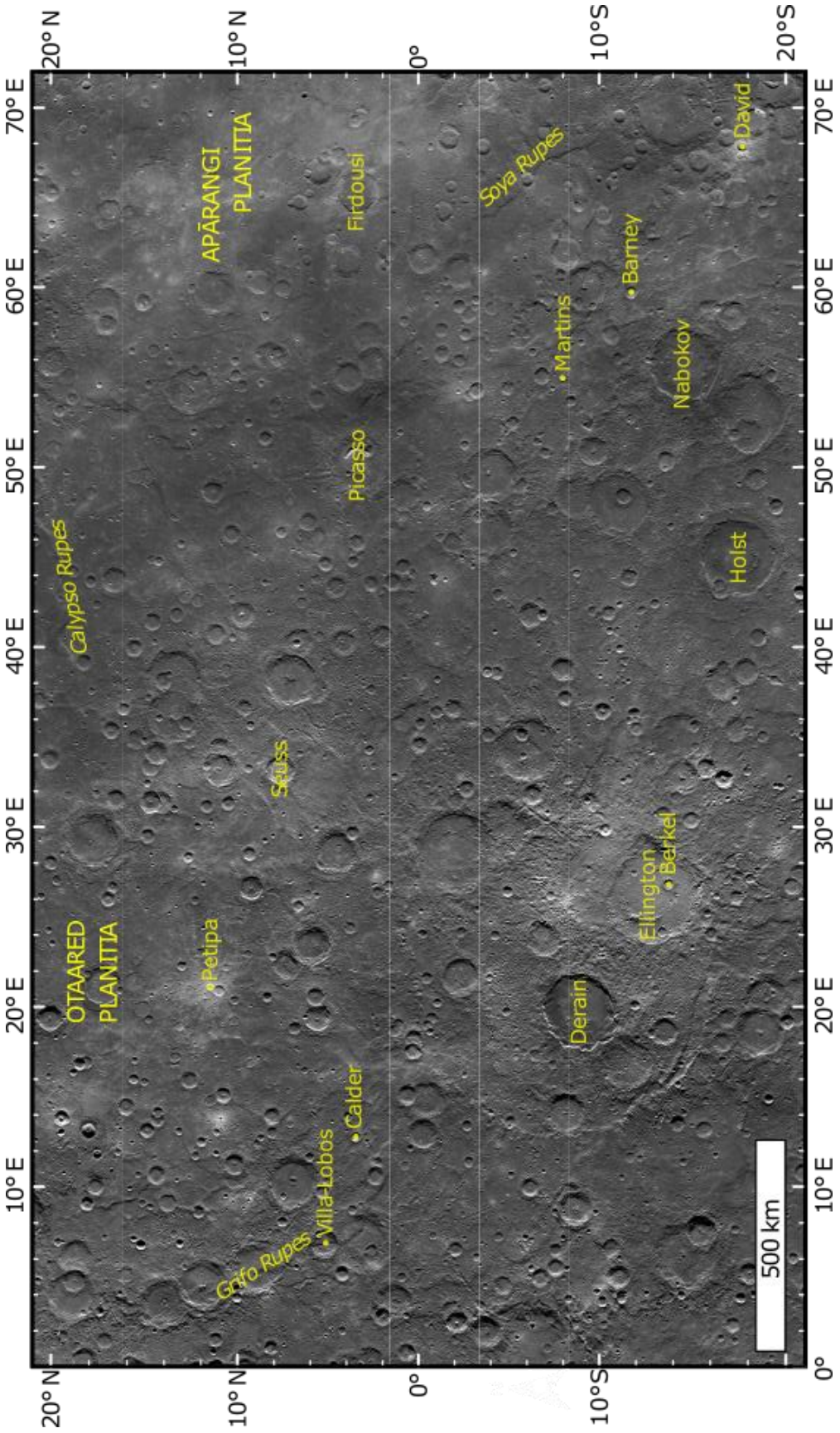

Figure 3.3: Overview of the Derain (H-10) quadrangle, showing nomenclature on an MDIS BDR basemap.

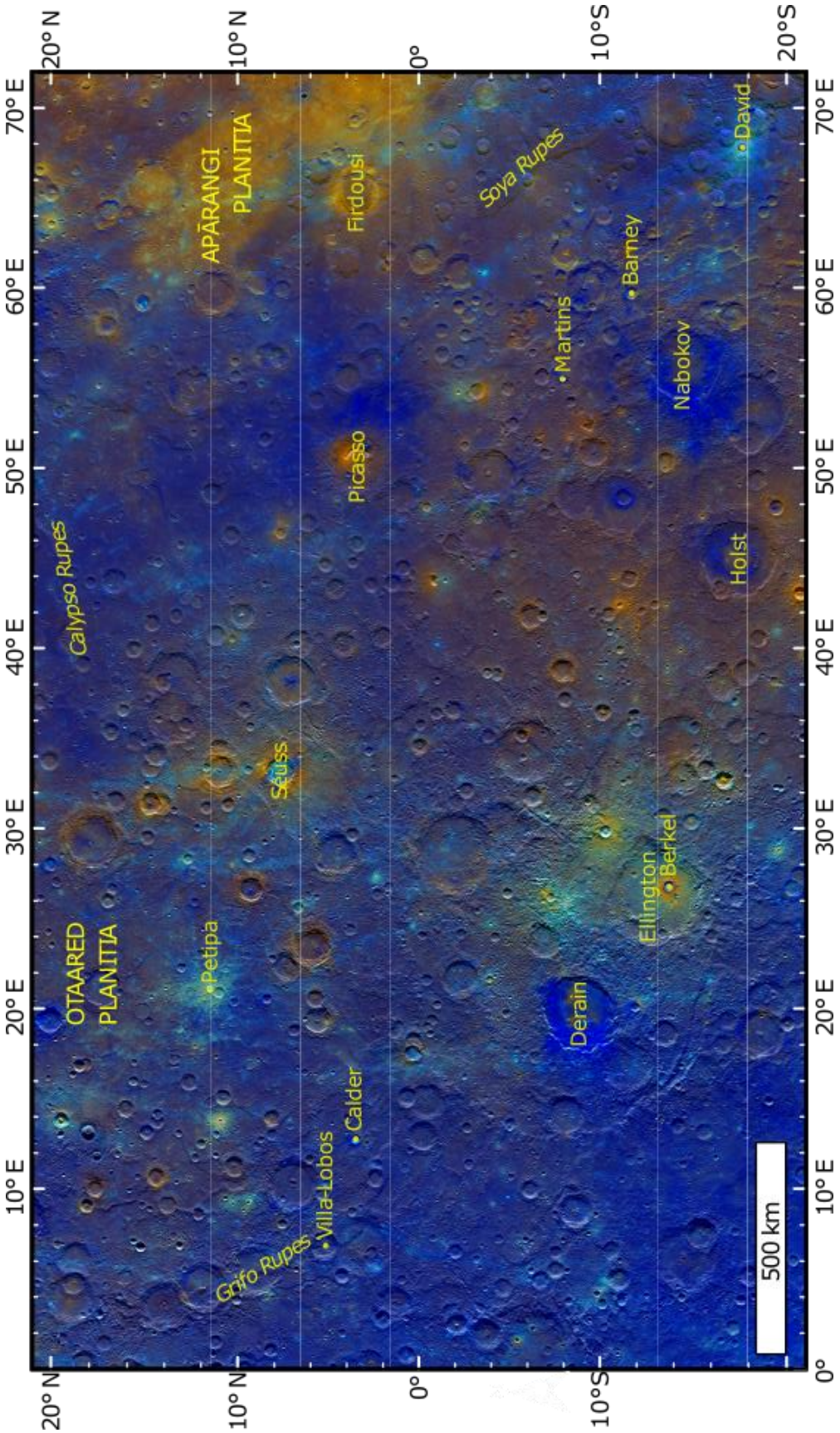

Figure 3.4: Overview of Derain (H-10) quadrangle showing enhanced colour basemap and nomenclature

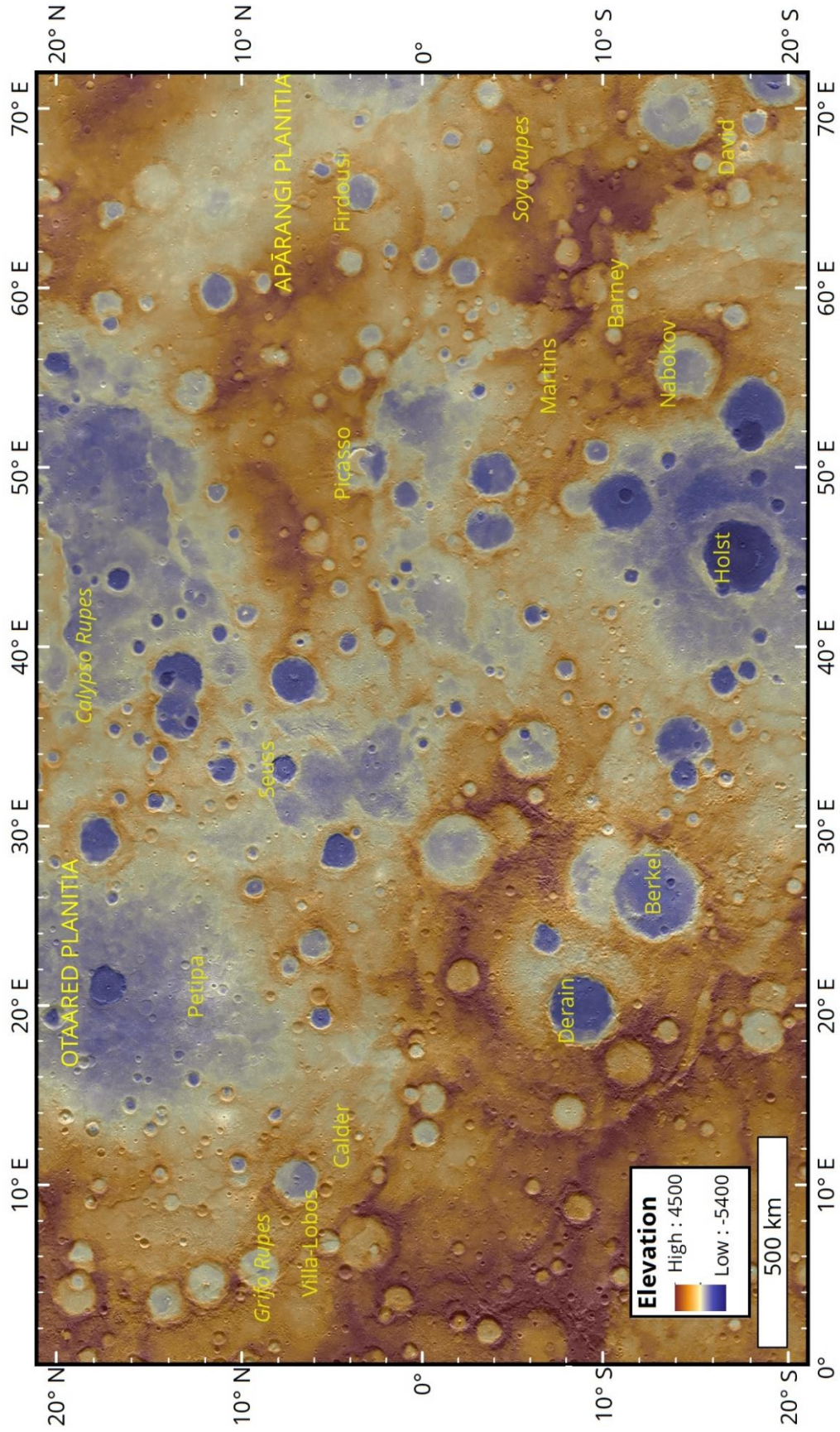

Figure 3.5: Topography of the Derain Quadrangle from the global DEM. Hot colours are areas of high topography, cold areas low topography.

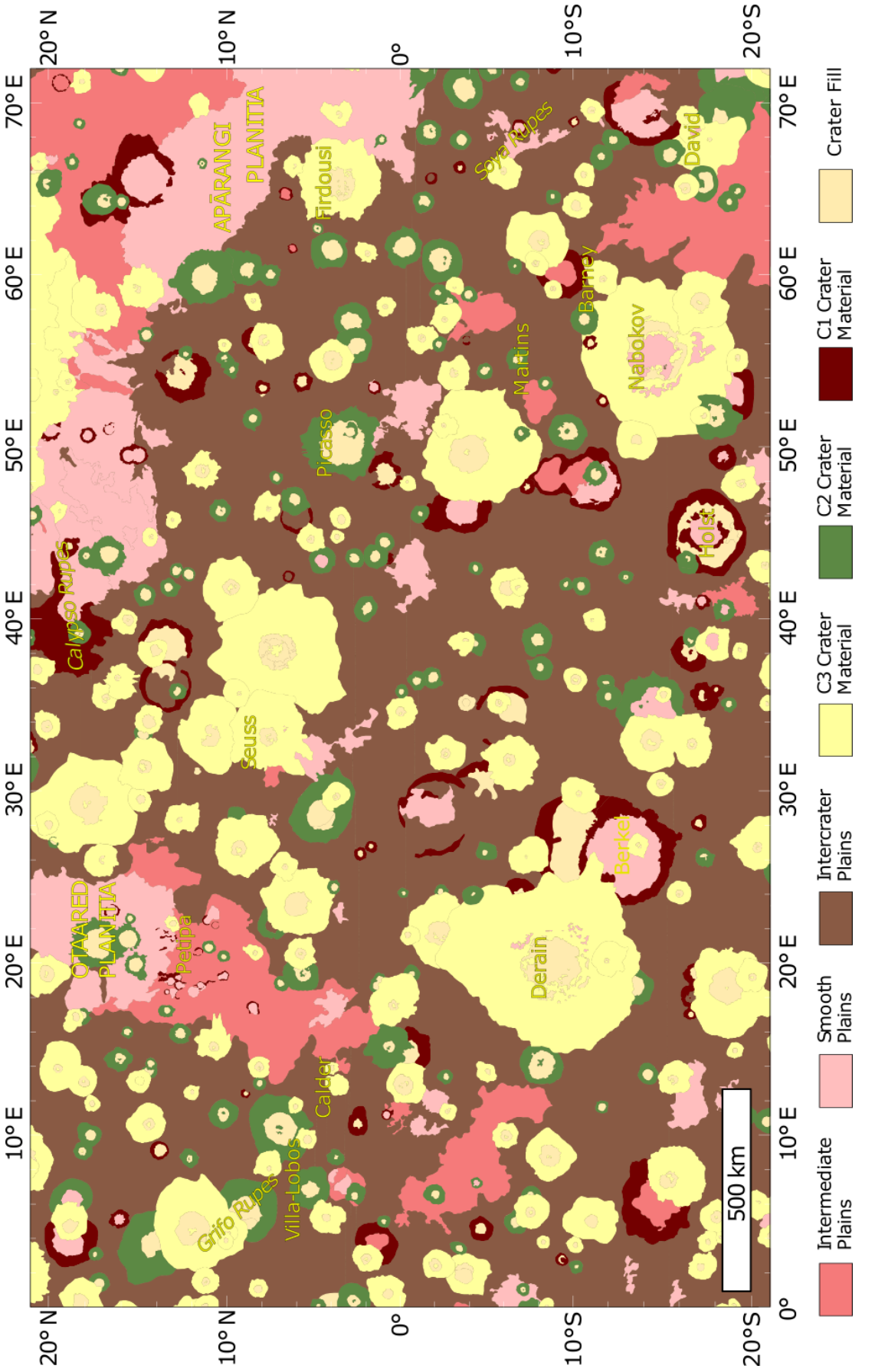

Figure 3.6: Overview of my mapping of the Derain quadrangle. The full-scale map is available in the accompanying map sheet (Appendix A).

3.2 Data

3.2.1 Basemaps

Mapping was completed using a variety of basemaps all produced by the USGS from MESSENGER data. All are available through the USGS's Planetary Data System (PDS). Unless otherwise stated all products were natively projected onto the 2015 Mercury datum with a planetocentric radius of 2439400 m and controlled by the global DEM. Throughout this section I express the size of the pixels on the basemaps in metres per pixel (mpp); however, it would be more accurately reported as pixels per degree, as the average pixel size varies slightly by latitude. These differences are so slight, particularly across an equatorial quadrangle such as Derain, that I have chosen to state resolution in mpp as this better articulates the scale of features visible. The difference in sun position for incidence angles on Mercury is shown in Figure 3.7, and a comparison between the various basemaps can be seen in Figure 3.8.

3.2.1.1 BDR (Basemap Reduced Data Record) 166 mpp Mosaic Basemap

I completed the majority of mapping using the BDR 166mpp average monochrome basemap of mosaiced images. It is the highest resolution mosaic with an average global resolution of 166 mpp. It is composed of images from multiple viewing geometries, but where possible uses imagery with moderate incidence angles. Images from both the narrow and wide-angle camera are used in the mosaic. The moderate incidence angle images make the BDR basemap good for seeing most geomorphology. The BDR mosaic can be seen in Figure 3.3.

3.2.1.2 BDR 250 mpp Mosaic Basemap

The 250 mpp average basemap is a moderate incidence angle mosaic produced early in the MESSENGER mission. While it has a lower spatial resolution than the 166 mpp BDR basemap, there are areas where this mosaic has better images for mapping or fewer joints in the mosaic than the BDR 166 mpp mosaic. As it was produced earlier in the MESSENGER mission, it is projected onto the old 2010 datum with no topographic control and a radius of 2440000 m, therefore I had to manually move linework mapped onto this mosaic onto the new mosaics and thereby to the new datum.

3.2.1.3 Low incidence angle 166 mpp Mosaic

The low incidence angle basemap is a mosaiced data set composed of low incidence angle (i.e., sun near overhead) images. The mosaic is composed of images with low emission angles and incidence angles close to 45°. It has an average resolution of 166mpp. Low incidence angle imagery displays albedo differences, and very few areas are in shadow, but surface geomorphology and texture are difficult to see for the same reason.

3.2.1.4 High incidence angle (west-facing) 166 mpp Mosaic

The west-facing high incidence angle mosaic comprises images with an ideal incidence angle of 78° with consistent illumination from the west. It is projected to an average 166mpp. This basemap was useful for providing images of areas in shadow on the BDR mosaic.

3.2.1.5 High incidence angle (east-facing) 166 mpp Mosaic

The east-facing high incidence angle mosaic comprises images with an ideal incidence angle of 78° with consistent east illumination. It is projected to an average 166 mpp. This basemap was useful for providing imagery for areas in shadow on the main BDR mosaic.

3.2.1.6 Enhanced Colour Mosaic

'Enhanced colour' (Figure 3.4) is a standard MESSENGER product that accentuates subtle colour differences. It was created using MDIS-WAC images in the 430, 750, 1000 nm bands. It places the second principal component in the red, the first principal component in the green, and the ratio of 430/1000 nm bands in the blue channel (Denevi et al., 2016; Denevi et al., 2009). Why these particular spectral properties were chosen has not been publicly released by the MESSENGER team. The first principal component should correspond to the standard reflectance. The second principal component should represent the spectral slope from short (more blue) to long (more red) wavelengths, and so a higher value will represent a more red pixel. The ratio of 430/1000 nm bands for the blue channel value is a ratio of blue to near-infrared, and so a higher value represents a more blue area. Constructing the basemap this way means that the red areas are generally 'redder' than the global average, and the blue areas generally 'bluer'.

Enhanced colour helps provide spectral context to morphological observations. It can be used in determining plains types (Denevi et al., 2013; Whitten et al., 2014). It is invaluable in mapping putative explosive volcanic deposits and hollows (Blewett et al., 2011; Prockter et al., 2010), which are identified by their form and their distinctive red facula or aqua-blue colours, respectively.

3.2.1.7 665 mpp Stereo Digital Elevation Model

The only topographic product that covers the whole of the Derain quadrangle is the global stereo-derived DEM (Becker et al., 2016). MDIS had no inbuilt stereo capability, so the DEM was created using unsupervised image pairs taken with different lighting conditions. The DEM was then verified using elevation data from the Mercury Laser Altimeter on MESSENGER (Becker et al., 2016). The DEM has a horizontal resolution of ~665 mpp, the vertical

precision, or an accompanying error raster has not been released. This is a major limitation of this dataset. The precision is dependent in the quality of the stereo pairs and so will highly variable across the planet. DEM's using supervised stereo pairs from MESSENGER images have achieved vertical precision of ~30 m (Preusker et al., 2017). Derain in the DEM is shown in Figure 3.5.

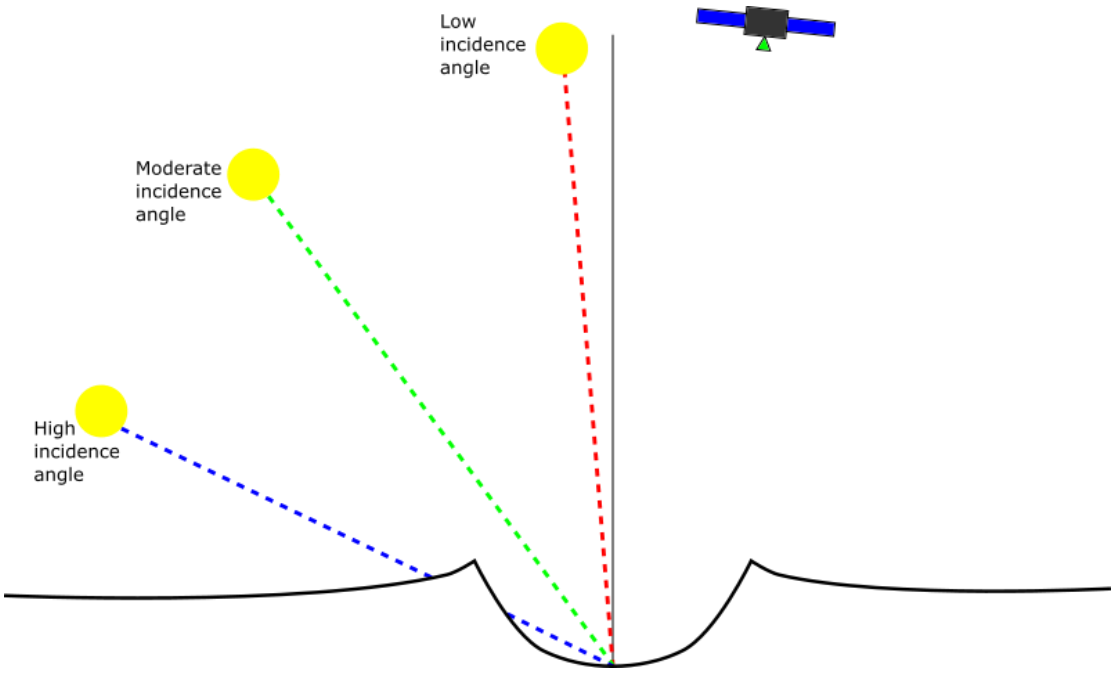

Figure 3.7: Cartoon showing difference in sun position in low (LOI), moderate, and high (HiE, HiW) incidence angle images.

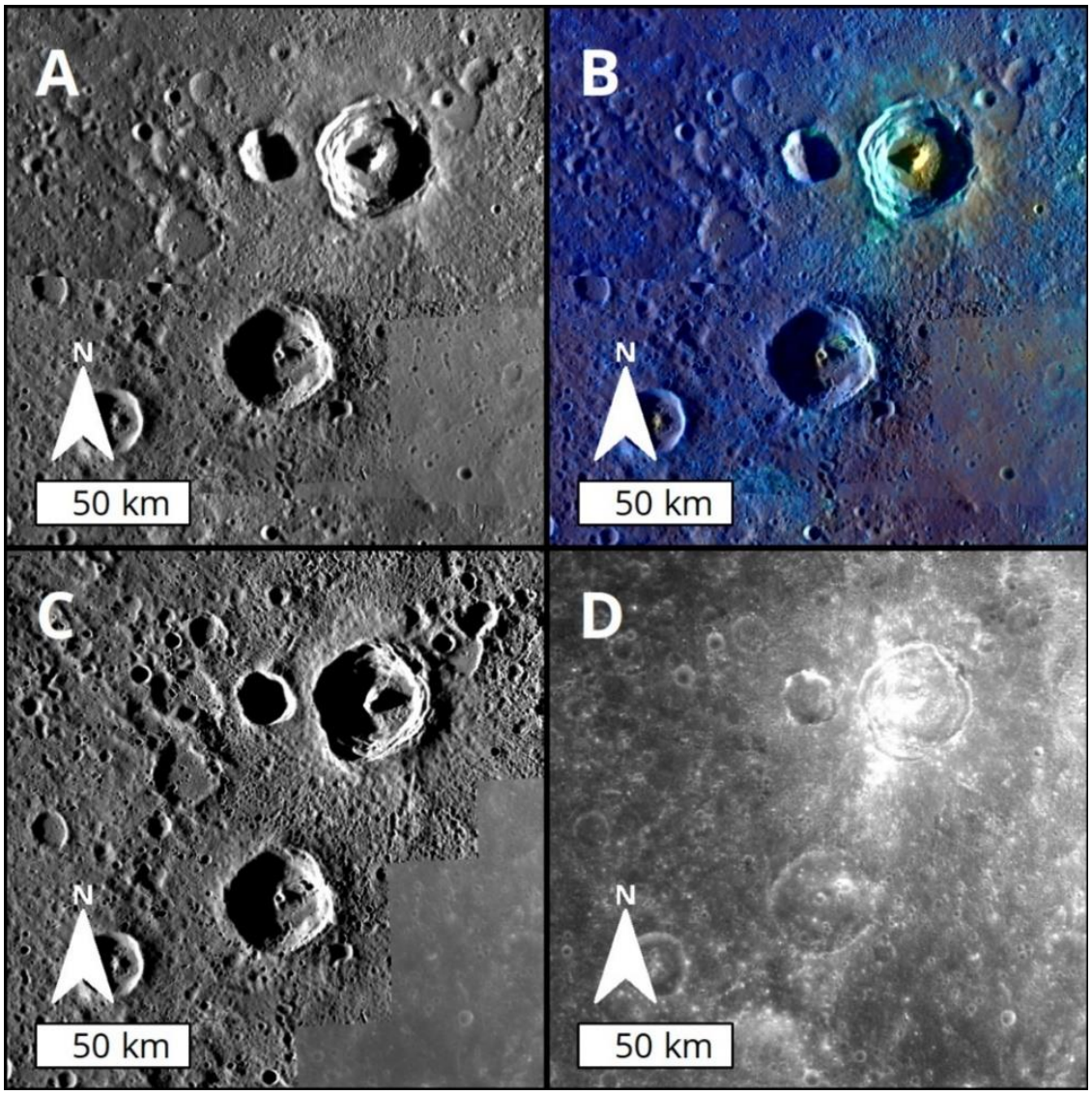

Figure 3.8: Comparison of the same area (centred at 13°E, 18.5°N) in: A, BDR basemap; B, Enhanced colour; C, High incidence angle west-facing mosaic; D, Low incidence angle mosaic.

3.2.2 Other datasets

3.2.2.1 MDIS-NAC/WAC Frames

In some areas, basemap mosaics were not ideal for determining the geology, either through lighting conditions or due to image joins. In these cases, I checked for suitable individual NAC/WAC images. The method for importing these images into a GIS-ready format is described in section 3.3.2.

3.2.2.2 MLA data

MLA (Mercury Laser Altimeter) data coverage is relatively sparse in the northern part of the quadrangle, and almost non-existent south of the equator (as shown in Figure 3.9). Although these data were available for use, they were not employed because no coverage was available for features where it would be useful.

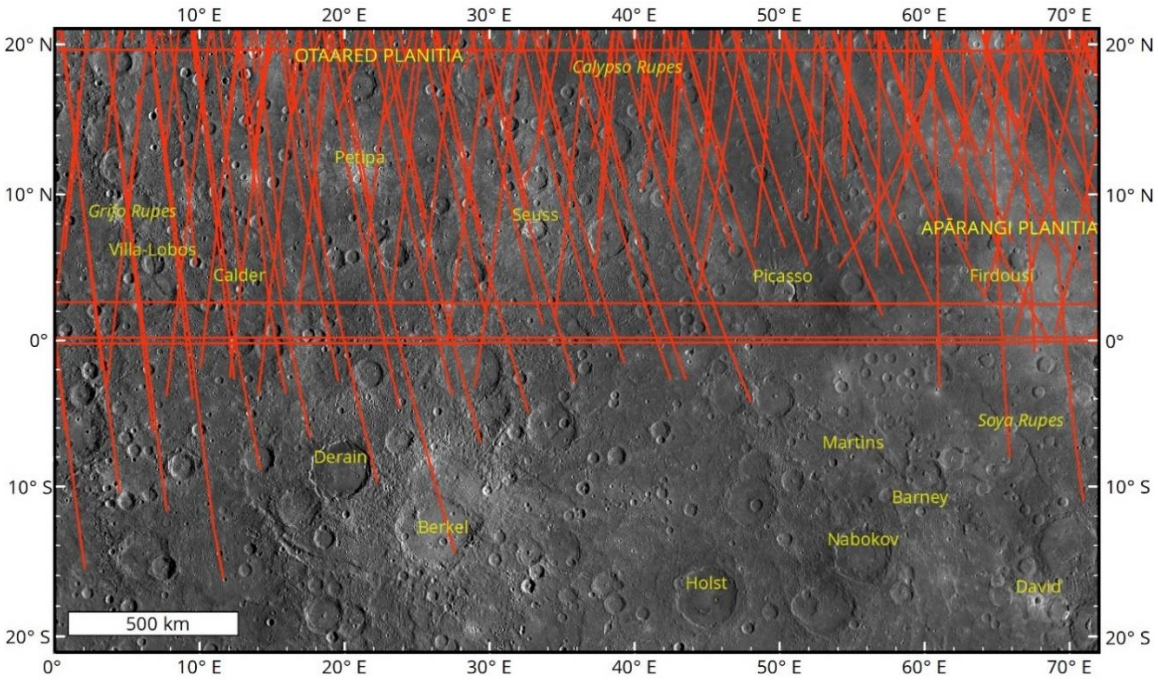

Figure 3.9: MLA tracks in the Derain quadrangle. Coverage is generally sparse, with better coverage in the north of the quadrangle. The E-W (horizontal) tracks are from flybys. As coverage is from the end of tracks, the instrument was towards the edge of its range, so shot spacing is poor along the track, and each shot has large errors and high noise.

3.3 Methods

3.3.1 Mapping Philosophy

Geological mapping is performed for a multitude of different purposes. The intended purposes of the map should be essential in guiding its production. This will necessarily involve simplification, as the geology is always more complex than can be shown on a single sheet. The map I have produced of the Derain quadrangle was created to provide part of a coherent, global

geological basemap to help understand Mercury's geological evolution, and to provide a geological framework for the BepiColombo mission. To ensure compatibility with the other European quadrangle maps (Galluzzi et al., 2016; Guzzetta et al., 2017; Mancinelli et al., 2016; Wright et al., 2019), a large portion of standards and definitions for my map were pre-determined. While ensuring my map conformed to the same standards, I had the freedom to map in a way to best represent the variation in the quadrangle's geology. I aimed to demonstrate the geological diversity accurately, within scale constraints, and to document the area in a way that can be useful for the BepiColombo mission. I have attempted to map in as much detail as possible, as it is possible to simplify later if a map is too cluttered for the 1:3 million publication scale. I also developed my definition of units within Derain to ensure a good fit with the quadrangle. This philosophy also guided my decision to include inferred contacts.

3.3.2 Software

3.3.2.1 Processing of data

The basemaps and other datasets used, other than a small number of global mosaics, are not stored by the PDS (Planetary Data System) in GIS-ready formats. Therefore, I had to process almost all data sets into GIS-ready products using the United States Geological Survey's (USGS) 'Integrated Software for Spectrometers and Imagers' (ISIS). The workflow for processing products is shown in Figure 3.10.

3.3.2.2 Geological mapping software

I completed mapping using ESRI ArcGIS 10.5 software. All linework was completed in ArcMap. I used ArcCatalog and ArcScene for map and feature administration and to visualise small areas in 3D. Features were mapped using polylines in feature classes, with unit symbology labelled using a point feature class. Unit polygons were generated using the 'Feature to Polygon'

tool, with labelling from points. Polygons were generated without a tolerance ensuring all linework was complete. The 'Data Reviewer' extension was used to check linework for dangles (sections of lines that do not connect to another feature). All mapping data was contained in a single file geodatabase.

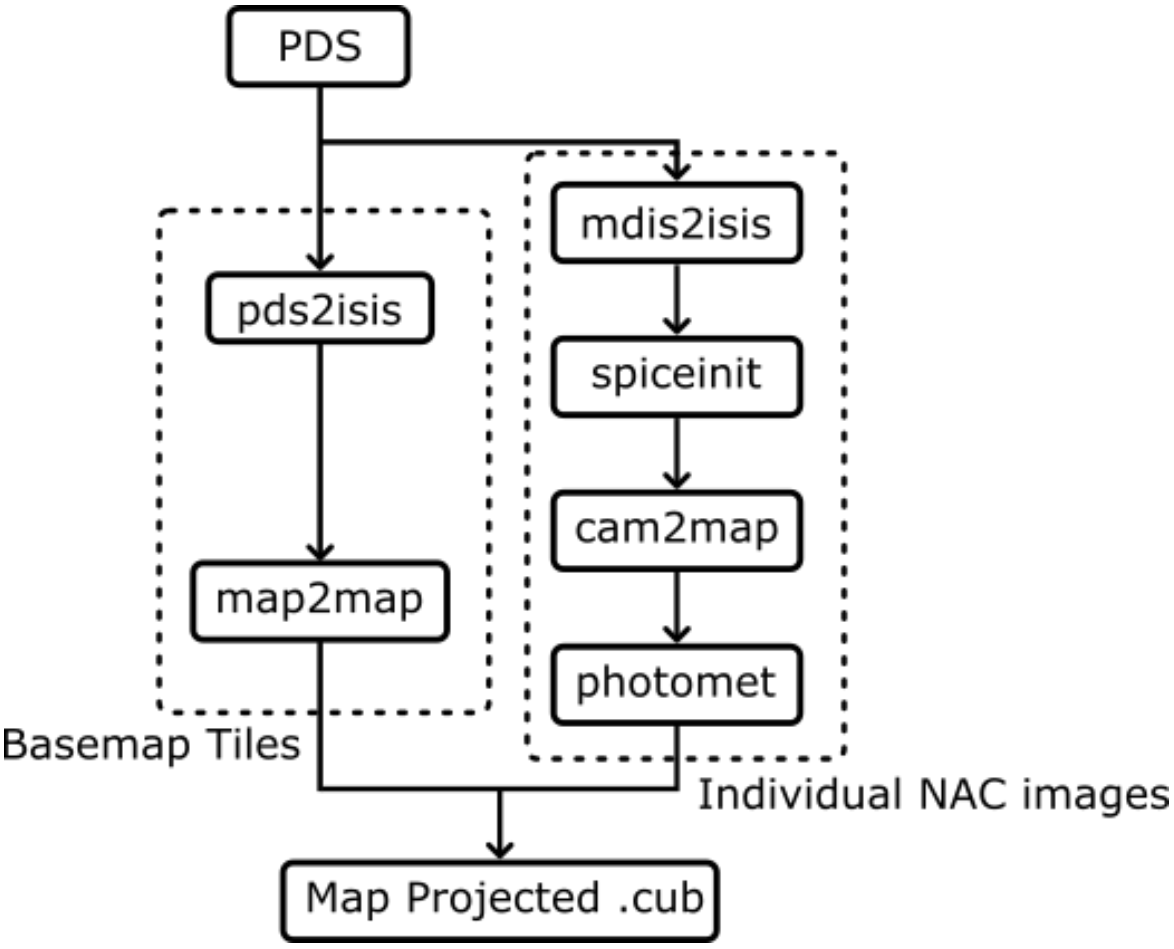

Figure 3.10: Processing steps (commands) to take MDIS basemaps or individual images from PDS storage format to map projected, GIS-ready products.

3.3.3 Projection

Mapping was performed using a Mercator projection using the USGS 2015 geoid. Using a Mercator projection is consistent with previous planetary geological mapping in equatorial latitudes. While a Mercator projection distorts shape and scale at high latitudes, it almost completely preserves shape and angle at the low latitudes spanned by this quadrangle. I used the 2015 geoid as this was the most up-to-date geoid at the start of the project.

It was also the native projection used by the most up-to-date MESSENGER products. Using the 2015 datum has led to small discrepancies with the adjacent H-5 Hokusai quadrangle (Wright et al., 2019), mapped on the 2011 spheroid. However, this and map products using the old 2011 datum will eventually be re-projected onto the more current 2015 geoid to better integrate quadrangle mapping into a global map.

3.3.4 Map Scale

The map was prepared for publication at 1:3 million scale, following previous Mercury maps. Mapping linework was drawn at a scale of 1:400 000. I chose this mapping scale to be in line with the USGS mapping standards (Tanaka et al., 2011), and later Planmap mapping guidelines (Rothery et al., 2017). It is slightly in excess of the USGS recommended scale, of four times the publication scale, in this case, 1:600 000. This scale is consistent with other Mercury mapping (e.g. Wright et al., 2019), and it allowed the smallest diameter mapped (5 km) craters to be digitised easily.

3.3.5 Mapping

In addition to mapping the area of the Derain quadrangle itself, I also mapped a 5° area external to the quadrangle to reconcile with adjacent quadrangle maps and to assist the creation of a global Mercury geological map.

Linework was drawn primarily using ‘streaming’ with 500 m spacing. Appropriately spaced streaming automatically places regularly spaced vertices, allowing accurate linework to be drawn without introducing additional sinuosity to lines, or unnecessarily increasing the size of linework through redundant vertices.

Where a mosaic was ‘choppy’ or fragmented due to misregistration or misprojection of component images, linework was drawn in a more

consistent mosaic and was then moved to geo-reference it to a known good image in the fragmented mosaic.

3.3.6 Crater Classification

The Derain quadrangle contains many impact craters with a range of sizes and degradation states. Craters were mapped as either small, if between 5 km and 20 km in diameter; or large, with a diameter greater than 20 km. Only large craters (D>20 km) have ejecta mapped, and degradation classified. This approach follows previous work, such as Galluzzi et al. (2016).

I classified craters in the 3-class crater classification system of Galluzzi et al. (2016). Examples of craters in these degradation classes can be seen in Figure 3.11. The 3-class system is one of two different classification systems for crater degradation on Mercury, with the other being the 5-class system first used in Mariner 10 mapping.

The 5-class system was first used in the original Mariner 10 mapping and has recently been updated with MESSENGER observations (Kinczyk et al., 2020). Some previous workers (e.g. Galluzzi et al., 2016) have found that the classification of the middle stages in this degradation system is often not reproduced as well between workers.

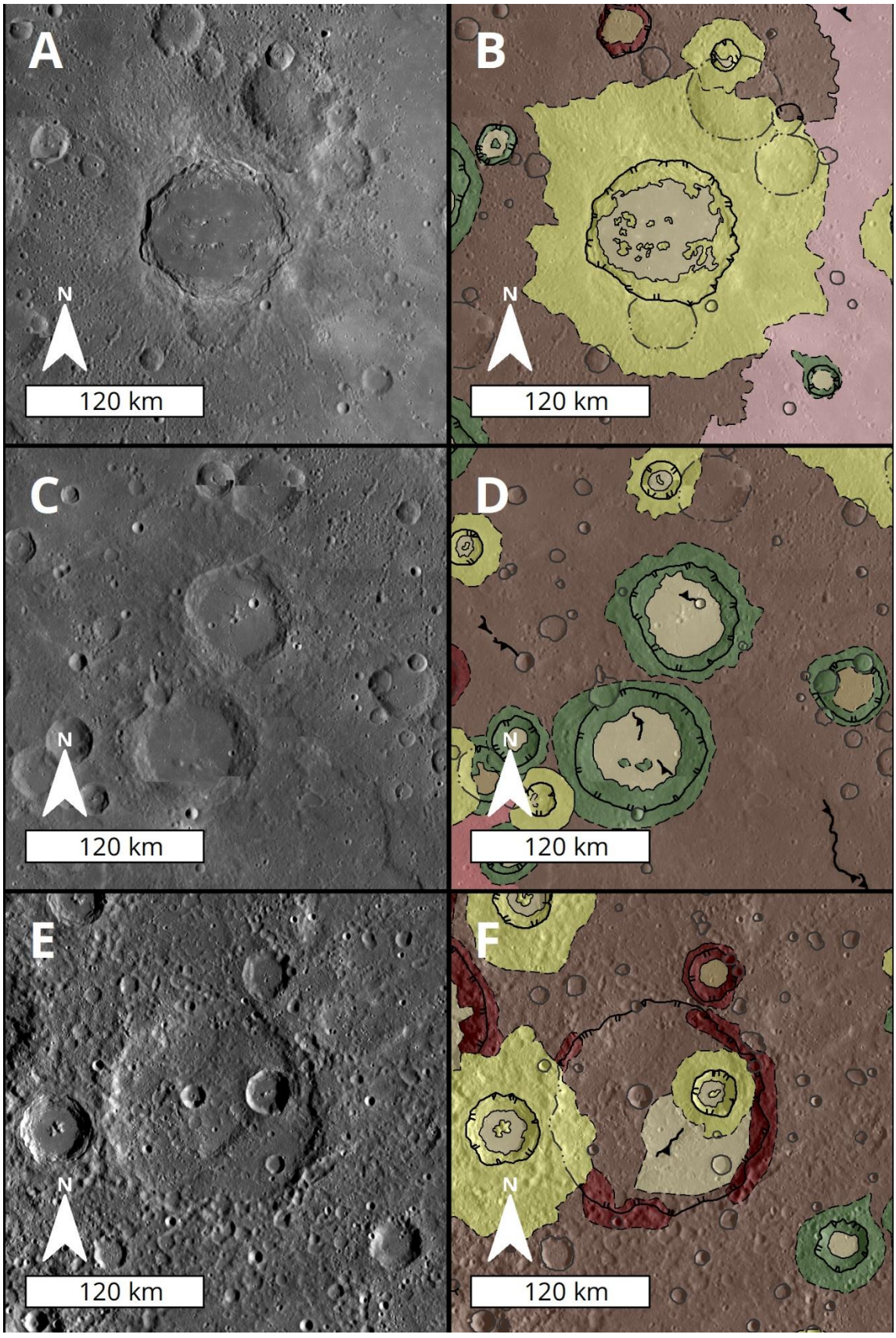

Figure 3.11: Comparison of C3 (A&B), C2 (C&D), and C1 (E&F) degradation classes in MDIS BDR mosaic imagery and as mapped.

The 5-class system may give a finer temporal resolution. Some workers have used it (e.g. Banks et al., 2017; Kinczyk et al., 2016) to attach an age statement to individual craters by equating the five classes of degradation to the five Hermean geological periods, similar to degradation classes on the Moon. The issue with attaching an age statement based purely on morphological features is that due to the high impact flux at Mercury, many craters have been heavily altered and degraded by subsequent nearby impacts and superimposed secondaries. This process is not evenly distributed, and degradation does not always fit with the superposition of ejecta. Where accelerated degradation is not immediately apparent, it still remains possible that it took place earlier in the crater's history. The misfit between superposition relationships and degradation classes was one of the primary reasons that Galluzzi et al. (2016) developed the 3 class system. Using the 3-class system, therefore, improves reproducibility, and reduces confusion when assigning an absolute age to the craters mapped.

3.4 Unit Descriptions

3.4.1 Contacts

Contacts between units were classified into three types, based on the clarity of the contact. Where the boundary between units was defined by a tectonic feature, such as a lobate scarp, the boundary is marked with the tectonic feature's ornamentation and can be considered a certain contact.

3.4.1.1 Certain Contact

Certain contacts were mapped where the position of a geological contact could be defined to within 500m. This is the case particularly for contacts between smooth plains and other units, and between crater fill and ejecta.

3.4.1.2 Approximate Contact

Approximate contacts were mapped where a contact could be seen to exist; but when the exact location could not be determined to within 500m. This has been used mainly for the gradational contacts between older degraded ejecta blankets and surrounding plains units.

3.4.1.3 Inferred contact

Inferred contacts were used sparingly in the production of the map. They were drawn for hypothetical contacts, for example, around the most degraded crater rims, where no ejecta blanket could be distinguished from the background, but a distinct crater rim could be seen. I have done this to allow the crater classification to be shown on the published map. While these do not mark a defined geomorphological boundary, they do mark the visible extent of a distinct geological feature. In my opinion, not visually representing these old, degraded craters on the published map is more misleading than including these uncertain boundaries.

3.4.2 Linear Features

3.4.2.1 Large Craters

Large craters are those over 20 km in diameter. On the map the crater rim is marked. Large craters have the interior fill and ejecta mapped and classified (see 3.4.3.4).

3.4.2.2 Small Craters

Small craters are craters with a diameter greater than 5 km and smaller than 20 km. Crater rims are marked with a polyline. Clear and obvious secondary fields or chains were not mapped individually but were mapped as secondary chains or fields to avoid cluttering the map and to show the geological relationships better.

3.4.2.3 Lobate Scarps

Lobate scarps are asymmetric scarps, with a gentle slope to the crest on one side and a sharp drop on the other side of the crest. The morphology is illustrated in the cartoon diagram in Figure 3.12. They are interpreted to have formed by the movement of underlying thrust faults.

3.4.2.4 Wrinkle Ridges

Wrinkle ridges are broadly symmetrical, rounded, ridges usually found in areas of smooth plains. Most are shorter than lobate scarps, and do not form as long, or continuous systems as lobate scarps.

The formation of wrinkle ridges is unambiguously related to contractive processes, either as folds or as a response to subsurface faulting in a more elastic layer than units where lobate scarps are found.

3.4.2.5 Wrinkle Ridge Rings

Wrinkle ridge rings are found in areas of smooth plains. While morphologically a wrinkle ridge, they present in a ring shape and are thought to have formed by exploiting the weakness of the outline of a completely buried crater.

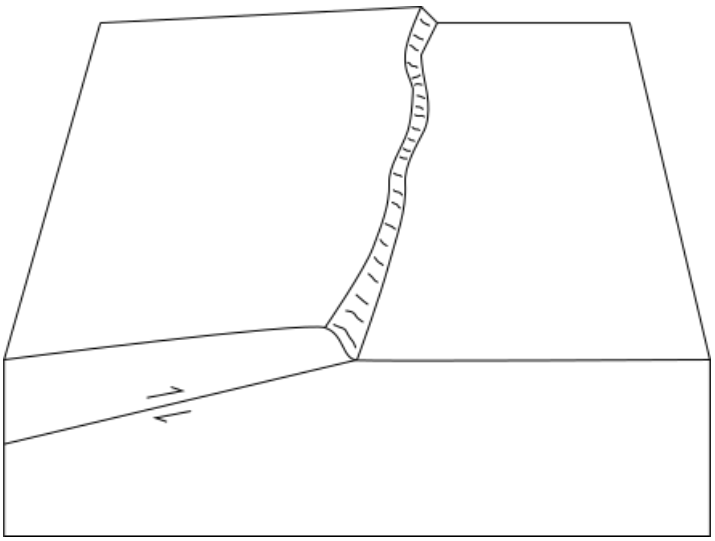

Figure 3.12: Cartoon showing the morphology of lobate scarps and their accepted formation through fault movement

3.4.2.6 Subdued Craters

These are craters that have been subdued by later plains, where the outline of a crater can be seen. Subdued craters are those where some part of the crater rim has been overlain by the smooth plains. If no part of the rim emerges above the smooth plains, but a trace of the crater morphology can still be seen, these are described as subdued or 'ghost' craters.

3.4.3 Units

Units have been defined primarily by geomorphological observations.

3.4.3.1 Smooth Plains

Smooth plains are a plains unit characterised by a paucity of superimposing impact craters and a smooth texture. They are defined by Trask and Guest (1975) as: 'relatively sparsely cratered, essentially level' but with 'ridges and scarps [...], giving a generally rolling appearance'. An example is shown in Figure 3.13.

The smooth plains of Apārangi Planitia generally have a sharp contact with surrounding units. Elsewhere contacts can be sharp or gradational. Gradational contacts are the norm around small scale smooth patches. Smooth plains do not typically host lobate scarps within them, but often host wrinkle ridges. The clearest examples of this in the quadrangle are in Apārangi Planitia. In places 'ghost' craters may be seen where the trace of a pre-existing crater can be seen expressed as wrinkle ridges or as a low ring-shaped ridge. Smooth plains are thought to represent extensive, low-relief lavas. Being the least cratered and least modified unit, they are the youngest plains unit. Smooth plains are generally red in the enhanced colour mosaic; this is easily seen in the very smooth plains of Apārangi Planitia.

3.4.3.2 Intermediate Plains

Intermediate plains are described in the original Mariner 10 maps. They were described by Spudis and Prosser (1984) as 'planar to undulating surfaces' with 'higher crater densities than smooth plains but less heavily cratered than intercrater plains'. Contacts with intercrater plains were often mapped as gradational. Work by Whitten et al. (2014) suggested that intermediate plains were not mappable as a global unit with MESSENGER data. However recent high-resolution mapping work (Galluzzi et al., 2016; Guzzetta et al., 2017; Mancinelli et al., 2016; Wright et al., 2019) has found it useful to continue to distinguish intermediate plains at the quadrangle level. Maps currently being produced by the USGS have instead described a similar unit as a subdivision of intercrater plains (Ostrach et al., 2019; Whitten et al., 2019).

I have mapped intermediate plains as a separate unit to subdivide the morphological and textural continuum that ranges from the archetypal smooth plains to the archetypal intercrater plains (noting, for example, the unbroken continuum of crater densities documented on plains units by Whitten et al., 2014). An example is shown in Figure 3.14. Intermediate plains are characterised by subdued appearance, with many small impact craters showing evidence of being mantled by an overlying unit, potentially volcanic or fluidised ejecta (Chapter 5). They have a higher crater density than smooth plains and a lower crater density than intercrater plains. Intermediate plains are relatively widespread in the Derain quadrangle, sometimes covering extensive areas, such as around Petipa. The area north and west of Apārangi Planitia is not a type locality for intermediate plains, it has only a few subdued craters, and has a paucity of large superimposing craters, but shows significantly more texture than the smooth plains and intercrater plains of Apārangi Planitia itself and in the adjoining area of the Eminescu quadrangle. Intermediate plains typically have gradational boundaries with other plains units.

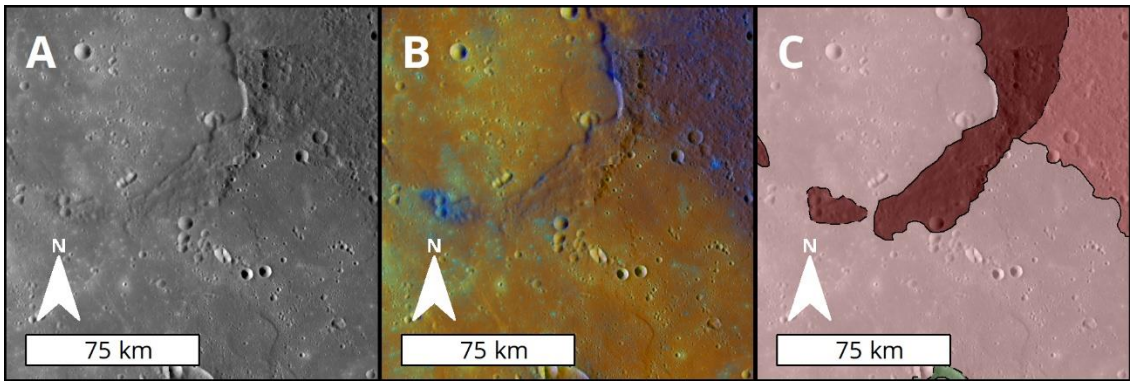

Figure 3.13: Area of Smooth plains at 65°E, 14°N. The smooth plains are embaying a C1 crater. A: MDIS BDR basemap mosaic. B: Enhanced colour basemap mosaic, this area has the archetypal high reflectance red colour. C: As mapped. The smooth plains here are red in the enhanced colour mosaic.

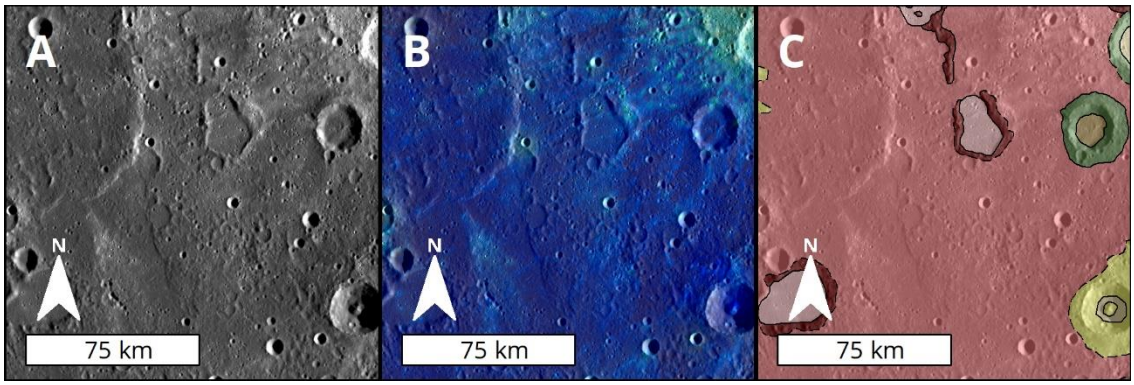

Figure 3.14: Area of intermediate plains at 19°E, 9°N shown in: A, MDIS basemap mosaic; B, Enhanced colour; C, As mapped. This area shows gentle rolling terrain with clearly subdued craters (C1 degradation), small lobate scarps and textural variation.

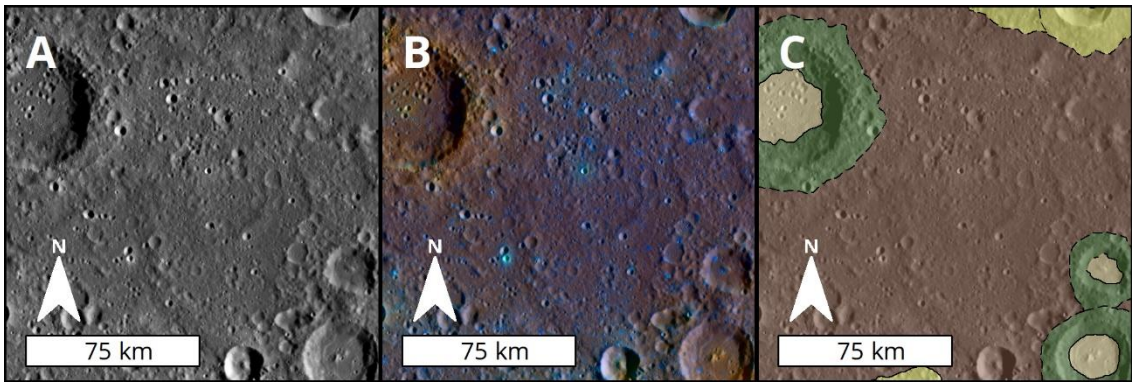

Figure 3.15 Area of intercrater plains at 40°E, 9°S. A: MDIS BDR basemap mosaic, B: Enhanced colour, C: As mapped. The unit is heavily cratered, with many large and small craters showing various states of degradation.

3.4.3.3 Intercrater Plains

Intercrater plains are the 'background' plains unit on Mercury. They were defined by Trask and Guest (1975) as 'level to gently rolling ground' with a principal characteristic of 'a high density of superimposed small craters in the size range 5-10 km'. An example of intercrater plains can be seen in Figure 3.15. While intercrater plains can be crater-saturated, most examples are not. Craters, likely to be secondaries but unattributable to a primary impact sites, are common. Crater morphologies show the full range of sizes and states of degradation. Topography on 50 km wavelengths is generally flat or gently rolling. Tectonism is expressed by lobate scarps, with no wrinkle ridges discernible. Boundaries with smooth plains are generally sharp, but at intermediate plains are often gradational. In enhanced colour, intercrater plains can be either red or blue, but usually have relatively low reflectance and appear dull.

3.4.3.4 Crater Materials

In keeping with convention, I have not mapped crater material and crater floor material for large (>20 km) diameter craters. I have mapped the crater floor as either smooth or hummocky floor material, or in rare cases (see below) as smooth plains.

Crater materials units encompass a crater's continuous ejecta, terracing, and peak elements. In older degraded craters, continuous ejecta cannot be easily distinguished, and instead the raised rim of the crater is mapped. The crater units are divided by degradation class according to the 3-class system.

C1 Craters

C1 craters are the most degraded craters in the classification system. They do not have continuous ejecta deposits, and the crater rim is usually heavily modified and may be discontinuous. C1 craters have no internal terracing, and crater floors can show evidence of extensive modification.

C2 Craters

C2 Craters are an intermediate classification. They always have a continuous rim, and usually have some areas of continuous ejecta. Some moderately or poorly developed internal terracing is relatively common.

C3 Craters

C3 craters are the least degraded class. They often show clearly defined terracing, continuous ejecta with well-defined margins, and (in larger craters) chains of secondary impacts. The crater rims are sharp, and the crater floor is usually pristine.

3.4.3.5 Crater floor material

Smooth crater floor material

Smooth crater floor material is a unit of crater floor material with a smooth, level profile; morphologically similar to smooth plains. There is little relief other than embayed peak elements that rise above it or, a few small superposing smaller craters. These units are generally interpreted as representing ponding of impact melt (Daniels and Neish, 2018; Wright et al., 2019).

Hummocky crater floor material

Hummocky crater floor material is the other main unit of crater floor deposits in the large craters. It is characterised by a rough, often rolling texture.

This could represent degraded smooth floor material (Galluzzi et al., 2016), or be the floor of a crater that was not covered over by ponded impact melt.

Smooth plains crater floor deposits

Occasionally crater floors have been mapped as smooth plains. This is where there is evidence that the crater floor is demonstrably younger than the crater forming event. This evidence includes smaller impact craters on the

floor of the host crater that are themselves superposed by smooth plains, or where surrounding smooth plains units have breached the crater rim.

3.4.4 Superficial units

3.4.4.1 Hollows

I recognised hollow fields based on their morphology, characterised by small rimless depressions, and colour, being a pale, aqua blue in enhanced colour imagery.

3.4.4.2 Putative Pyroclastic features

Two aspects of putative pyroclastic features were mapped: the putative eruptive centres, which are recognised morphologically as irregular rimless depressions, and the surrounding albedo features (faculae). These were mapped with a polyline marking the rim. Faculae, which show as bright red albedo features in enhanced colour, were mapped as polygons with transparent ornamentation. This allows these features to be shown without obscuring the underlying mapped geology.

3.4.4.3 Secondary crater chains and catenae

I mapped chains of small craters radiating from basins as polygons. These features were mapped consistently with previous work (Galluzzi et al., 2016; Guzzetta et al., 2017; Mancinelli et al., 2016; Wright et al., 2019), and to help demonstrate areas where significant modification due to secondary impacts may have occurred. Catenae, linear or curvilinear chains of craters, (Fegan, 2018) were mapped in this feature class.

3.4.4.4 Rays

In common with previous workers (Galluzzi et al., 2016; Guzzetta et al., 2017; Mancinelli et al., 2016; Wright et al., 2019), I mapped crater rays as a superficial feature. Rays are usually identifiable as an albedo feature in enhanced colour or in low sun-angle monochrome images. If attributable to

a source crater, they can be used to provide relative ages of units; if a unit overprints a ray, it must be younger than the ray-producing crater.

3.5 Summary

In this chapter, I have explained how I produced the map and given descriptions of the units mapped. In the next chapter, I discuss the nature and origins of these units in more detail, and present observations made during the mapping to provide a geological history of the Derain quadrangle.

CHAPTER 4
THE GEOLOGICAL HISTORY OF THE DERAIN (H-10) QUADRANGLE.

4.1 Introduction

The Derain quadrangle has proved to be an excellent example of the full range of Mercury's geology, as can be seen on the included map sheet (Appendix A). The quadrangle includes evidence of possible ancient basins and Low Reflectance Material (LRM) from the very early geological history, through excellent examples of plains with differing morphologies, right up to evidence of geologically recent faulting, explosive volcanism, and volatile driven hollows. In this chapter, I give a geological history of the quadrangle, starting with the very oldest features. I illustrate some of the history with the detailed history of exemplar localities in Derain.

4.2 Stratigraphy

4.2.1 The Oldest Units

4.2.1.1 Low Reflectance Material

Mercury's primary crust is not readily visible at the current surface. Modelling has suggested that the primary flotation crust was likely formed of graphite (Vander Kaaden and McCubbin, 2015). This, coupled with geochemical observations showing that Low Reflectance Material (LRM) is rich in carbon (2-3 wt.% more (Peplowski et al., 2016) than the global average of ~2.5 wt.% carbon (Nittler et al., 2011)), plus its low albedo has led to LRM being considered as remains of Mercury's primary flotation crust (Peplowski et al., 2016). The primary flotation crust of Mercury was likely very thin (~100 m thick) (Vander Kaaden and McCubbin, 2015). Previous work has shown that LRM appears to fade into the background over time as the best examples are

associated with excavation by fresh craters (Klima et al., 2018). LRM cannot be mapped definitively using the standard basemap products I have used, so I have used the global mapping of Klima et al. (2018) to show approximate coverage of LRM across the quadrangle in Figure 4.1. LRM in the Derain quadrangle is chiefly found in the ejecta of impact craters. There are notable expansive areas of LRM in the ejecta of Nabokov, Holst and Derain in the south of the quadrangle.

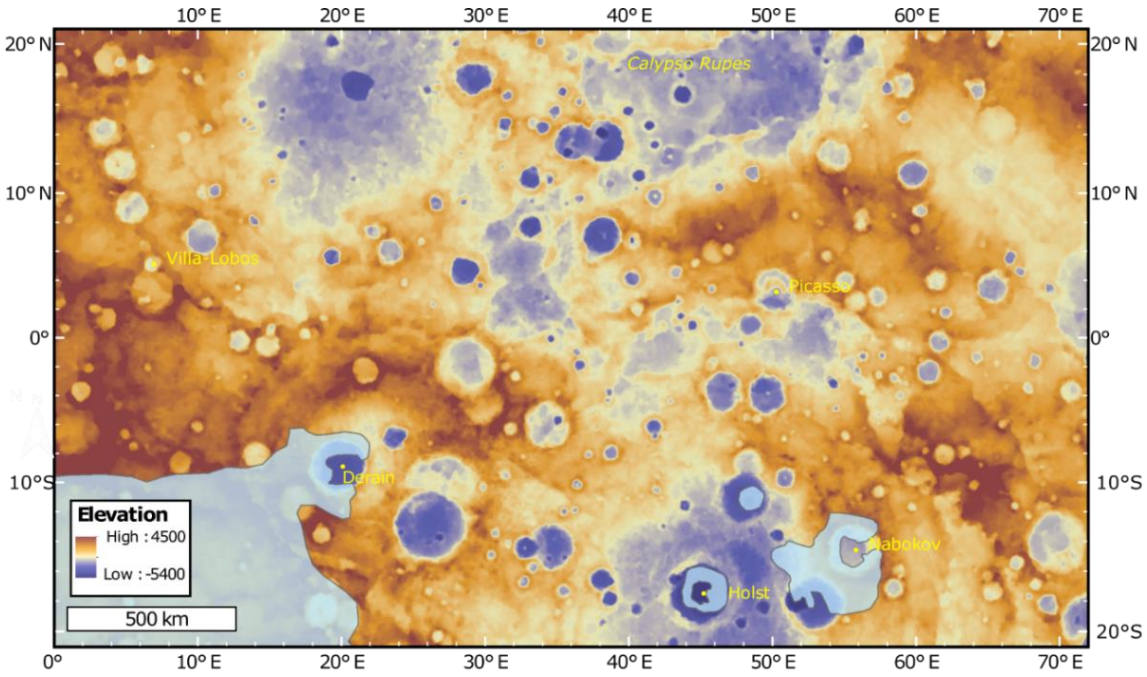

Figure 4.1: Distribution of LRM (blue highlight) across the Derain quadrangle. Approximate extents are taken from Klima et al. (2018). The distribution is concentrated in the south of the quadrangle, with an extensive area southwest of Derain. This is part of the largest area of LRM on the planet, clustered around the Debussy impact basin (12.5°E, 33.9°S).

Given that LRM is only really found in ejecta, it must have been excavated from depth, and not found in situ. As LRM is not found uniformly in the ejecta of fresh impact craters over a certain size, the depth of the LRM-bearing layer, and the likely depth of the earliest crust on Mercury, must be heterogeneous across the quadrangle. LRM is not expressed as a geomorphological feature and can be mostly seen the enhanced colour (Section 3.2.1.6 and shown in

Figure 3.4), and low incidence angle products (Section 3.2.1.3). Further understanding the exact composition of the LRM will be essential in understanding the formation history of Mercury, and so should be a high priority geochemical target for BepiColombo. The area in the ejecta southwest of Derain, towards the Debussy quadrangle, would be an excellent prospect for this as it is expansive, and appears relatively unweathered with high reflectance in the 600 nm band (Klima et al., 2018).

4.2.2 Intercrater plains

The oldest in situ geological unit in the Derain quadrangle is the intercrater plains. I mapped intercrater plains geomorphologically. At the present day, they are marked mainly by extensive modification by impact cratering. The impact craters on the intercrater plains are of all degradation classifications and represent a great range of ages.

The intercrater plains are widely thought to be predominantly volcanic in origin, partly due to a paucity of large craters, indicating a substantial amount of resurfacing in the intercrater plains (Fassett et al., 2011), as well as hosting some diagnostic morphological features such as infilled craters (Whitten et al., 2014). However, no unambiguously volcanic features, such as source vents or flow fronts, have been seen in the smooth plains (Byrne et al., 2013). Previously calculated crater ages of intercrater plains across the planet show a broad range of ages across the Tolstojan and pre-Tolstojan. The oldest units have been dated to ~4.1 Ga (Marchi et al., 2013). I have not completed my own crater counts of the intercrater plains within the Derain quadrangle as it is not possible to discern any sub-units, and only an aggregate age likely including areas of different ages would be obtainable.

Intercrater plains do not typically vary with topography and are not obviously ponded. Based on my mapping, I interpret the intercrater plains to be predominantly ancient volcanic units. Given the rapid regolith production at

the present day (Fassett et al., 2017), and increased cratering rate early in Mercury's history (Marchi et al., 2009), these flows likely incorporate ancient ejecta and regolith. The intercrater plains would therefore not represent a single geological event and span the first period of volcanic resurfacing in the quadrangle from the beginning of volcanism into the Tolstojan.

4.2.2.1 Large Basins

The stratigraphically oldest features in the Derain quadrangle for which there is unambiguous evidence are the large, ancient basins. The basins have been mostly overlain by intercrater plains, and are most easily visible in topography. In the catalogue produced by Orgel et al. (2020), the main large basins in the quadrangle are B30, B36, and B56, as shown in Figure 4.2 and Table 4.1. B30 and B56 both have a diameter of ~1400 km, whereas B36 is smaller with a diameter of 730 km. The only primary features visible in the Derain quadrangle is a section of rim to the west of the B36 basin. This lack of primary features, along with the large diameter makes it impossible to tell the basin type with any certainty. Were any of these basins to have mappable material they should be mapped as C1 (the most degraded class).

B36 (on the floor of which the Derain impact occurred) is stratigraphically the youngest of the large ancient basins, with a clear rim section still visible in the west and topographically overprinting sections of both the B30 and B56 basins. No interaction between B30 and B56 or their ejecta is visible at the present day, and so superposition cannot be used for relative dating for those two. However, if I were to speculate, I consider the B30 basin better developed in topography therefore it could be considered as less degraded than B56 and so younger. This would make the B56 basin the oldest feature in the quadrangle for which we have definitive evidence.

Two other basins that have been probable (B12) and tentative (B18) classification from Orgel et al. (2020) are in the quadrangle. These do not

noticeably interact with any of the other ancient basins, and so it is difficult to bring them into a stratigraphic order. As they are not as well defined as the certain basins, they may be older if they are real features.

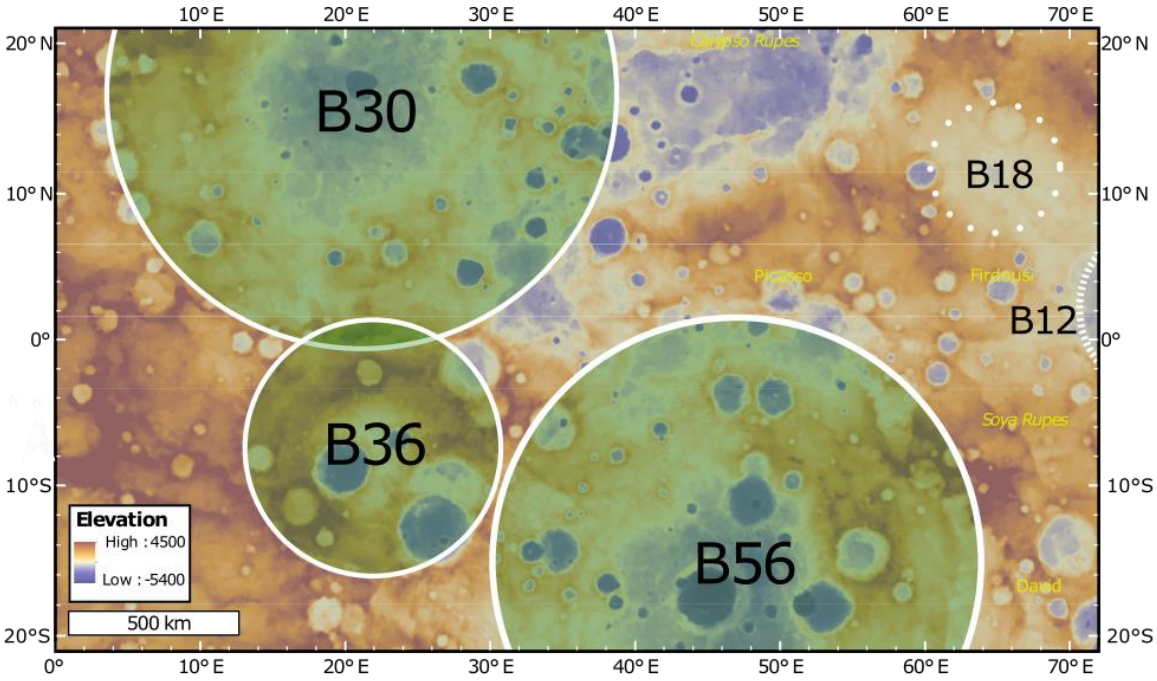

Figure 4.2: Large ancient basins in the Derain quadrangle from Orgel et al. (2020)*. B30, B36, and B56 are definite basins; B12 is a probable basin, and B18 a tentative basin in Orgel et al.* (2020) *classification. One basin diameter annuli to illustrate possible ejecta extent are not shown as they would cover the entire quadrangle.*

Name	Classification	Diameter (km)	Model Age
B56	Certain	1426	
B30	Certain	1404	
B36	Certain	737	$4.08^{+0.039}_{-0.053}\ Ga$
B12	Probable	594	$4.10^{+0.047}_{-0.070}\ Ga$
B18	Tentative	425	

Table 4.1: Ancient basin attributes. Adapted from Orgel et. al. (2020). Model ages calculated using Nekum et. al. (2001) production function.

4.2.2.2 C1 Craters

C1 craters are the most degraded crater type in the classification used. The crater classification I have used is geomorphic. This does not imply any age statement, because degradation rates are not even across Mercury and the high flux of secondaries, in particular, can quickly degrade craters (Galluzzi et al., 2016) and so prematurely degraded craters can sometimes be stratigraphically younger than less degraded craters. That said, my mapping shows in general, more degraded craters are usually stratigraphically older than less degraded. The vast majority of C1 craters are found within the intercrater plains (Figure 4.3). Those away from the intercrater plains have been clearly modified by nearby impacts or resurfacing. The C1 craters in the intercrater plains will include some of the oldest impacts currently visible in the quadrangle.

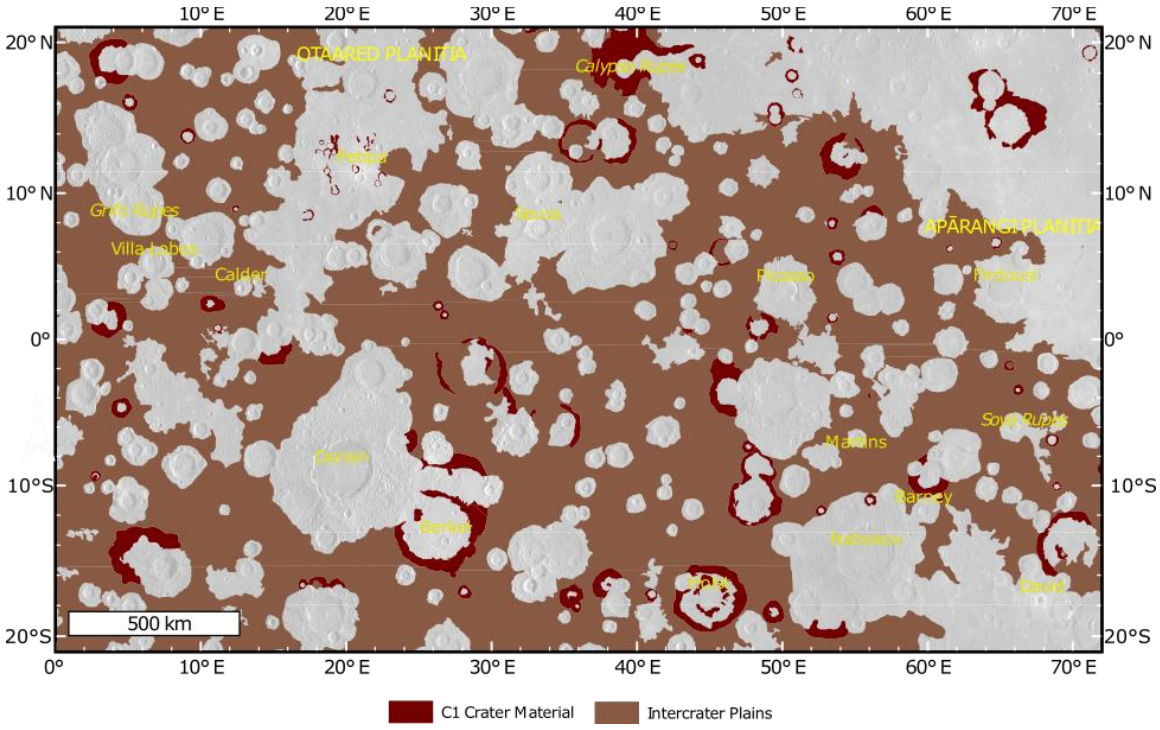

Figure 4.3: Location of intercrater plains and C1 crater material at the present day, areas covered by other units are shown with the background mosaic; however, intercrater plains likely covered the entire quadrangle at this point. These represent the oldest in situ units at the surface in the present day.

4.2.2.3 C2 Craters

C2 craters are the intermediate degradation classification. They are found in all units across the quadrangle, but are mostly found in the intercrater plains (Figure 4.4). The intermediate classification of crater degradation is difficult to put into the quadrangle stratigraphy as moderate additional degradation from nearby impacts can cause a relatively young crater to be degraded to C2 level. However, on the whole, they will generally be younger than C1 craters, and older than C3 craters. The distribution of C2 craters, with the majority being found in the intercrater plains, puts some at a similar stratigraphic level to the intercrater plains.

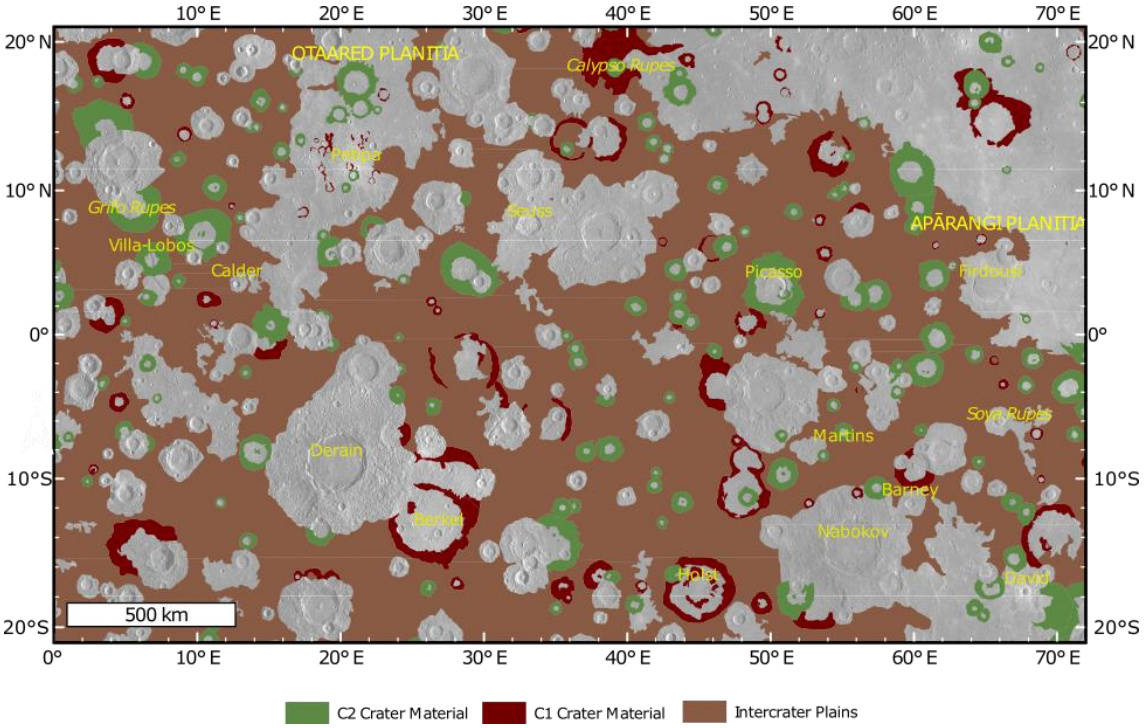

Figure 4.4: Distribution of C2 crater material (Green) across the Derain Quadrangle. Areas covered by younger units are shown with the background mosaic.

4.2.3 Intermediate Age Plains?

Intermediate plains were mapped in the Mariner 10 era based on their intermediate morphology between the intercrater and smooth plains (Grolier and Boyce, 1984; Guest and Greeley, 1983; King and Scott, 1990; McGill and

King, 1983; Schaber and McCauley, 1980; Spudis and Prosser, 1984; Strom et al., 1990; Trask and Dzurisin, 1984). Mariner 10 mapping suggested that this made them intermediate in age. If Mercury's effusive volcanism prior to the smooth plains were similar in mode, volcanic plains units intermediate in age would likely share characteristics with smooth plains, with deep fill covering a large area; while showing more texture from superimposing impacts, like the intercrater plains. The intermediate plains I have mapped across the Derain quadrangle (Figure 4.5) are large, poorly defined areas with few superimposing craters, and a seemingly thin veneer (not sufficient to bury pre-existing craters, likely <2 km) of resurfacing. For this reason, I think very few, if any, of these morphologically intermediate units are stratigraphically intermediate, and the majority likely postdate the smooth plains. Ages for these areas derived from crater counting are difficult as the intermediate plains have fewer large superimposing craters, uncertainty with some craters that may be thinly covered or pre-date cover. The gradational boundaries also cause ambiguity over the exact area to count. As can be seen in the large error ranges (+ or – up to 30%) in counts of both 20 and 10 km craters for intermediate plains in Whitten et al. (2014), it is very difficult to get robust crater counts for small areas of intermediate and intercrater plains.

Given this, I consider that the majority of mapped intermediate plains in the Derain quadrangle are not intermediate in age between the intercrater and smooth plains. I, therefore, more fully discuss them in stratigraphic order in section 4.2.5.

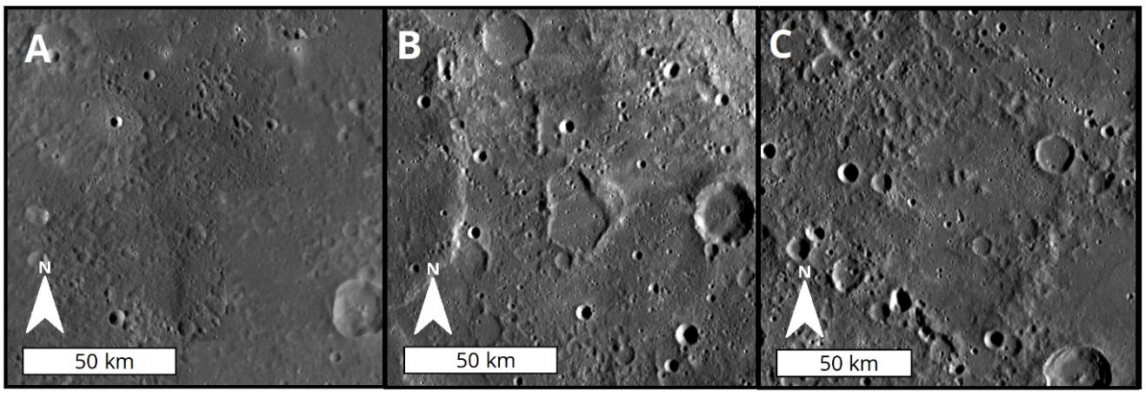

Figure 4.5: Areas mapped as intermediate plains. A (69°E, 15°N) shows a textured unit with few large superimposing craters. This is the area most likely to be intermediate in age. B, and C show morphologically intermediate areas with unambiguously smooth patches and subdued craters. While morphologically intermediate, these appear to be covered by a thin veneer and represent areas of more recent resurfacing, likely similar in age to smooth plains or younger.

4.2.4 Smooth plains

The smooth plains across the quadrangle (Figure 4.6) represent the youngest effusive volcanism in the quadrangle. To be mapped as smooth plains the resurfacing has to be sufficient that most small (<5-10 km) underlying craters are wholly covered, giving a smooth morphology, and considerably less km-scale roughness than the intercrater plains. The majority of smooth plains in the Derain quadrangle are found in three areas, Apārangi Planitia, Otaared Planitia and around Calypso Rupes. All the large areas of smooth plains are found in the north of the quadrangle. Along with these large areas, there are several small patches of smooth plains, some of which are discussed more thoroughly in Chapter 5. The smooth patches are distributed across the entire quadrangle. The smooth plains in the quadrangle do not show any flow features, such as valleys or streamlined kipukas. Nevertheless, the smooth plains in the quadrangle show evidence of large-scale resurfacing through ghost and subdued craters, and in enhanced colour, many show the characteristic red of volcanic smooth plains elsewhere on Mercury (Denevi et

al., 2013). The relative smoothness and lack of superimposing craters make smooth plains the youngest large-scale units in the quadrangle.

Generally, the smooth plains in Derain were likely erupted before the onset of widespread global contraction at around 3.5 Ga, because they are cut by lobate scarps (Section 4.3). However, the smaller patches, particularly those abutting against lobate scarps may be younger, as argued in Chapter 5.

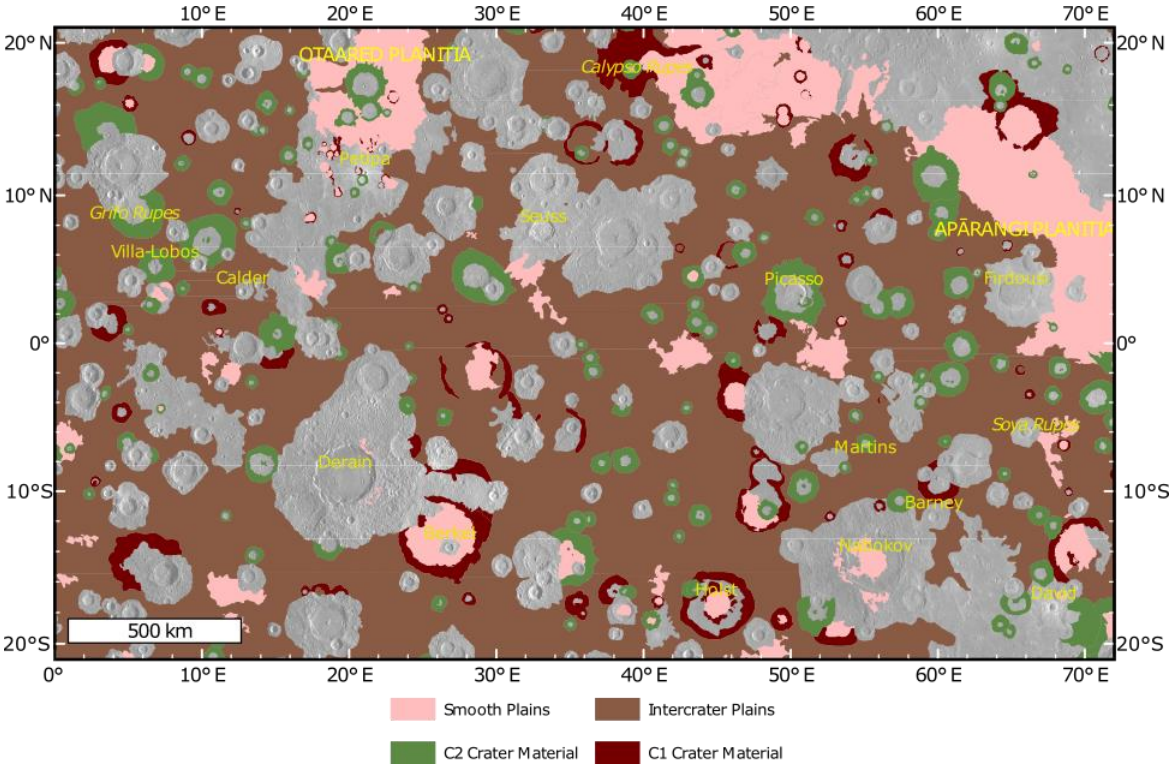

Figure 4.6: Smooth Plains added to Figure 4.4.

4.2.4.1 Otaared Planitia

Otaared Planitia is an area of smooth plains in a low-lying region in the northwest of the quadrangle. There are many pre-existing basin rims acting as kipukas above the fill, and a more textured appearance to the smooth unit than other smooth plains such as Apārangi Planitia (Section 4.2.4.2) which might reflect some of the pre-existing topography prior to resurfacing. This suggests the depth of lava cover here is relatively shallow, compared to Apārangi Planitia which doesn't show similar texture. The unnamed ~80 km diameter C2 basin in the centre of the smooth plains (highlighted with blue

arrows in Figure 4.7) has its ejecta embayed by the smooth plains unit. However, the basin fill has a very low depth to rim hight ratio and has a faulted margin to the west. This anomalous shallowing strongly suggests the fill is volcanic, and as this is isolated from the rest of Otaared Planitia must have been erupted from a different source than the main Otaared Planitia vent or vents. Other than a single tentative example (Wright et al., 2018), source vents for effusive volcanism have not been identified on Mercury, and most are thought to have been obscured by their own effusive products. Therefore, indications that a magmatic system with multiple source locations of effusive volcanism developed around Otaared Planitia is notable as it has not been well documented elsewhere on the planet. The uneven depth of cover suggested by craters being covered to different levels (Figure 4.7A) also may suggest multiple sources rather than massive scale resurfacing from a single large source.

Otaared Planitia has a gradational boundary into an area of very shallowly covered craters and morphologically intermediate, shallowly covered, pains to the south, around Pepita crater. The flooding of individual craters and crater chains suggests the eruption there was from multiple sources, and significantly lower in volume than other smooth plains such as Apārangi Planitia or Borealis Planitia.

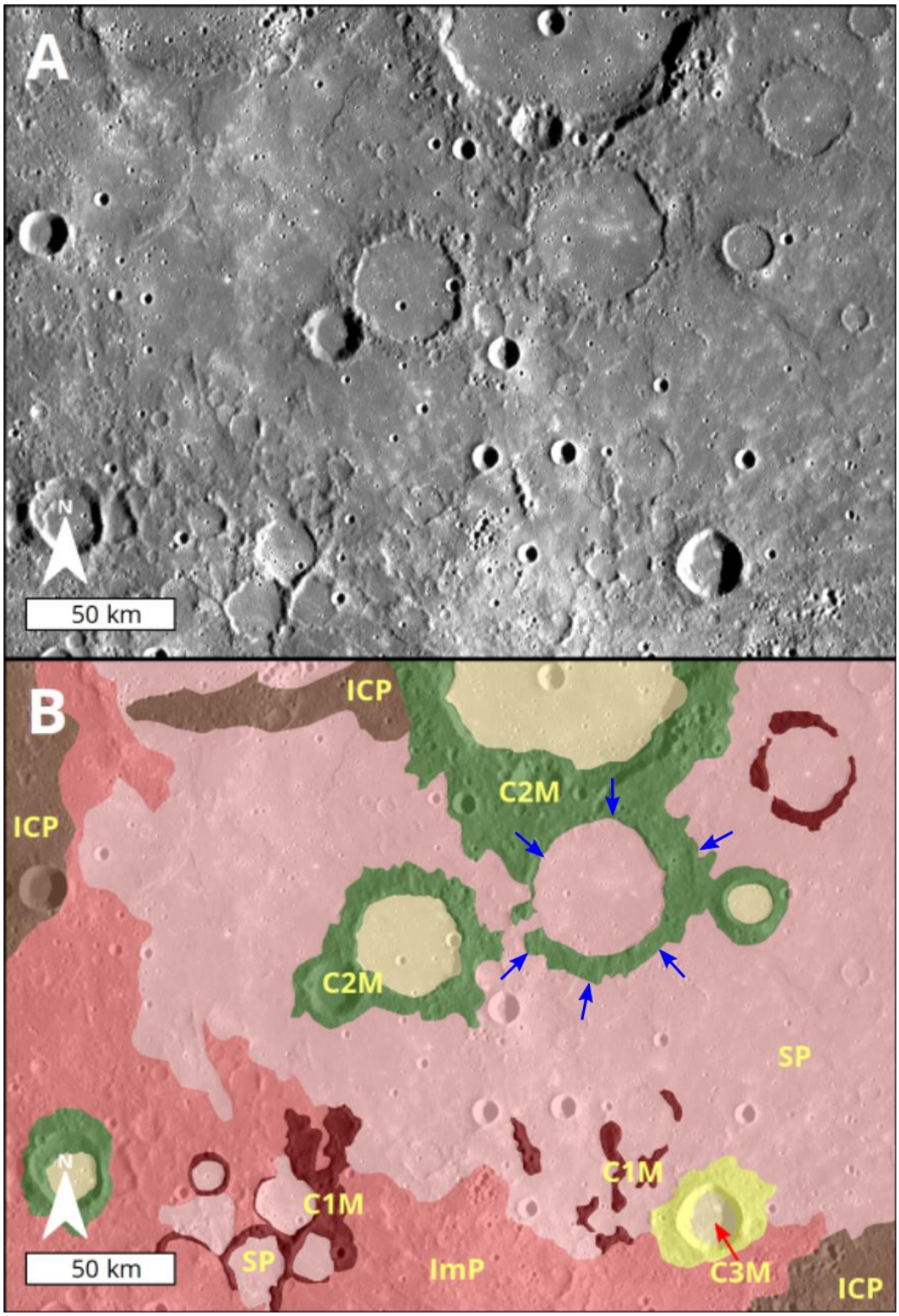

Figure 4.7: Complex contact between Smooth Plains and Intercrater Plains/Crater material at Otaared Planitia (20°E, 15°N). The contact with crater material towards the north of the frame is sharp and well defined, however towards the south it is gradational as it appears to shallowly flood a heavily cratered area (kipukas of C1 material above intermediate plains and smooth plains in the south of the frame). Partially flooded C2 crater highlighted with blue arrows.

4.2.4.2 Apārangi Planitia

Apārangi Planitia is a large expanse of smooth plains in the northwest of the quadrangle. It has a very smooth morphology and sharp contacts with the surrounding units. It is red in enhanced colour and is an excellent example of high reflectance red plains. The spectral boundary is sharp and coincident with the geomorphological boundary. The smooth plains cover is thick, as there are very few ghost craters. There are several N-S trending lobate scarps in the centre of the plains, close to the border with the Eminescu quadrangle.

Based on crater counts, Denevi et al. (2013) suggested this is the youngest large example of smooth plains on Mercury. Later work has found other areas with similar or slightly lower crater densities and gave a model age of 3.2 – 3.7 Ga (Byrne et al., 2016), but this is still among one the youngest large smooth plains on Mercury. This area is not superimposed by either C1 or C2 craters and embays the ejecta of a 25 km C2 crater in the centre of the plains. A few large C3 craters overlie the smooth units, most notably ejecta and secondary impacts from Firdousi impact basin, which acts as a local stratigraphic marker.

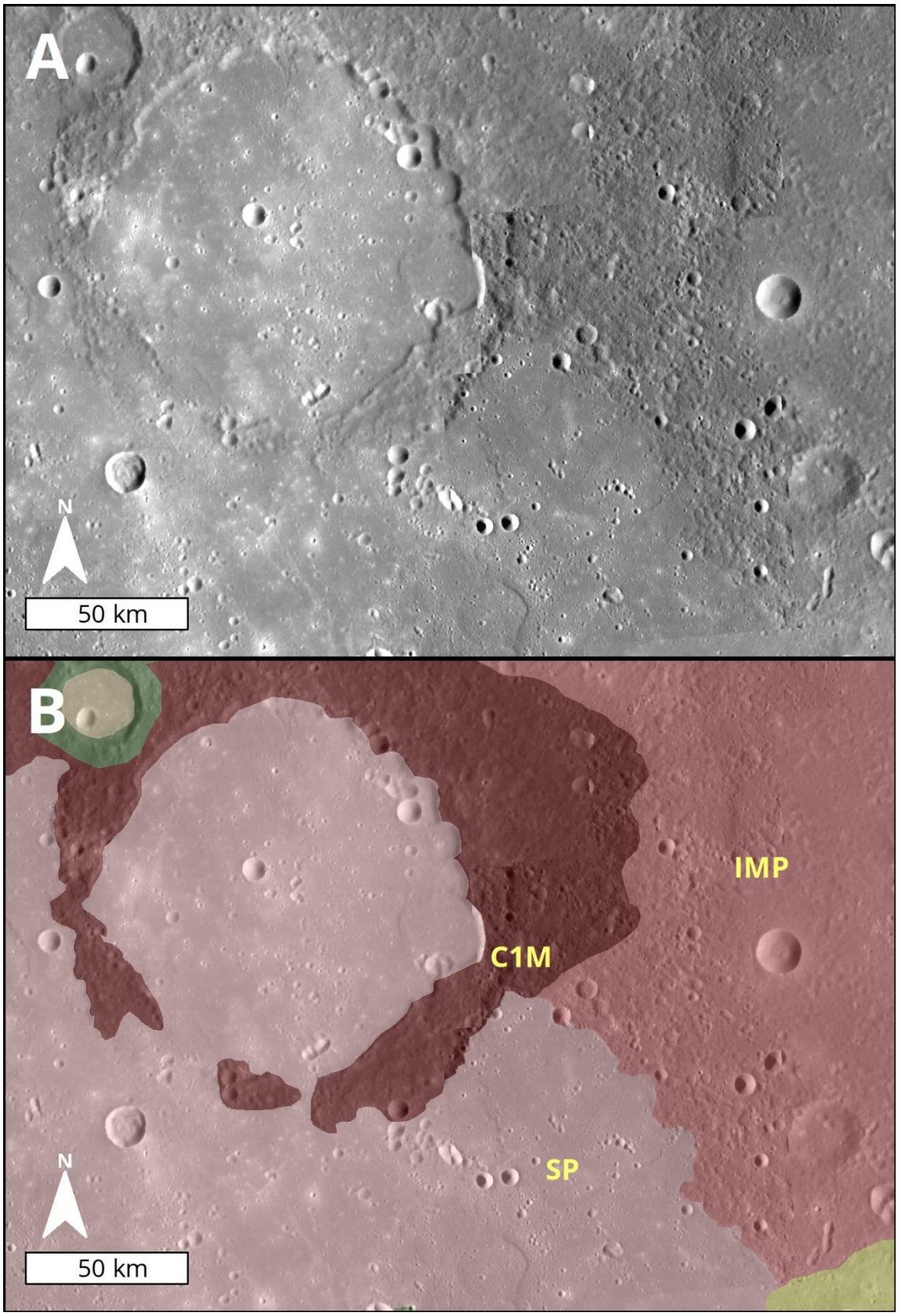

Figure 4.8: Contact between smooth and intermediate plains at Apārangi Planitia (67°N, 14°E). The contact is sharp and clearly defined.

4.2.4.3 Around Calypso Rupes

The smooth plains around Calypso Rupes are described and discussed at length in Chapter 5. They have relatively thin cover over the pre-existing terrain compared to the smooth plains Apārangi Planitia, with multiple ghost craters and embayed crater rims. The smooth plains appear to abut against the scarp of Calypso Rupes, and so likely post-date the significant movement that formed the visible surface scarp. This would place the smooth plains here later than the onset of global contraction, and so they would have to be younger than other large-scale smooth plains (Byrne et al., 2016). Unlike many other smooth plains, the smooth plains around Calypso Rupes are not associated with any marked colour difference to the surrounding plains units. The stratigraphic relationship to ejecta from Rachmaninoff, a large crater located just north of the Derain quadrangle, is not clear.

4.2.4.4 Intrusive Volcanism

Magmatism visible at the surface will only be a portion of Mercury's crust, and it is important to remember that the quadrangle's magmatic history will have included a significant amount of intrusive volcanism. On other planetary bodies, intrusive volcanism accounts for more volume than extrusive volcanism (Black and Manga, 2016; Head and Wilson, 1992). The proportion of intrusive to extrusive volcanism on Mercury is unknown as we do not have either radar or high-resolution gravity radar datasets to resolve that level of subsurface detail. There is still some evidence of sills or laccoliths from a candidate floor-fractured crater (Head et al., 2009). While Mercury's magmas would have been buoyant relative to the crust (Vander Kaaden and McCubbin, 2015), the globally contractive stress regime from around 3.6 Ga will have made magma ascent more difficult (Byrne et al., 2016), and may have promoted magma stall and intrusive emplacement. Even assuming equivalence between intrusive and extrusive volcanism, intrusive

magmatism will have been a significant process in the development of the Derain quadrangle. A cartoon demonstrating this is shown in Figure 4.9.

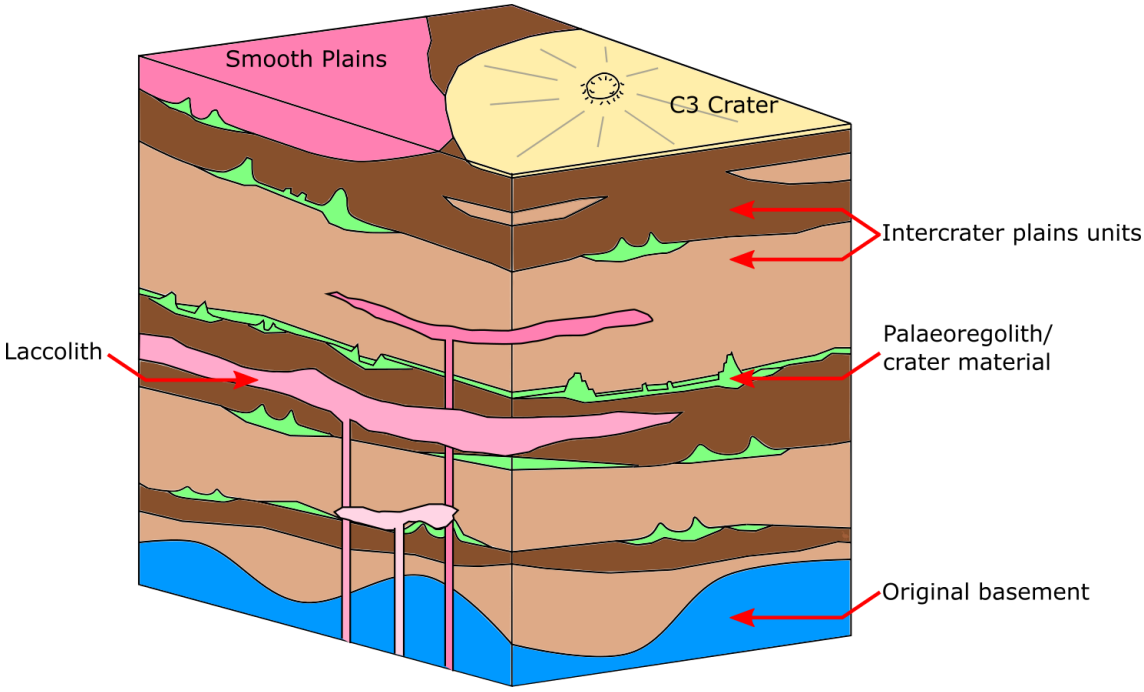

Figure 4.9: Cartoon cross-section of typical crust in Derain Quadrangle. Intercrater Plains are likely composed of multiple magmatic units, interbedded with ancient regolith. Laccoliths and sills likely cross-cut some of these units.

4.2.5 A mantled plains interpretation of the intermediate plains

As I discussed in section 4.2.3, the units that morphologically resemble intermediate plains across the quadrangle do not appear to be intermediate in age. The distribution of the mapped intermediate plains is shown in Figure 4.13.

The majority of intermediate plains in this quadrangle show clear evidence of shallow flooding with many craters showing shallower, flatter floors than would be expected if unmodified, and as well, the plains have a significantly more muted texture than the intercrater plains. This suggests low volume resurfacing of the area. If volcanic, magma ascent may have been aided by the fracture networks under craters, as the most prominently resurfaced

areas are within the shallowed craters. The resurfacing of the plains may not be volcanic, as impact-related resurfacing can cause morphologically smooth units in topographic lows; for example because of ponded impact melt (Osinski et al., 2011), or by processes similar to those that produced the lunar Cayley plains (Apollo Field Geology Investigation Team, 1973). However, on the balance of evidence, I generally prefer a volcanic origin for these mantled plains. The end date of large-scale effusive volcanism on Mercury (~ 3.5 Ga (Byrne et al., 2016)) is based on crater counts of the youngest large smooth units, such as Apārangi Planitia. All these areas have completely resurfaced the pre-existing plains erasing the underlying texture. These are high-volume eruptions. The onset of global contraction will have increased compressive stress over time, gradually making it harder for magma to reach the surface and erupt. However, it certainly does not appear that all effusive volcanism ceased at the onset of global contraction, as evidenced by volcanic resurfacing in Mansurian aged (~1.7 Ga – 300 Ma) basins (Wright et al., 2017). I think it is also quite possible that lower volume eruptions may have taken place away from these basins while effusive magmatism waned. A type locality for this would be intermediate plains around Petipa. These have a gradational boundary with the smooth plains of Otaared Planitia, and a gradational boundary with the surrounding intercrater plains.

4.2.6 Post-smooth plains

After the end of widespread effusive volcanism in Derain, the geology of the quadrangle has seen few events that have caused a widespread change at the quadrangle scale. This has been accomplished only by the large C3 basins such as Rachmaninoff, Derain, Nabokov, and Firdousi. This period likely saw the development of the fault scarps visible across the quadrangle, although the exact timing of this and some small patches of smooth plains are unclear (Chapter 5). The fault systems are described in detail in Section 4.3. While events were smaller and more localised, this stage of the quadrangle's

development includes some of the most intriguing features currently visible such as volatile-related processes, including hollows and evidence of explosive volcanism.

4.2.6.1 C3 Craters

C3 craters are the least degraded class of craters. This classification will include the vast majority of the youngest craters, as some stratigraphically young craters may be prematurely degraded by other impacts. They display coherent, continuous ejecta blankets, sharp rims and a pristine appearance. They superimpose all plains units (Figure 4.13) and so, must post-date the end of widespread effusive volcanism.

Ejecta from the C3 Rachmaninoff impact dominate the northeast of the Derain quadrangle (Figure 3.6), despite the basin interior lying entirely within the Hokusai quadrangle (Wright et al., 2019) to the north of the Derain quadrangle. Rachmaninoff Ejecta has a complex relationship with the smooth plains around Calypso Rupes, and the stratigraphic order is not clear. Rachmaninoff ejecta is likely to have caused faster degradation of plains units in its vicinity through the many secondaries and ejecta blocks ejected. I think the intermediate plains unit northwest of Apārangi Planitia may have been smooth plains before degradation with ejecta and secondaries from the Rachmaninoff impact. If this is the case, given the sharp contact between the smooth and intermediate plains, it would suggest the Rachmaninoff impact separated the two resolvable periods of plains emplacement near Apārangi Planitia (Figure 4.10). The first period of plains formation, before the Rachmaninoff impact, in the area mapped as intermediate plains southeast of Rachmaninoff. This appears to have then prematurely degraded from smooth plains to intermediate plains through secondary impacts and ejecta from Rachmaninoff. The second period of plains formation, after the Rachmaninoff impact, forming the smooth plains of Apārangi Planitia. This

geomorphic interpretation could fit with model ages of Apārangi Planitia, ~3.7-3.2 Ga (Byrne et al., 2016), and Rachmaninoff, ~3.6 Ga (Marchi et al., 2011). A cartoon representation of the series of events is shown in Figure 4.10.

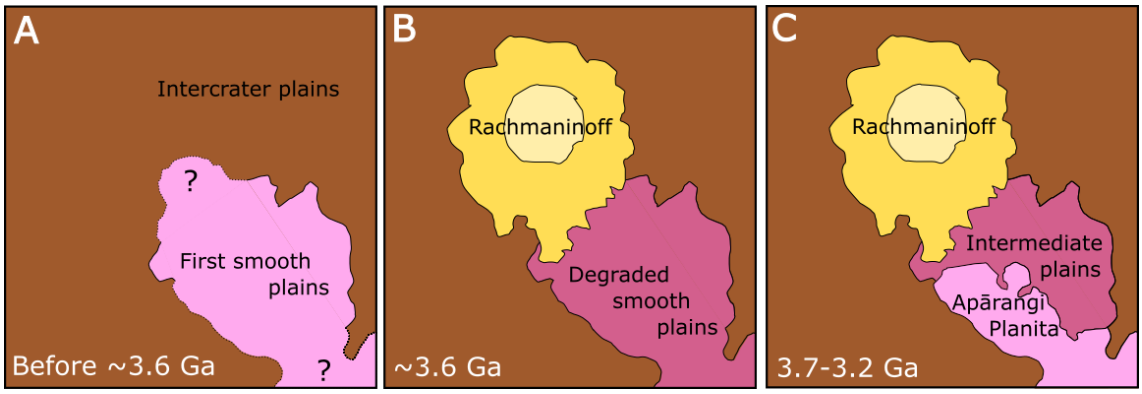

Figure 4.10: Cartoon showing possible development of the plains units around Apārangi Planitia.

Firdousi is a 95 km diameter C3 basin, with a smooth floor and poorly developed peak ring. Its ejecta overlies Apārangi Planitia and includes many radiating secondary crater chains. These are particularly useful as local stratigraphic markers to determine the order of formation of craters and basins.

Nabokov is a 157 km diameter basin in the south-east of the quadrangle. It has a well-developed peak ring, which forms a clear colour, and fairly well-defined geomorphic boundary between the volcanically resurfaced area interior of the peak ring, and a hummocky crater floor exterior to the peak ring. The impact produced small smooth plains external to the basin rim, I interpret these as impact melt 'splashes'. These are something of a rarity in the quadrangle. A well-developed ejecta blanket surrounds Nabokov and incorporates easily visible low reflectance material (LRM). The ejecta blanket is superimposed by a few later craters most notably an unnamed 68 km C3 crater to the southeast, whose ejecta overprints a small amount of Nabokov's crater floor and rim. Nabokov's crater rim is polygonal (Figure 4.11), which is

particularly visible in the southern and western rim. Polygonal craters do not appear to be more or less abundant on Mercury than on the other terrestrial planets, forming around 11% of a survey of craters (Weihs et al., 2015). The formation of polygonal craters on Mercury is not fully understood, but work on other bodies suggests it may be influenced by underlying pre-existing structural features (Aittola et al., 2010; Öhman et al., 2006; Pike, 1977).

Petipa is a small, 14 km diameter simple crater (Figure 4.12). Although below the size limit for individual mapping and so its ejecta is not classified or mapped, it has a clear ray system which was mapped. Its pristine appearance, bright diffuse ejecta and ray system marks it out as one of the youngest impacts in the quadrangle. High-resolution NAC images show potential mass-movement features in the crater interior (Figure 4.12).

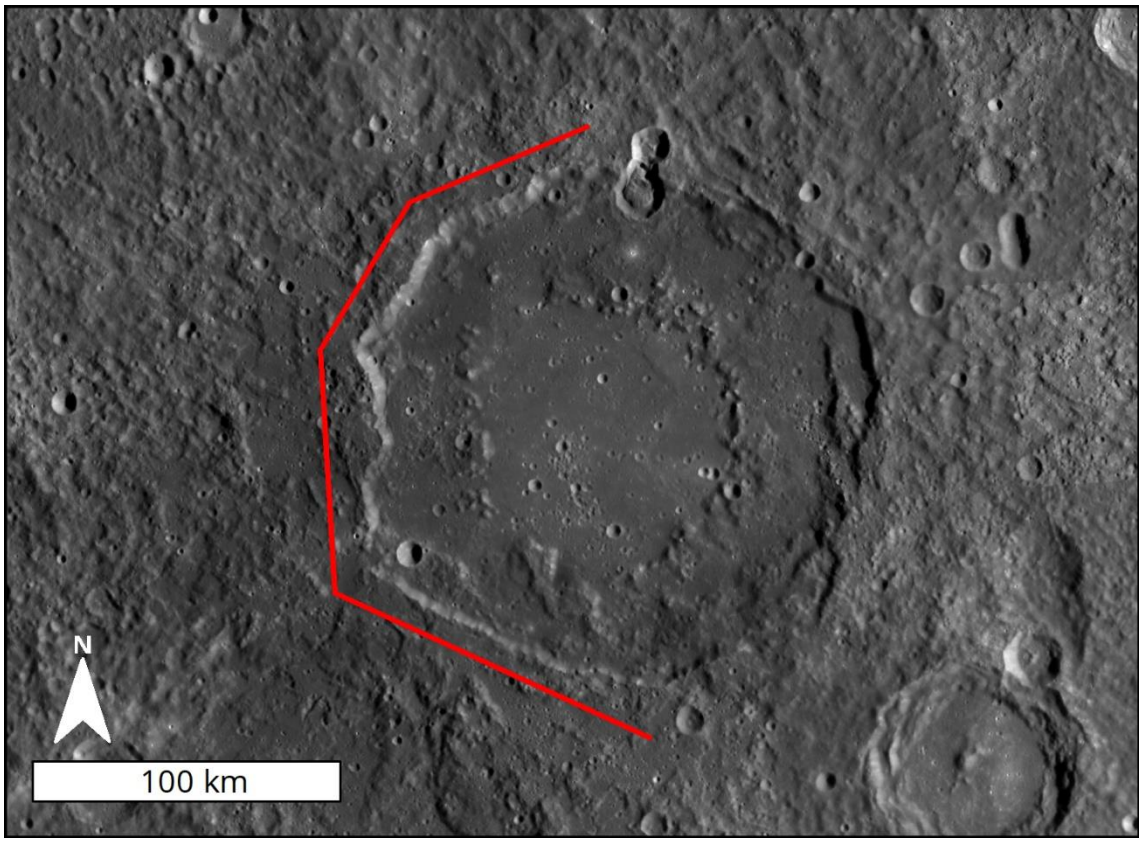

Figure 4.11: The polygonal Nabokov crater. Red lines to show approximation of general orientation of polygonal sections.

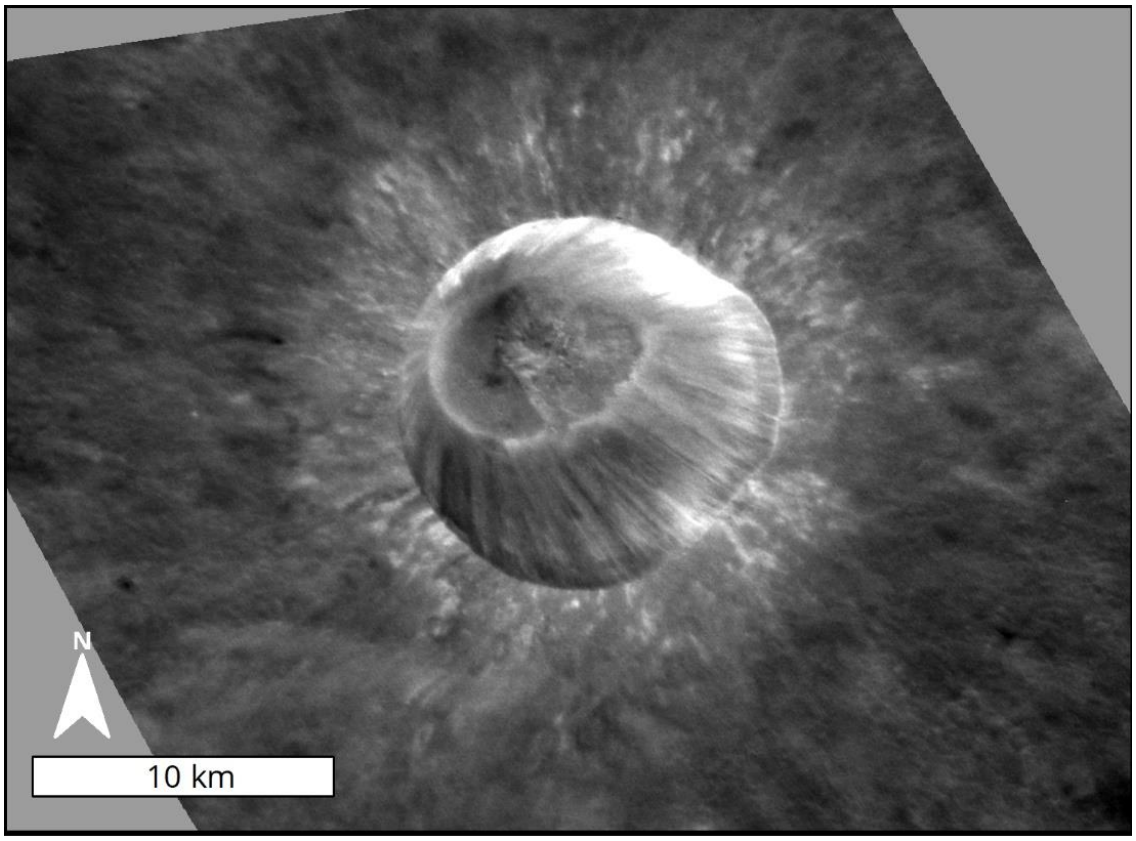

Figure 4.12: Petipa Crater (11.5°N, 21.0°W) in NAC image EN1035012166M. Note the exceptionally pristine appearance, with sharp rim and textured ejecta blanket. This crater hosts unusual slope lineae.

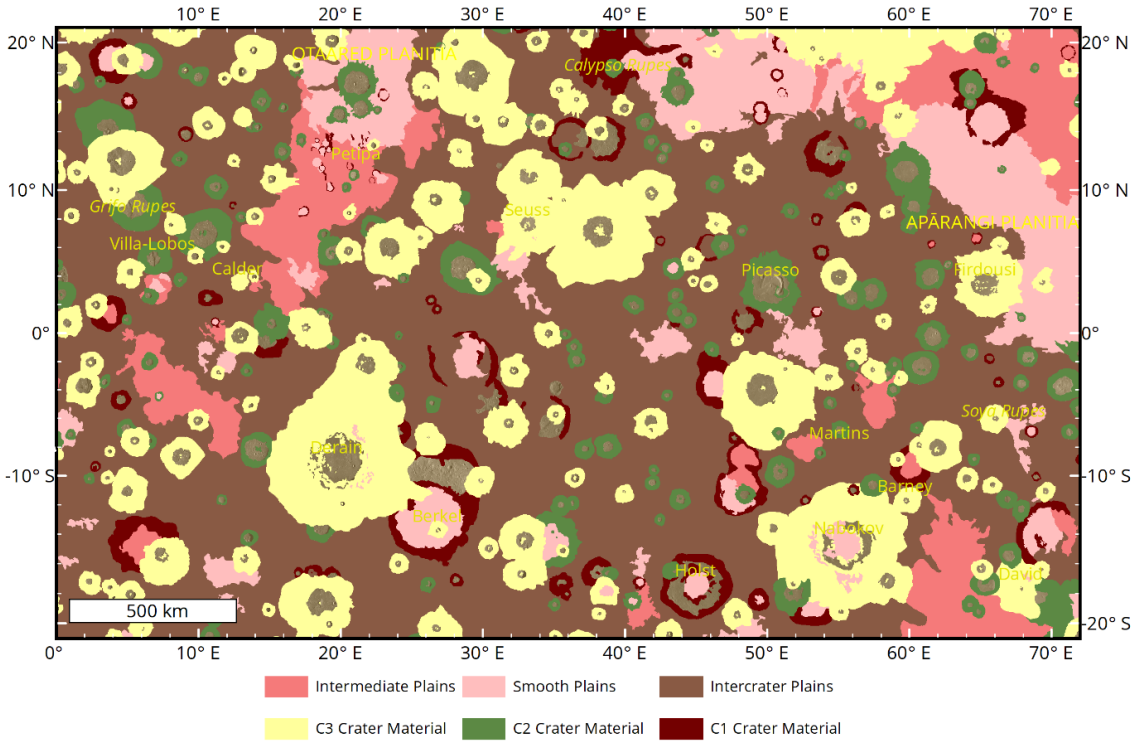

Figure 4.13: C3 and Intermediate Plains added to Figure 4.6.

4.2.6.2 Crater Rays

The very freshest craters on Mercury often have extensive ray systems visible in enhanced colour and low incidence angle imagery. These rays are one of the youngest features on the planet (Banks et al., 2017). These are useful both in diagnosing the degradation state of the crater (Kinczyk et al., 2020) and also in constructing both local and global stratigraphy. There are few (five) craters in the Derain quadrangle with rays. These are Pepita (described in 4.2.6.1), David, Berkel, and two small craters north and northwest of Berkel. These are all relatively small (< 30 km diameter) craters, with Petipa and an unnamed example northwest of Berkel <12 km diameter. These ray systems are all confined to the Derain quadrangle. These can be seen best in the enhanced colour mosaic (Figure 3.4)

Also present in the quadrangle are rays from other large impacts. These have distinctive spectral characteristics (Zambon et al., 2017), and are useful for building the global stratigraphy. Crater rays radial to the Hokusai and Debussy impacts are found across the quadrangle.

4.2.7 Faculae

Faculae on Mercury are bright red albedo features. They usually have diffuse outer boundaries. Most faculae, certainly within the Derain quadrangle, have irregular depressions towards their centres. Faculae and associated pits have been interpreted to be expressions of explosive volcanism (Jozwiak et al., 2018; Kerber et al., 2009; Thomas et al., 2014c; Weider et al., 2016).

In the Derain quadrangle faculae are mostly found in the southeast. Notably, this area has multiple large lobate scarps, such as Soya Rupes; however, there is no proven link between lobate scarps on locations of faculae (Klimczak et al., 2018).

The explosive volcanism identified likely represents one of the last volcanic processes in the quadrangle. While attempts to obtain an absolute date of diffuse faculae have been made using crater counting, the thinness of the facula material makes it hard to distinguish superimposing craters from the pre-existing craters that have remained visible because they are insufficiently mantled by the facula (Thomas et al., 2014b). That said, faculae clearly superimpose Rachmaninoff ejecta outside the quadrangle (Wright et al., 2019), and certainly post-date the end of widespread smooth plains volcanism.

Here I describe in more detail notable locations and areas of explosive volcanism in the Derain Quadrangle, as well as the single location of enigmatic 'pitted ground'.

4.2.7.1 Picasso

The most impressive and complex site of explosive volcanism in the Derain quadrangle is the facula and associated vent in the C2 Picasso impact crater (Figure 4.14).

The impact crater itself is interesting in its own right (Figure 4.14A). I have assigned it a C2 degradation class. However, for a C2 crater it has a well-developed ejecta blanket, albeit not uniform around the crater; but a poorly developed, ragged, interior wall. It hosts some peak-ring elements in the west of the crater. There is no unambiguous evidence of volcanic resurfacing of the crater floor. However, the crater floor does seem comparatively smoother, and shallower, than other craters with a similar degradation class. The crater floor is faulted by three E-W trending, but arcuate, fault scarps. The northernmost fault is the longest and forms an E-W trending 'S' shape. The western bend of this fault is almost paralleled by a second scarp to the south. A third scarp abuts the second scarp at 90° and continues east until the ejecta of a superimposing crater covers it. These scarps and a regional

slope towards the south, probably lead to a nearly 1 km drop in elevation observed across the crater floor. The faulting does not clearly cross the crater rim, although it may be associated with a small E-W scarp ~50 km west of the rim. The faulting is not sufficient to noticeably shorten the crater, such that the kinematics may be determined through measurement of shorted crater geometries as established by Galluzzi et al. (2015).

The pyroclastic volcanism in Picasso is evidenced through a diffuse, red facula and a large vent. The faculae in Picasso is approximately 85 km in diameter, and focussed towards the north of the vent (Figure 4.14B). The vent is visible as a long arc-shaped rimless depression up to 12 km wide and ~75 km long, concentric with the crater rim. It can be traced clockwise from north-northeast to south-southwest and appears to continue the arc of the peak ring that is visible from the west round to the north. It overprints a crater, superimposing both the crater fill and fault scarps. The peak ring, faulting, and crater all provide structural weakness that would aid propagation of magmatic plumbing systems, especially on a contracting planet, and would be likely to have influenced the vent location. Here magma has likely exploited the fracture network caused by the impact, and the faulting that underlies peak element to form the vent along the peak ring trace.

The vent is not uniform along its length, and both edges appear scalloped. The sharpness of detail within it is generally greater to the north. Towards the north of the vent, possible layering is visible on the vent walls (Figure 4.14D). The potential layering has an apparent dip towards the west. There are two explanations for this, either it is caused through slope failure, and mass-movement or the vent exposes two geological units at this location. These units could be multiple effusive magmatic units or a boundary between regolith units of different coherence. To see unit layering is rare on Mercury (Galluzzi et al., 2018) and further demonstrates the importance of this location for targeted imaging by BepiColombo. The facula associated

with the vent is also strongest to the north. The scalloped edges indicate that this was likely the source of multiple events of explosive volcanism (Pegg et al., 2019a), with at least four distinct main vents, but perhaps as many as eight (labelled 1-8 in Figure 4.14C).

Given that both the topography is sharpest, and facula is strongest to the north, I think it is most likely that the eruptions first happened in the most southerly vents and progressed northwards. Given the difference in facula intensity, I think there was a time interval between eruptions in the south and north. Therefore, the Picasso vent represents a location of multiple explosive volcanic eruptions at geologically different times. However, as the vents appear to overprint each other sequentially, large portions of the magma transport system must have been reused.

4.2.7.2 SE Explosive vents

The southeast of the quadrangle, around Martins crater and Soya Rupes, hosts the majority of evidence for explosive volcanism (Figure 4.15). Vents and faculae here are all much smaller than the examples in Picasso, and the faculae are weakly defined. This will partly be to do with the background plains here being more spectrally intermediate than those near Picasso, and so there is less contrast between the facula and surrounding plains.

The vents northeast of Martins (Figure 4.16) were difficult to map. The area shows a lot of irregular craters or depressions, and it is not clear from current imagery which depressions are impact craters, and which are explosive vents. It is clear that at least two of the depressions are vents, the southern one showing an irregular shape suggesting two eruptive sites. The proximity of the two clear vents, and other possible vent structures between them, likely indicates a shared magmatic plumbing system.

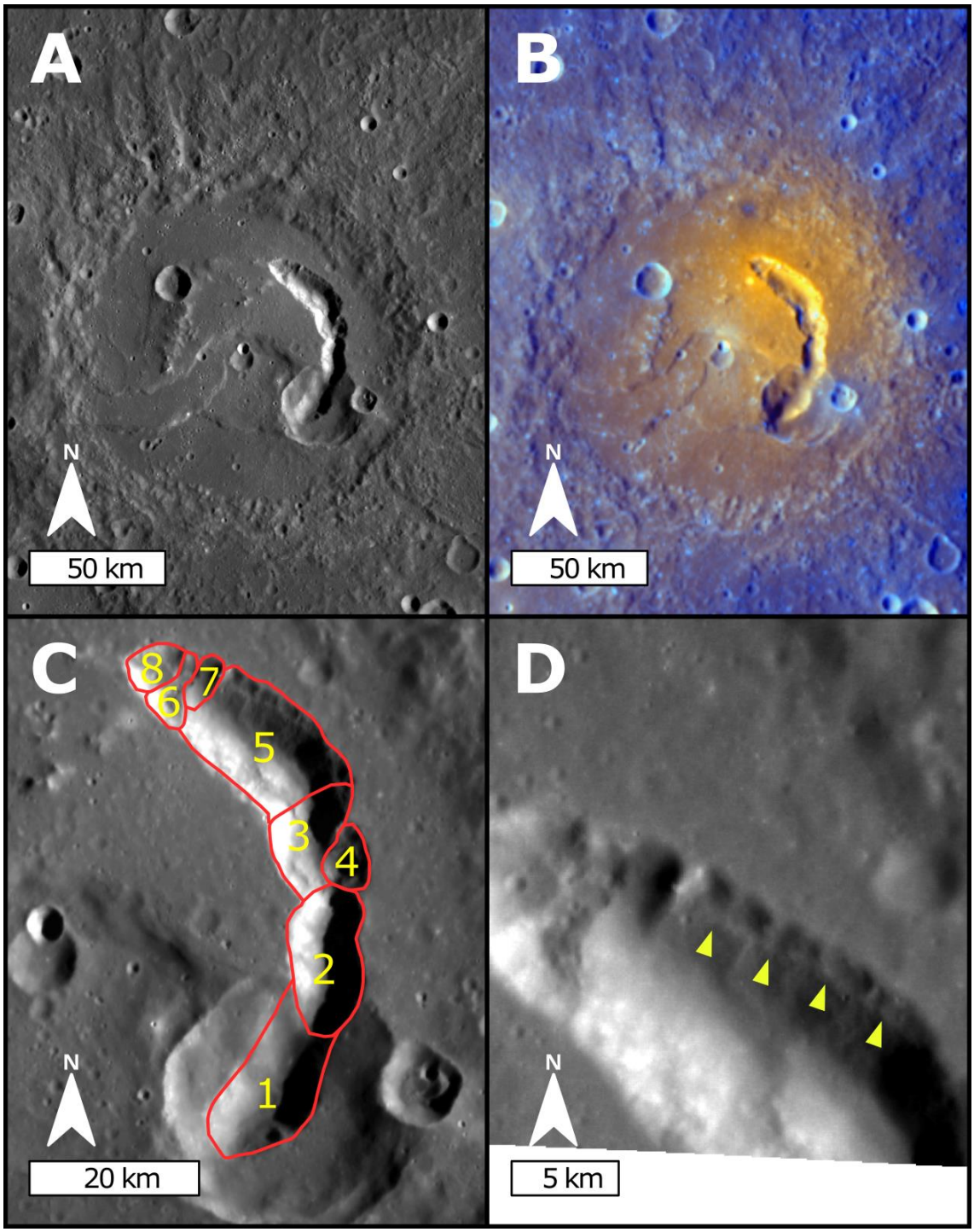

Figure 4.14: Explosive volcanism in Picasso. A and B: the Picasso impact crater in BDR mosaic (A) and Enhanced colour (B). The red facula is visible in enhanced colour; it is brightest towards the north of the curved depression of the explosive volcanic vent. C: the vent with identifiable eruption sites marked and labelled oldest (1) to youngest (8). D: the layer visible on the northern wall of eruption site 5 highlighted by yellow arrows (NAC image: EN0249843269).

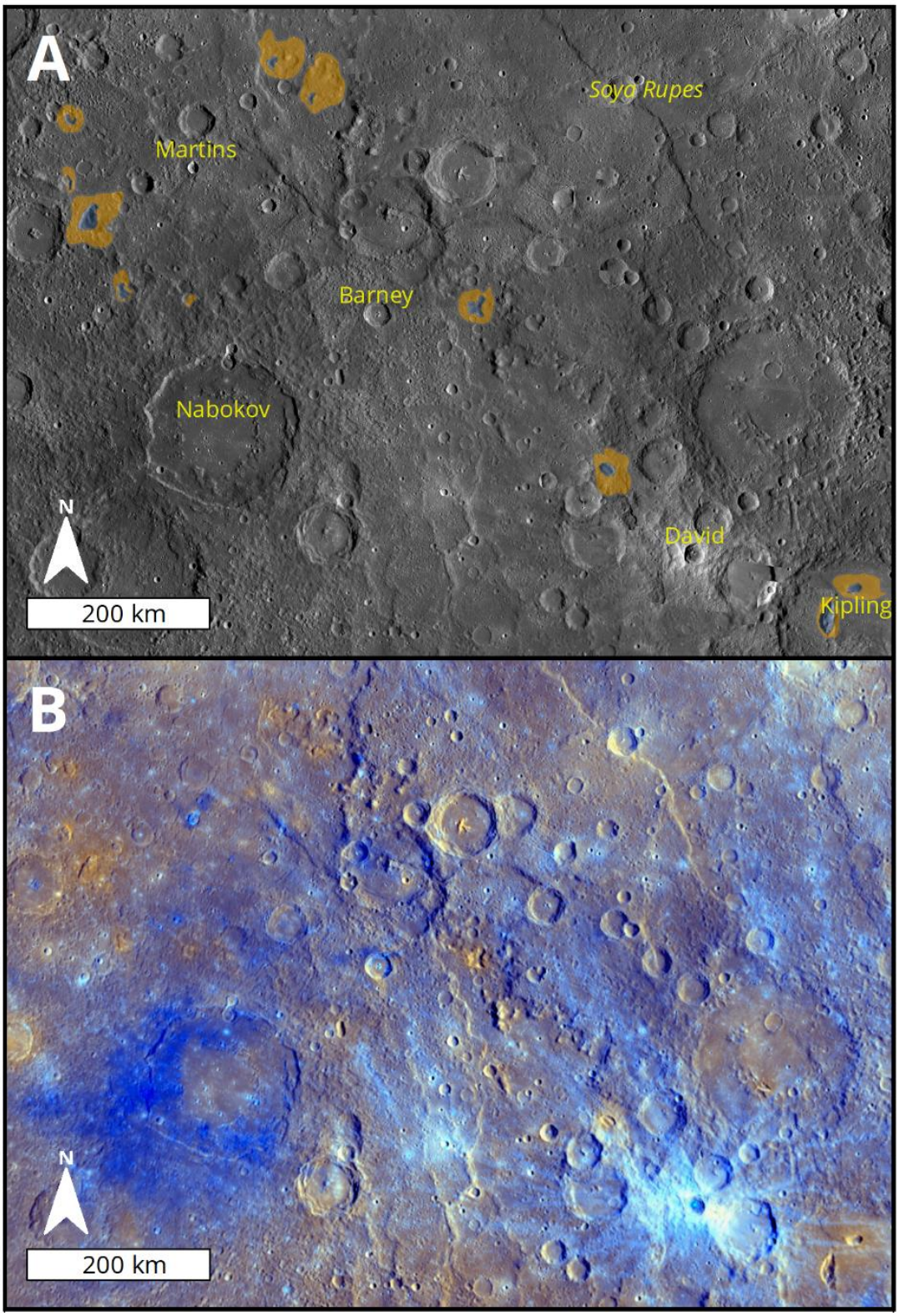

Figure 4.15: Faculae surrounding explosive volcanic vents in the southeast of the Derain quadrangle, view centred on 61°E, 12°S. A: the area in the BDR mosaic with mapped faculae marked in orange. B: the same area in enhanced colour. The area also contains NW-SE trending faults, at Soya Rupes, the unnamed scarp between Martins and Barney craters, and the N-S faulting between Nabokov and David.

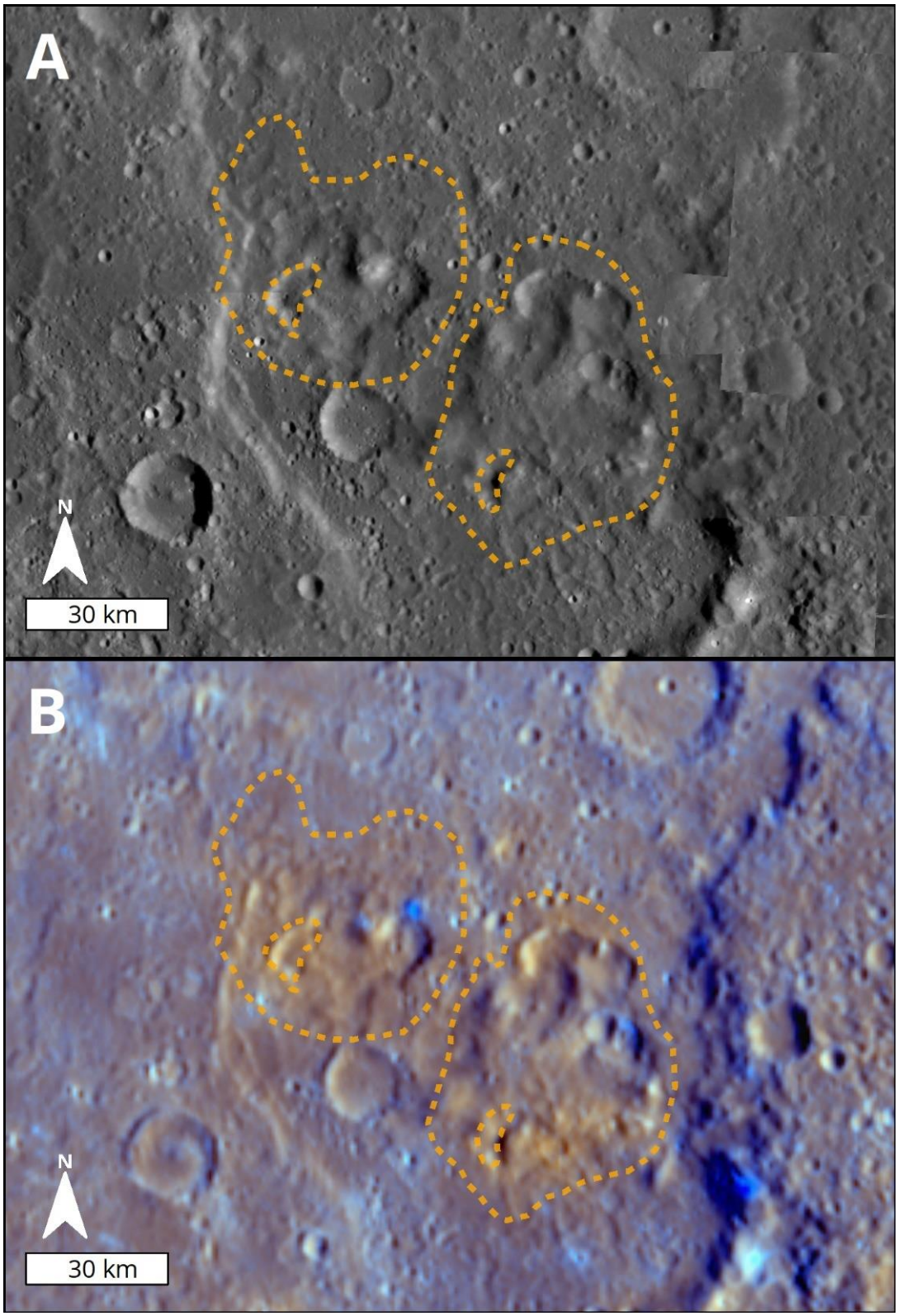

Figure 4.16: Volcanic vents northeast of Martins crater, centred on 58°E, 5°S, in BDR mosaic (A) and enhanced colour (B). The mapped extent of faculae and vents shown with the orange dashed line. The facula extent is not clear. Irregular depressions may represent other vent locations, but images in the area make it hard to distinguish vents from degraded impact craters.

4.2.7.3 Pitted ground

There are outcrops of enigmatic pitted ground features in the basin floor of Derain (Jozwiak et al., 2018; Thomas et al., 2014c) (Figure 4.17). Derain is a C3, 183 km diameter, peak ring basin in the southwest of the Derain quadrangle. The basin has a very smooth floor, and smooth plains (likely impact melt) appears to have embayed some of the terraces. There are few peak ring elements visible in the east part of the basin floor. The basin fill in the inner ring and east of the outer ring is considerably higher albedo, and generally 'redder' in enhanced colour than the fill in the outer ring. Superposing craters in this area excavate high albedo material suggesting the low albedo material common in the outer ring underlies the higher albedo cover. These observations suggest partial volcanic resurfacing, but there is no unambiguous evidence that this was later volcanic resurfacing as opposed to impact melt. Small patches of smooth plains, almost certainly impact melt, are found exterior to the basin rim (highlighted in Figure 4.17A). The basin rim has some scalloping and is pristine.

In the Derain impact structure, the pitted ground presents as rimless, flat-floored, depressions similar in appearance to hollows (Section 4.2.8), but with the rusty red colouration normally associated with faculae and explosive volcanism. The floors of the pits are generally very flat, and their rims irregular. Pitted ground is found close to the peak ring or, in the west, where a peak ring might have continued. There is one particularly striking area of pitted ground in the east of the Derain basin which appears as one very large flat-floored pit. The irregular shape and edges may suggest it arose by the coalescence of smaller pits. In the west of the basin floor, the pits are much smaller, similar to typical examples in other localities outside of the quadrangle.

There is no generally agreed upon formation mechanism for pitted ground (Jozwiak et al., 2018; Thomas et al., 2014c). Other pitted ground is found close to hollows, and this is true of the outcrop in Derain. They are not associated with any surrounding deposit other than a general increased brightness of the area they form in, and so are either not linked to any large explosive activity, or such activity is not visible within current images. Other workers (Thomas et al., 2014c; Wright, 2019) have suggested that pitted ground may have formed by devolatilization of a volatile-rich layer by the emplacement of overlying lava flows. This could explain the lack of any diffuse explosive halos away from the depressions, colour from the explosive lava-volatile interactions, and distribution of pitted ground close to hollows. Formation through devolatilization would likely rely on some volcanic resurfacing within the Derain basin. The pitted ground is found in the area of higher albedo that is most likely to represent volcanic surfacing; however, volcanic resurfacing cannot be definitively proven.

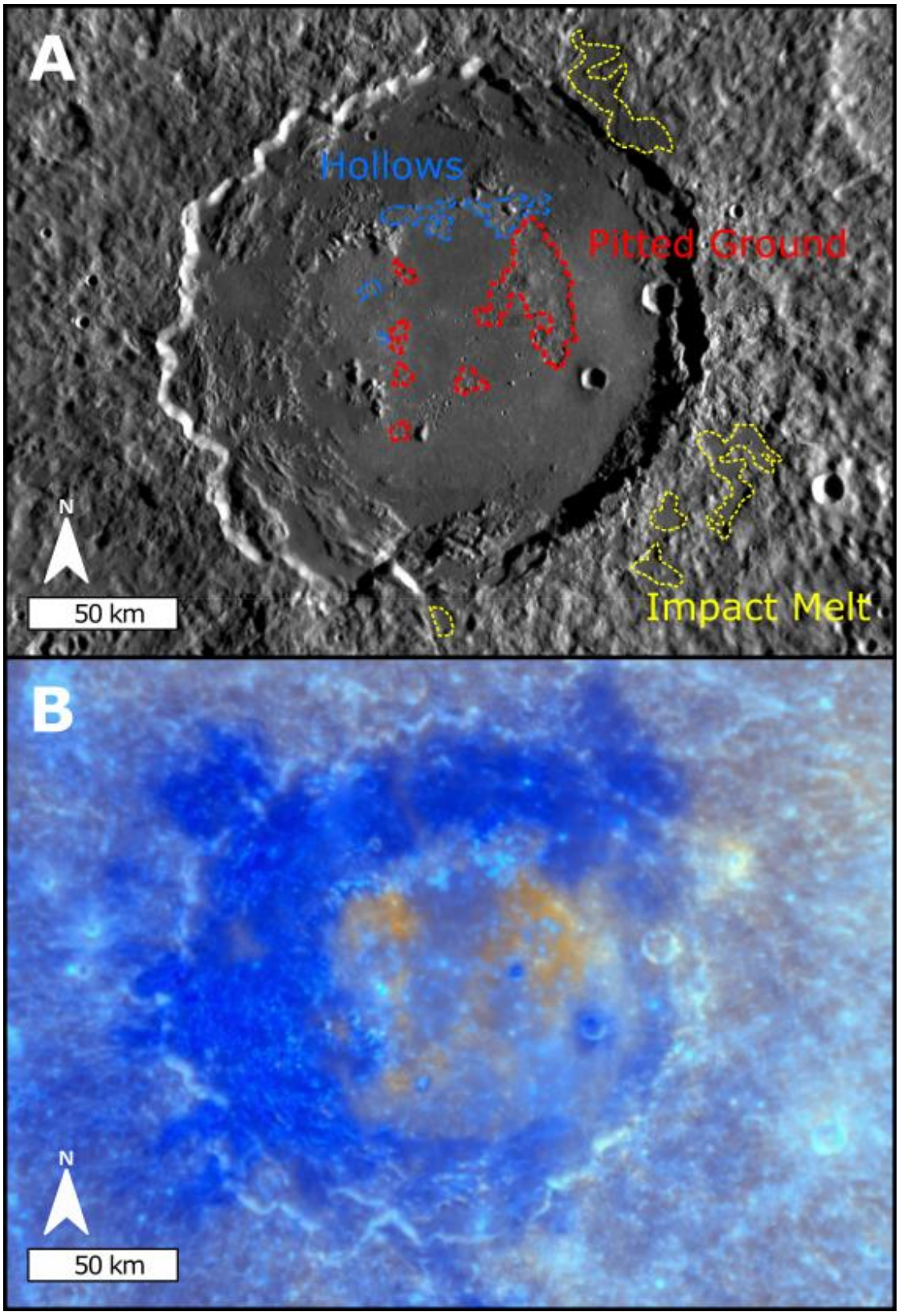

Figure 4.17: Derain impact basin in BDR mosaic (A) and Enhanced Colour (B). Pitted ground is highlighted with a red dashed outline, hollows in blue, and impact melt in yellow. Morphologically the pitted ground and hollows are quite similar but show very differently in enhanced colour.

4.2.8 Hollows

The discovery of hollows on Mercury was one of the great surprises of the MESSENGER mission. They are shallow, flat-floored, irregular depressions with distinctive colour properties, and are thought to form via loss of volatiles (Blewett et al., 2013, 2011). There are few localities that host hollows in the Derain (H-10) quadrangle compared to other mapped quadrangles. As I required both morphological and spectral evidence (via enhanced colour) to map an area as hollows, it is likely that smaller areas of hollows may be identified with images with better spatial resolution. The better imagery required would include both colour images to determine if some sites with hollow like morphology have associated colour signatures; and morphological images, as high enough resolution images are not available for all areas with blue colour. All the hollows I mapped are in or surrounding pristine impact craters, such as Berkel, Derain, and Suess (Figure 4.18A and B). Thus, the location of hollows appears to be controlled by the availability of recently excavated material. The siting of all hollows at pristine craters suggests that hollows in the H-10 quadrangle are also geologically recent, and likely one of the youngest features in the quadrangle.

Most examples of hollows in the quadrangle are typical of those described by other workers (Blewett et al., 2011; Thomas et al., 2014a); however, those at Martins crater are peculiar (Figure 4.18C and D). Martins is a 12 km C3 crater, which was named at my request because it is associated with features of special interest (Chapter 6). The main area of hollows is located on the northeast edge of the crater and comprises a broadly circular, pock-marked area of small irregular depressions. This area is unusual as the floors of the depressions are not obviously flat, nor are they surrounded by a high albedo material as is typical. This area is also different from typical hollows as the area has many small, distinct, depressions. Typically, as hollows become larger they appear to coalesce; this cannot be seen here. Images available of

this area are not at an ideal resolution, or lighting conditions for viewing the depressions and new, better, imagery could later show the morphology to resemble typical hollows better. Unlike most hollows in the Derain quadrangle, the main area of hollows is found outside the crater rim. This main area of hollows occurs in a sharply defined, broadly circular area; most other examples in H-10 form uneven, random, patterns. This would suggest that volatile bearing regolith is found in very restricted geographic areas or some other control on the hollow forming process. Given this area's unusual morphology, I have considered they may be impact related, possibly a cluster of secondary impacts, rather than hollows. I rejected this because the area is both associated with a hollow-like colour anomaly that other nearby pristine similarly sized impacts do not show; as well as visibly overprinting the rampart of Martins crater, without causing any rim collapse as a series of small impacts would be expected to do. That the features have not coalesced suggests the hollows were unlikely to be active over a long period. The quasi-circular shape could be linked to a pre-existing impact crater. Exactly why hollow forming material would be concentrated in a completely covered impact crater is not clear. Therefore, I think the best explanation for this patch is a set of small, likely short-lived, hollows.

Also of note at Martins crater, are slope lineae on the crater walls. The slope lineae are previously undescribed mass-movement features and are discussed at length in Chapter 6. They are likely young as micro-meteorite impacts and space weathering would erase small thin features quickly.

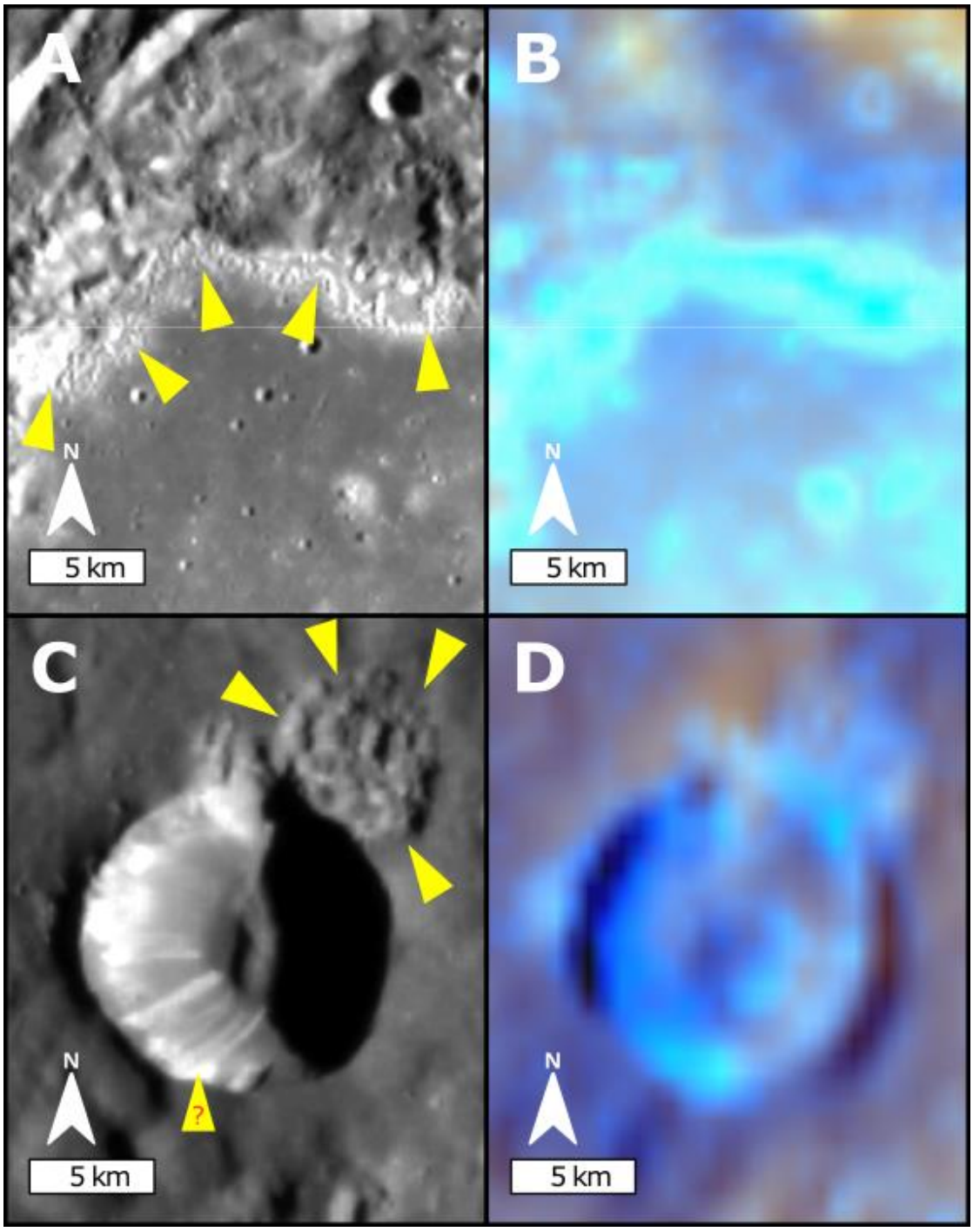

Figure 4.18: Hollows (marked with yellow arrows) at Suess crater (A and B), and Martins crater (C and D) in BDR mosaic (A and C) and Enhanced Colour (C and D).

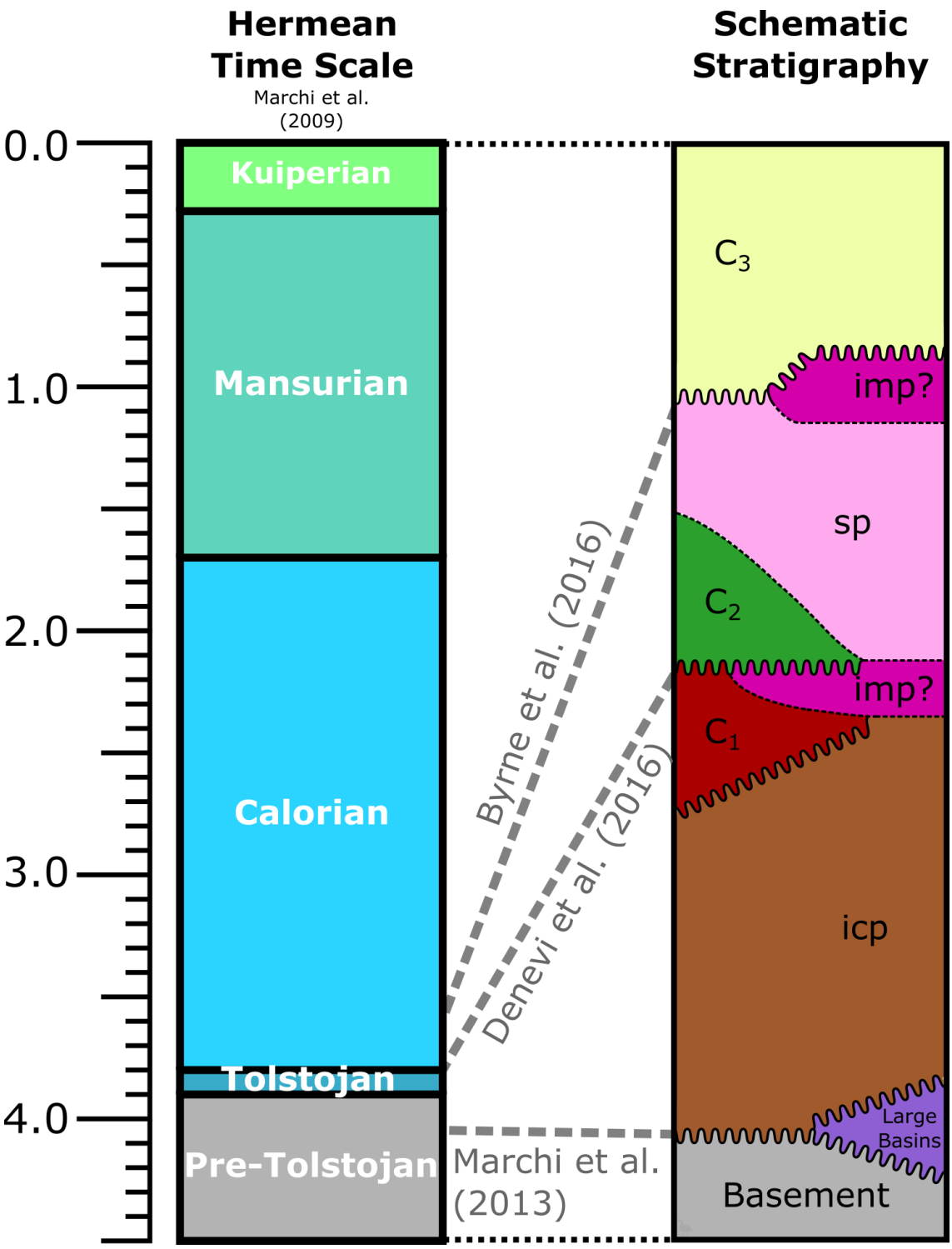

Figure 4.19: Schematic stratigraphy of the Derain (H-10) Quadrangle. On the left is the Hermean time system as revised by Banks et al. (2017) and Ernst et al. (2017) based on the Marchi et al. (2009) crater production function. On the right is a schematic stratigraphic column. Undulating boundaries indicate erosive contacts. Dated time intervals connect the columns from the literature.

4.2.9 Correlation of units

I have constructed a schematic stratigraphy of the quadrangle from the history presented in this chapter in Figure 4.19. I have followed Galluzzi et al. (2016), the stratigraphy is idealised, and not every relationship has been observed in the quadrangle, but all can be inferred.

4.3 Structural History

4.3.1 Lobate Scarps

The most obvious tectonic features in the Derain quadrangle are the lobate scarps making up large thrust systems, particularly Calypso, Soya, and Grifo Rupēs (the latter two of which were named after name requests by myself). Thrust fault scarps are found in all plains units, although they are most common within the intercrater plains. Globally, all mapped thrust faults that interact with smooth plains superimpose and postdate the smooth plains, bar one (Watters et al., 2009) which has an ambiguous relationship. Therefore, the majority of faulting visible at the present day is likely to have been active after the end of large scale effusive volcanism and so after the onset of global contraction. It is possible, and likely that faulting took place before this, but cannot be easily dated in the intercrater plains, or was covered over by large effusive volcanism. Some efforts have been made to date fault systems using buffered crater counting and cross-cutting relationships (Fegan et al., 2017; Ferrari et al., 2015; Giacomini et al., 2015). Ferrari et al. (2015) and Giacomini et al. (2015) use buffered crater counts to date to lobate scarp systems (Enterprise and Blossom Rupēs in the Debussy and Eminescu quadrangles respectively) to between 3.8 – 3.6 Ga and 3.7 – 3.5 Ga respectively, both well in the Calorian and around the onset of global contraction. Faulting has continued into the Kuiperian, and small thrusts tens of metres in relief were discovered in low altitude, high-resolution MDIS images (Watters et al., 2016). Given the rapid production of regolith and

topographic diffusion on Mercury (Fassett et al., 2017), these are certainly very young, and dating efforts have suggested ages of less than 50 Ma. While none of these small lobate scarps have been found in the Derain quadrangle, higher resolution imaging from BepiColombo may well reveal smaller fault scarps.

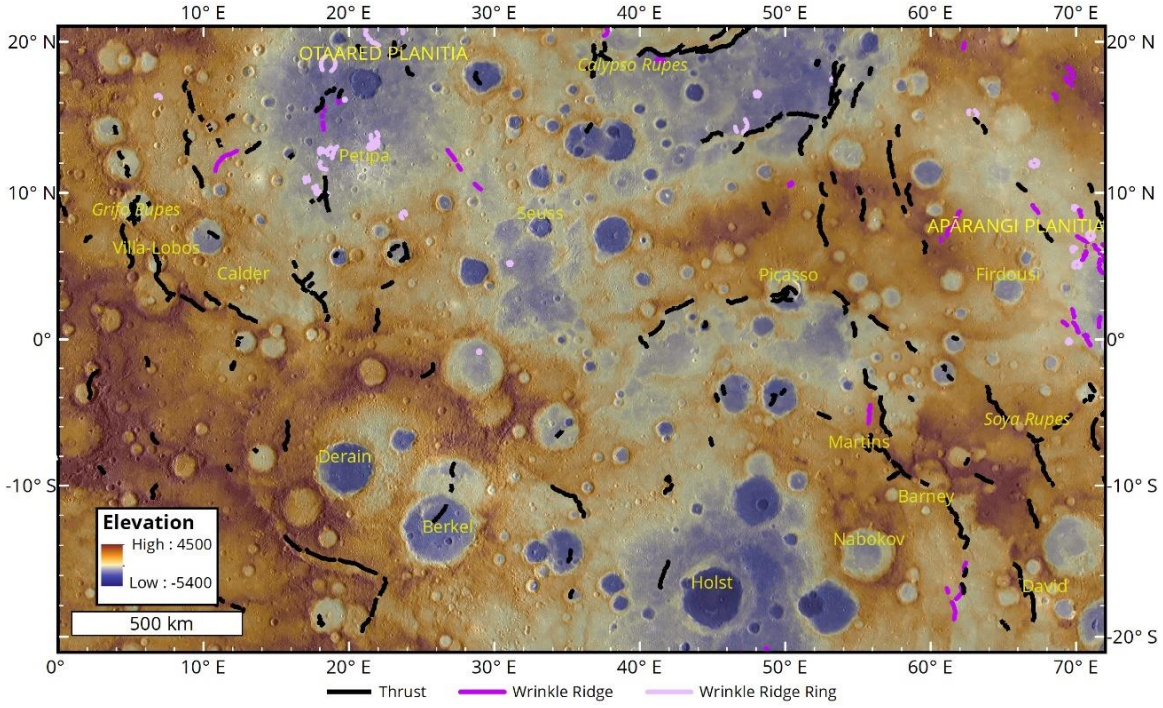

Figure 4.20: Distribution of tectonic features across the Derain quadrangle.

As can be seen in Figure 4.20, faulting occurs in large systems across the quadrangle and as smaller isolated scarps away from the large named fault systems. Some of these form locally significant systems, but on the whole, these are mainly small and isolated. Faults across the quadrangle generally trend N-S. Although there are notable exceptions at Calypso Rupes, and the small system ~200 km south of Calypso Rupes, and those that appear to follow the edges of ancient basins.

Here I describe the two most prominent tectonic features across the quadrangle in more depth.

4.3.1.1 Grifo Rupes

Grifo Rupes is a ~600 km long fault system running approximately north-northwest to south-southeast in the northwest part of the quadrangle. It is not a single monolithic scarp but is a system comprising of approximately three principle scarps forming the main fault trace, with multiple small faults en-echelon with the main scarps, or nearby. Topographic difference across the scarp varies, from ~200 m towards the north, to just over 600 m near Villa-Lobos Crater in the south as measured using the global DEM. These small scarps are most clearly visible in the smooth fill of the craters crosscut by the main scarps. The main fault scarp at the southern end of Grifo Rupes, through and to the south of Villa-Lobos Crater (Figure 4.21), has three distinct sections, running ~0° through Villa Lobos, then 160°, and then at 125°, to form a bow shape (Figure 4.21B). This appears to be along a continuous scarp. The fault here resembles the bow shape of Beagle Rupes (in the Eminescu quadrangle), which was interpreted as a main front with lateral ramps (Rothery and Massironi, 2010). This section of Grifo Rupes is likely similar if a less extreme case. Therefore, it probably does not represent a purely compressive fault, and the ramps will have accommodated some strike-slip component. One of these lateral ramps fully cuts across and shortens the Villa-Lobos crater. Assuming the crater was originally circular, the direction and degree of shortening allow kinematics of the fault to be calculated. Galluzzi et al. (2015) calculated that the fault through Villa-Lobos was steeply dipping with a true dip of 29°, and the angle between the fault strike and slip vector of 133°. If the slip vector was pure compression this angle should be 90°, therefore showing this lateral ramp has a degree of strike-slip movement, so suggesting the other ramp has a similar amount of strike-slip motion on it.

Towards the north of the system, the fault changes vergence (Box A, Figure 4.21). This could be explained as a pop-up from a fault forming in the fold above the fault structure, as shown in Figure 4.22.

Grifo Rupes generally follows the edge of the large B30 basin (Figure 4.2). The basin rim from such a large structure will have been an area of weakness that could promote the development and growth of faults.

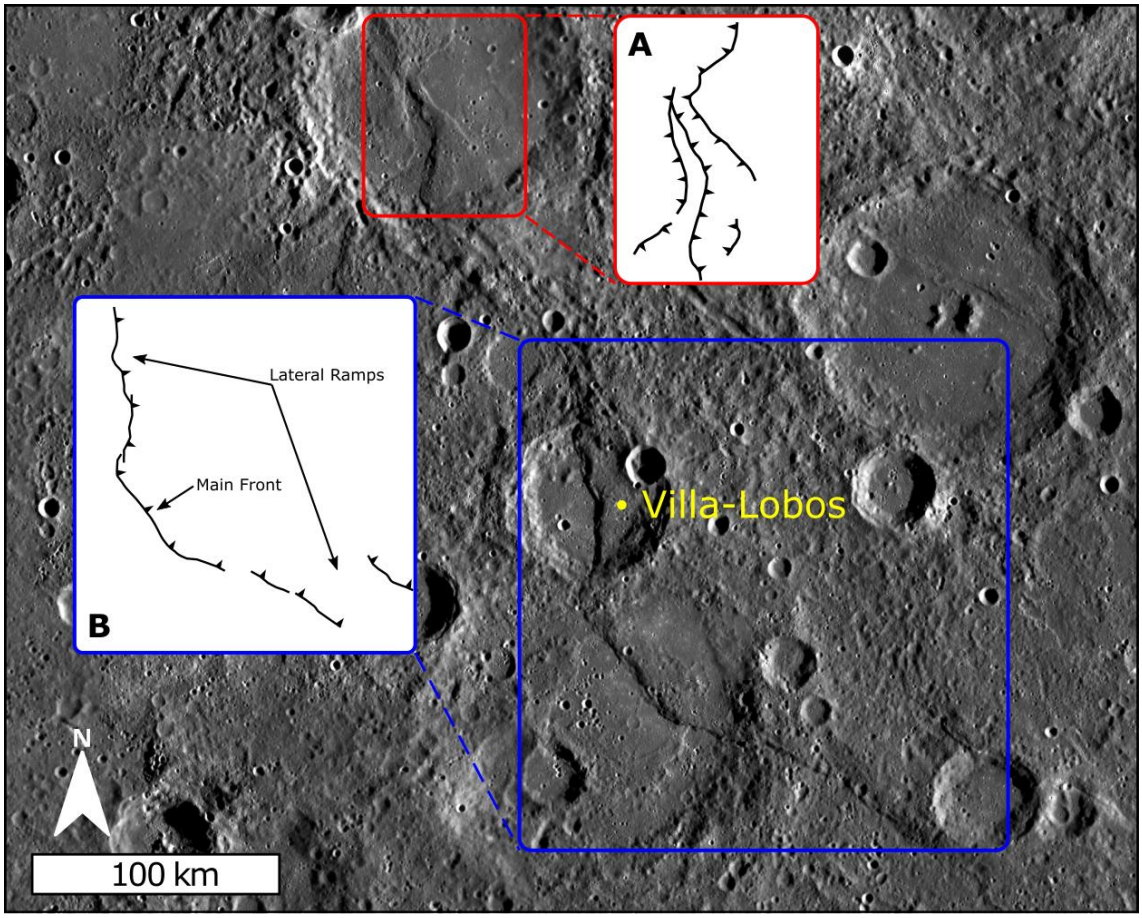

Figure 4.21: Part of Grifo Rupes. Box A shows the complex assemblage of fault segments of different vergence in an unnamed crater. Box B shows the fault around the Villa-Lobos Crater. The main front and Lateral ramps are labelled.

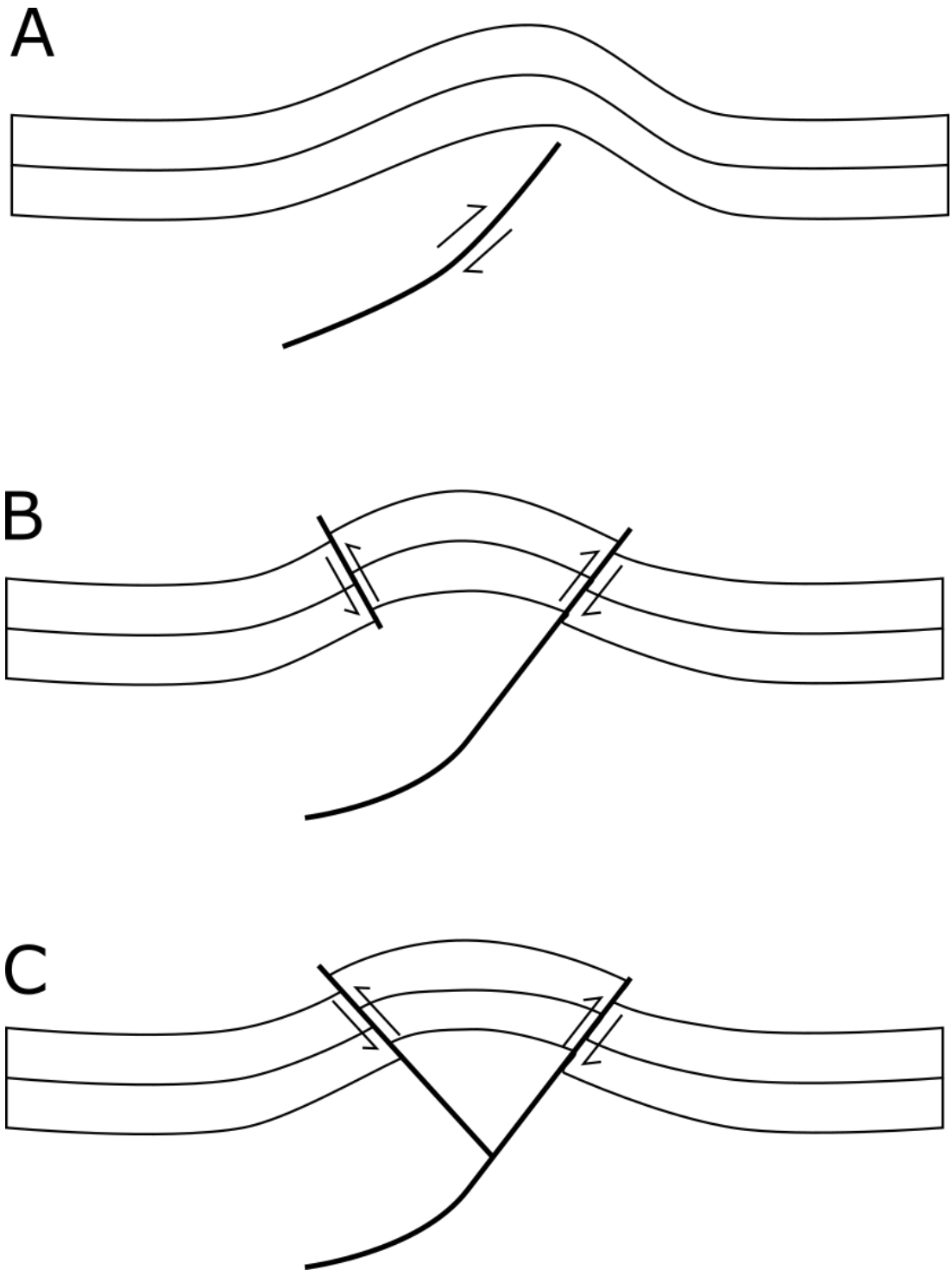

Figure 4.22: Cartoon of a possible formation mechanism of opposite verging faults via a pop-up structure in Grifo Rupes (e.g. Figure 4.21 Box A).

4.3.1.2 Calypso Rupes

Calypso Rupes is a ~370 km, east-west trending fault system in the north of the Derain quadrangle. To the east, the fault peters out generally at the ejecta of the C3 Rachmaninoff crater, although some small scarp sections look to

cut the ejecta. I interpret this to show that the majority of movement on the scarp predates the Rachmaninoff impact, but the system remained active after the formation of the basin. This, coupled with the fresh appearance of tectonism across the system, means Calypso Rupes would be a good target for high-resolution imaging to look for small, recent fault movements. The topographic difference across the scarp ~ 1000-1200 m measured using the global DEM.

Calypso Rupes shows complex morphometry that is incompatible with pure compression (Figure 4.23). Of particular interest is the curved section in the west of the main fault break (Box A, Figure 4.23) Here the system has two parallel fault scarps, at the top and bottom of the main break in slope. The scarps are of the same vergence. If all the scarps likely formed in the same stress field, this curvilinear fault set cannot be pure compression. If the scarps are purely compression, there must have been substantial changes in the stress field while these faults were active. Given that all scarps seem to have a similar state of degradation I think this unlikely.

At the western edge of the northern fault set, there is a small extensional graben. Elsewhere on Calypso Rupes, these have been interpreted as an extension over a monoclinal fold on the hanging-wall; this type of feature may be referred to as a keystone graben (Wise, 1963). The more northerly scarps in this set appear more degraded than both the scarps to the south of the main break and this graben. So, I think the faulting at the top of the current break in slope may predate the faulting at the base of the scarp. The graben would then be associated with the more recent faulting as the base of the break in slope. The shape of the faults here may follow the trace of a ~60 km diameter former impact basin. This is speculative as no other trace remains of it, but it could have provided a set of weakness to be exploited.

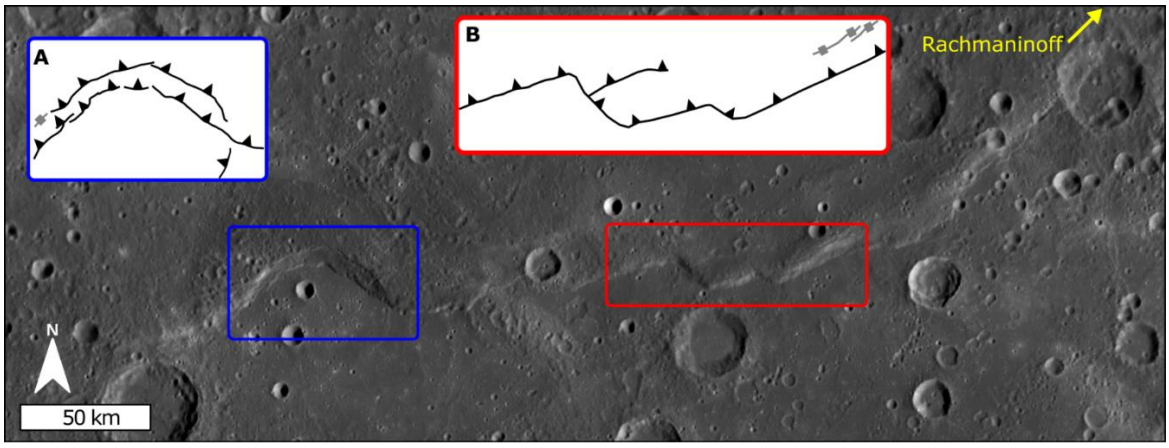

Figure 4.23: Calypso Rupes (centred at 43°E, 20°N). Inserts show sketch maps of fault structure. Thrust scarps are shown in black, extensional graben in grey.

The other key area of tectonic interest at Calypso Rupes is shown in box B in Figure 4.23. This section has two steps that at first look appear to have acted as right-lateral strike-slip faults to offset the trace of Calypso Rupes. However, when examined in detail, there is no clear evidence to suggest these sections deformed active fault scarps. Topographic profiles across these sections do not show the characteristic asymmetric gradual ramp to the scarp and steep break over the scarp typical of lobate scarps on Mercury. The scarps are visually steep and do not appear to be relay ramps. I, therefore, think it likely that this section of Calypso Rupes cannot be purely compressive.

Localised extension can be seen in the small grabens above the scarp in the east of this section. Like the example already described further west, these were likely formed by extension in the monocline in the hanging-wall. These features are small, <2 km across, and around 20 km long. Their elevation is not resolvable in the global DEM and so is likely to be in the tens of metres. Such small-scale features are unlikely to survive for any length of time on Mercury and could be indicative of recent tectonism at Calypso Rupes (Banks et al., 2015)

The relationship between Calypso Rupes and areas of smooth plains apparently ponded against it is discussed in Chapter 5.

4.3.2 Wrinkle ridges

The other main type of structural feature visible at the surface is rounded wrinkle ridges. In contrast to lobate scarps, wrinkle ridges have a symmetrical, rounded profile and generally do not form large scale linear systems. There are two main populations of wrinkle ridge I have mapped: linear wrinkle ridges, and those forming a ring shape. They are otherwise indistinguishable. Both populations of wrinkle ridges are found exclusively in the smooth and intermediate plains of the Derain quadrangle. Most linear wrinkle ridges trend broadly north-south. Given that solar illumination in the global mosaics is likely to highlight this orientation preferentially, this may not be a fair representation of wrinkle ridge orientation. Recognising and correcting for illumination bias in the visibility of tectonic features in MESSENGER images is a thorny problem that has not yet been overcome (Fegan, 2018; Fegan et al., 2017).

Wrinkle ridges are thought to form under compressive stress and may be a surface expression of thrust faults (Byrne et al., 2014). The wrinkle ridge rings are presumably formed by faulting exploiting the weakness between a smooth plains unit and a buried crater wall, hence forming an outline of a buried crater. The symmetrical appearance of wrinkle ridges can be explained by the smooth plains remaining more elastic than the intercrater plains, and therefore accommodating strain by folding above a non-surface-breaking fault.

Numerical modelling has been used to suggest that faults forming wrinkle ridges are deep-rooted, that the faults underlying some wrinkle ridges likely project 10–15 km into the crust (Peterson et al., 2020, 2019), considerably deeper than the 3 km estimated thickness of the northern smooth plains (Head et al., 2009; Ostrach et al., 2015). This would be consistent with faulting from global contraction, given the horizontal stresses required to form such

large, deep faults. Other geomorphological studies suggest that some wrinkle ridge faults in the northern smooth plains are shallowly rooted (Crane and Klimczak, 2017). Crane and Klimczak (2017) also suggested a latitude dependence in the northern smooth plains, and therefore structures formed through tidal despinning may act as an influence on wrinkle ridges. There is too small a geographic expanse of smooth plains and wrinkle ridge to be able to make similar inferences from the available data in the Derain quadrangle. It is not clear whether the wrinkle ridges in the Derain quadrangle are thick or thin-skinned. The low number of wrinkle ridges and the problem that the illumination bias cannot be overcome with the sparse MLA coverage makes it hard to determine if wrinkle ridges are predominately related to tidal despinning or are primary features from global contraction. The faults that formed the wrinkle ridges were, however, undoubtedly either formed or reactivated when the present wrinkle ridges formed.

4.3.3 Grabens

Evidence of extensional tectonics on Mercury is limited. The best examples of extensional features are the radial grabens that comprise Pantheon Fossae in the Caloris Basin. Known examples are usually restricted to the interior of large basins and have been linked to the contraction of cooling melt or isostatic effects (Blair et al., 2013). Examples of extensional grabens within the Derain quadrangle, other than small local extensional grabens in thrust related monoclines (Section 4.3.1.2), are limited to the interior of the Derain impact basin.

4.4 Conclusion

Based on my observations and mapping, my interpretation of the geological history of the quadrangle is as follows:

1. The primary crust formed. This is now visible as LRM that has been excavated in examples such as around Nabokov and southeast of the Derain basin.
2. The volcanic secondary crust began to be emplaced. This older volcanism now forms the intercrater plains.
3. Throughout this period there will have been many impact basins formed, including the large, buried basins as well as all C1 and most C2 craters.
4. Effusive volcanism began to wane at around 3.5 Ga. These younger volcanic plains are today the major areas of smooth plains, for example Apārangi Planitia.
5. At around this point, the faulting currently visible would have started with the onset of global contraction. This has continued globally to the geologically recent.
6. Some patches of smooth plains and some mantled intermediate plains will have formed. This represents the youngest resurfacing outside impact craters.
7. Explosive volcanism formed faculae. Absolute ages are unclear but given that vent sites show evidence of multiple eruptions this will have happened over an extended period of time.
8. Hollows currently visible formed. This suggests volatile material is still close to the surface in parts of the quadrangle.

My mapping of the Derain quadrangle has shown the area to be an excellent area for showing the full range of geology on Mercury. However, there are still unanswered questions, and further work would enable the quadrangle to be better understood.

There is great potential to improve our knowledge of the fault systems in Derain, especially at Calypso and Grifo Rupēs. These systems have interesting kinematics, exhibiting some strike-slip behaviour rather than pure

compression. Future work on the fault kinematics at these systems will be useful in properly understanding the history of faulting and stress regime across the planet.

The emplacement mechanism and age of the mantled intermediate plains will be useful in understanding the resurfacing history on Mercury and could be used to elaborate the global stratigraphy further. The increased geochemical capabilities of BepiColombo (Cremonese et al., 2020; Fraser et al., 2010; Hiesinger et al., 2020) will enable mapping to represent the geology at the surface more accurately. Determining geochemical boundaries could help greatly in making sense of the morphological boundaries mapped. For instance, Fe/Mg ratios may help determine if large units are derived from the same mantle source, if so this may indicate they are close in age.

In Chapter 5 and Chapter 6, I describe two types of previously unknown (or, at least, under-reported) features that came to my attention during my study of H-10. Small ponded patches of smooth plains (Chapter 5), and a survey of possible volatile-related slope-related processes in H-10 and beyond (Chapter 6) instigated after I recognised the unusual nature of Martins crater (Section 4.2.8).

CHAPTER 5
SMALL SCALE SMOOTH PLAINS ON MERCURY

5.1 Introduction

Unravelling the history of magmatism and tectonism at the surface of Mercury is vital to understand the planet's geological history fully. Magmatically derived units on Mercury are typically classified based on their geomorphology (Byrne et al., 2013; Denevi et al., 2013; Whitten et al., 2014). Younger units are generally smooth and relatively un-cratered, whereas more ancient units are more heavily cratered and textured.

Mariner 10 mappers subdivided Mercury's plains into three main plains units; Smooth, Intermediate, and Intercrater plains (De Hon et al., 1981; Grolier and Boyce, 1984; Guest and Greeley, 1983; King and Scott, 1990; Schaber and McCauley, 1980; Trask and Dzurisin, 1984; Trask and Guest, 1975). These are described in more depth in Chapter 3 and Chapter 4. Some workers also mapped a 'very smooth plains' unit (e.g. Strom et al., 1990). As noted in Chapter 3 and Chapter 4, the same three or four plains units are not recognised in all MESSENGER-era geological mapping (Whitten et al., 2014). Furthermore, it should be noted that smooth plains is a geomorphically descriptive term, without genetic implications. Different units mapped as smooth plains may have different modes of emplacement.

It is essential when examining a planetary surface to be familiar with similar features on other bodies. When examining Mercury, the Moon is often used as an analogue, as both are similar sized, airless rocky bodies, although clearly they are not identical. The most extensive lunar smooth plains features are the maria. Lunar maria have been shown to be large basaltic

flows, and thus to represent a volcanically emplaced smooth plains unit. There is potential evidence of young effusive volcanism on the Moon, with some workers suggesting activity within the past 100 Ma at 'irregular mare patches' (Braden et al., 2014). Other smooth plains units such as the Cayley formation, or lunar light plains, have been shown to form from impact ejecta processes (Apollo Field Geology Investigation Team, 1973).

The vast majority of smooth plains mapped on Mercury are of large surface area and usually occupy topographic lows. Most of these deposits are interpreted to be volcanic in origin (Denevi et al., 2013). Based on analysis of impact crater size-frequency statistics, the largest areas of smooth plains are thought to have formed ~3.7 Ga, and the youngest extensive example ~3.5 Ga (Byrne et al., 2016; Denevi et al., 2013). This has been taken to indicate that widespread effusive volcanism ceased at around 3.5 Ga, possibly as secular cooling reduced the availability of melt (Evans et al., 2015), or relatedly the secular cooling causing the onset of Mercury's global contraction at around this time making it harder to open magma conduits to the surface (Byrne et al., 2016). Therefore, tectonic features should postdate Mercury's large volcanic plains. However, evidence of effusive magmatism in relatively undegraded impact craters was noted by Byrne et al. (2016) and Prockter et al. (2010). Clear evidence of effusive magmatism has been found in Mansurian age (1.7 – 0.3 Ga) impact basins of effusive volcanism (Wright et al., 2017) This is a clear indication that although widespread, large scale effusive volcanism may have ceased at the onset of global contraction, small-scale effusive volcanism continued. Notably, impact craters are places where local subsurface fractures can be envisaged as allowing magma egress to the surface despite the global contractional regime.

During my mapping of the Derain (H-10) quadrangle, I found several small, (area <15,000 km^2) patches of smooth plains (Figure 5.1), some of which do not lie within impact craters (e.g. Malliband et al., 2018). Of these, some

examples abut lobate scarps. Only a very few brief mentions (Denevi et al., 2013; Head et al., 2009) exist in the literature about similar small smooth patches on Mercury, and none seeks to explain them, or even describe them in detail. However, they are significant because the position of such patches abutting (ponded against) contractional tectonic features (lobate scarps) suggests that the smooth patches are even younger than the scarps, which would make them significantly younger than the more extensive smooth plains occurrences that are cut by thrusts. For these observations to inform our understanding of the geological history of Mercury, we must understand what they represent and how they were emplaced. In this chapter, I describe the smooth patches I have found (located in Figure 5.1), both in and beyond the Derain quadrangle, and discuss hypotheses for their genesis. I begin with crater-hosted smooth patches, before describing examples that appear to be ponded against lobate scarps.

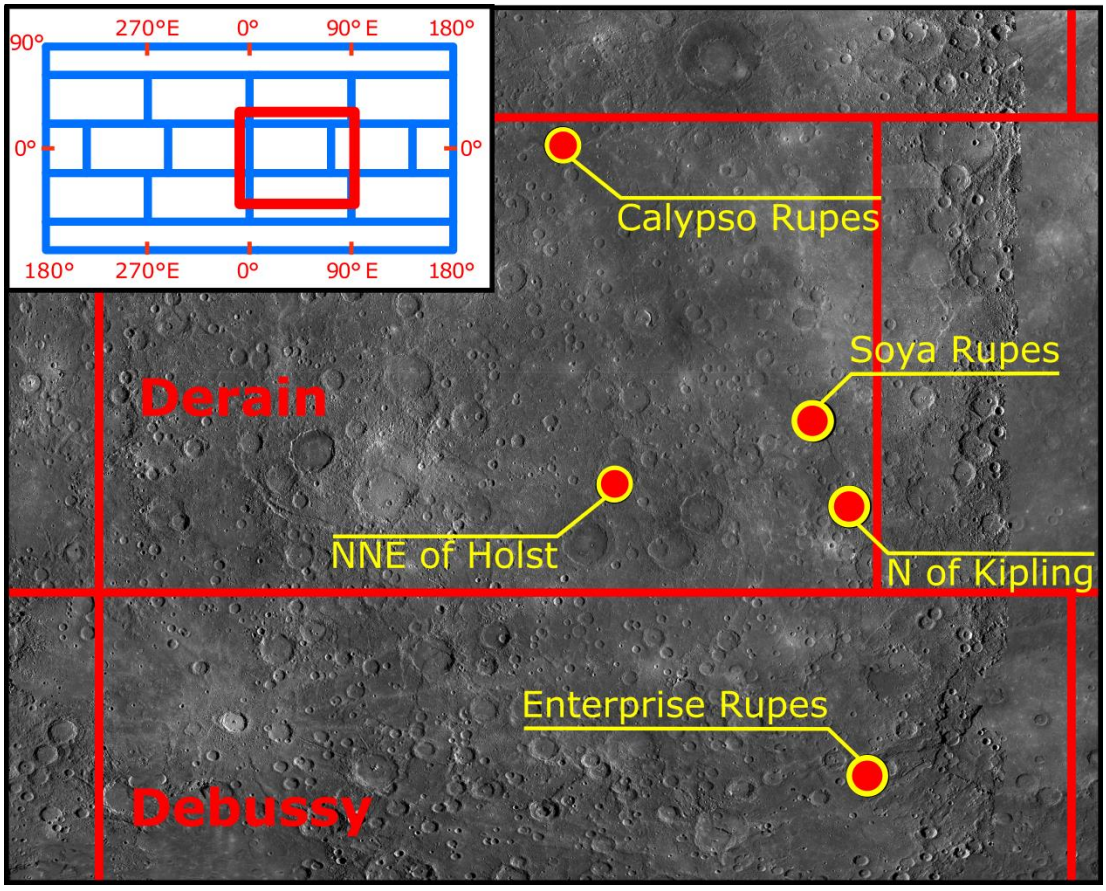

Figure 5.1: Location of smooth patches discussed in this chapter.

5.2 Observations

5.2.1 Crater-hosted small smooth patches

Unnamed crater (70°N, 14°S), ~50 km north of Kipling

This unnamed C1 basin in the Derain quadrangle, ~170 km in diameter, shows clear evidence of resurfacing (Figure 5.2). Towards the south-east, the basin floor is heavily cratered, and its rim is degraded. Towards the northwest, the basin floor is smooth and has only a few subdued craters. The peak ring stands proud of the resurfaced portion in the west of the crater. The key evidence that the smooth floor material is later resurfacing, rather than impact melt, is: (i) the presence of subdued or 'ghost' craters which appear to have been almost totally buried by the smooth material and thus demonstrating a significant time gap that allowed smaller impact craters to accumulate on the basin floor before the smooth floor material was emplaced; and (ii) the marked textural difference between the northwest and south-east of the crater floor.

The resurfaced area is generally redder than the surrounding plains and the south-east basin floor. It is located around 130 km south of the smooth plains at Soya Rupes (Section 5.2.2.2), and ~100 km east of an explosive volcanic vent.

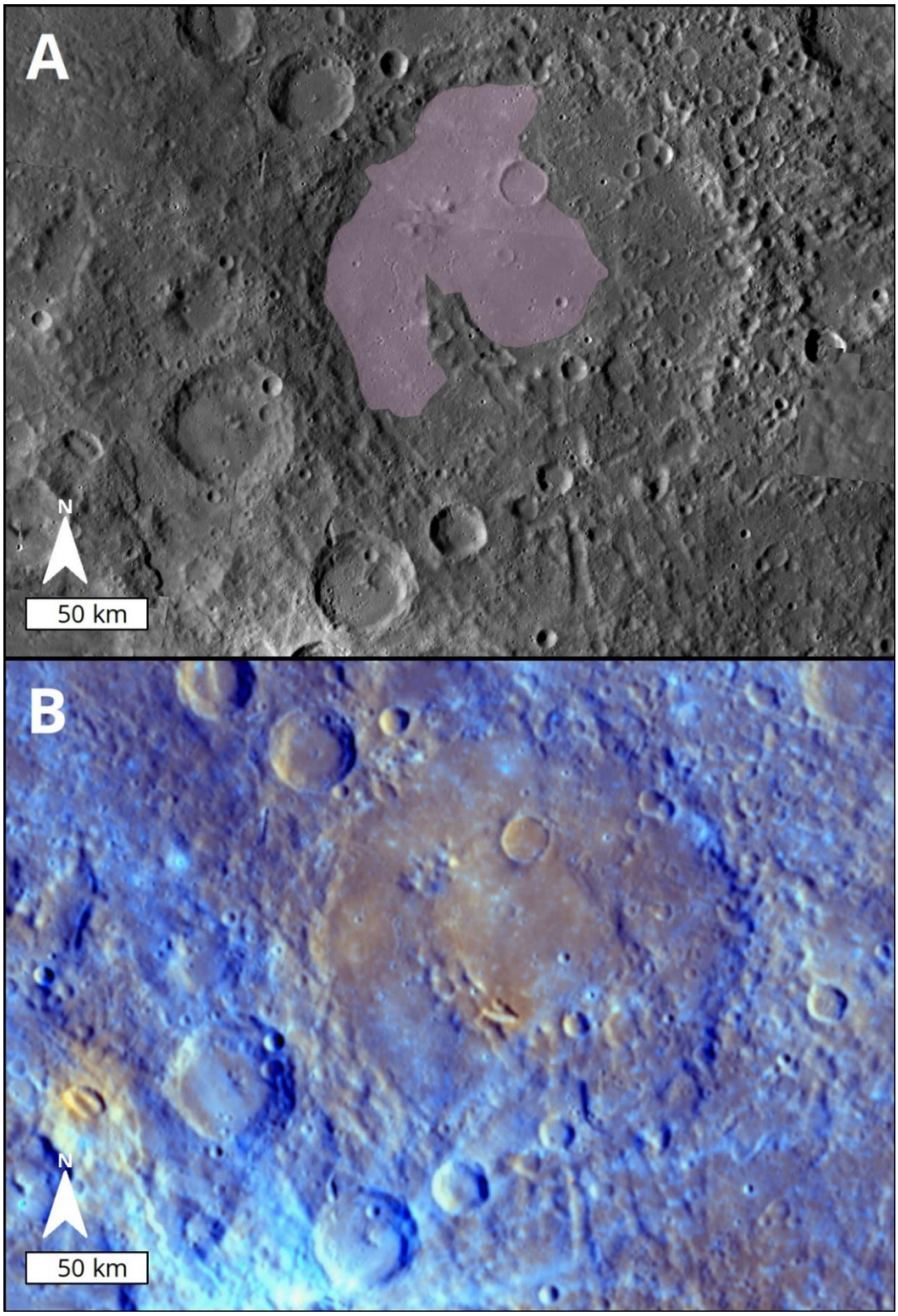

Figure 5.2: Partially resurfaced basin floor (70°N, 14°S). A: the crater in standard BDR mosaic; note the partially subdued peak ring and subdued craters in the smooth plains to the north and west of the basin. B: The crater in enhanced colour, the resurfaced area is generally redder than the rest of the basin floor and surrounding plains. Also, visible west of the basin is the red facula, putatively formed by an eruption from a pyroclastic vent.

5.2.1.1 Unnamed crater (48°E, 11°S), 280 km north-northeast of Holst

Smooth plains occur within a ~140 km diameter degraded (C1) basin in the south of the Derain quadrangle (Figure 5.3). The smooth plains must postdate the impact as they can be clearly seen to embay the ejecta of the large impact in the centre of the basin, and near the western edge of the basin a few small, subdued craters can be seen.

The basin is located within approximately 1.5 diameters of the rim of the Holst basin, and approximately two diameters of the Nabokov basin. Holst is slightly less degraded than the unnamed basin and has a similar number of superimposing craters. The albedo of the smooth unit inside this crater is not notably different from the surrounding plains. A ~40 km crater superimposing the basin but embayed by the smooth plains has excavated low reflectance material (LRM). There is a small scarp visible in the smooth plains, but this crater is not located close to any major lobate scarp systems. There is no nearby site of explosive volcanism.

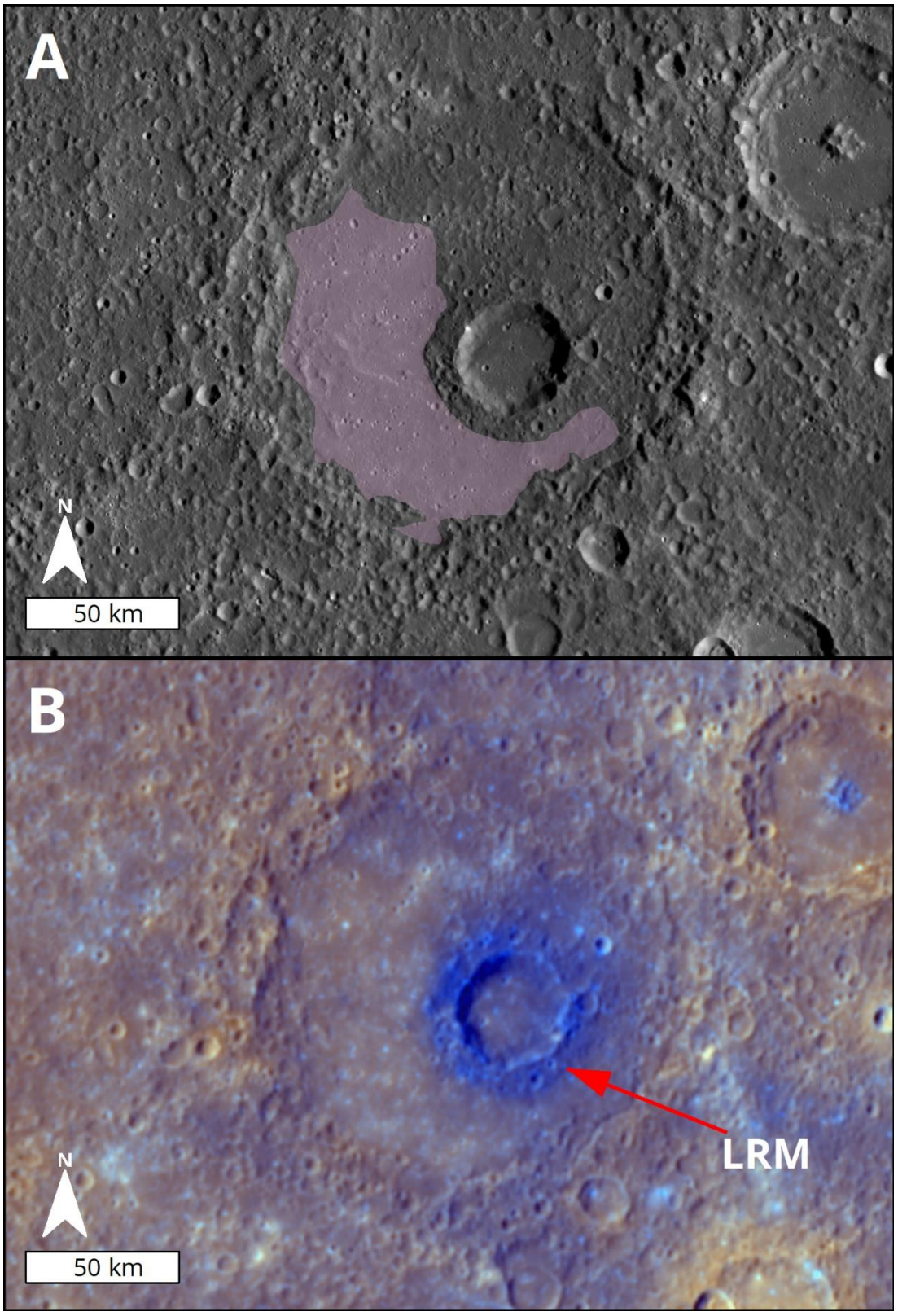

Figure 5.3: A: BDR mosaic of the basin at 48°E, 11°S. B: Enhanced colour image of the same area. Note the LRM material excavated in the ejecta of the crater in the centre is asymmetric, with the LRM extending further on the more textured northeast side.

5.2.2 Smooth ponded patches associated with lobate scarps

5.2.2.1 Calypso Rupes

One of the most striking examples of smooth plains abutting lobate scarps is the smooth plains close to Calypso Rupes, within the Derain (H-10) quadrangle. The area is shown in Figure 5.4. It is near to, and has a contact with, the continuous ejecta of the large, young (C3), Rachmaninoff impact basin. It is not immediately clear what the order of superposition is between the Rachmaninoff ejecta and the smooth units, as the boundary between them is at the limit of the continuous ejecta. The relationship of the ejecta overlying a similarly smooth resurfaced crater nearby (48°E, 23°N), and secondary chains that are approximately radial to Rachmaninoff and superimposing the smooth patches, suggest that the smooth plains here predate the Rachmaninoff impact. Some fresh scarps associated with Calypso Rupes appear to crosscut the continuous ejecta of Rachmaninoff, and so the system likely had, at least some, activity after the Rachmaninoff impact.

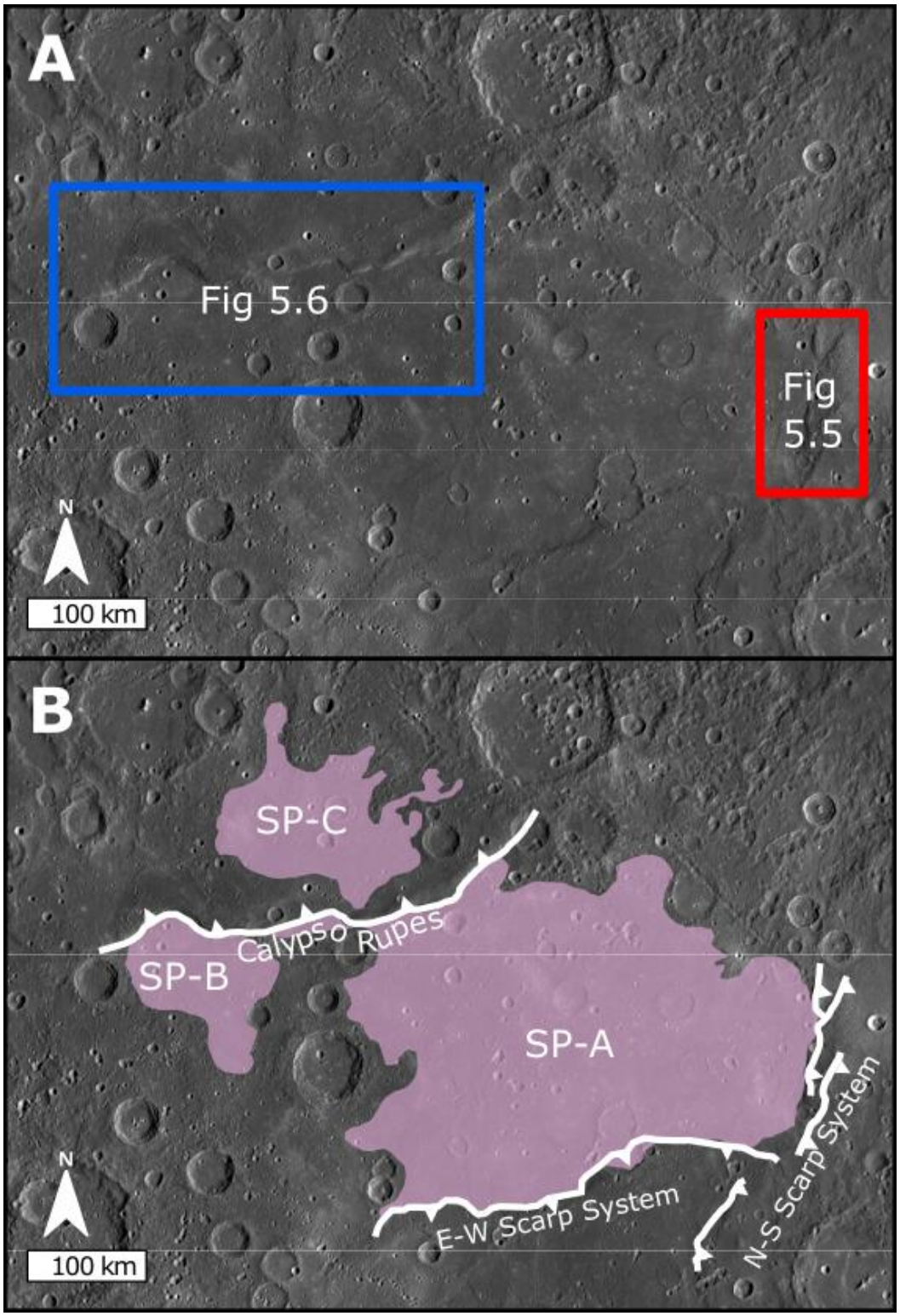

Figure 5.4: Smooth plains around Rupes. A: MDIS NAC/WAC mosaic basemap. B: Sketch map of smooth plains units and lobate scarps. Scarps are shown in white with teeth towards the hanging wall. Areas of smooth plains are highlighted. The Rachmaninoff basin is out of view to the northeast, but continuous ejecta from the impact is present in the northeast of the figure. Locations of Figure 5.5 and Figure 5.6 are highlighted.

The area shows patches of smooth plains abutting Calypso Rupes. The plains unit appears to be thicker closer to the scarp, because close to the scarp the plains show no subdued craters (i.e., the plains unit is so thick that any pre-existing craters are invisible), whereas subdued craters become more abundant at greater distances from the scarp where the plains unit is probably thinner. This is particularly evident in the south.

The main area of smooth plains (labelled SP-A in Figure 5.4), is broadly bounded by Calypso Rupes to the north, Rachmaninoff ejecta to the north-east, an unnamed north-south fault system to the east (Figure 5.5), an unnamed east-west scarp system to the south, and a high relief ridge to the west. The contact to the north, at Calypso Rupes, is the clearest of all SP-A's contacts. The contact is also sharply defined at the boundaries with the north-south scarp system to the east (Figure 5.5). The contact at the unnamed east-west system to the south is not as clearly defined; however, the SP-A is less distinct and appears to be thinner here. The boundary with Rachmaninoff ejecta is gradational, which makes it difficult to determine if it is topographically controlled.

The area labelled SP-B in Figure 5.4 is also located on the footwall side of Calypso Rupes. The boundary with Calypso Rupes is the sharpest and best defined (Figure 5.6) of all the examples. It is separated from the larger SP-A by a gradational boundary onto a topographic rise (Figure 5.6). The rise has a similar texture to the unit on the hanging-wall north of Calypso Rupes. I mapped both the rise and the unit above the hanging-wall as intermediate plains in my quadrangle map (Chapter 4). The topographic rise includes an area of non-resurfaced large craters (<20 km diameter) and their ejecta. The rise and un-resurfaced craters here appear to have acted as a topographic control on both SP-A and SP-B. To the west, SP-B is bounded by the ejecta of a relatively undegraded (C2) crater. The ejecta of the crater to the west of SP-B and those south of the rise appears to be embayed by the smooth plains

units (Figure 5.7A and C). To the south, SP-B has a gradational boundary into intermediate plains. This is similar to the general thinning to shallower cover to the south shown by the SP-A. SP-B has a much smaller area than SP-A and is more topographically confined.

On the north (hanging wall) side of Calypso Rupes, there is another smooth patch (SP-C in Figure 5.4). SP-C has gradational boundaries into the surrounding plains units. The boundary is most distinct close to Calypso Rupes, with a noticeable textural change at the small scarp north of the main Calypso Rupes scarp (yellow arrows in Figure 5.6). This back-thrust crosscuts a crater that has its ejecta embayed by SP-C. While the gradational boundary makes the exact extent of SP-C subjective, a good approximation can be drawn with a contour (at -140 m below the USGS global DEM average), so the smooth plains appear to be topographically restricted.

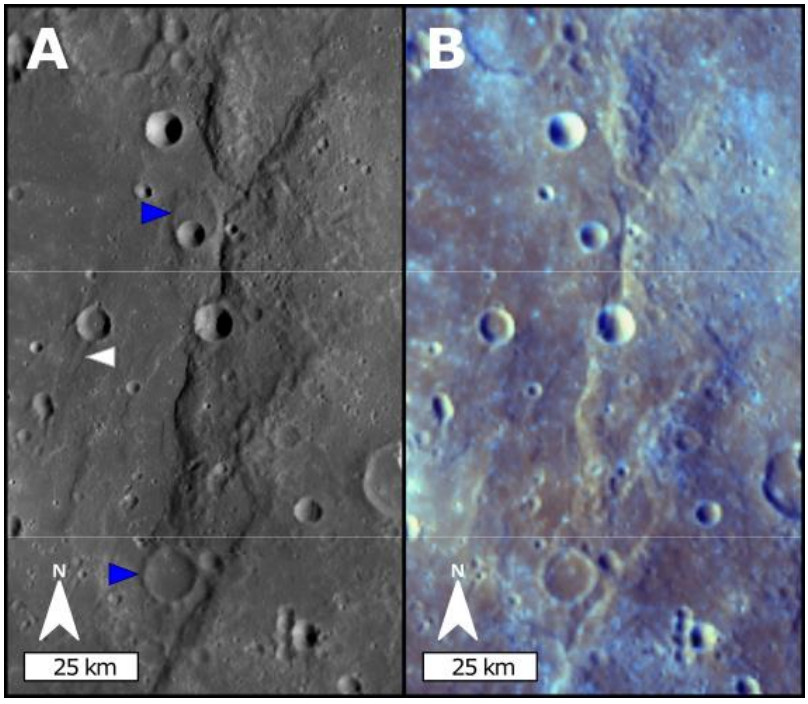

Figure 5.5: The boundary between SP-A (to the west) and the unnamed north-south trending set of lobate scarps in BDR basemap (A) and enhanced colour (B). Subdued craters are visible in SP-A (blue arrows). A possible extensional feature is highlighted with the white arrow. The units have a slight colour difference, but the contact is considerably clearer in the geomorphology.

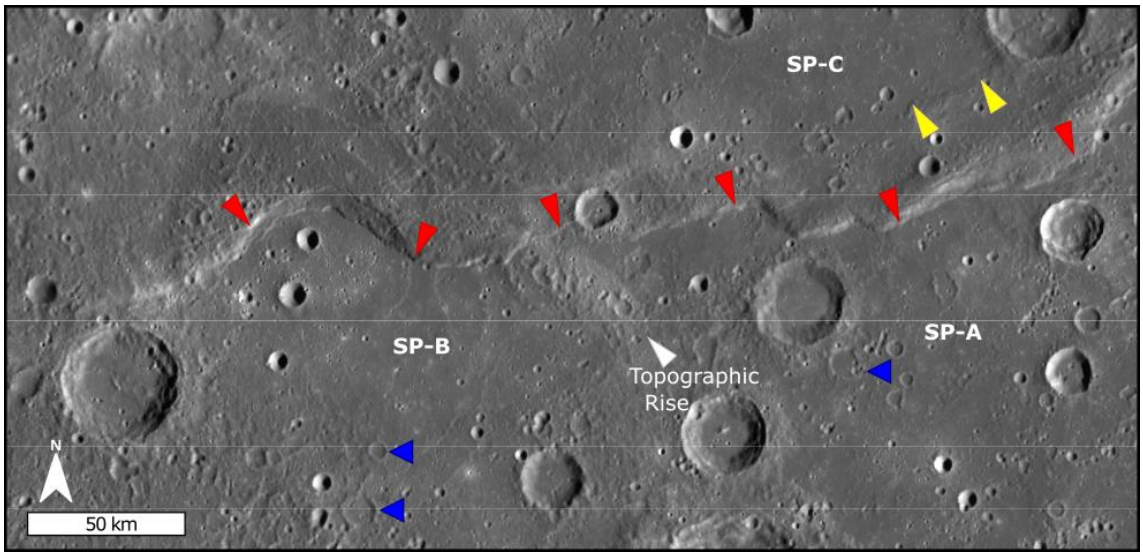

Figure 5.6: The Scarp and Smooth plains around Calypso Rupes. In the west of the frame is the boundary between SP-B and Calypso Rupes, note the sharp contact with the scarp (red arrows) and the more textured surface on the hanging wall side of the scarp. The boundary of SP-B to the south with the intercrater plains is more gradational with more subdued craters (e.g., blue arrows). The topographic rise that separates SP-A and SP-B has gradational boundaries with both. The texture at the top of the rise is similar to the texture on the hanging wall side of the Calypso Rupes scarp (red arrows). To the east, the Calypso Rupes scarp has a sharp boundary with SP-A to the south, and a gradational boundary into SP-C to the north. There is a small fault marking a boundary of SP-C marked with yellow arrows.

5.2.2.2 Soya Rupes

I identified another example of smooth plains abutting a lobate scarp at Soya Rupes in the south-east of the Derain quadrangle (Figure 5.7). These patches are much smaller than those at Calypso Rupes and do not extend as far from the scarp. The craters are more shallowly covered than at Calypso Rupes, and so this example appears to be a thinner 'veneer' than the smooth plains at Calypso Rupes. Smooth plains patches are not found along the entire length of the Soya Rupes fault system; there are none north of the fresh, unnamed crater. As can be seen in Figure 5.7B, the smooth patches are generally redder than their surroundings in enhanced colour.

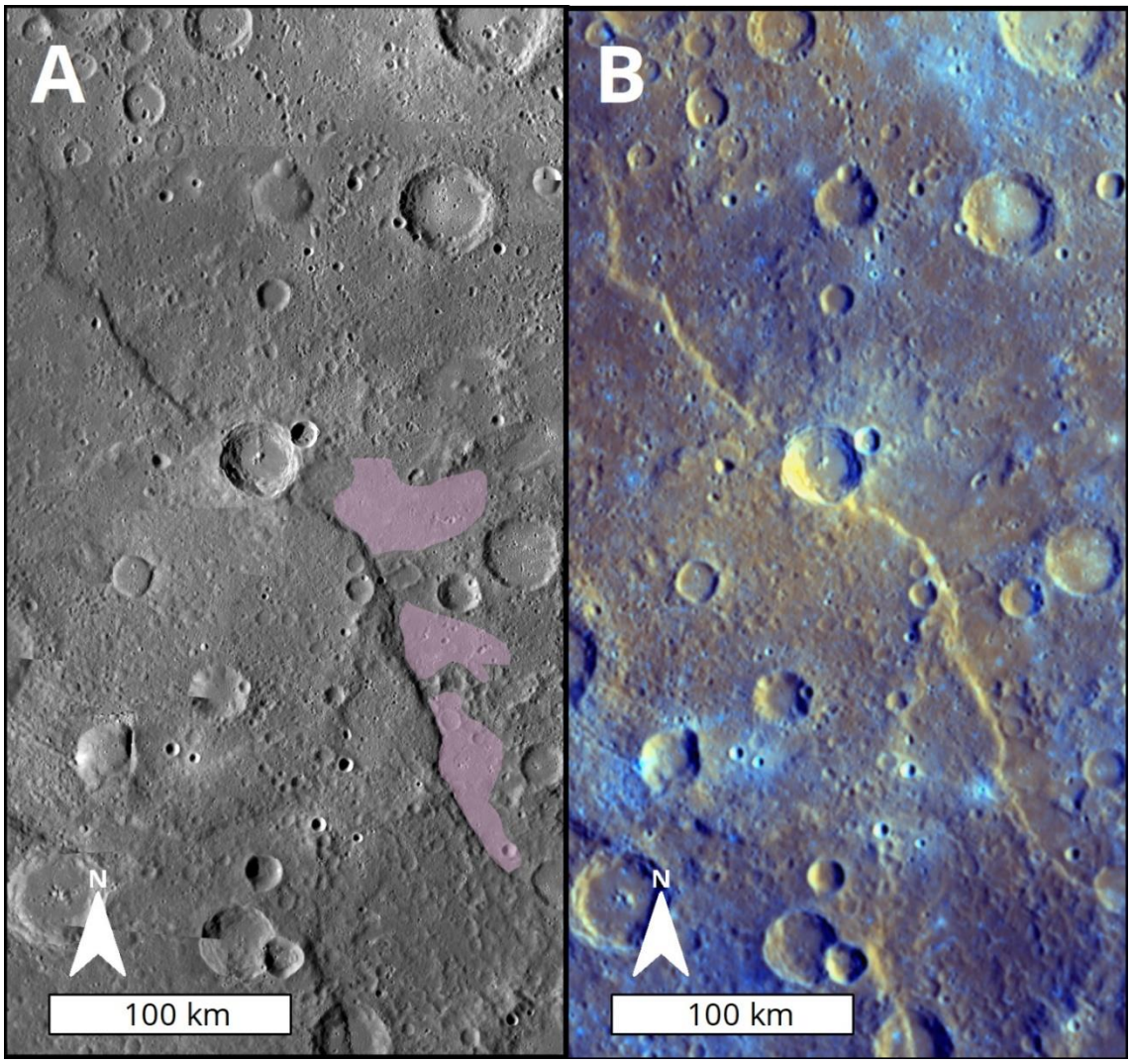

Figure 5.7: Soya Rupes. A: The areas of smooth plains abutting Soya Rupes are highlighted, on a BDR basemap. B: the same area shown in an enhanced colour mosaic. Note the redder colour in the location of the smooth patches.

5.2.2.3 Near Enterprise Rupes (70.5°E, 38°S; 75.5°E, 38.5°; and 73°E, 42°S)

This area comprises three distinct but spatially proximal areas of smooth plains, all of which are located in the north-east of the Debussy quadrangle. The area with these three smooth patches is located between approximately 50 and 400 km from the rim of the Rembrandt basin.

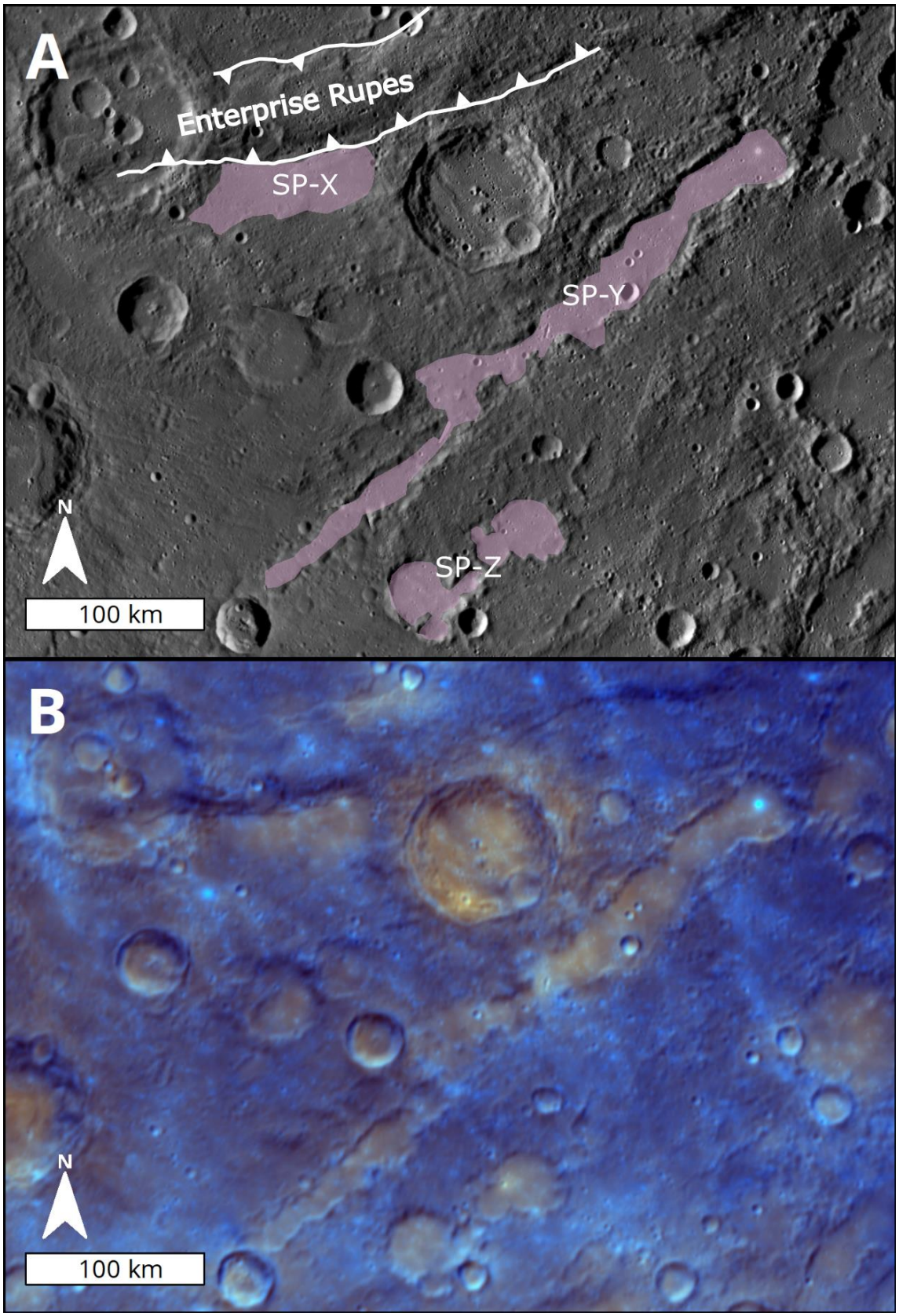

Figure 5.8: Small smooth plains units near Enterprise Rupes. A: sketch-map with BDR Mosaic basemap. The patch abutting Enterprise Rupes is labelled SP-X, the catena SP-Y, and the resurfaced craters SP-Z. B shows the area in enhanced colour.

The first example, at 70.5°E, 38°S, is a small area of smooth plains (SP-X in Figure 5.8) abutting against the scarp of Enterprise Rupes. The contact is sharp to the north against the scarp of Enterprise Rupes but is gradational to the south. The gradational boundary is over a much shorter distance than the boundaries at Calypso Rupes (Section 5.2.2.1) and seems to grade out at a similar topographic level. There are no visibly subdued craters in this area, and so resurfacing is inferred primarily from the texture being considerably smoother than the surrounding plains, and the fact that the ejecta of the unnamed craters to the east (class C3) and west (class C2) are subdued and embayed by the smooth plains. In enhanced colour, the smooth plains are redder than the surrounding units.

The second area of smooth plains at 75.5°E, 38.5°S (SP-Y in Figure 5.8), resurfaces the floor of a catena. The catena is approximately radial to the nearby Rembrandt impact basin. There is a sharp contact between the smooth plains and surrounding terrain at the catena walls. The resurfacing has covered any septa within the resurfaced portion of the catena. This suggests the resurfacing may have been close to overflowing the catena, or the septa were heavily degraded when resurfaced. To the southwest end, the plains are limited to the catena but have also resurfaced outside the catena in a local topographic depression; there is a very sharp boundary with the surrounding terrain here, as well as a few small (<5 km diameter) prominences above the smooth unit that are not obviously flooded. The resurfaced area is redder in enhanced colour than the surrounding terrain.

The third and smallest example of smooth patches visible in Figure 5.8 is at 73°E, 42°S (SP-Z) and comprises a small set of resurfaced craters south of the resurfaced catena. The smooth plains here exist entirely within these craters. In the easternmost crater, the resurfacing has filled the crater to just below the exterior rim and has completely covered the crater rim between it and its neighbour. The plains within the craters are redder in enhanced colour than

the plains exterior to the crater groups. There are several similar smooth patches in the wider area, often within a crater, or crater groups.

5.3 Discussion

The examples I have described show a range of areal extent (Table 5.1), degree of resurfacing, and geographic location. To better understand what these features represent, I examine this variety of size and form and compare with possible alternative formation models. Given that some of these features are close to large impact basins, I first consider an impact origin, similar to the lunar Cayley plains. I next consider whether they could have formed by effusive volcanism. Finally, I also consider, and reject, the suggestion that the lobate scarps postdate the smooth plains, with the faults exploiting a mechanical weakness between the smooth plains and a smooth volcanic unit.

Location		Area (km^2)
Calypso Rupes	SP-A	78417
	SP-B	9144
	SP-C	14413
Soya Rupes	North	1657
	Middle	876
	South	1199
Enterprise Rupes	SP-X	2305
	SP-Y	5482
	SP-Z	14413
	North of Kipling	8799
	North of Holst	5098

Table 5.1: Area of mapped smooth units

5.3.1 Impact origin

Samples from the 1972 Apollo 16 landing on the morphologically smooth Cayley plains (Figure 5.9), showed an impact-derived breccia (Oberbeck et al., 1973), despite being considered volcanic before landing (Kain et al., 1971). To avoid making the same mistakes impact-derived smooth plains have been considered as an origin for morphologically smooth units on Mercury from the earliest Mariner 10 (1974-1975) images (Strom et al., 1975; Trask and Strom, 1976; Wilhelms, 1976).

Cayley type plains were described as the largest single identifiable rock unit on the near side of the Moon other than mare basalts (Apollo Team, 1973), and therefore their origin was an important scientific question. When the Apollo 16 landing site was selected during geological mission planning, the Cayley plains were described as a 'volcanic constructional unit' (Kain et al., 1971). The pre-mission working hypothesis was for formation as a series of lava flows interbedded with ancient regolith, thus representing an area with multiple volcanic events with some temporal separation. Apollo 16 transects sampled the Cayley plains extensively at nine locations. These were from the rims of different sized craters to obtain information on the vertical variability of the unit as well as lateral variability. This showed the Cayley formation to be a breccia unit, with variable sizes of clasts. This is not consistent with an effusive volcanic origin. There was some evidence of loose stratification and a thickness of at least 200 m (Apollo Field Geology Investigation Team, 1973).

Given the texture and structures observed in samples, as well as clasts showing evidence of shock deformation, the Cayley formation is now widely considered to be a fluidised, impact-ejecta derived unit (Apollo Field Geology Investigation Team, 1973; Head et al., 2007; Oberbeck et al., 1973). Fluidised ejecta is a term used to describe different processes on different bodies. It is used to describe crater ejecta that has been influenced by surface or

subsurface volatiles (e.g., rampart craters on Mars and ejecta on the Earth); or for flows formed by large blocks ejected from the main impact excavating many times their mass of smaller fragments and producing a flow that ponds in low lying areas. There is no evidence for flows fluidised by interaction with volatiles in either the lunar Cayley plains or the SSPs on Mercury, and this meaning of the term is not discussed further in this chapter. The loose stratification and variety of breccia types have been used to suggest the presence of multiple impact events, although recent work suggests ejecta from a single event can be emplaced as multiple layers (Osinski et al., 2011). Geochemical dating using Ag/Ag suggest Cayley plains date to between 3.8 and 3.4 Ga, and so is consistent with emplacement from the Imbrium impact at 3.85 Ga (Joy et al., 2011; Norman et al., 2010), and mapped as such in the unified lunar geological map (Fortezzo et al., 2020) The patches of smooth plains around the Apollo 16 landing site are found in areas of low local topography (Figure 5.9.).

The Cayley plains studies demonstrated that areally extensive, morphologically smooth units on planetary surfaces can be derived from fluidised ejecta, and do not have to be molten rock from impact processes, or emplaced volcanically. Consequently, there was uncertainty from the Mariner 10 images of Mercury if the smooth plains of Mercury were volcanic or of impact origin. MESSENGER images and data provided morphological, spectral, and geochemical evidence (Byrne et al., 2013; Denevi et al., 2013; Vander Kaaden et al., 2017) that clearly showed many locations had a volcanic origin, but the existence of other smooth plains of impact origin could not be ruled out.

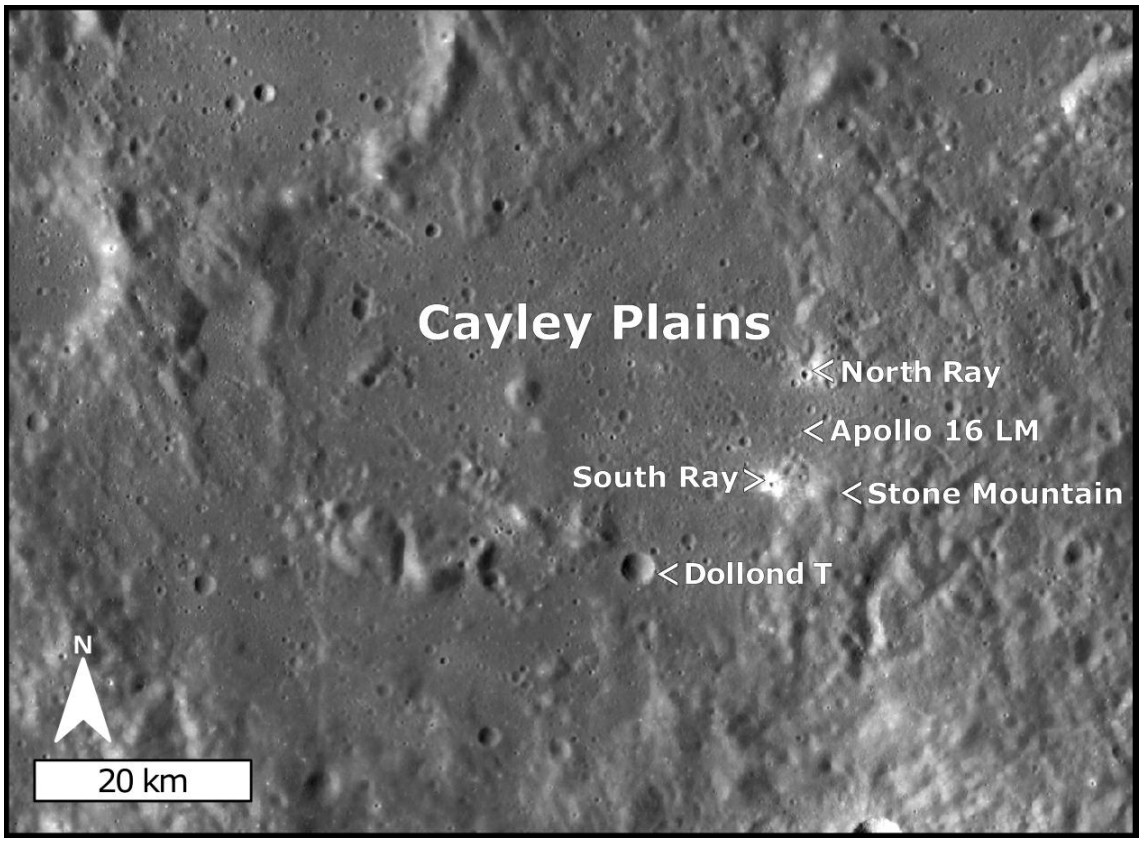

Figure 5.9: Cayley plains around the Apollo 16 landing site in the Descartes Highlands from the LROC-WAC mosaic. The Cayley plains fill the low-lying areas.

As well as Cayley type plains, impacts can also generate impact melt. Many areas of impact melt have been identified on Mercury (e.g. Prockter et al., 2010). Mercury has a much faster average impact speeds (~42.5 km/s) than the Moon (19.4 km/s) (Le Feuvre and Wieczorek, 2011; Strom et al., 2011, 2008) so impact melt scaling laws (Cintala and Grieve, 1998) predict that an impact on Mercury will produce more impact melt than on the Moon. Mathematical modelling suggests over 40% of impact melt from large impacts could be ejected outside the crater rim (Abramov et al., 2012; Cintala and Grieve, 1998; Whitten and Head, 2015).

Impact-derived smooth plains on Mercury were examined by Whitten and Head (2015), who attempted to distinguish between impact and volcanic origins for morphologically smooth units in and around the Rembrandt impact basin. The Rembrandt impact basin is the second-largest well-

preserved basin (~720 km diameter) on Mercury and has clear interior and exterior smooth plains units. This provides a good location to examine impact derived smooth plains on Mercury.

The potential impact-related smooth plains identified by Whitten and Head (2015) were distinguished by having a lower albedo than volcanic plains and by impact crater size-frequency statistics. These data were interpreted to show that the smooth plains had a similar age to that of the Rembrandt impact, in contrast to the younger high reflectance plains. Impact model studies of the Moon, scaled to Mercury's gravity and impact speed, suggest that Cayley type smooth plains formed by the flow of secondary ejecta excavated by primary ejecta chunks would be found in an annulus between 1.3 and 2.6 basin radii from the basin rim (Whitten and Head, 2015). As almost all the mapped impact-derived smooth units were within 1.3 radii, Whitten and Head (2015) suggest the identified impact-derived smooth plains are more likely to be derived from impact melt.

Recent work by Daniels and Neish (2018) suggests that the emplacement of impact melt on Mercury is controlled more by gravity than topography. On the Moon, impact melt ponds outside the crater rim are predominantly found close to the lowest point in the rim, suggesting flow only through the topographically lower point. In contrast to the Moon, on Mercury impact melt is not preferentially found near the lowest points of crater rims. This suggests that the increased momentum from the impact can eject the melt further, and so the topography of the impact crater has less influence over where exterior impact melt will pond. Daniels and Neish (2018) conclude that gravity is the predominant control on the location of exterior impact melts on Mercury. Their work focused on easily identified impact melt ponds close to Kuiperian impacts and does not give insights into identifying older or more distal impact melt. That said, impact melt on Mercury is likely to be found closer to the impact than any Cayley-type plains.

It is clear from these previous studies that impact-derived smooth plains are almost certainly present on Mercury. The candidate examples of Whitten and Head (2015) are thought to have formed from impact melt, and no previous work has found definitively identified Cayley type plains derived from ejecta. This will be very difficult without samples as, unlike volcanism, there are few recognised diagnostic morphological features. Geochemically they should resemble local plains as they necessarily incorporate local material (Oberbeck, 1975). It is likely though that a distal smooth unit could form on Mercury, given the similarity between cratering processes on the Moon and the innermost planet.

The currently suggested impact-derived smooth units on Mercury were identified using albedo from WAC colour imaging and crater counting. Using crater counting as an identification criterion more widely is difficult. This is because it requires both a candidate impact to be compared to, a well-defined candidate impact age, and for the unit to be sufficient in area to obtain a reliable crater age. Mercury has a large population of secondary craters dominating crater populations up to 15 km in diameter (Strom et al., 2011, 2008), therefore to obtain a reliable crater age an area must be large enough to have numerous craters over 15 km. Albedo can be used globally, but it is important to note that smooth units with a lower albedo have been identified by other workers as having a volcanic origin (Denevi et al., 2013), including the example at Calypso Rupes.

Impact-derived smooth plains should subtly differ morphologically from volcanically emplaced smooth plains. While volcanic plains will emanate from vents or fissures at the surface and cover the existing plains outwards from the source, impact units form by settling on the ground from above, and initially drape areas of both high and low topography, before draining into areas of low topography. Therefore, smearing of areas of high topography near impact-derived plains and gradational boundaries should be expected.

To compare the areas I identified to the work of Whitten and Head (2015), I used the eight colour mosaic to obtain the mean 1000 nm reflectance value for the smooth patches identified. I did this using the ArcGIS's 'Zonal Statistics as a Table' function to calculate the mean value of band 8 in the eight-colour mosaic for polygons covering the geomorphic smooth patch. The results are shown in Table 5.2. The values for each area are between 0.0800 and 0.0881. All these values are lower than the global average of intermediate albedo plains of 0.096 (Denevi et al., 2009), but are similar to the reflectance value for the circum-Caloris plains. Using these values in isolation may suggest that the examples identified are all impact derived. However, qualitatively most of the examples here, other than at Calypso Rupes, are redder in enhanced colour and appear to have higher values of 1000 nm reflectance, than the surrounding terrain. The examples near Enterprise Rupes were categorised by Whitten and Head (2015) as volcanic units. Also, the smooth plains south of Calypso Rupes were explicitly highlighted by Denevi et al. (Denevi et al., 2013) as an example of low reflectance smooth plains that were probably volcanically derived and were suggested as possibly representing a more mafic lithology. Therefore, while reflectance values can be instructive, they do not currently provide a singular method to distinguish between impact and volcanically derived smooth plains reliably.

	Location	Mean 1000nm reflectance	Standard Deviation	Range	Pixel Count
Calypso Rupes	SP-A	0.0819	0.0061	0.0751	163591
	SP-B	0.0800	0.0036	0.0402	19084
	Soya Rupes	0.0848	0.0032	0.0202	2505
Enterprise Rupes	SP-X	0.0832	0.0041	0.0263	4816
	SP-Y	0.0864	0.0052	0.0589	11429
	North of Kipling	0.0881	0.0040	0.0331	18371
	North of Holst	0.0831	0.0035	0.0218	10633
Average values from Whitten and Head (2015)	Low reflectance material	0.071			
	Circum-Caloris Plains	0.085			
	Spectrally Intermediate Plains	0.096			
	High-reflectance (volcanic) red plains	0.116			

Table 5.2: Mean 1000 nm reflectance values for described smooth plains patches and comparison values from Whitten and Head (2015)

5.3.2 Volcanic origin

Volcanically emplaced smooth plains have been observed across the solar system, including on the Moon and Mercury. While Mariner 10 mappers identified many candidate volcanic plains, it was not until MESSENGER flybys that volcanic plains were unambiguously recognised on Mercury (e.g. Head et al., 2009). The large areas of smooth plains are thought to have been emplaced at around 3.7–3.9 Ga (Denevi et al., 2013). A contractional stress regime makes it hard for eruption pathways to remain open, inhibiting prolonged large-scale eruptions. Current thinking suggests large scale effusive volcanism ceased at around 3.5 Ga (Byrne et al., 2016) at the onset of global contraction, but smaller-scale effusive volcanism probably continued (Byrne et al., 2016; Fegan et al., 2017; Wright et al., 2017). There is also evidence for late-stage explosive volcanism (Jozwiak et al., 2018; Thomas et al., 2014b), and while undoubtedly very different from the effusive volcanism potentially forming small smooth plains, does show that eruption of material through Mercury's crust was possible after the onset of global contraction.

Lobate scarps and wrinkle ridges are widely recognised to be surface expressions of contraction faults linked to Mercury's global contraction. Apparent superposition of some smooth patches against lobate scarps means these smooth patches are younger than the lobate scarps. Therefore, the origin of the smooth patches at lobate scarps must have been after global contraction was established.

If the plains were emplaced volcanically, we must have a conceptional model for how magma could reach the surface under a contractional regime. To reach the surface magma must first find or create a conduit. The most mechanically efficient way of moving magma is by using existing structural weaknesses such as faults, or deep fracture networks under craters (Jozwiak

et al., 2018). Other workers have suggested that faults may provide a weakness to allow magmatic ascent for Mercury's explosive volcanism (Klimczak et al., 2018).

Given that a global compressive regime will make it harder for conduits to form, faults may provide areas of least compressive stress. Fault scarps on Mercury are rarely long, continuous features. As can be seen clearly at Calypso Rupes in Figure 5.4 and Figure 5.6, fault scarps can be curved, overlapping, or kinked. This means not every fracture plane can be orthogonal to the maximum compressive stress, which would aid the opening of conduits. As well as not outcropping as simple planes at the surface, 'fault planes' are not single flat planes and will be a damaged zone of interconnected fractures and geometries, which will be oriented with slight differences in the local stress field. At Calypso Rupes, there are small extensional grabens on the ridge crest, showing that a locally extensional stress field was present at some point in the scarp's history.

As well as providing deep fracture systems, and areas of reduced general compressive stress; after fault movement, there is a brief period where local stresses will relax (Sibson, 1992). This would aid the opening of conduits, especially in areas of reduced compressive stress. Once a conduit has formed, it can remain open for as long as the fluid pressure in the conduit exceeds the surrounding compressive stresses (Jozwiak et al., 2018; Wilson and Head, 1981). Fluid pressure in the mantle would be dependent on the rate and volume of magma produced. Magma production on Mercury has likely decreased over time as evidenced by the cessation of large scale volcanism at 3.5 Ga (Byrne et al., 2016), although the thermal history of Mercury, and thus, magma production on Mercury is not fully understood (Michel et al., 2013; Ogawa, 2016). It is unlikely though that such a conduit would remain open for an extended period, which would help explain why

the smooth plains observed typically flood an area only thinly and are not areally expansive.

Faults are therefore good candidate sites for any effusive volcanism under a globally compressive regime. They both provide ascent pathways and locations and time intervals of lower stress to allow magma to reach the surface. There is evidence of later magmatic resurfacing of Mansurian basins (Byrne et al., 2016; Wright et al., 2017); therefore, magma ascent is possible beneath large basins. The exploitation of deep fracture networks will aid this; however, it is not clear how a localised difference in the stress field would be produced. That late-stage magma ascent can happen in basins strengthens the argument for magma ascent being possible at lobate scarps where there is clear evidence of both fracture networks and localised extension.

A confident identification of volcanically emplaced plains by remote sensing would require either morphological features such as flow features (e.g., pressure ridges), or geochemical evidence of magmatic phases (e.g. spatially resolved element difference between smooth patches and surrounding plains). Unfortunately, the highest resolution data from MESSENGER are not of sufficient resolution to be able to see this morphology or find geochemical indicators in the areas I have identified. Improved resolution imaging and better spatial resolution of the instruments on BepiColombo's planetary orbiter (Benkhoff et al., n.d.; Cremonese et al., 2020; Fraser et al., 2010; Hiesinger et al., 2020) may be able to determine if any of these features are present or absent.

5.3.2.1 Small smooth plains followed by faulting

Another possibility is that the superposition relationships have been disrupted by faults exploiting a mechanical weakness between smooth and other plains units. If so, the smooth plains would predate the faulting.

An approximation for the depth of the covering unit at small smooth patches can be calculated using approximations for the rim height of ghost, or subdued craters.

Location	Crater	Diameter (km)	Original rim height (km)
Calypso Rupes (A)	1	25.9	$0.73^{+0.93}_{-0.41}$
	2	26.9	$0.75^{+0.96}_{-0.42}$
	3	22.8	$0.69^{+0.82}_{-0.37}$
	4	13.5	$0.53^{+0.49}_{-0.26}$
	5	9.5	$0.42^{+0.44}_{-0.21}$
Crater North of Kipling	1	18.5	$0.62^{+0.68}_{-0.32}$
	2	6.8	$0.31^{+0.26}_{-0.14}$
Soya Rupes	1	8.1	$0.36^{+0.34}_{-0.18}$
	2	8.9	$0.40^{+0.39}_{-0.20}$

Table 5.3: Calculated original rim heights of partially subdued craters in identified smooth patches. Errors estimated by using the slope fit errors reported by Pike (1988).

The height of the original, pristine, crater rims can be estimated using power scaling laws from Barnouin et al. (2012) and Pike (1988). To be visible at the present day the subdued crater cannot have been completely covered by the smooth unit. Therefore, an upper limit of the depth of the overlying smooth unit can be obtained.

As there are subdued craters in the smooth patches at Calypso Rupes (A), Soya Rupes, and the crater north of Kipling, I was able to calculate an estimate of fill depth in these patches (Table 5.3). I drew two lines of diameter across each flooded crater and calculated the rim heights from the mean of these two measurements. For craters below 13 km I assumed the original crater had a simple morphology and used: $h = 0.052 \times D^{0.930}$ where h is original rim height, and D is crater diameter (Pike, 1988). As most craters on Mercury between 13- 30 km diameter are immature-complex, rim heights for these

craters were estimated assuming all these craters were originally immature-complex: $h = 0.150 \times D^{0.487}$ (Pike, 1988). This follows the methodologies of Whitten and Head (2015) and Semenzato et al (2020).

It is important to note that these estimates calculated are an upper bound of fill at the location of the crater. That portions of these crater's rims are visible means they were not completely covered. There are also large potential errors on these calculated original rim heights. The calculated values are, however, all below 1 km suggesting the smooth cover is thin compared to their lateral extent. Given the smaller craters identified are closer to the edge of the smooth patch there may also be lateral variation, as also evidenced by the gradational boundaries (e.g. Figure 5.6) Given that the depth of the brittle-ductile transition in the crust on Mercury is probably ~30 km (Watters and Nimmo, 2010), the depth of the mechanical weakness provided by the base of the smooth plains (estimated to be less than 1 km, Table 5.3) will be small in comparison to the vertical scale of the faults on Mercury. The mechanical weakness would also be at a much shallower angle than the thrusts associated with lobate scarps previously measured (Galluzzi et al., 2015).

It certainly cannot be the case that an interface with pre-existing lavas around Calypso Rupes provided a mechanical weakness despite likely having the deepest fill. At Calypso Rupes, the lobate scarp crest does not appear flooded, and smooth plains are found on both the hanging wall and footwall sides; therefore, the lobate scarp must predate the plains units. Pre-existing smooth plains with faulting later does not explain small smooth plains units away from lobate scarps either. Therefore, I consider it implausible that small smooth patches pre-date the associated faults.

5.4 What do the identified examples represent?

The small smooth plains patches I have identified vary in size, geological setting, and physical properties such as thickness and albedo. However, they each cover a low region in the local topography. Absolute ages of the smooth patches are not determinable because of their small size (issues with crater counting similar units is discussed in section 3.4.3.2); however, they usually appear to be one of the most recent features in the local stratigraphy based on morphology, impact crater numbers, and superposition relationships. Some examples appear to superpose adjacent lobate scarps, and so formed late in the history of global contraction.

Given the diversity of settings (in craters, in catenae, on footwall and hanging wall of lobate scarps, in other ponded settings) the explanation for small scale smooth plains may not lie in a single mechanism, still less a single episode, of smooth plains emplacement. It might not be possible to definitively distinguish between the different suggested modes of emplacement described in using current quantitative datasets.

5.4.1 Soya Rupes

The patches of smooth plains at Soya Rupes have a relatively small areal extent and so probably represent a thinner veneer of resurfacing than the more voluminous smooth patches at Calypso or Enterprise Rupes. This example is not close to large, recent basins; the nearest large Mansurian or Kuiperian craters are Firdousi, Bagryana and Nabokov, the rims of which are more than three basin diameters away. Of these craters, only Nabokov can be seen to produce impact melt exterior to the basin rim. The Soya Rupes patches are over 1000 km from the rim of the Rembrandt impact basin. The detailed geomorphological mapping underway around Rembrandt (e.g. Pegg

et al., 2019b and Semenzato et al. 2018), would be an effective way to show if an annulus of small smooth plains extends as far out as my examples, and help determine if these patches are plausibly impact-related plains, either Cayley type or distal impact melt.

The 1000 nm reflectance values of the smooth patches are dissimilar to those of high reflectance volcanic plains, potentially suggesting an impact origin, but the colour is redder than the surrounding plains. The patches at Soya Rupes are close to the crater-hosted smooth patch north-northwest of Kipling. It is not possible to determine the exact emplacement mechanism with any confidence. However, for this example, I favour a volcanic origin, given the distance from likely impacts, and a relatively favourable setting for volcanism. The small size and thin veneer could make the origin of these smooth patches challenging to determine via geochemical signatures definitively. The ground resolution of MESSENGER instruments is insufficient to give compositional information for such small areas. Also, as the resurfacing unit appears to be thin, any cover from impact gardening caused by superimposing impacts will potentially excavate material from underlying units. The signal may also be diminished by any ejecta cover from nearby impacts in other units.

5.4.2 Crater North of Kipling

Like all the identified examples, the reflectance of the smooth patch in the crater north-northwest of Kipling is low compared to the volcanic red plains. It is, however, not notably close to recent large basins. The closest large, recent impacts are Nabokov, approximately three basin diameters away, and the Rembrandt basin, approximately 1.5 basin diameters away. The smooth plains in the crater north-northwest of Kipling are significantly younger than the crater that hosts them, based on the marked difference in texture between the smooth plains and the un-resurfaced crater floor. This textural

contrast and sharp contact do not show any indication of resurfacing outside the mapped smooth unit. This would suggest that if impact processes formed this patch, the processes were extremely localised, and did not drape the surrounding area at all. The lack of a clear candidate source impact, in addition, lends no credence to the idea of impact-related plains here. The morphology and distribution more closely resemble what would be expected for materials of an effusive volcanic origin.

Close to this smooth patch there is evidence of resurfacing in the nearby Steichen Crater (~200 km) and the Soya Rupes Smooth Patches (~100 km); as well as nearby explosive volcanic vents in Kipling and Capote craters (~ 200 and 300 km) and 100 km west (65°E, 15°S) (section 4.2.7.2 and Figure 4.15). The Steichen resurfacing is evidenced by the near-complete filling of the basin floor and a ghosted crater. Resurfacing and explosive volcanism is common in this area of Mercury. With deep fractures, and located close to a major fault system, it is in a good location for late-stage effusive volcanism. A magmatic plumbing system might also have aided the explosive volcanism nearby.

The clear evidence for other volcanic processes nearby and the lack of any clear source impact for impact derived resurfacing leads me to favour a volcanic origin for the smooth plains in the unnamed crater north-northwest of Kipling.

5.4.3 Crater north-northeast of Holst

The smooth plains patch in the south and west of the unnamed crater north-northeast of Holst has embayed the ejecta of a 40 km, C2 crater on the floor of the main crater. The more textured crater floor, without smooth plains, along with an adjoining crater, have infilled craters and the texture appears subdued compared with the sounding intercrater plains. This draping of the surrounding low-lying terrain should be consistent with how plains emplaced

by fluidised ejecta would be expected to drape and drain into topographic lows. Draining into a topographic low could explain the sharp, topographically-defined contact with the ejecta of the 40 km crater, and the gradational boundaries in the subdued basin floor. If impact derived, a source is not clear. The small smooth patch is less than two basin radii from the rims of both the Holst and Nabokov basins. Of these, Nabokov has some external smooth plains, likely impact melt, but Holst has none. Both are plausible source locations.

A volcanological origin could be possible, and there is no definitive morphological evidence for impact origin. It could be that impact resurfacing subdued the crater interior, part of which was then resurfaced volcanically. The smooth plains are redder in enhanced colour than the surrounding crater floor, and a small fault outcropping in the smooth portion shows faulting in the crater at some point.

This example is one of the best candidates for Cayley type fluidised impact ejecta resurfacing. However, it is not possible with current observations to discount a volcanic origin.

5.4.4 Near Enterprise Rupes

All the examples near Enterprise Rupes, the smooth plains abutting the scarp (SP-X), in the subdued catena (SP-Y), and in the subdued craters (SP-Z) are very close to the Rembrandt basin. This location, and the quantitatively low 1000 nm reflectance, is consistent with (but does not prove) an impact origin. Despite this, Whitten and Head (2015) classified both patches as volcanic. This was probably because they are proximal to other smooth plains identified as volcanic, and they do appear to be more reflective in the 1000 nm band compared to surrounding areas, even if the absolute reflectance value is not high. It seems unlikely that impact processes could have flooded a catena without also draping nearby topography, whereas plains emplaced

effusively are more likely to fill a depression from the centre upwards. Also, the interior of Rembrandt is known to have been volcanically resurfaced, and the sites of smooth plains that I have identified could be locations where magma associated with Rembrandt fill exploited other deep fracture systems as side conduits. I, therefore, agree with Whitten and Head (2015) that these features are more likely of volcanic origin.

5.4.5 Calypso Rupes

The smooth plains here are very close to the large (approx. 320 km diameter), Mansurian-age Rachmaninoff impact basin. Rachmaninoff has small areas of external smooth patches that have been interpreted by multiple workers as impact melt (Prockter et al., 2010; Wright et al., 2019). These areas of impact melt are principally found outside the western and southern rim of the basin. The smooth plains at Calypso Rupes are separated from this area of impact melt by continuous ejecta. The smooth plains at Calypso Rupes at their furthest distance from Rachmaninoff are approximately 2.5 basin diameters from the rim, similar to the impact-related smooth plains near Rembrandt (Whitten and Head, 2015). The smooth plains around Calypso Rupes are also spectrally blue. Together, these observations provide a plausible argument for an impact origin.

However, unlike at Rembrandt, there are no areas (other than at Calypso Rupes and the impact melt proximal to the rim) of smooth plains near Rachmaninoff that could plausibly be interpreted as impact-related. Such an incredibly inhomogeneous distribution of such a quantity of impact melt would require an unusual impact geometry, but there is no evidence of this in the distribution of Rachmaninoff's continuous ejecta. Instead, this suggests volcanic emplacement as the preferred mode of origin for smooth plains patches near Calypso Rupes. This was also suggested by Denevi et al. (2013),

who identified larger areas of smooth terrain as an exemplar of low reflectance volcanic plains.

I suggest that Calypso Rupes provides an ideal location for late-stage effusive volcanism, with the fault showing evidence of uneven strain such as localised extension, overlapping fault scarps, and definite bend or slip-strike section on the fault. The fracture networks created by the faulting would therefore have provided multiple ascent routes for magma. Morphologically, the strong relation to topography also suggests a volcanic origin. Again, it is not possible to definitively determine how the smooth plains at Calypso Rupes were emplaced. Based on my observations, I think a volcanic origin is the most plausible mode of emplacement.

5.5 Conclusion

I have identified several examples of small-area smooth plains. The examples described here are a fraction of those that could be identified globally through local-scale geological mapping or a specific global survey.

The areas identified are too small to accurately date using measurement of impact crater size-frequency distributions. Given that some abut lobate scarps, it is likely that at least these formed after the onset of global contraction, and so after large scale, effusive magmatism had ceased. The crater-hosted examples must have formed a significant time after crater formation, given the observations of ghost craters.

The most likely methods of emplacement of these small patches are through impact processes, as either impact melt or fluidised ejecta; or volcanically. With the current data available, it is not possible to definitely ascribe an emplacement mechanism. On the current balance of evidence, I have identified volcanic emplacement as the more likely process. Given the observations I have made, and observation by previous workers, I favour a

magmatic origin for most of the areas described in this chapter. Furthermore, most areas described are not notably close to a large impact, and so it is not obvious where impact-derived plains could have been derived from.

The exact origin of small, young smooth plains is an interesting question that may be better answered through targeted observations by BepiColombo (Rothery et al., 2020). Higher resolution imagery from the SIMBIO-SYS instrument (Cremonese et al., 2020) may help identify characteristic geomorphological markers, such as flow fronts or even source vents if patches formed through effusive volcanism. If impact related, patches may show draping over or draining off exposed areas of higher topography. Finer scale composition and geochemical data could show evidence for volcanism, for example Mg and Fe abundances different from surrounding units.

Improved geochemical information, both in resolution and greater range of datasets, from BepiColombo should help distinguish if the plains show any of the mineral phases associated with other late-stage effusive volcanism, or if they geochemically more resemble average Mercury plains and ejecta deposits.

Distinguishing between impact and late-stage effusive volcanism is essential to better understanding the full history of effusive volcanism on Mercury. It will also help to further understand Mercury's thermal history, magma mobility under a globally compressive regime, as well as getting a more complete history of geological processes on the planet. It may be useful as a comparison for understanding lunar volcanism after the cessation of mare volcanism.

CHAPTER 6
SLOPE PROCESSES ON MERCURY

6.1 Introduction

Mass movement, or mass wasting, is a term to describe a variety of slope processes causing material, and hence mass, to move down a slope. I use it, in the generally accepted sense, to refer to a range of features without invoking any specific genesis or process. Mass movement has been recognised on many solar system bodies, including airless bodies such as the Moon (e.g. Bart, 2007; Kokelaar et al., 2017; Xiao et al., 2013b), Ceres (Hughson et al., 2018), Vesta (Krohn et al., 2014; Scully et al., 2015), and Phoebe (Giese et al., 2006). These features have been interpreted to have a variety of triggering mechanisms and display various morphologies. These include rockfalls where large particles (e.g. boulders) fall down steep slopes moving individually (Bickel et al., 2020); granular avalanches, where a flow of small grains moves downslope in a self-supporting flow (Kokelaar et al., 2017); and gullies, which include distinctive erosion alcoves and channels, terminating at a depositional fan (Bart, 2007; Conway et al., 2019). On airless bodies, mass movements often represent geologically recent or active changes in landscapes, and understanding these processes is essential in understanding recent geological activity on these bodies.

While there is published work describing the variety of mass wasting deposits and processes on other bodies, to date there have been few studies of these processes on Mercury. The most comprehensive study of mass wasting features on Mercury is that of Brunetti et al. (2015). This study compared mass movements inside simple, bowl-shaped, craters on Mercury and the Moon. Brunetti et al. (2015) mapped the extent of large mass movements on crater walls, and found, on average, a deposit area of 46 km^2 for Mercury.

The mass movements, described as rockslides, appear to have formed through rotational slip. That study concluded that rockslides on Mercury typically had a smaller volume of material moved than rockslides on the Moon.

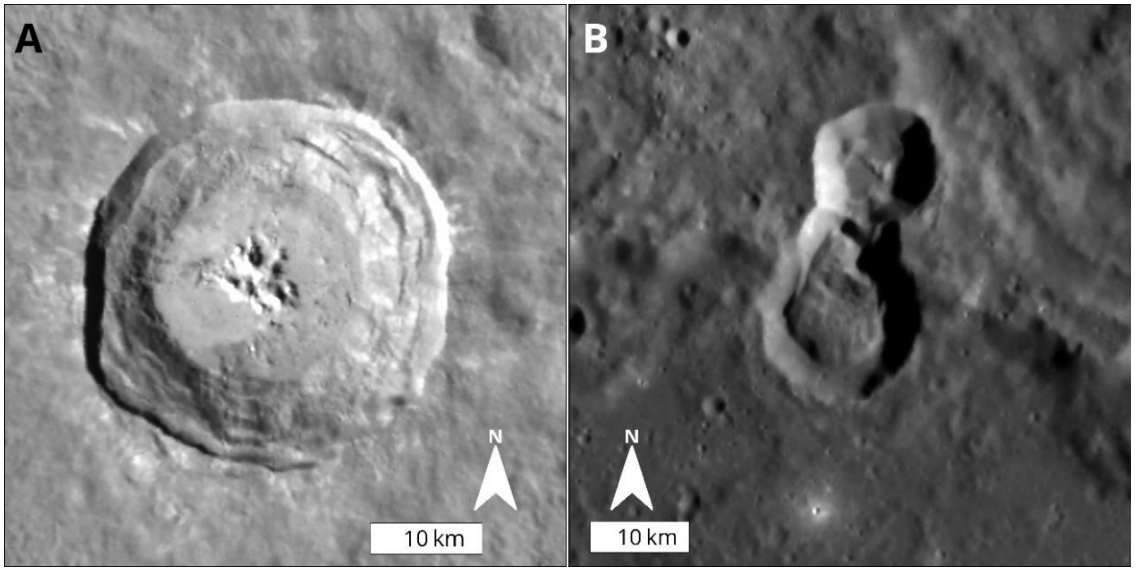

Figure 6.1: Crater terracing (A) in Fonteyn crater, and crater rim collapse (B) in an unnamed small crater on the edge of the Nabokov basin.

Crater wall collapse (Figure 6.1) appears to be one of the most apparent mass movement processes on Mercury. While not particularly common, similar features can be found in simple craters over the Derain quadrangle.

The other published study on Mercurian mass movements is by Xiao and Komatsu (2014) who reported seven impact craters with ejecta flows. Ejecta flows occur where ejecta is emplaced as a flow, draping the topography and producing an ejecta blanket with an easily defined boundary, rather than one with diffuse margins, as is formed if ejecta is emplaced ballistically. Xiao and Komatsu (2014) suggested that these ejecta flows were emplaced as dry granular flows.

Here, I show evidence of smaller scale, laterally restricted mass movements. Evidence of this type of mass movement on Mercury has previously been

limited to a single documented example, found in the pyroclastic vent northeast of Rachmaninoff crater (within Nathair Facula) (Figure 6.2 and Figure 6.3). I show further examples of this type of mass movement (Figure 6.2). These examples exhibit more than one morphology and may represent more than one process or triggering mechanism.

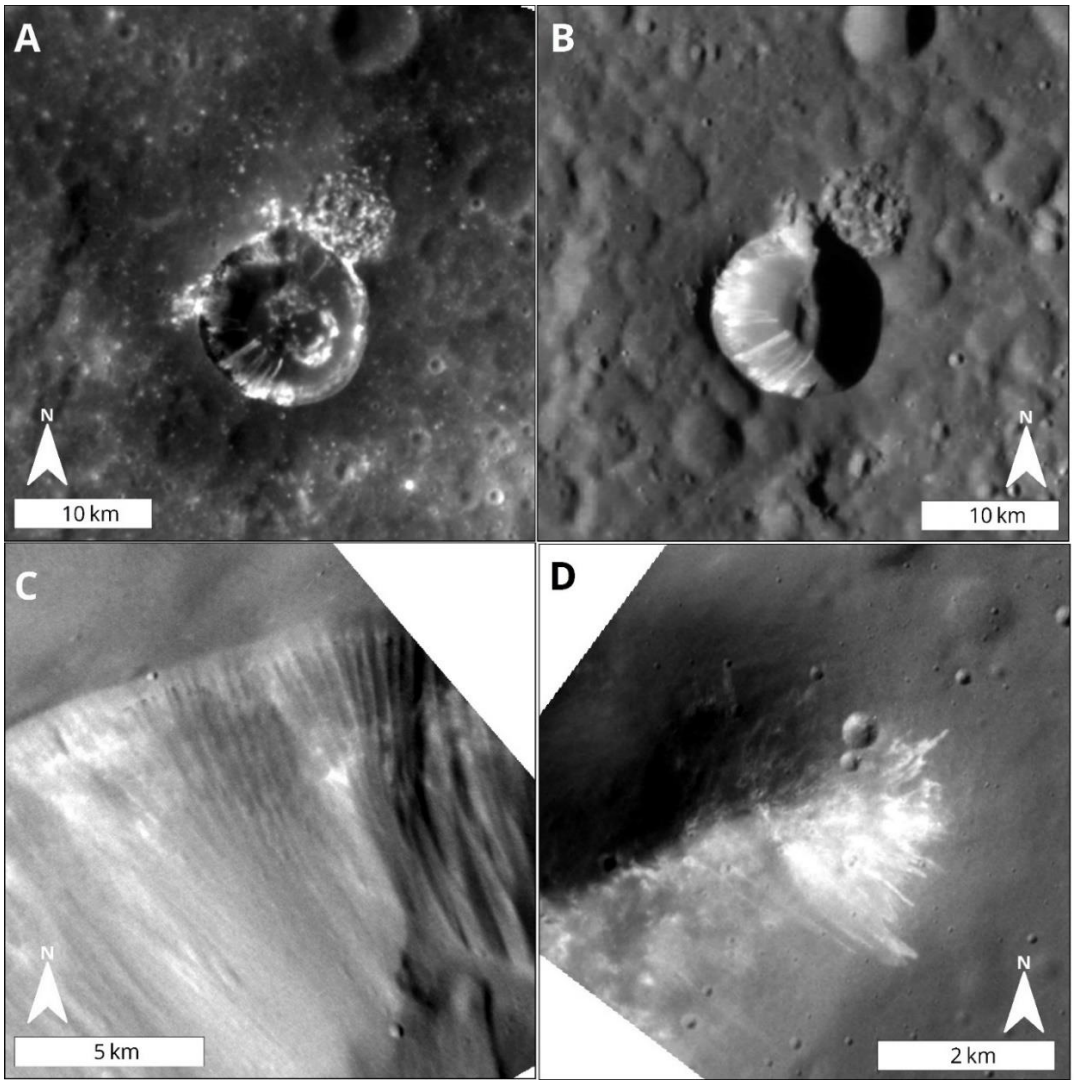

Figure 6.2: Mass-movement feature on Mercury. A: Martins crater in low incidence angle images, showing high albedo lineae, and a possible bright layer below the crater rim. Dark Material outside the crater matches well with distribution of LRM. The same area is shown in B, with the high albedo lineae still clearly visible. C: Gully-like features in the vent in Nathair Facula. These are particularly evident in the right of the image. To the west of the image, these features appear more apparent as albedo features. D: high albedo features on a peak ring element inside Rustaveli.

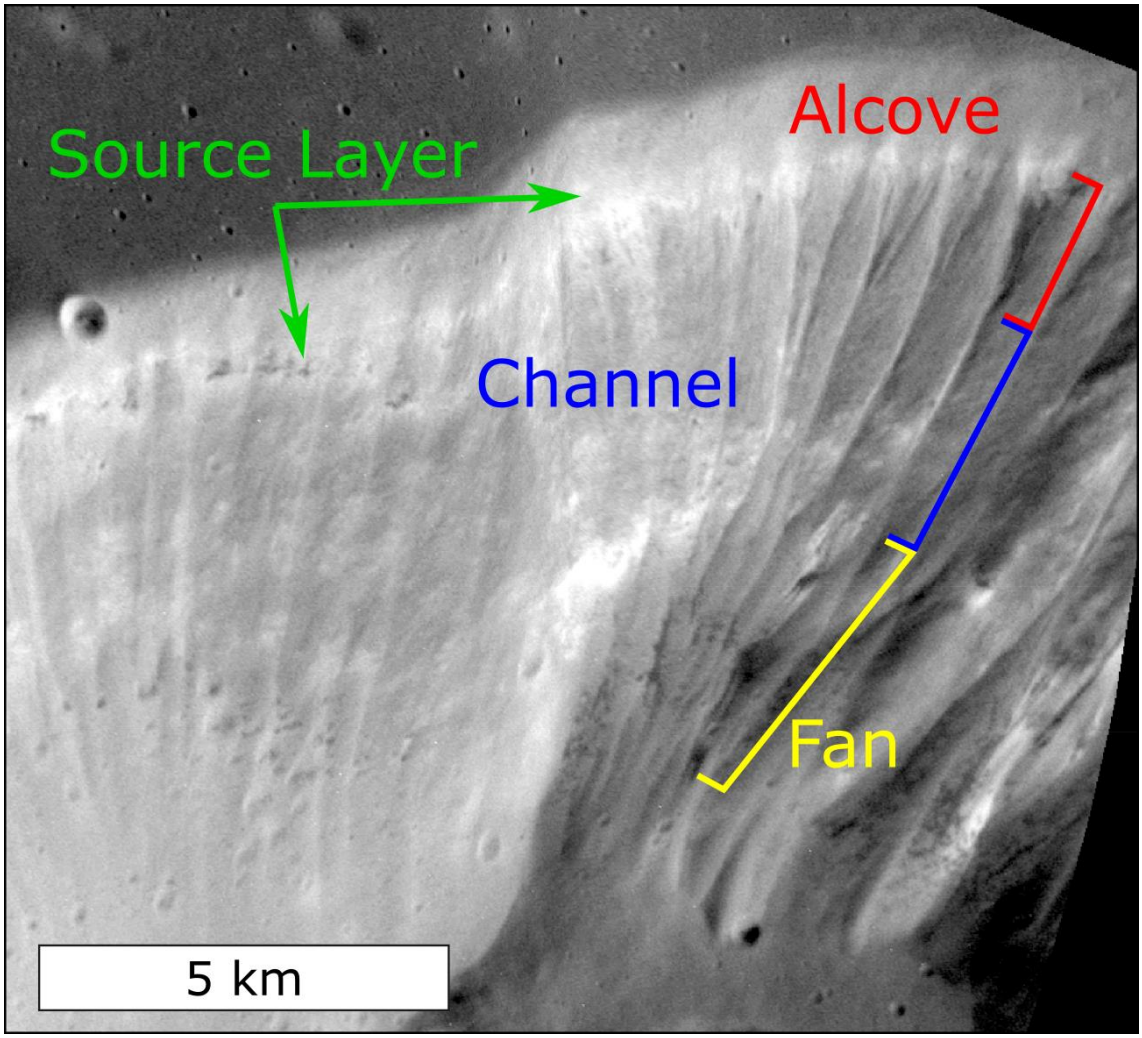

Figure 6.3: Gully like features in vent associated with Nathair Facula. There are multiple gully like features with erosive alcoves, incised channels, and depositional fans. MDIS-NAC image: EN1059620367M.

6.2 Identification of Mass Movements

I made my initial identification of a new example of laterally restricted mass movements while performing my mapping of the Derain quadrangle in Martins crater (as shown in Figure 6.2A and 1B). The observed features are narrow, high albedo features and appear to be orientated broadly slope parallel. Hereafter I describe these features as lineae (singular linea). This is an IAU descriptor term for 'dark or bright elongate markings'. This describes the newly identified features well and does not imply any form of genesis. In

high-resolution, low incidence angle images (Figure 6.2B) the features can be seen to originate just below the crater rim. This region in which the lineae originate looks to be at the same height as a high albedo layer on either side of the lineae on the southwestern crater wall. This high albedo layer appears to occur at around the same height wherever it is seen on the crater wall, but it cannot be seen to be continuous around the crater wall and may vary in stratigraphic thickness. Martins crater is in an area of low reflectance material (LRM), surface material that is significantly less reflective than typical plains units on Mercury. LRM has been associated with both Mercury's primary crust (Peplowski et al., 2016) and hollows (Blewett et al., 2011), thought to be a volatile driven landform. In enhanced colour images (Denevi et al., 2016) parts of the crater wall show a pale blue colour that is characteristic of hollows.

The features in Martins crater appear to have similarities to features in the wall of the vent in Nathair Facula, noted by the MESSENGER team on the project website but never expanded further (Figure 12.7, p.328 in Blewett et al., (2018) illustrates it and notes hollows and layering, but does not remark on the gullies). The features in the vent wall can be seen in topography visible in the high-resolution images, showing gully-like (alcove, channel, fan) morphologies. Like the lineae previously noted, these features also originate in a bright layer just below the vent rim.

The examples in Martins crater and in the Nathair Facula vent are located in young features with visually steep slopes. As the features identified are small scale, they are easily missed and are not clearly resolved in the images used in the global mosaics. To determine if these features occur more widely across Mercury, I completed a regional survey (described in Section 6.3).

6.2.1 Other slope degradation processes on Mercury

To determine if any of the slope features I identified on Mercury are unusual, it is important to understand how recently created slopes (e.g., associated with recently formed impact craters) typically degrade on Mercury. When examining young slopes in high-resolution images, many steep slopes show a 'cross-hatch' pattern, particularly on the walls of simple craters (Figure 6.4A and B). This pattern has many narrow ledges that do not extend far around the crater. This is particularly evident in Figure 6.4B. There is little marked albedo difference in the examples of normal slope degradation I have found. Features similar to this can be seen in high-resolution images from the Lunar Reconnaissance Orbiter (LRO) narrow-angle camera (Kreslavsky et al., 2018a). On the Moon, this has been interpreted as evidence of regolith creep (Xiao et al., 2013b), and is shown in Figure 6.4C and D. Creep is the slow, gradual movement of regolith down slopes. Various processes can disturb the ground enough to cause the regolith to move. These processes include thermal expansion and contraction, and micrometeorite bombardment (Grier and Rivkin, 2019). Given the similarity between these features on the Moon and Mercury, I interpret common 'crosshatch' features to represent gradual and widely distributed creep on Mercury.

Impact processes can also create features that can be mistaken for mass movements. I found a small number of examples of ejecta scour causing lineations on young slopes. These can be identified by the lineations being parallel with one another, rather than slope parallel, and ejecta draping other topography in the image.

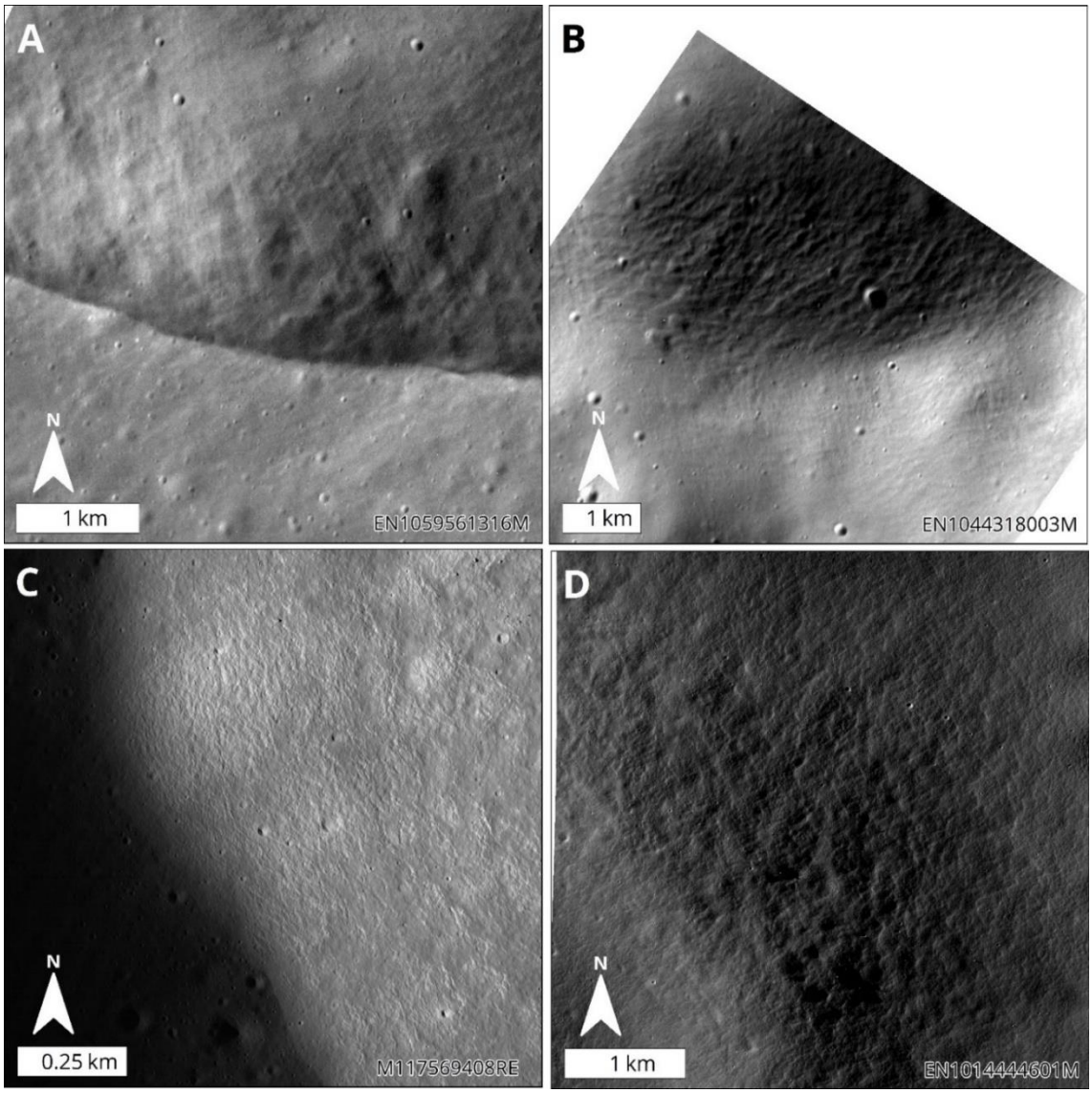

Figure 6.4: Examples of slope creep seen on Mercury (A&B) (MDIS-NAC) and the Moon (C&D) (LROC-NAC). Slope creep seen in A and B is the most common slope process visible in high-resolution images. This bears a striking resemblance to examples of slope creep identified on the Moon by Xiao et al. (2013b) (C and D).

6.3 Systematic Survey

6.3.1 Motivation

To determine if the lineae I identified were comparable to those on other airless bodies I completed a systematic survey of all narrow-angle camera (NAC) images with a resolution of 20 mpp or better in the Hokusai (H-05) quadrangle (Figure 6.5). To conduct a survey of all high-resolution images

acquired by MESSENGER would have been impractical due to the huge number of images, so I chose to do a single quadrangle to give a large dataset over a wide geographic area for which reviewing all images was feasible. I chose the Hokusai quadrangle due to the excellent coverage of high-quality NAC images, as well as topography data from a quadrangle digital elevation model (DEM) derived from stereo WAC images, with a resolution of ~222 mpp, (Stark et al., 2017), and good coverage from the Mercury Laser Altimeter (MLA) instrument with good data quality and better point spacing than equatorial or southern hemisphere quadrangles. The quadrangle DEM was used to calculate slopes with a much shorter wavelength than the global DEM. While MLA tracks have not ultimately been able to provide any useful profiles in this study, they were used by DLR in the production of the quadrangle level DEM to verify and reconcile the stereo DEM to global topography. This quadrangle has areas of all major units identified on Mercury (Wright et al., 2019), but contains a larger than average proportion of smooth plains. This is not likely to have biased the survey because relatively undegraded craters, which are most likely to show visible evidence of mass movement, should occur in similar densities on both smooth and intercrater plains.

6.3.2 Method

I performed a reconnaissance imaging survey with geological context from the Mercury Dual Imaging System (MDIS) 166 mpp monochrome mosaic (Hawkins et al., 2007). The NAC images used in the survey were corrected using standard radiometric and photometric procedures using the U.S. Geological Survey's Integrated Software for Imagers and Spectrometers (ISIS) version 3, as described in Chapter 3 (Section 3.2.2.1). I projected the images used in the survey into a Lambert conformable conic projection, with a central meridian at 45° and standard parallels at 30° and 58°. I then imported

the images into a raster catalogue in ESRI ArcMap 10.5. I examined each image individually with a linear minimum-maximum stretch determined by each image's statistics. If an image showed any downslope mass movement beyond normal slope degradation patterns, I marked this in the attribute table. All possible identifications were assigned a confidence value from 1 to 5, with 5 being certain, and 1 being most ambiguous. A feature with a classification of 5 shows clear individual lineations, and a feature classified as 1 would represent some kind of slope anomaly, but could be ejecta scour and/or due to an image artefact, and so could not be confidently identified as a definite mass movement. Individual lineae were then mapped as individual polylines to give frequency, orientation, and length information. The polylines were drawn from the top of a topographic feature or albedo feature to the furthest extent downslope of the topographic or albedo feature. In the case of albedo features the line was drawn for each lobe. Different feature classes were used to distinguish between albedo and topographic features.

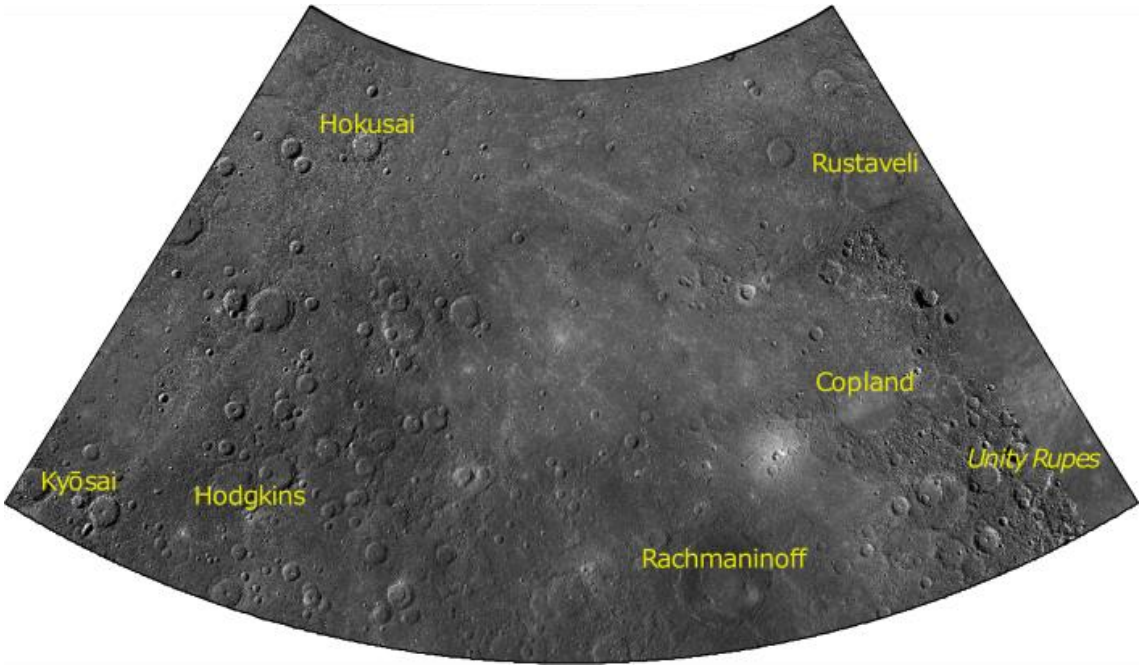

Figure 6.5: Overview of Hokusai (H-05) quadrangle with major features named. Basemap: MDIS BDR 166 mpp.

I surveyed all 9099 images that intersected the quadrangle. I then used slope maps produced from the quadrangle DEM to resurvey images containing a slope angle of over 30°. I chose an angle of 30° as it is approximately the angle of repose for unconsolidated dry sand on Earth (Carrier, 1991). While the lower gravity on Mercury may have a small effect on this (Kleinhans et al., 2011), the principle control will be grain size and shape (Zhou et al., 2002). Given the uncertainties in both the angle of repose and slope angle, using a value 30° seems reasonable. To correct these maps for latitude distortions, I followed the method of Conway et al. (2015). I first calculated the fractional slope in a conformable (Mercator) projection. This was then projected into a simple cylindrical projection, and then corrected using:

$$s_c = 180 \,/\, \pi \; atan\left({s_m}/{cos(L)}\right)$$

where s_c is the corrected slope value, s_m is the fractional slope, and L is the latitude ((Conway et al., 2015). This corrected slope map was then projected into the latitude appropriate lambert conformable conic projection.

6.3.3 Results

6.3.3.1 Survey of all images in H05 Quadrangle

Of the 9099 NAC images in the survey, 298 contained no useable data (entirely dark or only noise visible) or had over 50% of the image in shadow (as images with over 50% shadows showed little resolvable detail). Of the remaining 8801 images the vast majority showed no evidence of any mass movement beyond Mercury-typical slope degradation via creep, as described in section 6.2.1. However, I also identified 67 images containing some evidence of lineae. These images contain 123 examples of potential, laterally restricted, mass movements. These are principally lineae identifiable as albedo features (n=84), but there is a still large minority (n=39) seen mainly as topographic features. All topographic features, and most albedo lineae,

are found on visually steep, fresh slopes. I found examples on slopes in both impact craters and inside putative volcanic vents (Kerber et al., 2009; Thomas et al., 2014c). Results are summarised in Table 6.1, and positive results are shown in full in Appendix B-1.

Summary of Results	
Total Images	9099
Unusable	298
Images with possible slope feature	67

Table 6.1: Summary of results from survey of H05 quadrangle

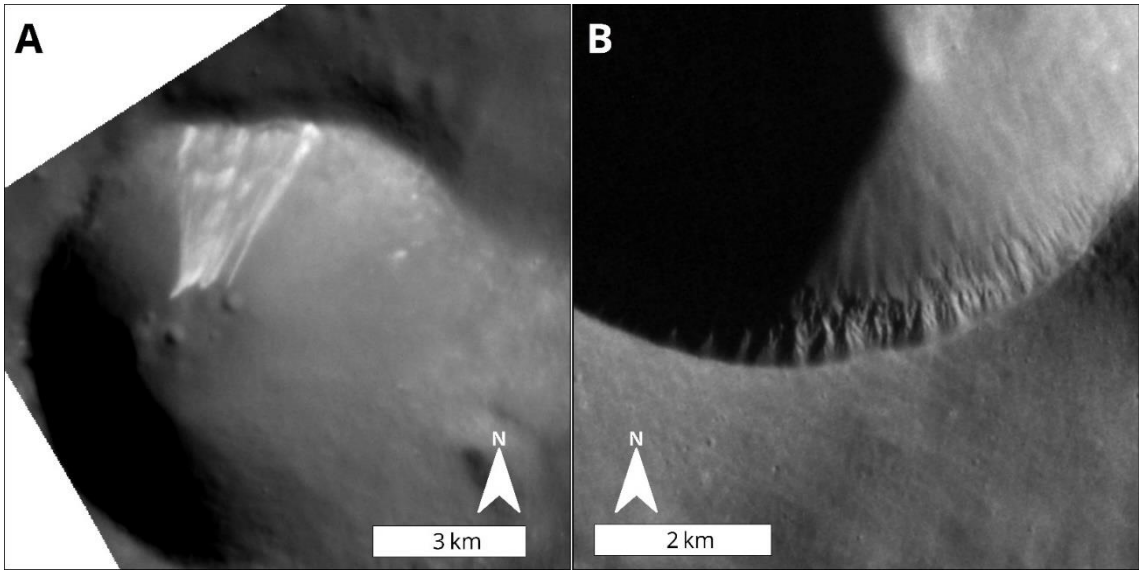

Figure 6.6: Examples of albedo features (A) and topographic features (B). The slope lineae in A (84.8°E, 51.0°N) are significantly higher in albedo than the surrounding slope, but appear to be otherwise featureless, with no topographic expression visible. Topographic features can only be inferred from suitably illuminated images. B (62.8°E, 41.6°N) is an example of spur and gully morphology. It is the only clear example of spur and gully features in the entire dataset.

6.3.3.2 Characteristics

I categorised the lineae features as either albedo features, where the mass movement is defined by an albedo boundary, or topographic features where

the movement is more clearly visible in topography (Figure 6.6, full results in Appendix B-2). The latter included some features in a single crater (Figure 6.6 B) that resemble 'spur and gully' morphologies seen on other bodies (Krohn et al., 2014; Peulvast et al., 2001). I used the digitisation of each gully or lobe of albedo feature (as described in 6.3.2) to calculate lengths of each feature. The length of these lineae ranges from 170 m to 8.91 km. Of the 123 features measured, 61% (75) were under 1 km in length, with a median length of 790 m. The range of lengths is comparable with mass-movements on other planetary bodies, although the mean value is shorter; Xiao et al., (2013b) reported morphologically similar flows with lengths generally >3 km on the Moon, and Krohn et al. (2014) reported mass wasting deposits on Vesta with lengths of up to ~ 9 km. Mercury has higher gravity at the surface than both the Moon and Vesta, which may affect the scaling of mass movement features.

6.3.3.3 Slope Orientation

I used the digitisation of individual slope features to search for any preferential orientations of slope features. Orientations were calculated separately for both albedo and topographically defined lineae.

The 36 individually identified topographic features predominantly form on northwest and southeast facing slopes. The apparent preferred orientation observed is probably a consequence of the small number of geographic locations sampled. Topographic features are only found in 3 locations across the Hokusai quadrangle, and 33 of the 36 examples are either in the Nathair Facula vent or in a single unnamed impact crater. The morphology of slope features differs at the two main locations. Therefore, I am not confident that the trend is demonstrated across a wide enough geographic region, nor am I sure that these features are sufficiently similar to each other, to consider

the orientation data for the topographic features as reliable or representative of a single meaningful dataset.

Of the 84 individual albedo lineae I mapped across the Hokusai quadrangle, 54 are found on slopes facing between 115°E and 245°E. This trend is shown more clearly in Figure 6.7. As the Hokusai quadrangle is in the northern hemisphere of Mercury, this represents a strong bias for albedo lineae occurring on equator-facing slopes.

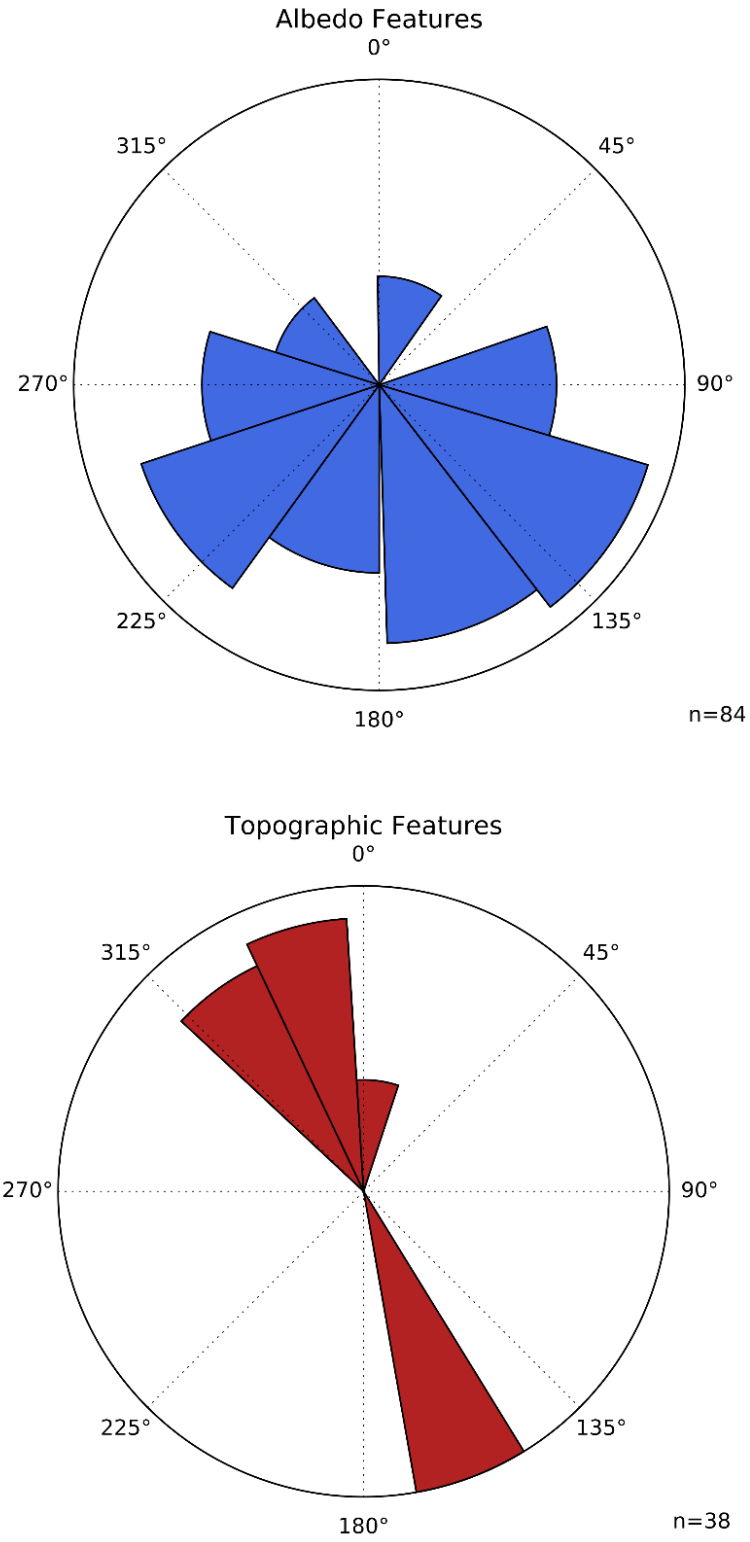

Figure 6.7: Rose diagrams showing downslope orientation of, A - albedo features, and B - topographic features. Both diagrams use equal area petals, whereby the value relates to the area of the 'petal', like a histogram, rather than the radius as in a traditional rose diagram. As downslope direction is used, the feature is located on the face of the crater opposite the petal.

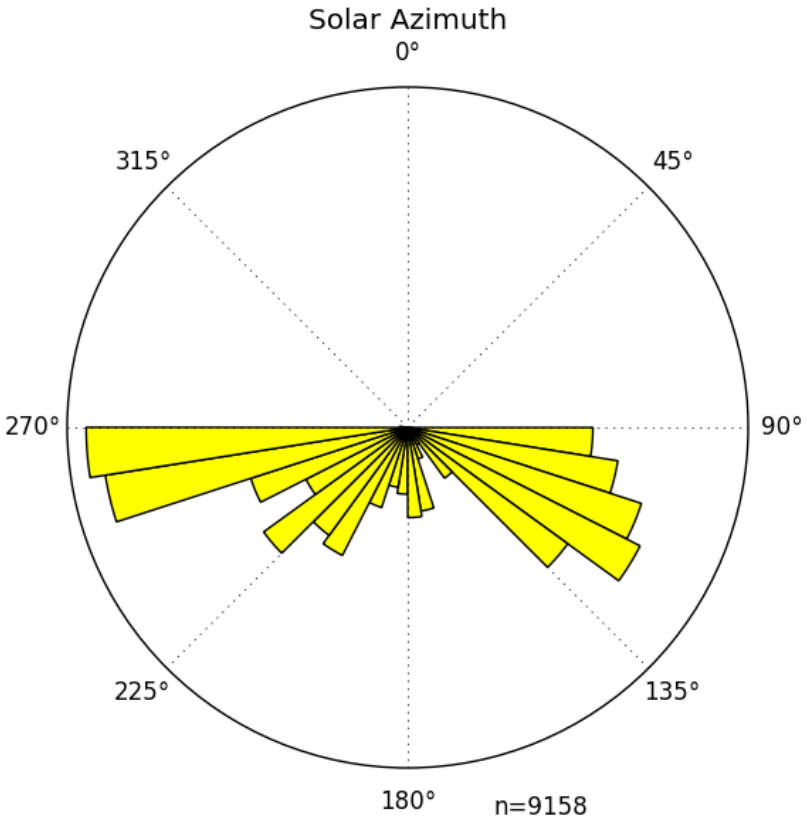

Figure 6.8: Rose diagram (equal area) showing solar azimuth (the position of the Sun relative to the image). Most images are illuminated primarily from the east or west and so should illuminate equator- and solar-facing images similarly. This suggests that a bias in lineae caused by illumination angle should be found on east or west-facing slopes.

A possible cause for this orientation bias in mass-movement features, being more common on equator-facing slopes, could be the illumination angle of the images. The illumination of all the images examined in the Hokusai quadrangle is shown in Figure 6.8. This shows the direction of the position of the sun relative to the centre of the image. All images are illuminated with a sun position south of the image, as is expected as all images are in the northern hemisphere. However, most images are illuminated from the west-southwest or east-southeast, rather than due south (Figure 6.8). These images should have both the north and south-facing slopes illuminated, unless the incidence angle was very low (i.e., the sun is very low in the sky).

Therefore, I conclude that the trend for albedo features to form on the equator-facing slopes is not likely to be purely due to illumination bias. Furthermore, in contrast to the topographically defined features, I do not consider this trend to be obviously due to individual location biases, as albedo defined slope lineae were identified in more images, and at more sites.

6.4 Discussion

6.4.1 Morphology

The systematic survey revealed two styles of laterally restricted mass movement in the Hokusai quadrangle. The predominant styles found in the survey are features marked by albedo difference. Adjacent albedo lineae appear to originate from a similar height; usually, towards the top of the slope on which they are located. Most locations identified contain multiple lineae. In a few cases, the albedo feature appears digitate (e.g., Figure 6.6A). Albedo lineae are geographically distributed across the quadrangle, although there are some clusters, such as around the Rustaveli impact crater.

The other type of linea observed are those defined primarily by topography, found mainly in the Nathair Facula vent (Figure 6.9), and in an unnamed crater at 62.8°E, 41.6°N (Figure 6.6B). Examples in the unnamed crater are similar to spur and gully type morphologies, with an erosive alcove, but no clear channel or fan. Spur and gully type features are not seen anywhere else in my survey of Hokusai. Given this markedly different morphometry and isolated occurrence, this represents a distinct sort of feature and mass movement process, not identified elsewhere.

In contrast, the topographic features in the Nathair Facula vent are gully like, with clear alcove, channels, and fans visible. As well at the Nathair Facula vent, the gullies are spatially close to albedo features visible in images at less

favourable viewing angles (Figure 6.9). There is an overlap between what may be a poorly imaged topographic feature in Figure 6.9B and the faint albedo lineae in Figure 6.9A and C. Notably, in Figure 6.9C the albedo lineae appear darker than the surrounding image, rather than brighter as all other identified albedo lineae are. While this is not conclusive, this suggests that these gully mass-movements could be the same or very similar to the more widespread albedo lineae, just under more favourable lighting conditions.

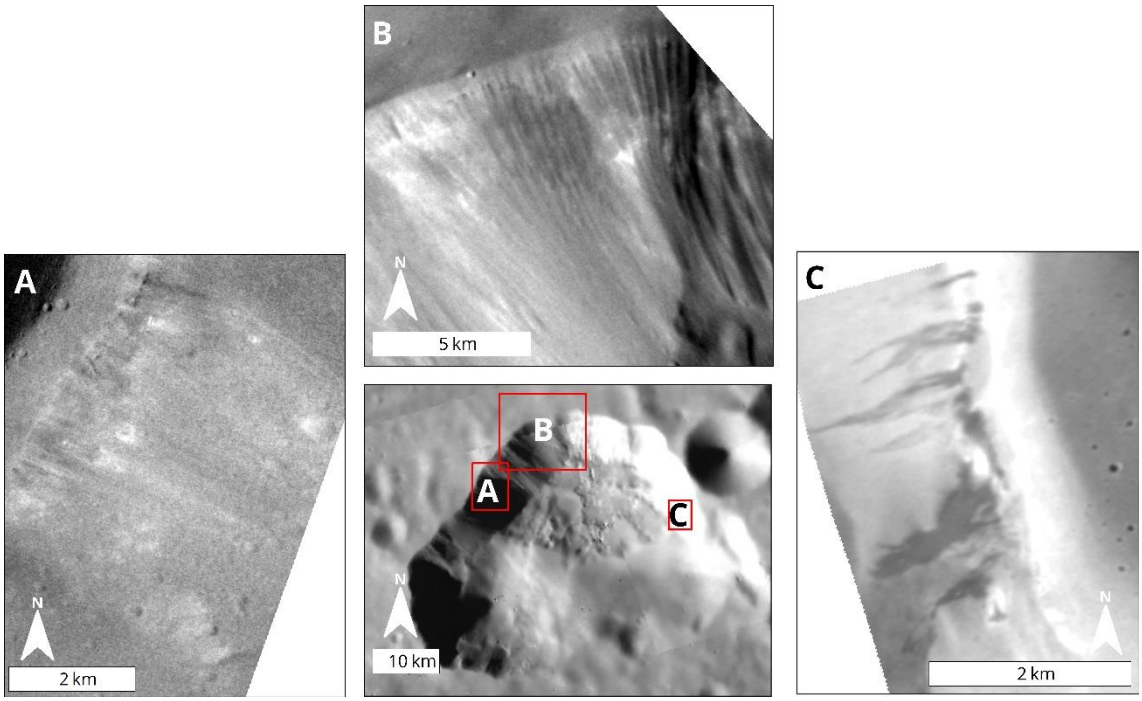

Figure 6.9: Features as seen around the vent in Nathair Facula. Albedo features, as seen in A and C occur in close proximity to excellent examples of topographic features. These images were all taken at different incidence and emission angles. It is therefore likely that topographic features are more easily seen in moderate to high incidence angle or low emission angle images.

6.4.2 Slope Angle

The high albedo lineae are typically found in locations that appear to have visually steep slopes. In a few cases, DEMs generated from stereo images (Fassett, 2016) show quantifiably steep slopes, to reinforce the impression of relief gleaned from visual examination of plan-view images. Producing stereo

DEMs for every candidate feature was impossible as many locations have no suitable image pairs to produce a DEM. In addition, production of stereo derived DEMs is time-consuming and could not be performed for the large number of remaining candidates. However, the Hokusai quadrangle benefits from a good quality regional DEM, produced from regional stereo images and tied to MLA data (Stark et al., 2017). To determine a link to quantifiable steep slopes, I used this DEM to create a slope map to find the steepest pixel in each image footprint. I could then see how many of the images with a quantifiable steep slope, here defined as over 25°, had a slope feature, producing a dataset of images with a known steep slope. Note that this approach will generally underestimate slope value on short hillslopes, because the resolution of the DEM is ~222 mpp, less than the resolution of the images, and so cannot capture the full slope range within every small crater.

Of the 9099 images reviewed, 866 had a slope >25°. Only 31 of the images with a steep slope showed evidence of mass-movement, beyond what I have previously described as Mercury-typical. This is 46% of the images with an identified mass-movement. However, it is only 4% of the 866 images with a steep slope. Therefore, while mass-movements seem to predominantly occur on steep slopes, many steep slopes do not show any evidence of mass-movements, and that a further control on the formation of laterally restricted mass-movements is likely at play.

6.4.3 Age

As previously discussed, slope lineae are found primarily on steep slopes. Previous work on the Moon has shown that small, recent craters become shallower over time, and the shallowing and movement of material downslope can be modelled as diffusion (Fassett and Thomson, 2014; Soderblom, 1970). Fassett et al. (2017) demonstrated that small craters on

Mercury (in the northern Smooth Plains), shallow and degrade quicker than similar craters in the lunar maria. As a crater degrades, the depth/diameter of the crater decreases as material is transported from crater walls to crater floor. This diffusion of material downslope, evidenced in the slope creep observed on Mercury (e.g. Figure 6.4A and B) will work to erase albedo lineae that are no longer active. Therefore, the time it takes for the 'cross-hatch' slope degradation to resurface the entire length of the slope provides a removal timescale for the albedo lineae. No absolute time scale has been reported, but regolith diffusivity on Mercury is approximately twice the rate of lunar regolith. Given similar features on the moon were not found in pre-Copernican (<1.1 Ga) craters (Kokelaar et al., 2017), and landscape evolution is faster on Mercury, the lineae on Mercury must be younger than this. If the landscape diffusion rate of Fassett et al. (2017) holds for the locations hosting lineae, a maximum age of ~550 Ma can be estimated.

Due to the small size of these features and their wide geographic distribution, it is impossible to derive a date from crater counting. However, given that lineae are present in craters superimposing the Mansurian Rustaveli crater, these lineae must be Mansurian or Kuiperian in age.

The examples located in the Nathair Facula vent must post-date the last major eruption, as these features would almost certainly be disrupted by the eruption or covered by the resulting pyroclastic deposit. The bright pyroclastic deposit of Nathair Facula in turn overprints Rachmaninoff ejecta and so must postdate the Rachmaninoff impact. It has been suggested that the age of the Rachmaninoff basin is 3.6 Ga (Marchi et al., 2011). Crater counting of the Nathair Facula bright deposit by Thomas et al. (2014c) suggests an age of 3.3 Ga. The facula is diffuse and thought to be a thin veneer over an underlying surface. Thomas et al. (2014c) makes it clear that this date may well represent the underlying surface, and so should be taken as a maximum possible age for the facula itself. There is geomorphic

evidence for pyroclastic vent activity on Mercury into the Mansurian, and possibly Kuiperian periods (Jozwiak et al., 2018). As Nathair Facula is the brightest region on Mercury, and deposits are generally thought to darken to background over time, it is almost certainly one of the most recent centres of pyroclastic volcanism on Mercury. There is also considerable evidence of Nathair Facula being the site of multiple eruptive events (Pegg et al., 2019a). Therefore, while the vent Nathair Facula may be as old as 3.3 Ga, it is likely that the current vent walls and mass-movements within are younger.

Mercury's stratigraphy was divided into five time systems based on Mariner 10 data (Spudis and Guest, 1988). Recent work based on MESSENGER data has revised the onset of Mansurian and Kuiperian periods (Banks et al., 2017). This has significantly revised the beginning of the Mansurian forward from ~3.0-3.5 Ga to ~1.7 Ga, and the Kuiperian forward from 1.0 Ga to 280 Ma. This is consistent with our better understanding of Mercury, as well as new evidence of geological processes on Mercury in the geologically recent past. As some of the identified mass movements are hosted in Mansurian craters, this would give a maximum absolute age of 1.7 Ga. As there are some potential features in Hokusai, a Kuiperian crater, slope features could also have formed after 280 Ma.

The lineae appear to be predominantly on visually steep craters, most of which are near-pristine in morphology. This suggests that the lineae features are young. It is difficult to give an absolute age for any small slope on Mercury, although absolute estimates for the maximum ages of slopes hosting lineae range from 550 – 280 Ma.

6.5 Mass-movement features on other airless bodies

Laterally restricted mass movements have been observed on other airless bodies. It is logical to compare the features that I have observed on Mercury to other, better studied, features to see if similar factors are in play.

6.5.1 The Moon

Lunar examples are the most useful to compare to Mercury. The Moon is a rocky, airless body, and is the solar system body that is most similar to Mercury. Previous workers have shown a variety of styles of lunar mass movement. This is demonstrated by Xiao et al. (2013b), where a variety of mass wasting landforms are categorised and described. The most similar category of features described is flow features, subdivided into two types, sweeping and channelised. Both flow types appear to show 'characteristics of high fluidisation', but unfortunately Xiao et al. (2013b) offer no morphological definitions of these characteristics. The subdivisions between sweeping and channelled flows is the presence (channelised) or absence (sweeping) of an erosional alcove.

Examples of channelised flows presented by Xiao et al. (2013b) show some 'spur and gully' morphologies. These are features where erosional alcoves have left prominent, jutting spurs on the wall (Hargitai, 2015). These have been observed on other bodies in the solar system such as Mars and Vesta (Conway et al., 2019; Krohn et al., 2014; Shinbrot et al., 2004).

Xiao et al. (2013b) described other morphological styles of lunar mass movements. These include slides and rockfalls.

A different classification for some Lunar mass movements was proposed by Kokelaar et al (2017). This scheme focuses more on the likely mode of movement of the mass movement features, such as slides, falls, or creep.

There are considerably more catalogued locations of channelised mass movements on the Moon (e.g. Chandnani et al., 2019; Kokelaar et al., 2017; Senthil Kumar et al., 2013; Xiao et al., 2013) than I have been able to find on Mercury in my survey. While the Moon has been surveyed over a larger area with considerably higher resolution imagery, it has a far higher density of features than the quadrangle I surveyed on Mercury. This could be due to the better coverage of high-resolution images and constant incident angles provided by NASA's Lunar Reconnaissance Orbiter (LROC) available on the Moon. LROC-NAC has near-global coverage at ~0.5 mpp, whereas the best resolution images in my survey were at ~2.4 mpp. The highest resolution images taken by MESSENGER were ~0.7 mpp and MESSENGER obtained only 852 images with resolution of <1 mpp.

The thermal environment of Mercury, with its ~600 K variation between day and night temperatures, will increase thermal stress. This, coupled with Mercury's higher rate of micro-meteorite bombardment, is thought to lead to regolith production at Mercury being faster than on the Moon, leading to regolith around three times thicker on Mercury than on the Moon (Kreslavsky et al., 2014; Zharkova et al., 2019). Mercury's considerably thicker regolith will also probably make it more difficult to produce mass movements involving large quantities of solid rock on Mercury.

Bart (2007) identified gully-like features on the Moon with the highest resolution images obtained from NASA's Lunar Orbiter in 1966/1967. Lunar Orbiter images can resolve objects ~1-2 m across but are not as sharp or clear as images from modern cameras such as LROC or MESSENGER-NAC (Figure 6.10). These gully-like features can be seen in considerably more detail in LROC-NAC images, but are not easily visible in LROC-WAC images. The features would be classified by Xiao et al. (2013b) as channelised flows, and often show a spur and gully morphology that appears to expose rock or a

coherent regolith layer at the surface. This contrasts a little with their appearance in the Lunar Orbiter data, with prominent examples appearing to be more isolated, and with more distinct erosional alcoves.

I have compared the examples of mass movement that I have found on Mercury to examples on the Moon. Morphologically the topographic and albedo features on the Moon most similar to the Mercury features are the features labelled as 'flows' by Xiao et al. (2013b). A good lunar location with comparable mass movement features to the Hermean examples identified are the 'sweeping flows' in Couder crater (Figure 6.10). They are distinguished by a high albedo compared to the surrounding crater wall. Individual flows originate and terminate at various heights on the crater wall. The features are often digitate, with multiple flow fronts from an individual source area. The Hermean example which most resembles this is the example of lineae on a peak ring element in Rustaveli (Figure 6.10). This also shows 'sweeping' flows, with digitate lobes. It is hard to say with certainty exactly where the flows on the Rustaveli peak ring element originate; it is therefore quite possible the individual flow fronts originate at multiple heights on the slope.

While these two features are quite similar morphologically, the comparison is not so robust when looking at other Mercury features. Lunar examples in Couder are visible in LROC-NAC downsampled to 112 mpp to compare to low angle images of Martins crater on Mercury (Figure 6.10). However, as the features in Couder are high albedo, they are more easily visible in low-resolution images than the typical, low albedo, sweeping and channelised flows elsewhere on the Moon. Other lunar examples do not show up clearly at ~20 mpp or in LROC-WAC images. The best images of the albedo lineae on Mercury (Figure 6.3 and Figure 6.9) suggest they originate at a single layer. This is not the case with the lunar examples.

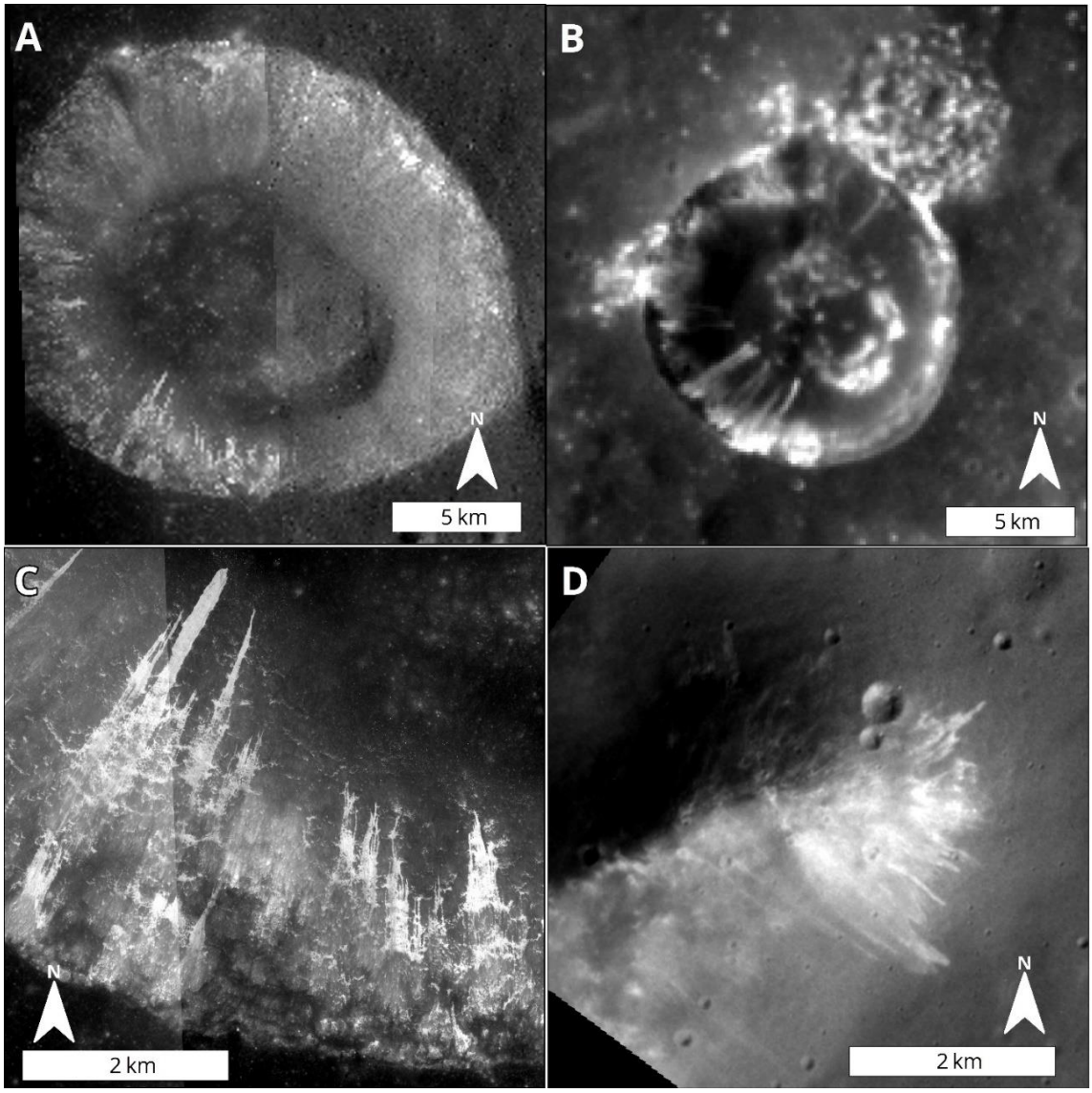

Figure 6.10: A – Lunar Couder crater resampled from LROC NAC images to 112 m/pixel (NAC Images: M1173655305R, M1173648197L, M1101817103R, M1101817103L, M1173655305L). B – Martins crater on Mercury in the best available resolution of 112 m/pixel. Streaks are still visible in Couder crater but are less clear, and do not appear so developed as those in Martins Crater. C – Full resolution LROC image (~30 cm/pixel) of flows on the south slope of Couder (NAC Images: M1101817103L&R). D – Lineae on a peak ring element in Rustaveli on Mercury (~8 m/pixel). The flows in Couder do not look dissimilar to those on the peak ring element in Rustaveli. LROC-NAC images courtesy of NASA/GSFC/ASU.

In the alternative classification of lunar mass movement features of Kokelaar et al (2017) the majority of sweeping flows identified by Xiao el al (2013b) would likely be debris flows. Debris flows can be erosive and tend to move as dry avalanches (Kokelaar et al., 2017).

The subset of Hermean mass movement features that I have classified as topographic have different morphologies (Section 6.4.1). The spur and gully type features in the unnamed crater (62.8°E, 41.6°N), exposing spurs of bedrock or more competent regolith, most resemble the channelled flows in the Xiao et al. (2013b) lunar classification, for example on the north crater wall of Dawes (Figure 6.11). Similar channelised flows are reported in many more locations across the Moon, including many in the lunar maria. However, on Mercury I have only been able to identify a single location containing these morphologies in the unnamed crater at 62.8°E, 41.6°N. Formation of spur and gully features requires erosion into a competent layer of rock or very well consolidated regolith. Thus, spur and gully features are most likely to be found in localities with a thin covering of regolith. Regolith cover on smooth plains is probably thinner than the global average, but Mercury's smooth plains regolith cover is thicker than smooth plains (e.g. maria) on the Moon (Fassett et al., 2017; Fassett and Thomson, 2014). As a competent layer is found at a greater depth on the surface of Mercury, this can explain the paucity of spur and gully features on Mercury compared to the Moon.

The gully-like topographic features in the Nathair Facula vent are notably dissimilar to documented lunar flows. The gullies at Nathair Facula have a clear V-shaped alcove, and a deeply incised, erosional gully. The closest analogues I have found are the lunar gullies described by Senthil Kumar et al. (2013). They describe several gully-like features with alcove, channel, and fan sections in a small crater superimposing the Schrödinger Basin. The gullies are visible in high-resolution LROC-NAC images under favourable lighting geometries. Many examples do not appear to be so clearly developed

as the Hermean gullies, with channels often not appearing as deeply incised, or alcoves sharply defined. Depth measurements by Senthil Kumar et al. (2013) from LOLA laser altimetry, however, suggest that lunar channels have a depth of between 5 and 30 m. I do not have quantitative estimates for the depth of Hermean examples as they are not resolved in the best stereo DEMs available (Fassett, 2016), nor MLA data. However, lunar examples appear to be of a similar scale to Hermean examples and are sometimes reported as co-located with dark slope lineae (Senthil Kumar et al., 2013). This is similar to the examples in the Nathair Facula vent (Figure 6.9). Senthil Kumar et al. (2013) suggest the lunar examples may have formed episodically as a result of seismic shaking from nearby impacts. This could be the case for Mercury, and I discuss this in section 6.6.2.

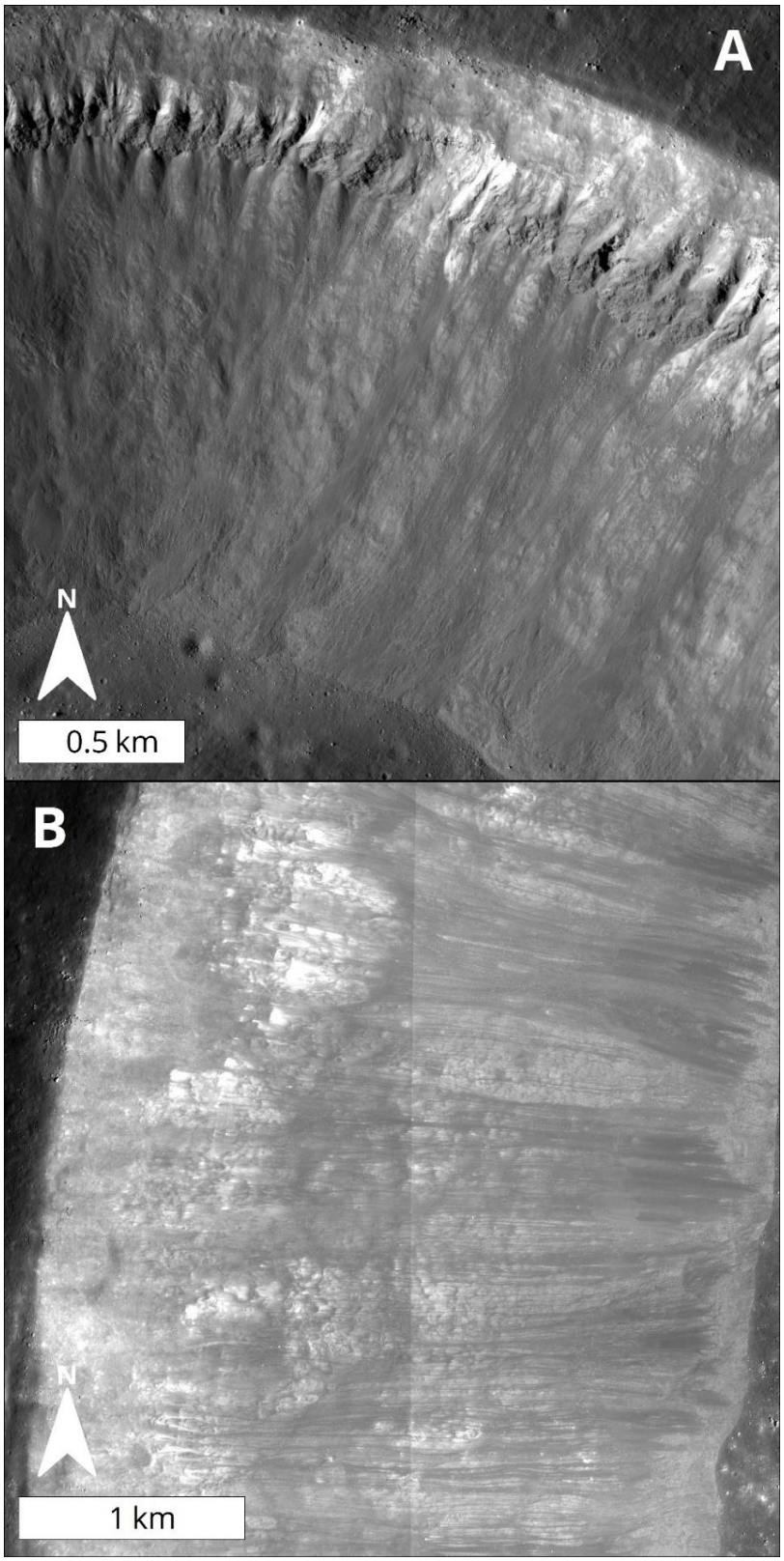

Figure 6.11: Dawes crater on the Moon. A - spur and gully like morphology transitioning into 'sweeping flows' (LROC-NAC: M180994913L) and B - more typical sweeping flows on the western crater wall (LROC-NAC: M190423336L&R). LROC-NAC images courtesy of NASA/GSFC/ASU.

6.5.2 Vesta

Vesta is the second-largest asteroid in the asteroid belt. While it is a differentiated body, it has not achieved hydrostatic equilibrium and has an oblate spheroid shape. Vesta was orbited in 2011 and 2012 by NASA's Dawn spacecraft, which provided a large suite of images and other data, and enabled work on Vesta as a dynamic body (e.g. Buczkowski et al., 2012; Neumann et al., 2014; Scully et al., 2015).

Geological mapping showed that mass movement features are common on Vesta (Krohn et al., 2014; Otto et al., 2013), and represent one of the key processes shaping the present-day surface geomorphology.

Krohn et al. (2014) examined mass movement features across two quadrangles of Vesta using geological mapping. They found a variety of large-scale lobate flows, perhaps analogous to some sweeping flows (Xiao et al., 2013b) on the Moon. Also documented were spur and gully features. These were found in multiple craters (Figure 6.12), along with spur and 'flow' features at Matronalia Rupes. Krohn et al. (2014) also identified large blocks slumping on Matronalia Rupes, a lobate scarp. This is not dissimilar to slump features seen in craters on the Moon and Mercury (Figure 6.1B, and in Xiao et al., 2013b). Krohn et al. (2014) attribute the formation of all these features to dry processes. The lower gravity of Vesta was used to explain how mass-wasting features have a longer runout compared to the Moon by reducing particle settling times once material has begun moving (Krohn et al., 2014).

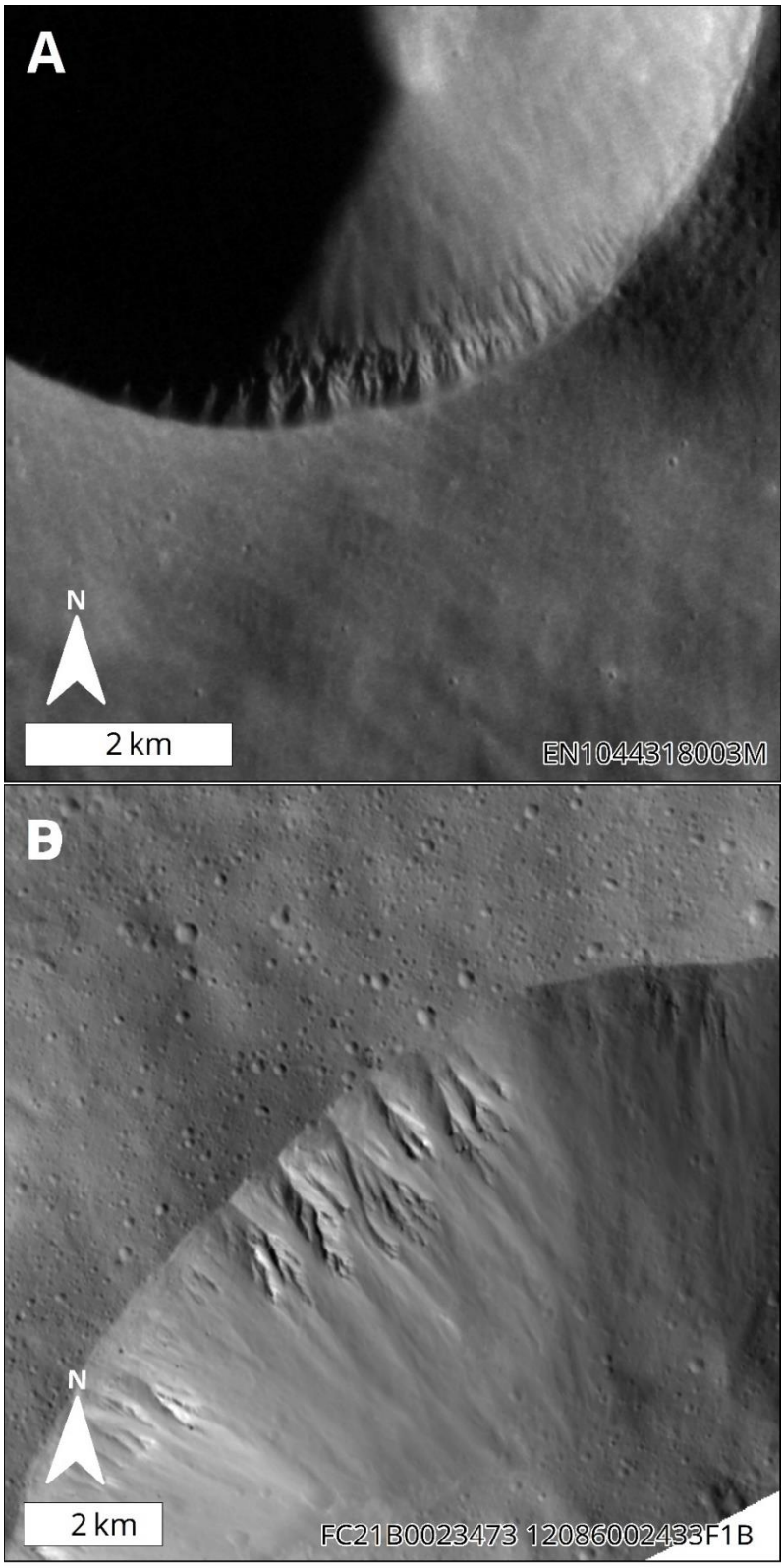

Figure 6.12: A: Spur and Gully type features in an unnamed crater on Mercury. These are similar, if considerably smaller than examples in Fonteia Crater on Vesta (B).

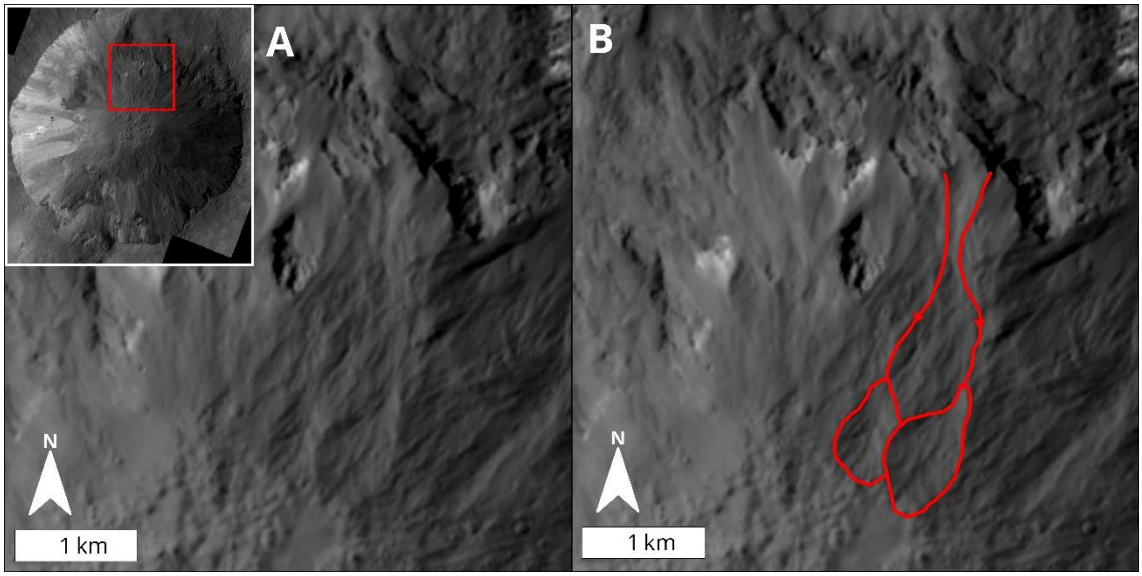

Figure 6.13: Curvilinear gullies of Scully et al. (2015) in Cornelia crater on Vesta. A and B show the same field of view with gullies and lobate fans highlighted in B.

Other work by Scully et al. (2015) also reports gully like features on Vesta. These are classified as either linear or curvilinear gullies. The linear gullies of Scully et al. (2015) would have been classified as spur and gully features by Krohn et al. (2014). They suggested that these curvilinear gullies formed by transient fluid flow because they were unaware of any mechanism that can produce curvilinear erosive features without a fluidising agent. In the planetary context, fluidised mass-movements do not necessarily require a liquid component; gas can also entrain regolith and enable a mass-movement to behave as a fluid (Cedillo-Flores et al., 2011; Pasquon et al., 2019). Scully et al. (2015) proposed that the most likely fluidising agent on Vesta is liquid water released from ice-bearing deposits in the subsurface of Vesta that was heated and released by impact heating processes. The curvilinear nature of these gullies (Figure 6.13) and the presence of linear gullies on Vesta is key to the inference of the fluid role in the formation of the curvilinear gullies. Scully et al. (2015) did not quantify how curvilinear the Vestan gullies are with any sinuosity values. Experimental data was used by Scully et al. (2015) to suggest that water evaporation rates may allow liquid

water to survive on the surface of Vesta at the low pressures and temperatures expected after impact for long enough to form the features. Water was stable in experimental conditions on a timescale of minutes to hours, suggested by numerical modelling to be a reasonable duration for the gullies to form by transient water flow.

Other than the curvilinear gullies, Vestan mass-movement features are similar to those seen on the Moon. This suggests that, despite great geological differences, there are similarities in morphologies of mass-movement features on airless bodies, and hence, in all likelihood, also in processes. Given the prevalence of mass-movement features on Vesta and the Moon, it is curious that they are much less prominent on Mercury. This could be a result of the limitations of the available images with sufficient resolution, or due to a genuine dearth of currently visible mass-movement relative to other bodies. Formation of mass wasting deposits on Mercury could occur at a similar rate to other planetary bodies but be degraded more quickly because of Mercury's higher rate of regolith production (Fassett et al., 2017).

6.6 Triggering mechanism

In this section, I consider possible triggering mechanisms for the mass-movements I have described.

6.6.1 Impact-induced Seismicity and ground effects

On the Moon, the most efficient and therefore most likely triggering mechanism for mass wasting processes is impact-related ground movement and moonquakes (Xiao et al., 2013). This can be from shock waves from impacts causing shaking and avalanching on slopes close to the angle of repose. Impacts can also promote mass-movements through the weakening of ground through the propagation of fracture zones. Work has shown that

Mercury has a higher impact flux than the Moon (Strom et al., 2011, 2008), and craters and landforms are thought to degrade around twice as fast as those on the Moon (Fassett et al., 2017). This would suggest that impact events capable of triggering mass movements are more frequent on Mercury. However, the steep slopes required for the observed mass movements will also degrade more quickly, so there is potentially a higher rate of impact triggered mass wasting beginning in small fresh craters on Mercury, but compared to the Moon, mass wasting would cease quicker as craters there rapidly degrade and slopes lessen. If mass-movements on Mercury are primarily triggered by impact shaking, it should be a common feature of pristine impact craters. This was not the case in my survey, or in the survey of the highest resolution MESSENGER images (Kreslavsky et al., 2018b). Future targeted imaging of a sample of pristine impact craters with BepiColombo may test this more rigorously.

6.6.2 Seismicity from fault movement

Tectonism has been an important process throughout Mercury's history (Banks et al., 2015; Byrne et al., 2016) and is thought to be principally driven by Mercury's global contraction, and potentially, the effects of tidal despinning earlier in its history (Byrne et al., 2014; Matsuyama and Nimmo, 2009; Watters et al., 2015). The main morphological manifestations of tectonism are lobate scarps and wrinkle ridges. Lobate scarps are asymmetric scarps, up to a few km high, and are thought to be morphological expressions of thrust faulting. They occur all over Mercury's surface, in both smooth and intercrater plains, as small, isolated scarps as well as large, interconnected fault systems with scarps detaching onto other segments and en-echelon sections. High-resolution images from the end of the MESSENGER mission revealed small pristine scarps (Watters et al., 2016), orders of magnitude smaller with tens of metres relief, close to large lobate scarp

systems. Given the rate of landscape evolution on Mercury, Watters et al. (2016) determined these features to be younger than 50 Ma. It is, therefore, likely that Mercury remains tectonically active in the present. Seismically-induced shaking is linked to the triggering of mass movements on the Earth (e.g. Barlow et al., 2015; Chigira et al., 2010); Mars (Neuffer and Schultz, 2006); and, as previously mentioned, on the Moon. Both Mercury (Watters et al., 2016) and the Moon (Watters et al., 2019) have had geologically recent movements on thrust faults. Locations of recent fault movement can be understood globally from LROC images, and some activity is thought to be younger than 50 Ma (Watters et al., 2012). The known locations of recently geologically active faults on Mercury (Watters et al., 2016) are limited to areas covered in very high-resolution, low altitude imaging. Due to MESSENGER's orbital constraints, this means Hermean examples are all found above 30°N. However, they are widely distributed by longitude in the areas imaged with sufficient resolution.

Thus, tectonic activity could be a triggering mechanism for the observed mass movement deposits. To test this, I calculated the shortest distance from centres of mass-movement deposits to their closest tectonic feature, as mapped by Wright et al. (2019), using ArcGIS's 'Near' function. This follows a similar technique used by Watters et al. (2019) on the Moon. I chose to use feature centres, marking each topographic feature (e.g. crater, vent, or peak-ring element) hosting slope lineae, this should provide a more representative set of statistics as statistics from each individual feature would be dominated by the locations with many features. This gave 22 sites. The average centre was ~130 km from a tectonic feature. I then compared this to five sets of 22 points randomly distributed across the H05 (Hokusai) quadrangle. The range of these results was wide: mean distances from scarps of between 66 km and 97 km were found from the random point data sets. Surprisingly, these are all well below the average 134 km distance to scarps found for the areas with

mass movements. This may be explained by many feature centres being located in Hokusai or Rustaveli craters or ejecta. These are both impacts with large and relatively undisturbed ejecta blankets that could cover pre-existing tectonic features. This also means no tectonism large enough to produce a currently visible surface scarp has occurred since the lineae formed. As shown in Figure 6.14, the majority of locations of mass-movements are located in or close to these ejecta blankets. I therefore cannot demonstrate a quantifiable connection between locations with mass-movement deposits and tectonic features, and in fact the opposite seems to be true.

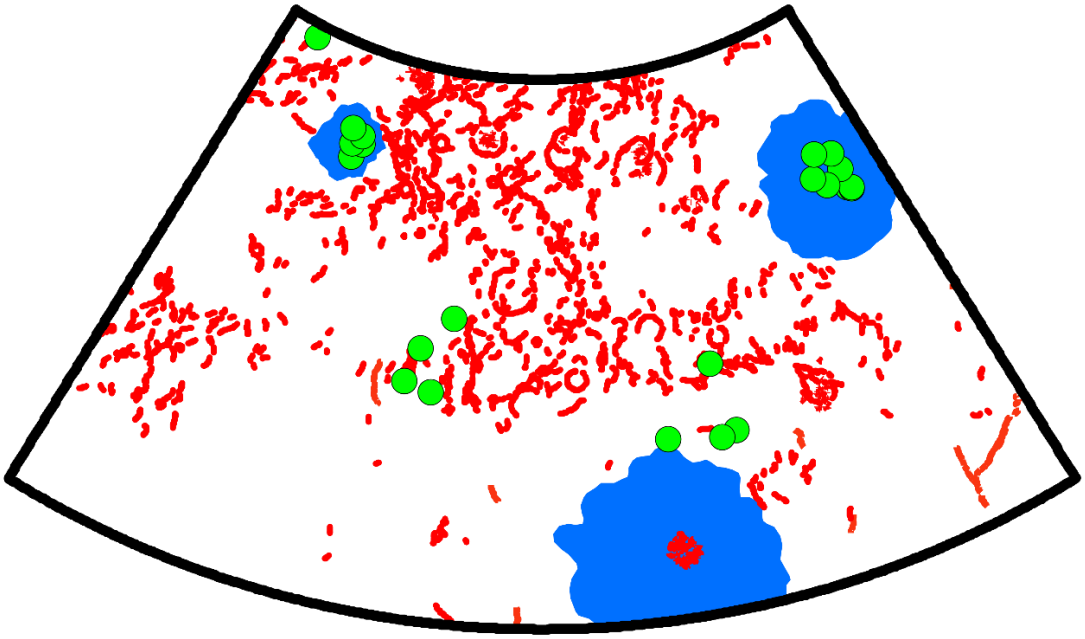

Figure 6.14: Locations of mass movements (green points), tectonic features (red lines) and large young ejecta blankets (blue areas) in the Hokusai quadrangle. The sites of mass movement are often in, or close to, large young ejecta blankets, which will have probably covered older tectonic features. This probably explains why sites of mass movement were further from the nearest tectonic feature than random points.

6.6.3 Volatile loss

One of the great surprises of the MESSENGER mission was the discovery of evidence of recent volatiles at the surface of Mercury (Blewett et al., 2011;

Evans et al., 2012; Neumann et al., 2013b; Weider et al., 2016, 2012). This has been particularly associated with landforms known as hollows. Hollows are sub-kilometre scale, flat-floored, rimless depressions (Thomas et al., 2014c), and are widely distributed across Mercury. It is generally accepted that hollows form by the loss of a volatile phase; however, the precise mechanism of volatile release is not yet known. Previous work has suggested a preference for hollows to occur on equator-facing slopes and a weak correlation with proximity to the planet's 'hot poles' (Blewett et al., 2013; Thomas et al., 2014c). The strongest control, however, appears to be that hollows are usually found in impact craters that have excavated 'Low Reflectance Material' (LRM) and spectrally blue plains (Blewett et al., 2013; Thomas et al., 2014c). It is thought that LRM may therefore be the remains of Mercury's putative graphite flotation crust (Murchie et al., 2015b; Peplowski et al., 2016; Vander Kaaden and McCubbin, 2015).

As previously noted, albedo lineae show a strong tendency to occur on equator-facing slopes. This suggests a possible link to insolation. It is also the case that many of the best examples of these features are found in areas that show evidence of crustal volatiles. The locations I have found with the clearest lineae are in the Nathair Facula vent, and around Rustaveli (e.g., Figure 6.6A, Figure 6.10D). Rustaveli, whilst not located in an area of LRM or blue plains, is a large, recent impact crater, and hosts hollows. The peak ring element in Rustaveli (Figure 6.10D) contains hollows (e.g., Figure 12.13 in Blewett et al., 2018). The vent in Nathair Facula is not located in an area with widespread evidence of hollows, but high-resolution imaging of the vent wall (Figure 6.3 and Figure 6.9) reveals that the layer from which the gully features originate shows a hollow-like morphology (Figure 12.7 in Blewett et al., 2018). Another line of evidence for volatiles being present around Nathair Facula is the vent itself, which is a site of explosive volcanism. Violent escape of volatiles is thought to be necessary to drive this process; recent work

suggests that during ascent magma volatiles were added to magma either from the subsurface or magma circulation (Jozwiak et al., 2018).

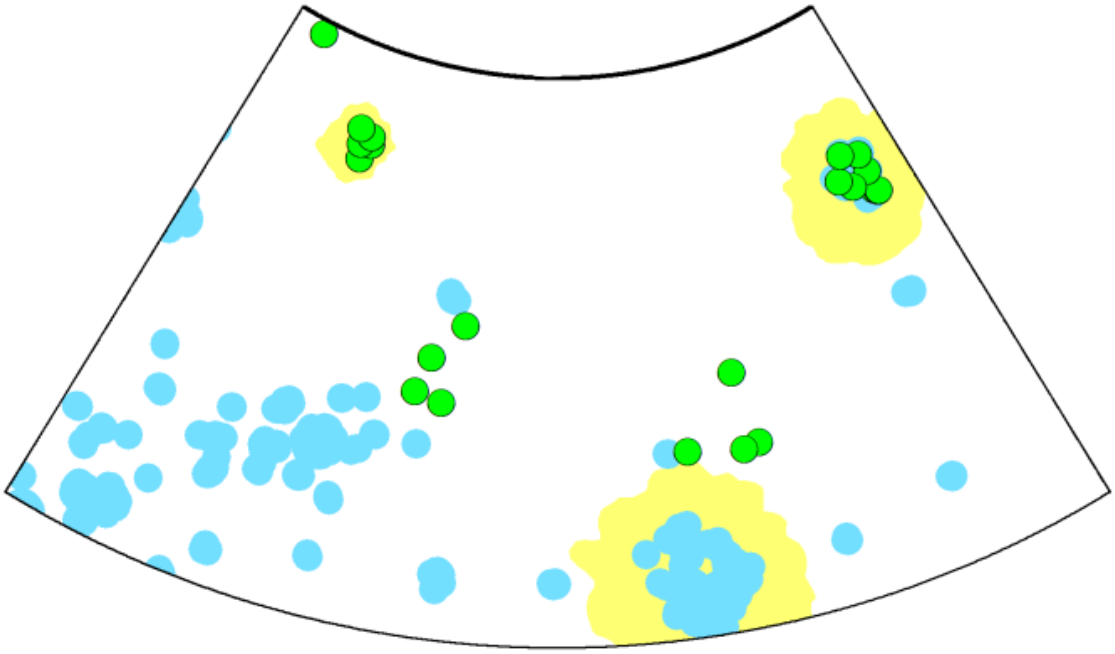

Figure 6.15: Locations of mass movements (green points), hollows (blue) and large young ejecta blankets (yellow areas) in the Hokusai quadrangle. Mass movements are found very close to site of hollows in the crater to the northeast (Rustaveli)

A different study (Weider et al., 2016) suggested that in the specific case of the Nathair Facula vent volatiles were incorporated from the country rock. Recent work has suggested that this vent is a site of multiple explosive volcanic eruptions (Pegg et al., 2019a), and so a degree of volatile recharge is likely. Martins crater, which hosts lineae but does not contain any examples of landforms created by explosive volcanism, is also located at a site of documented hollows (Thomas, 2015).

The prevalence of lineae in areas with documented hollows and on equator-facing slopes could suggest the formation of lineae is initiated by volatile loss. A conceptual mechanism for this would be insolation driving the loss of volatile material in the upper portion of the slope, causing the regolith to lose coherence, thus becoming critically over-steepened, and triggering a dry

granular flow downslope. Triggering of lineae by volatile loss explains the observed orientation preference. This is not, however, beyond doubt and other lineae do not show any evidence in images of originating at a defined stratigraphic layer. Lineae, nevertheless, do not appear to originate at many different heights at single locations. High-resolution images of lineae sites could more fully address this.

6.7 Conclusion

I have identified and described several different mass movement features on Mercury. It is likely that these have not all formed in the same way. The key types I have identified are a small number of spur and gully type features, and bright slope lineae.

Spur and gully features on Mercury probably formed where there is a consolidated layer at the surface. They are not as common as on other bodies, probably due to the rapid formation of regolith on Mercury. The acquisition of many more high-resolution images of fresh impact craters by BepiColombo will be useful to understand the distribution of these morphologies and could serve as a proxy for depth of unconsolidated regolith.

Slope lineae appear similar to features on other airless bodies thought to have formed by dry granular processes, and I have seen no evidence, such as curvilinear lineae, of formation involving a separate fluidising agent. Hermean slope lineae therefore probably also formed by dry granular flow. It is not clear exactly what triggers slope lineae on Mercury. This problem is exacerbated by the fact that, despite examining many images, only a few examples of these features were found. Based on these limited examples, I have found no obvious spatial link between mass-movement deposits and tectonic features or nearby large fresh impacts. Limits in image resolution and coverage, as well as many small impacts widely distributed across the

surface, mean these cannot be ruled out as triggering mechanisms. There is some evidence of slope lineae forming primarily on equator-facing slopes and, in some cases, close to volatile-driven landforms. Therefore, given the current evidence, I favour the idea that slope lineae are initiated by volatile loss, causing a loss of cohesion of the regolith. This loss of cohesion on a slope greater than the angle of repose could cause a dry, avalanching, granular flow.

High-resolution images, particularly from the southern hemisphere, and global coverage of higher resolution geochemical data from BepiColombo will be useful in both obtaining a more complete global dataset of slope lineae, as well as providing better images of known examples. This understanding of distribution and morphological information, along with spatially resolved geochemical data, will be invaluable in more definitely establishing the triggering mechanism.

CHAPTER 7
FUTURE WORK

My thesis has been based around the mapping of the Derain quadrangle, and the detailed studies that arose from it. Given my results, and pitfalls encountered, here I propose potential future work, and modifications to methods I would make.

7.1 Mapping

The mapping method I used was robust and has produced a map suitable for integration into a global 1:3 million scale geological basemap. I plan to integrate with surrounding quadrangle maps using the 5° overlaps mapped with other quadrangles. The main focus of integration will be with the map from Wright et al. (2019) of the Hokusai quadrangle to the north, as this is the longest border with a map that has been integrated into the global map. The map is shown in context with other completed quadrangle maps in Figure 7.1.

When integrating my quadrangle map, I would like to spend time to split the intermediate plains unit into separate intermediate age, and mantled plains. This, however, brings more interpretation into what is, fundamentally, a geomorphological map. I am confident the morphology is clear enough to distinguish between mantled and intermediate age plains. This will help better represent the quadrangle stratigraphy.

My mapping has highlighted areas for future study within the quadrangle. Faulting in the quadrangle rarely seems to be purely compressive, as would be expected if global contraction was the main driver of tectonics. The kinematics of Calypso Rupes, in particular, is unlike any lobate scarp system I have seen on Mercury, and future work should focus on its complex

kinematics and apparent strike-slip sections. The small extensional features at Calypso Rupes suggest that the system may be a good candidate for recent fault movement that may be visible with targeted high-resolution imaging by BepiColombo.

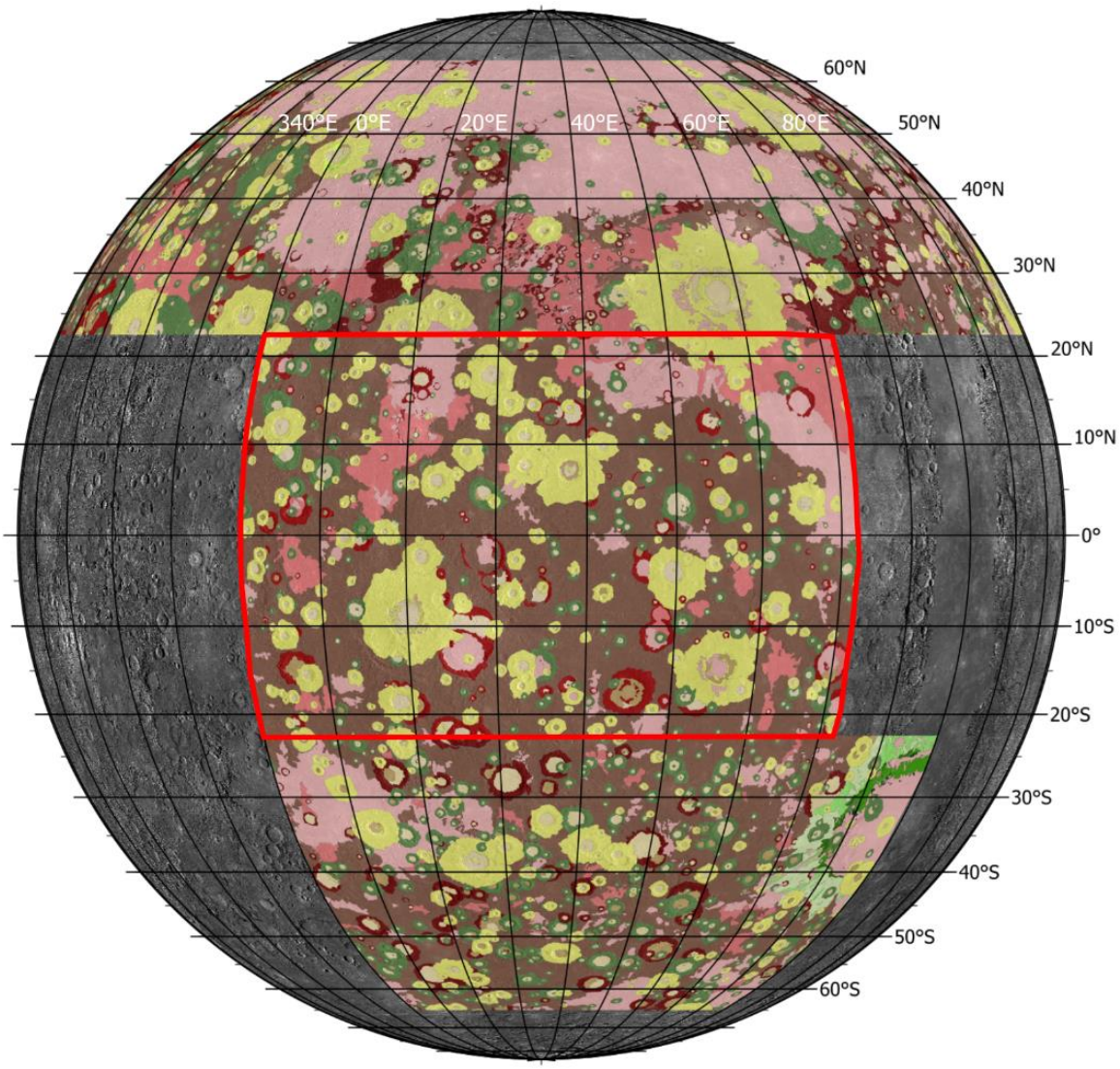

Figure 7.1: Completed geological mapping of Mercury. The Derain quadrangle is highlighted in red. To the north of Derain is the Hokusai quadrangle (Wright et al., 2019), which adjoined the Victoria quadrangle to the west (Galluzzi et al., 2016), and Radiolaria quadrangle to the east (Mancinelli et al., 2016). To the south of Derain is the Debussy Quadrangle (Pegg et al., 2019b). Orthographic projection centred at 35°E, 0°N.

Also of interest for future work would be further work on the explosive volcanism within the quadrangle. Understanding the multiple eruptions at the vent within Picasso: for example, determining the duration of activity of the system, or how the system recharged, is essential to understand the history of volatiles in the area. New datasets such as high-resolution images to look for cross-cutting relationships would be useful. Future work to understand the distribution of explosive volcanism on Mercury could use the southeast of the quadrangle as a good case study. This area has multiple sites of explosive volcanism, with examples of both single and multiple event sites. The same area also shows tectonism, with Soya Rupes and other, unnamed, fault systems. The tectonism here may be linked to small scale effusive volcanism (Chapter 5). While no quantifiable link has been found on a global scale between tectonism and explosive volcanism (Klimczak et al., 2018), this could be because of the large number of faults and explosive sites. Therefore, studies on a regional scale, such as southeast Derain quadrangle, should be examined to verify this lack of a link at the local or regional scale.

7.2 Small Smooth Plains

Small patches of smooth plains have not previously been noted abutting lobate scarps. Given the datasets available, I was not able to make definitive conclusions on the emplacement mechanisms of the smooth patches described. The most likely emplacement mechanisms are impact derived resurfacing, or effusive volcanism. Until new datasets are obtained, it will not be possible to distinguish between these emplacement mechanisms definitively. BepiColombo will be able to provide higher resolution imagery, which may be able to distinguish volcanic features such as flow fronts or source vents. Improved geochemical data from BepiColombo may be able to distinguish if smooth plains have a distinctive geochemical signal. A distinct geochemical signal, for example, a higher ratio of Mg/Fe than the

surrounding plains, may suggest a volcanic origin; if a signal is similar to surrounding plains, or nearby crater ejecta, it may suggest an impact origin.

While new data from BepiColombo will be essential in distinguishing origin, computer modelling could be useful in the meantime. I have suggested the stress release at lobate scarps may allow short periods of effusive volcanism. Computer modelling of stress at faults on Mercury, building on work proposed on better understanding the kinematics of non-pure compression on Mercury, could test this. Comparison could then be made to models of dyke propagation to test if stress release would be sufficient to allow dyke propagation to the surface, and so effusive volcanic vents to form. These models would be useful in understanding the distribution of stress and magma migration more generally on Mercury.

7.3 Slope Lineae

Other workers had not previously described the slope lineae I found through mapping. I completed a systematic survey of the Hokusai quadrangle looking at all high resolution (<20 mpp) images. To get a better understanding of the numbers and distribution of these features would require a global survey of all MESSENGER images <20 mpp. It would be best to focus on northern hemisphere quadrangles, as they have the best coverage of high-resolution images; and on those quadrangles with high-resolution stereo DEMs, to be able to examine slope angles. A global inventory would help test triggering hypotheses, such as whether my observation that most slope lineae are found on equator-facing slopes is replicated globally. More locations and images may also give improved morphometry for slope lineae.

To better understand if lineae are seismically triggered, computer modelling of the degree of shaking that might be expected on Mercury from various sized impacts could be employed. Given Mercury's thick regolith and high impact flux knowing what size of impact at what distance can trigger

sufficient shaking to destabilise material on ~20 - 30° slopes is essential in fully evaluating any role of seismic shaking in triggering slope lineae. Given that seismic shaking is linked to slope processes on the Moon, this work could be modified to understand lunar slope processes better.

Given that all the existing images of slope lineae were obtained without a targeted imaging campaign, targeted images from SIMBIO-SYS on BepiColombo will potentially help find new examples. It may also acquire images from multiple lighting geometries of known examples, which will help with understanding morphology or provide images suitable for stereo DEM creation.

CHAPTER 8
CONCLUSIONS

I have produced the first geological map of the Derain quadrangle, using MESSENGER data. I have done this to the same standards as previous MESSENGER era 1:3 million scale mapping (Galluzzi et al., 2016; Guzzetta et al., 2017; Mancinelli et al., 2016; Wright et al., 2019), and which are also being followed by subsequent OU PhD projects (Man et al., 2020; Pegg et al., 2019b). The map I have produced is compatible with this prior mapping and will be integrated into a high-resolution geological basemap. My mapping showed that two plains classifications are insufficient to represent the diversity of plains material in the Derain quadrangle. Plains units exist on a continuum. The intermediate plains may represent two distinct stages of resurfacing, and future mapping should attempt to distinguish these. From my mapping, I have also developed a geological history of the quadrangle.

My mapping led to detailed studies of interesting features. This research found that:

- There are multiple sites of small patches (<15,000 km^2) of smooth plains, both within and outside the Derain Quadrangle. Several of these are found abutting lobate scarps so must post-date widespread global contraction and consequently the end of widespread effusive volcanism.
- It is not possible to definitively ascribe a formation mechanism to the small patches of smooth plains. The most likely mechanisms are either late-stage volcanism or impact-related processes. In most cases, I favour a volcanic origin.
- I have identified slope lineae, a previously unknown mass-wasting process on Mercury. I have also identified a location of spur-and-gully

mass-wasting. This provides new evidence of recent landforms on Mercury.

- The results of a systematic survey show slope lineae are not commonly found in either high-resolution images, quantifiably steep slopes, or fresh slopes.

Those slope lineae that I identified are predominantly on equator-facing slopes. This, coupled with examples in the Nathair Faculae vent being sourced from a hollow forming layer, suggests a possible link to volatiles triggering lineae. No quantifiable link was made to impact-induced or tectonic seismicity.

REFERENCES

Abramov, O., Wong, S.M., Kring, D.A., 2012. Differential melt scaling for oblique impacts on terrestrial planets. Icarus 218, 906–916. https://doi.org/10.1016/j.icarus.2011.12.022

Aittola, M., Öhman, T., Leitner, J.J., Kostama, V.P., Raitala, J., 2010. The structural control of venusian polygonal impact craters. Icarus 205, 356–363. https://doi.org/10.1016/j.icarus.2009.08.004

Anderson, B.J., Acuña, M.H., Korth, H., Purucker, M.E., Johnson, C.L., Slavin, J.A., Solomon, S.C., McNutt, R.L., 2008. The structure of Mercury's magnetic field from MESSENGER's first flyby. Science 321, 82–85. https://doi.org/10.1126/science.1159081

Anderson, B.J., Acuña, M.H., Korth, H., Slavin, J.A., Uno, H., Johnson, C.L., Purucker, M.E., Solomon, S.C., Raines, J.M., Zurbuchen, T.H., Gloeckler, G., McNutt, R.L., 2010. The magnetic field of Mercury. Space Science Reviews 152, 307–339. https://doi.org/10.1007/s11214-009-9544-3

Anderson, B.J., Acuña, M.H., Lohr, D.A., Scheifele, J., Raval, A., Korth, H., Slavin, J.A., 2007. The magnetometer instrument on MESSENGER. Space Science Reviews 131, 417–450. https://doi.org/10.1007/s11214-007-9246-7

Andrews, G.B., Zurbuchen, T.H., Mauk, B.H., Malcom, H., Fisk, L.A., Gloeckler, G., Ho, G.C., Kelley, J.S., Koehn, P.L., Lefevere, T.W., Livi, S.S., Lundgren, R.A., Raines, J.M., 2007. The energetic particle and plasma spectrometer instrument on the MESSENGER spacecraft. Space Science Reviews 131, 523–556. https://doi.org/10.1007/s11214-007-9272-5

Antoniadi, E.M., Antoniadi, Michel, E., 1934. La planete Mercure et la rotation des satellites; etude basee sur les resultats obtenus avec la grande lunette de l'observatoire de Meudon, pmrs. Paris.

Apollo Field Geology Investigation Team, 1973. Apollo 16 Exploration of Descartes: A Geologic Summary. Science 179, 62–69. https://doi.org/10.1126/science.179.4068.62

Asphaug, E., Reufer, A., 2014. Mercury and other iron-rich planetary bodies as relics of inefficient accretion. Nature Geoscience 7, 564–568. https://doi.org/10.1038/ngeo2189

Banks, M.E., Xiao, Z., Braden, S.E., Barlow, N.G., Chapman, C.R., Fassett, C.I., Marchi, S.S., 2017. Revised constraints on absolute age limits for Mercury's Kuiperian and Mansurian stratigraphic systems. Journal of Geophysical Research: Planets 122, 1010–1020. https://doi.org/10.1002/2016JE005254

Banks, M.E., Xiao, Z., Watters, T.R., Strom, R.G., Braden, S.E., Chapman, C.R., Solomon, S.C., Klimczak, C., Byrne, P.K., 2015. Duration of activity on lobate-scarp thrust faults on Mercury. Journal of Geophysical Research E: Planets 120, 1751–1762. https://doi.org/10.1002/2015JE004828

Barlow, J., Barisin, I., Rosser, N., Petley, D., Densmore, A., Wright, T., 2015. Seismically-induced mass movements and volumetric fluxes resulting from the 2010 Mw=7.2 earthquake in the Sierra Cucapah, Mexico. Geomorphology 230, 138–145. https://doi.org/10.1016/j.geomorph.2014.11.012

Barnouin, O.S., Zuber, M.T., Smith, D.E., Neumann, G.A., Herrick, R.R., Chappelow, J.E., Murchie, S.L., Prockter, L.M., 2012. The morphology of craters on Mercury: Results from MESSENGER flybys. Icarus 219, 414–427. https://doi.org/10.1016/j.icarus.2012.02.029

Bart, G.D., 2007. Comparison of small lunar landslides and martian gullies. Icarus 187, 417–421. https://doi.org/10.1016/j.icarus.2006.11.004

Becker, K.J., Robinson, M.S., Becker, T.L., Weller, L.A., Edmundson, K.L.,

Neumann, G.A., Perry, M.E., Solomon, S.C., 2016. First Global Digital Elevation Model of Mercury. 47th Lunar and Planetary Science Conference 47, Ab. #2959.

Benkhoff, J., Murakami, G., Baumjohann, W., Besse, S., Bunce, E., Casale, M., Cremonese, G., Glassmeier, K.H., Hayakawa, H., Hiesinger, H., Heyner, D., Huovelin, J., Hussmann, H., Iafolla, V., Iess, L., Kasaba, Y., Kobayashi, M., Milillo, A., Mitrofanov, I., Montagnon, E., Novara, M., Orsini, S., Quemerais, E., Reininghaus, U., Saito, Y., Santoli, F., Stramaccioni, D., Sutherland, O., Thomas, N., Yoshikawa, I., Zender, J., in press. BepiColombo - Mission Overview and Science Goals. Space Science Reviews 216.

Benkhoff, J., van Casteren, J., Hayakawa, H., Fujimoto, M., Laakso, H., Novara, M., Ferri, P., Middleton, H.R., Ziethe, R., 2010. BepiColombo-Comprehensive exploration of Mercury: Mission overview and science goals. Planetary and Space Science, Comprehensive Science Investigations of Mercury: The scientific goals of the joint ESA/JAXA mission BepiColombo 58, 2–20. https://doi.org/10.1016/j.pss.2009.09.020

Benz, W., Slattery, W.L., Cameron, A.G.W., 1988. Collisional stripping of Mercury's mantle. Icarus 74, 516–528. https://doi.org/10.1016/0019-1035(88)90118-2

Bickel, V., Aaron, J., Manconi, A., Loew, S., Mall, U., 2020. A global rockfall map of the Moon powered by AI and Big Data, in: EGU General Assembly. https://doi.org/10.5194/egusphere-egu2020-10003

Black, B.A., Manga, M., 2016. The eruptibility of magmas at Tharsis and Syrtis Major on Mars. Journal of Geophysical Research: Planets 121, 944–964. https://doi.org/10.1002/2016JE004998

Blair, D.M., Freed, A.M., Byrne, P.K., Klimczak, C., Prockter, L.M., Ernst, C.M., Solomon, S.C., Melosh, H.J., Zuber, M.T., 2013. The origin of graben and ridges in Rachmaninoff, Raditladi, and Mozart basins, Mercury. Journal of Geophysical Research: Planets 118, 47–58. https://doi.org/10.1029/2012JE004198

Blewett, D.T., Chabot, N.L., Denevi, B.W., Ernst, C.M., Head, J.W., Izenberg, N.R., Murchie, S.L., Solomon, S.C., Nittler, L.R., McCoy, T.J., Xiao, Z., Baker, D.M.H., Fassett, C.I., Braden, S.E., Oberst, J., Scholten, F., Preusker, F., Hurwitz, D.M., 2011. Hollows on Mercury: MESSENGER evidence for geologically recent volatile-related activity. Science 333, 1856–1859. https://doi.org/10.1126/science.1211681

Blewett, D.T., Ernst, C.M., Murchie, S.L., Vilas, F., 2018. Mercury's Hollows, in: Solomon, S.C., Nittler, L.R., Anderson, B.J. (Eds.), Mercury: The View after MESSENGER. Cambridge University Press. https://doi.org/10.1017/9781316650684

Blewett, D.T., Robinson, M.S., Denevi, B.W., Gillis-Davis, J.J., Head, J.W., Solomon, S.C., Holsclaw, G.M., McClintock, W.E., 2009. Multispectral images of Mercury from the first MESSENGER flyby: Analysis of global and regional color trends. Earth and Planetary Science Letters. https://doi.org/10.1016/j.epsl.2009.02.021

Blewett, D.T., Stadermann, A.C., Susorney, H.C., Ernst, C.M., Xiao, Z., Chabot, N.L., Denevi, B.W., Murchie, S.L., McCubbin, F.M., Kinczyk, M.J., Gillis-Davis, J.J., Solomon, S.C., 2016. Analysis of MESSENGER high-resolution images of Mercury's hollows and implications for hollow formation. Journal of Geophysical Research: Planets 121, 1798–1813. https://doi.org/10.1002/2016JE005070

Blewett, D.T., Vaughan, W.M., Xiao, Z., Chabot, N.L., Denevi, B.W., Ernst, C.M., Helbert, J., D'Amore, M., Maturilli, A., Head, J.W., Solomon, S.C., 2013.

Mercury's hollows: Constraints on formation and composition from analysis of geological setting and spectral reflectance. Journal of Geophysical Research: Planets 118, 1013–1032. https://doi.org/10.1029/2012JE004174

Braden, S.E., Stopar, J.D., Robinson, M.S., Lawrence, S.J., van der Bogert, C.H., Hiesinger, H., 2014. Evidence for basaltic volcanism on the Moon within the past 100 million years. Nature Geoscience 7, 787–791. https://doi.org/10.1038/ngeo2252

Brown, S.M., Elkins-Tanton, L.T., 2009. Compositions of Mercury's earliest crust from magma ocean models. Earth and Planetary Science Letters 286, 446–455. https://doi.org/10.1016/j.epsl.2009.07.010

Brunetti, M.T., Xiao, Z., Komatsu, G., Peruccacci, S., Guzzetti, F., 2015. Large rock slides in impact craters on the Moon and Mercury. Icarus 260, 289–300. https://doi.org/10.1016/j.icarus.2015.07.014

Buczkowski, D.L., Wyrick, D.Y., Iyer, K.A., Kahn, E.G., Scully, J.E.C., Nathues, A., Gaskell, R.W., Roatsch, T., Preusker, F., Schenk, P.M., Le Corre, L., Reddy, V., Yingst, R.A., Mest, S., Williams, D.A., Garry, W.B., Barnouin, O.S., Jaumann, R., Raymond, C.A., Russell, C.T., 2012. Large-scale troughs on Vesta: A signature of planetary tectonics. Geophysical Research Letters 39, L18205. https://doi.org/10.1029/2012GL052959

Bunce, E.J., Martindale, A., Lindsay, S., Muinonen, K., Rothery, D.A., Pearson, J., McDonnell, I., Thomas, C., Thornhill, J., Tikkanen, T., Feldman, C., Huovelin, J., Korpela, S., Esko, E., Lehtolainen, A., Treis, J., Majewski, P., Hilchenbach, M., Väisänen, T., Luttinen, A., Kohout, T., Penttilä, A., Bridges, J., Joy, K.H., Alcacera-Gil, M.A., Alibert, G., Anand, M., Bannister, N., Barcelo-Garcia, C., Bicknell, C., Blake, O., Bland, P., Butcher, G., Cheney, A., Christensen, U., Crawford, T., Crawford, I.A., Dennerl, K., Dougherty, M., Drumm, P., Fairbend, R., Genzer, M., Grande, M., Hall,

G.P., Hodnett, R., Houghton, P., Imber, S., Kallio, E., Lara, M.L., Balado Margeli, A., Mas-Hesse, M.J., Maurice, S., Milan, S., Millington-Hotze, P., Nenonen, S., Nittler, L., Okada, T., Ormö, J., Perez-Mercader, J., Poyner, R., Robert, E., Ross, D., Pajas-Sanz, M., Schyns, E., Seguy, J., Strüder, L., Vaudon, N., Viceira-Martín, J., Williams, H., Willingale, D., Yeoman, T., 2020. The BepiColombo Mercury Imaging X-Ray Spectrometer: Science Goals, Instrument Performance and Operations. Space Science Reviews 216, 126. https://doi.org/10.1007/s11214-020-00750-2

Byrne, P.K., Klimczak, C., Sengör, A.M.C., Solomon, S.C., Watters, T.R., Hauck, S.A., 2014. Mercury's global contraction much greater than earlier estimates. Nature Geoscience 7, 301–307. https://doi.org/10.1038/ngeo2097

Byrne, P.K., Klimczak, C., Williams, D.A., Hurwitz, D.M., Solomon, S.C., Head, J.W., Preusker, F., Oberst, J., 2013. An assemblage of lava flow features on Mercury. Journal of Geophysical Research E: Planets 118, 1303–1322. https://doi.org/10.1002/jgre.20052

Byrne, P.K., Ostrach, L.R., Fassett, C.I., Chapman, C.R., Denevi, B.W., Evans, A.J., Klimczak, C., Banks, M.E., Head, J.W., Solomon, S.C., 2016. Widespread effusive volcanism on Mercury likely ended by about 3.5 Ga. Geophysical Research Letters 43, 7408–7416. https://doi.org/10.1002/2016GL069412

Cameron, A.G.W., 1985. The partial volatilization of Mercury. Icarus 64, 285–294. https://doi.org/10.1016/0019-1035(85)90091-0

Carrier III, W.D., 1991. Physical Properties of the Lunar Surface. Lunar Sourcebook 475, 522–530.

Cavanaugh, J.F., Smith, J.C., Sun, X., Bartels, A.E., Ramos-Izquierdo, L., Krebs, D.J., McGarry, J.F., Trunzo, R., Novo-Gradac, A.M., Britt, J.L., Karsh, J., Katz, R.B., Lukemire, A.T., Szymkiewicz, R., Berry, D.L., Swinski, J.P., Neumann,

G.A., Zuber, M.T., Smith, D.E., 2007. The Mercury laser altimeter instrument for the MESSENGER mission. Space Science Reviews 131, 451–479. https://doi.org/10.1007/s11214-007-9273-4

Cedillo-Flores, Y., Treiman, A.H., Lasue, J., Clifford, S.M., 2011. CO2 gas fluidization in the initiation and formation of Martian polar gullies. Geophysical Research Letters 38, L21202. https://doi.org/10.1029/2011GL049403

Chabot, N.L., Ernst, C.M., Denevi, B.W., Harmon, J.K., Murchie, S.L., Blewett, D.T., Solomon, S.C., Zhong, E.D., 2012. Areas of permanent shadow in Mercury's south polar region ascertained by MESSENGER orbital imaging. Geophysical Research Letters 39, L09204. https://doi.org/10.1029/2012GL051526

Chabot, N.L., Ernst, C.M., Denevi, B.W., Nair, H., Deutsch, A.N., Blewett, D.T., Murchie, S.L., Neumann, G.A., Mazarico, E., Paige, D.A., Harmon, J.K., Head, J.W., Solomon, S.C., 2014. Images of surface volatiles in Mercury's polar craters acquired by the MESSENGER spacecraft. Geology 42, 1051–1054. https://doi.org/10.1130/G35916.1

Chandnani, M., Herrick, R.R., Kramer, G.Y., 2019. Geologic Investigation of Deep Simple Craters in the Lunar Simple-to-Complex Transition. Journal of Geophysical Research: Planets 2018JE005903. https://doi.org/10.1029/2018JE005903

Chapman, C.R., 1967. Optical evidence on the rotation of Mercury. Earth and Planetary Science Letters 3. https://doi.org/10.1016/0012-821x(67)90065-9

Chigira, M., Wu, X., Inokuchi, T., Wang, G., 2010. Landslides induced by the 2008 Wenchuan earthquake, Sichuan, China. Geomorphology 118, 225–238. https://doi.org/10.1016/j.geomorph.2010.01.003

Cintala, M.J., Grieve, R.A.F., 1998. Scaling impact melting and crater dimensions:Implications for the lunar cratering record. Meteoritics and Planetary Science 33, 889–912. https://doi.org/10.1111/j.1945-5100.1998.tb01695.x

Colombo, G., 1965. Rotational period of the planet Mercury. Nature 208, 575. https://doi.org/10.1038/208575a0

Connerney, J.E.P., Ness, N.F., 1988. Mercury's magnetic field and interior., Mercury. University of Arizona Press, Tucson, AZ.

Conway, S.J., Balme, M.R., Kreslavsky, M.A., Murray, J.B., Towner, M.C., 2015. The comparison of topographic long profiles of gullies on Earth to gullies on Mars: A signal of water on Mars. Icarus 253, 189–204. https://doi.org/10.1016/j.icarus.2015.03.009

Conway, S.J., de Haas, T., Harrison, T.N., 2019. Martian gullies: a comprehensive review of observations, mechanisms and insights from Earth analogues. Geological Society, London, Special Publications 467, 7–66. https://doi.org/10.1144/SP467.14

Crane, K.T., Klimczak, C., 2017. Timing and rate of global contraction on Mercury. Geophysical Research Letters 44, 3082–3089. https://doi.org/10.1002/2017GL072711

Cremonese, G., Capaccioni, F., Capria, M.T., Doressoundiram, A., Palumbo, P., Vincendon, M., Massironi, M., Debei, S., Zusi, M., Altieri, F., Amoroso, M., Aroldi, G., Baroni, M., Barucci, A., Bellucci, G., Benkhoff, J., Besse, S., Bettanini, C., Blecka, M., Borrelli, D., Brucato, J.R., Carli, C., Carlier, V., Cerroni, P., Cicchetti, A., Colangeli, L., Dami, M., Da Deppo, V., Della Corte, V., De Sanctis, M.C., Erard, S., Esposito, F., Fantinel, D., Ferranti, L., Ferri, F., Ficai Veltroni, I., Filacchione, G., Flamini, E., Forlani, G., Fornasier, S., Forni, O., Fulchignoni, M., Galluzzi, V., Gwinner, K., Ip, W., Jorda, L.,

Langevin, Y., Lara, L., Leblanc, F., Leyrat, C., Li, Y., Marchi, S., Marinangeli, L., Marzari, F., Mazzotta Epifani, E., Mendillo, M., Mennella, V., Mugnuolo, R., Muinonen, K., Naletto, G., Noschese, R., Palomba, E., Paolinetti, R., Perna, D., Piccioni, G., Politi, R., Poulet, F., Ragazzoni, R., Re, C., Rossi, M., Rotundi, A., Salemi, G., Sgavetti, M., Simioni, E., Thomas, N., Tommasi, L., Turella, A., Van Hoolst, T., Wilson, L., Zambon, F., Aboudan, A., Barraud, O., Bott, N., Borin, P., Colombatti, G., El Yazidi, M., Ferrari, S., Flahaut, J., Giacomini, L., Guzzetta, L., Lucchetti, A., Martellato, E., Pajola, M., Slemer, A., Tognon, G., Turrini, D., 2020. SIMBIO-SYS: Scientific Cameras and Spectrometer for the BepiColombo Mission. Space Science Reviews 216, 75. https://doi.org/10.1007/s11214-020-00704-8

Daniels, J.W., Neish, C.D., 2018. Impact Melt Emplacement on Mercury, in: 49th Lunar and Planetary Science Conference 19-23 March, 2018. The Woodlands, Houston, Texas, Ab. #1380.

Davies, M.E., Dornik, S.E., Gault, D.E., Strom, R.G., 1978. Atlas of Mercury. NASA Special Publication 423.

De Hon, R.A., Scott, D.H., Underwood Jr, J.R., 1981. Geologic Map of the Kuiper (H-6) Quadrangle of Mercury. United States Geological Survey, Geologic Investigations Series, Map I-1233.

Denevi, B.W., Ernst, C.M., Meyer, H.M., Robinson, M.S., Murchie, S.L., Whitten, J.L., Head, J.W., Watters, T.R., Solomon, S.C., Ostrach, L.R., Chapman, C.R., Byrne, P.K., Klimczak, C., Peplowski, P.N., 2013. The distribution and origin of smooth plains on Mercury 118, 891–907. https://doi.org/10.1002/jgre.20075

Denevi, B.W., Ernst, C.M., Prockter, L.M., Robinson, M.S., 2018. The Geologic History of Mercury, in: Solomon, S.C., Nittler, L.R., Anderson, B.J. (Eds.), Mercury: The View after MESSENGER. Cambridge University Press. https://doi.org/10.1017/9781316650684

Denevi, B.W., Robinson, M.S., Solomon, S.C., Murchie, S.L., Blewett, D.T., Domingue, D.L., McCoy, T.J., Ernst, C.M., Head, J.W., Watters, T.R., Chabot, N.L., 2009. The evolution of Mercury's crust: A global perspective from MESSENGER. Science 324, 613–618. https://doi.org/10.1126/science.1172226

Denevi, B. W., Seelos, F.P., Ernst, C.M., Keller, M.R., Chabot, N.L., Murchie, S.L., Domingue, D.L., Hash, C.D., Blewett, D.T., Denevi, B.W., Seelos, F.P., Ernst, C.M., Keller, M.R., Chabot, N.L., Murchie, S.L., Domingue, D.L., Hash, C.D., Blewett, D.T., 2016. Final Calibration and Multispectral Map Products from the Mercury Dual Imaging System Wide-Angle Camera. 47th Lunar and Planetary Science Conference ab# 1264.

Dunne, J.A., Burgess, E., 1978. The voyage of Mariner 10 : mission to Venus and Mercury, NASA Special Publication. NASA, Washington, DC, USA.

Ebel, D.S., Alexander, C.M.O., 2011. Equilibrium condensation from chondritic porous IDP enriched vapor: Implications for Mercury and enstatite chondrite origins. Planetary and Space Science 59, 1888–1894. https://doi.org/10.1016/j.pss.2011.07.017

Ernst, C.M., Chabot, N.L., Barnouin, O.S., 2018. Examining the Potential Contribution of the Hokusai Impact to Water Ice on Mercury. Journal of Geophysical Research: Planets 123, 2628–2646. https://doi.org/10.1029/2018JE005552

Ernst, C.M., Denevi, B.W., Ostrach, L.R., 2017. Updated Absolute Age Estimates for the Tolstoj and Caloris Basins, Mercury, 48th Lunar and Planetary Science Conference. The Woodlands, Houston, Texas, Ab#. 2934.

Evans, A.J., Brown, S.M., Solomon, S.C., 2015. CHARACTERISTICS OF EARLY MANTLE CONVECTION AND MELTING ON MERCURY, in: LPI. The

Woodlands, Houston, Texas, Ab. #2414.

Evans, L.G., Peplowski, P.N., Rhodes, E.A., Lawrence, D.J., McCoy, T.J., Nittler, L.R., Solomon, S.C., Sprague, A.L., Stockstill-Cahill, K.R., Starr, R.D., Weider, S.Z., Boynton, W. V., Hamara, D.K., Goldsten, J.O., 2012. Major-element abundances on the surface of Mercury: Results from the messenger gamma-ray spectrometer. Journal of Geophysical Research: Planets 117, E00L07. https://doi.org/10.1029/2012JE004178

Fassett, C.I., 2016. Ames stereo pipeline-derived digital terrain models of Mercury from MESSENGER stereo imaging. Planetary and Space Science 134, 19–28. https://doi.org/10.1016/j.pss.2016.10.001

Fassett, C.I., Crowley, M.C., Leight, C., Dyar, M.D., Minton, D.A., Hirabayashi, M., Thomson, B.J., Watters, W.A., 2017. Evidence for rapid topographic evolution and crater degradation on Mercury from simple crater morphometry. Geophysical Research Letters 44, 5326–5335. https://doi.org/10.1002/2017GL073769

Fassett, C.I., Head, J.W., Baker, D.M.H., Zuber, M.T., Smith, D.E., Neumann, G.A., Solomon, S.C., Klimczak, C., Strom, R.G., Chapman, C.R., Prockter, L.M., Phillips, R.J., Oberst, J., Preusker, F., 2012. Large impact basins on Mercury: Global distribution, characteristics, and modification history from MESSENGER orbital data. Journal of Geophysical Research E: Planets 117, E00L08. https://doi.org/10.1029/2012JE004154

Fassett, C.I., Kadish, S.J., Head, J.W., Solomon, S.C., Strom, R.G., 2011. The global population of large craters on Mercury and comparison with the Moon. Geophysical Research Letters 38, L10202. https://doi.org/10.1029/2011GL047294

Fassett, C.I., Thomson, B.J., 2014. Crater degradation on the lunar maria: Topographic diffusion and the rate of erosion on the Moon. Journal of

Geophysical Research E: Planets 119, 2255–2271. https://doi.org/10.1002/2014JE004698

Fegan, E.R., 2018. Crustal History Indicators on Mercury. PhD Thesis, The Open University.

Fegan, E.R., Rothery, D.A., Marchi, S., Massironi, M., Conway, S.J., Anand, M., 2017. Late movement of basin-edge lobate scarps on Mercury. Icarus 288, 226–234. https://doi.org/10.1016/j.icarus.2017.01.005

Ferrari, S., Massironi, M., Marchi, S., Byrne, P.K., Klimczak, C., Martellato, E., Cremonese, G., 2015. Age relationships of the Rembrandt basin and Enterprise Rupes, Mercury. Geological Society, London, Special Publications 401, 159–172. https://doi.org/10.1144/SP401.20

Fortezzo, C.M., Spudis, P.D., Harrel, S.L., 2020. RELEASE OF THE DIGITAL UNIFIED GLOBAL GEOLOGIC MAP OF THE MOON AT 1:5,000,000-SCALE. 51st Lunar and Planetary Science Conference, Ab. #2760.

Fraser, G.W., Carpenter, J.D., Rothery, D.A., Pearson, J.F., Martindale, A., Huovelin, J., Treis, J., Anand, M., Anttila, M., Ashcroft, M., Benkoff, J., Bland, P., Bowyer, A., Bradley, A., Bridges, J., Brown, C., Bulloch, C., Bunce, E.J., Christensen, U., Evans, M., Fairbend, R., Feasey, M., Giannini, F., Hermann, S., Hesse, M., Hilchenbach, M., Jorden, T., Joy, K., Kaipiainen, M., Kitchingman, I., Lechner, P., Lutz, G., Malkki, A., Muinonen, K., Näränen, J., Portin, P., Prydderch, M., Juan, J.S., Sclater, E., Schyns, E., Stevenson, T.J., Strüder, L., Syrjasuo, M., Talboys, D., Thomas, P., Whitford, C., Whitehead, S., 2010. The Mercury imaging X-ray spectrometer (MIXS) on BepiColombo. Planetary and Space Science 58, 79–95. https://doi.org/10.1016/j.pss.2009.05.004

Galluzzi, V., Carli, C., Zambon, F., Giacomini, L., Guzzetta, L., Ferranti, L., Palumbo, P., 2017a. The Intermediate Plains of Mercury: considerations

on a debated unit, in: European Planetary Science Congress 2017. Ab. #976.

Galluzzi, V., Di Achille, G., Ferranti, L., Popa, C., Palumbo, P., 2015. Faulted craters as indicators for thrust motions on Mercury. Geological Society, London, Special Publications 401, 313–325. https://doi.org/10.1144/SP401.17

Galluzzi, V., Giacomini, L., Lucchetti, A., Pajola, M., Palumbo, P., Cremonese, G., 2018. Bedrock layering revealed by hollows on Mercury, European Planetary Science Congress 2018, held 16-21 September 2018 at TU Berlin, Berlin, Germany, id.EPSC2018-1186.

Galluzzi, V., Guzzetta, L., Ferranti, L., Di Achille, G., Rothery, D.A., Palumbo, P., 2016a. Geology of the Victoria quadrangle (H02), Mercury. Journal of Maps 12, 227–238. https://doi.org/10.1080/17445647.2016.1193777

Galluzzi, V, Guzzetta, L., Mancinelli, P., Giacomini, L., Ferranti, L., Massironi, M., Palumbo, P., Pauselli, C., Rothery, D.A., 2016b. MERGING OF NEW 1:3M MERCURY GEOLOGIC MAPS AT NORTHERN MID-LATITUDES: STATUS REPORT. 47th Lunar and Planetary Science Conference, The Woodlands, TX, USA. Ab.# 2119

Galluzzi, V., Guzzetta, L., Mancinelli, P., Giacomini, L., Malliband, C.C., Mosca, A., Wright, J., Ferranti, L., Massironi, M., Pauselli, C., Rothery, D.A., Palumbo, P., 2017b. The 1:3M geologic map of Mercury: progress and updates, in: EGU General Assembly.

Giacomini, L., Massironi, M., Marchi, S., Fassett, C.I., Di Achille, G., Cremonese, G., 2015. Age dating of an extensive thrust system on Mercury: implications for the planet's thermal evolution. Geological Society, London, Special Publications 401, 291–311. https://doi.org/10.1144/SP401.21

Giese, B., Neukum, G., Roatsch, T., Denk, T., Porco, C.C., 2006. Topographic modeling of Phoebe using Cassini images. Planetary and Space Science 54, 1156–1166. https://doi.org/10.1016/J.PSS.2006.05.027

Goldsten, J.O., Rhodes, E.A., Boynton, W. V., Feldman, W.C., Lawrence, D.J., Trombka, J.I., Smith, D.M., Evans, L.G., White, J., Madden, N.W., Berg, P.C., Murphy, G.A., Gurnee, R.S., Strohbehn, K., Williams, B.D., Schaefer, E.D., Monaco, C.A., Cork, C.P., Del Eckels, J., Miller, W.O., Burks, M.T., Hagler, L.B., Deteresa, S.J., Witte, M.C., 2007. The MESSENGER gamma-ray and neutron spectrometer. Space Science Reviews 131, 339–391. https://doi.org/10.1007/s11214-007-9262-7

Gomes, R., Levison, H.F., Tsiganis, K., Morbidelli, A., 2005. Origin of the cataclysmic Late Heavy Bombardment period of the terrestrial planets. Nature 435, 466–469. https://doi.org/10.1038/nature03676

Goudge, T.A., Head, J.W., Kerber, L., Blewett, D.T., Denevi, B.W., Domingue, D.L., Gillis-Davis, J.J., Gwinner, K., Helbert, J., Holsclaw, G.M., Izenberg, N.R., Klima, R.L., McClintock, W.E., Murchie, S.L., Neumann, G.A., Smith, D.E., Strom, R.G., Xiao, Z., Zuber, M.T., Solomon, S.C., 2014. Global inventory and characterization of pyroclastic deposits on Mercury: New insights into pyroclastic activity from MESSENGER orbital data 119, 635–658. https://doi.org/10.1002/2013JE004480

Grier, J.A., Rivkin, A.S., 2019. Regolith and Dust: Movement and Transport, in: Airless Bodies of the Inner Solar System. Elsevier, pp. 165–185. https://doi.org/10.1016/b978-0-12-809279-8.00008-1

Grolier, M.J., Boyce, J.M., 1984. Geologic map of the Borealis region (H-1) of Mercury. USGS Miscellaneous investigations series Map I--1660 21.

Guest, J.E., Greeley, R., 1983. Geologic map of the Shakespeare (H-3) quadrangle of Mercury. United States Geological Survey, Miscellaneous

Investigations Series, Map I-1408.

Guzzetta, L., Galluzzi, V., Ferranti, L., Palumbo, P., 2017. Geology of the Shakespeare quadrangle (H03), Mercury. Journal of Maps 13, 227–238. https://doi.org/10.1080/17445647.2017.1290556

Hargitai, H., 2015. Spur-and-Gully, in: Encyclopedia of Planetary Landforms. Springer New York, New York, NY, pp. 2046–2052. https://doi.org/10.1007/978-1-4614-3134-3_634

Hawkins, S.E., Boldt, J.D., Darlington, E.H., Espiritu, R., Gold, R.E., Gotwols, B., Grey, M.P., Hash, C.D., Hayes, J.R., Jaskulek, S.E., Kardian, C.J., Keller, M.R., Malaret, E.R., Murchie, S.L., Murphy, P.K., Peacock, K., Prockter, L.M., Reiter, R.A., Robinson, M.S., Schaefer, E.D., Shelton, R.G., Sterner, R.E., Taylor, H.W., Watters, T.R., Williams, B.D., 2007. The Mercury Dual Imaging System on the MESSENGER Spacecraft. Space Science Reviews 131, 247–338. https://doi.org/10.1007/s11214-007-9266-3

Head, J.W., Chapman, C.R., Domingue, D.L., Hawkins, S.E., McClintock, W.E., Murchie, S.L., Prockter, L.M., Robinson, M.S., Strom, R.G., Watters, T.R., 2007. The geology of Mercury: The view prior to the MESSENGER mission. Space Science Reviews 131, 41–84. https://doi.org/10.1007/s11214-007-9263-6

Head, J.W., Chapman, C.R., Strom, R.G., Fassett, C.I., Denevi, B.W., Blewett, D.T., Ernst, C.M., Watters, T.R., Solomon, S.C., Murchie, S.L., Prockter, L.M., Chabot, N.L., Gillis-Davis, J.J., Whitten, J.L., Goudge, T.A., Baker, D.M.H., Hurwitz, D.M., Ostrach, L.R., Xiao, Z., Merline, W.J., Kerber, L., Dickson, J.L., Oberst, J., Byrne, P.K., Klimczak, C., Nittler, L.R., 2011. Flood volcanism in the northern high latitudes of Mercury revealed by MESSENGER. Science 333, 1853–1856. https://doi.org/10.1126/science.1211997

Head, J.W., Murchie, S.L., Prockter, L.M., Robinson, M.S., Solomon, S.C., Strom, R.G., Chapman, C.R., Watters, T.R., McClintock, W.E., Blewett, D.T., Gillis-Davis, J.J., 2008. Volcanism on Mercury: Evidence from the First MESSENGER Flyby. Science 321, 69–72. https://doi.org/10.1126/science.1159256

Head, James W, Murchie, S.L., Prockter, L.M., Solomon, S.C., Chapman, C.R., Strom, R.G., Watters, T.R., Blewett, D.T., Gillis-Davis, J.J., Fassett, C.I., Dickson, J.L., Morgan, G.A., Kerber, L., 2009. Volcanism on Mercury: Evidence from the first MESSENGER flyby for extrusive and explosive activity and the volcanic origin of plains. Earth and Planetary Science Letters, MESSENGER's First Flyby of Mercury 285, 227–242. https://doi.org/10.1016/j.epsl.2009.03.007

Head, James W., Murchie, S.L., Prockter, L.M., Solomon, S.C., Strom, R.G., Chapman, C.R., Watters, T.R., Blewett, D.T., Gillis-Davis, J.J., Fassett, C.I., Dickson, J.L., Hurwitz, D.M., Ostrach, L.R., 2009. Evidence for intrusive activity on Mercury from the first MESSENGER flyby. Earth and Planetary Science Letters 285, 251–262. https://doi.org/10.1016/j.epsl.2009.03.008

Head, J.W., Wilson, L., 1992. Lunar mare volcanism: Stratigraphy, eruption conditions, and the evolution of secondary crusts. Geochimica et Cosmochimica Acta 56, 2155–2175. https://doi.org/10.1016/0016-7037(92)90183-J

Helbert, J., Maturilli, A., D'Amore, M., 2013. Visible and near-infrared reflectance spectra of thermally processed synthetic sulfides as a potential analog for the hollow forming materials on Mercury. Earth and Planetary Science Letters 369–370, 233–238. https://doi.org/10.1016/j.epsl.2013.03.045

Hiesinger, H., Helbert, J., Alemanno, G., Bauch, K.E., D'Amore, M., Maturilli, A., Morlok, A., Reitze, M.P., Stangarone, C., Stojic, A.N., Varatharajan, I.,

Weber, I., 2020. Studying the Composition and Mineralogy of the Hermean Surface with the Mercury Radiometer and Thermal Infrared Spectrometer (MERTIS) for the BepiColombo Mission: An Update. Space Science Reviews 216, 110. https://doi.org/10.1007/s11214-020-00732-4

Hill, G.W., 1898. Note on the mass of Mercury. The Astronomical Journal 19, 157. https://doi.org/10.1086/103022

Hughson, K.H.G., Russell, C.T., Williams, D.A., Buczkowski, D.L., Mest, S.C., Pasckert, J.H., Scully, J.E.C., Combe, J.-P., Platz, T., Ruesch, O., Preusker, F., Jaumann, R., Nass, A., Roatsch, T., Nathues, A., Schaefer, M., Schmidt, B.E., Chilton, H.T., Ermakov, A., Singh, S., McFadden, L.A., Raymond, C.A., 2018. The Ac-5 (Fejokoo) quadrangle of Ceres: Geologic map and geomorphological evidence for ground ice mediated surface processes. Icarus 316, 63–83. https://doi.org/10.1016/J.ICARUS.2017.09.035

James, P.B., Zuber, M.T., Phillips, R.J., Solomon, S.C., 2015. Support of long-wavelength topography on Mercury inferred from MESSENGER measurements of gravity and topography. Journal of Geophysical Research: Planets 120, 287–310. https://doi.org/10.1002/2014JE004713

Joy, K.H., Kring, D.A., Bogard, D.D., Mckay, D.S., Zolensky, M.E., 2011. Re-examination of the formation ages of the Apollo 16 regolith breccias. Geochimica et Cosmochimica Acta 75, 7208–7225. https://doi.org/10.1016/j.gca.2011.09.018

Jozwiak, L.M., Head, J.W., Wilson, L., 2018. Explosive volcanism on Mercury: Analysis of vent and deposit morphology and modes of eruption. Icarus 302, 191–212. https://doi.org/10.1016/j.icarus.2017.11.011

Kain, K.R., Koppa, R.J., Olmstead, J.G., Montgomery, T.O., 1971. Apollo 16 Lunar Surface procedures, NASA Manned Spacecraft Center.

Kerber, L., Head, J.W., Blewett, D.T., Solomon, S.C., Wilson, L., Murchie, S.L.,

Robinson, M.S., Denevi, B.W., Domingue, D.L., 2011. The global distribution of pyroclastic deposits on Mercury: The view from MESSENGER flybys 1-3. Planetary and Space Science 59, 1895–1909. https://doi.org/10.1016/j.pss.2011.03.020

Kerber, L., Head, J.W., Solomon, S.C., Murchie, S.L., Blewett, D.T., Wilson, L., 2009. Explosive volcanic eruptions on Mercury: Eruption conditions, magma volatile content, and implications for interior volatile abundances. Earth and Planetary Science Letters, MESSENGER's First Flyby of Mercury 285, 263–271. https://doi.org/10.1016/j.epsl.2009.04.037

Kinczyk, M.J., Prockter, L.M., Byrne, P.K., Susorney, H.C.M., Chapman, C.R., 2020. A morphological evaluation of crater degradation on Mercury: Revisiting crater classification with MESSENGER data. Icarus 341, 113637. https://doi.org/10.1016/j.icarus.2020.113637

King, J.S., Scott, D.H., 1990. Geologic map of the Beethoven quadrangle of Mercury. USGS Miscellaneous investigations series Map I--2048.

King, S.D., 2008. Pattern of lobate scarps on Mercury's surface reproduced by a model of mantle convection. Nature Geoscience 1, 229–232. https://doi.org/10.1038/ngeo152

Kleinhans, M.G., Markies, H., de Vet, S.J., in 't Veld, A.C., Postema, F.N., 2011. Static and dynamic angles of repose in loose granular materials under reduced gravity. Journal of Geophysical Research 116, E11004. https://doi.org/10.1029/2011JE003865

Klima, R.L., Denevi, B.W., Ernst, C.M., Murchie, S.L., Peplowski, P.N., 2018. Global Distribution and Spectral Properties of Low-Reflectance Material on Mercury. Geophysical Research Letters 45, 2945–2953. https://doi.org/10.1002/2018GL077544

Klimczak, C., Crane, K.T., Habermann, M.A., Byrne, P.K., 2018. The spatial distribution of Mercury's pyroclastic activity and the relation to lithospheric weaknesses. Icarus 315, 115–123. https://doi.org/10.1016/j.icarus.2018.06.020

Klimczak, C., Ernst, C.M., Byrne, P.K., Solomon, S.C., Watters, T.R., Murchie, S.L., Preusker, F., Balcerski, J.A., 2013. Insights into the subsurface structure of the Caloris basin, Mercury, from assessments of mechanical layering and changes in long-wavelength topography. Journal of Geophysical Research: Planets 118, 2030–2044. https://doi.org/10.1002/jgre.20157

Kokelaar, B.P., Bahia, R.S., Joy, K.H., Viroulet, S., Gray, J.M.N.T., 2017. Granular avalanches on the Moon: Mass-wasting conditions, processes, and features. Journal of Geophysical Research: Planets 122, 1893–1925. https://doi.org/10.1002/2017JE005320

Kreslavsky, M.A., Head, J.W., Neumann, G.A., Zuber, M.T., Smith, D.E., 2014. Kilometer-scale topographic roughness of Mercury: Correlation with geologic features and units. Geophysical Research Letters 41, 8245–8251. https://doi.org/10.1002/2014GL062162

Kreslavsky, M.A., Zharkova, A.Y., Head, J.W., 2018a. Meter-Scale Surface Textures on Mercury: Comparison with the Moon. Lunar and Planetary Science Conference, Ab. #1394.

Kreslavsky, M.A., Zharkova, A.Y., Head, J.W., 2018b. Decameter-Scale Regolith Textures on Mercury. Mercury: Current and Future Science of the Innermost Planet, Ab. #6050.

Krohn, K., Jaumann, R., Otto, K., Hoogenboom, T., Wagner, R., Buczkowski, D.L., Garry, B., Williams, D.A., Yingst, R.A., Scully, J., De Sanctis, M.C., Kneissl, T., Schmedemann, N., Kersten, E., Stephan, K., Matz, K.-D.,

Pieters, C.M., Preusker, F., Roatsch, T., Schenk, P., Russell, C.T., Raymond, C.A., 2014. Mass movement on Vesta at steep scarps and crater rims. Icarus 244, 120–132. https://doi.org/10.1016/J.ICARUS.2014.03.013

Kruss, M., Wurm, G., 2018. Seeding the Formation of Mercurys: An Iron-sensitive Bouncing Barrier in Disk Magnetic Fields. The Astrophysical Journal 869, 45. https://doi.org/10.3847/1538-4357/aaec78

Lawrence, D.J., 2017. A tale of two poles: Toward understanding the presence, distribution, and origin of volatiles at the polar regions of the Moon and Mercury. Journal of Geophysical Research: Planets 122, 21–52. https://doi.org/10.1002/2016JE005167@10.1002/(ISSN)2169-9100.JGRE25

Le Feuvre, M., Wieczorek, M.A., 2011. Nonuniform cratering of the Moon and a revised crater chronology of the inner Solar System. Icarus 214, 1–20. https://doi.org/10.1016/j.icarus.2011.03.010

Lucchetti, A., Pajola, M., Galluzzi, V., Giacomini, L., Carli, C., Cremonese, G., Marzo, G.A., Ferrari, S., Massironi, M., Palumbo, P., 2018. Mercury Hollows as Remnants of Original Bedrock Materials and Devolatilization Processes: A Spectral Clustering and Geomorphological Analysis. Journal of Geophysical Research: Planets 123, 2365–2379. https://doi.org/10.1029/2018JE005722

Lyttleton, R.A., 1969. On the internal structures of Mercury and Venus. Astrophysics and Space Science 5, 18–35. https://doi.org/10.1007/BF00653933

Malin, M.C., 1976. Observations of intercrater plains on Mercury. Geophysical Research Letters 3, 581–584. https://doi.org/10.1029/GL003i010p00581

Malliband, C.C., Rothery, D.A., Balme, M.R., Conway, S.J., 2018. Small smooth units ('young' lavas?) abutting lobate scarps on Mercury. Mercury:

Current and Future Science 2018, Ab. #6092.

Man, B., Rothery, D.A., Balme, M.R., Conway, S.J., Wright, J., 2020. Geological Mapping of the Neruda Quadrange (H13) of Mercury. Planetary Geological Mappers Meeting, Ab. #7028.

Mancinelli, P., Minelli, F., Pauselli, C., Federico, C., 2016. Geology of the Raditladi quadrangle, Mercury (H04). Journal of Maps 12, 190–202. https://doi.org/10.1080/17445647.2016.1191384

Marchi, S., Chapman, C.R., Fassett, C.I., Head, J.W., Bottke, W.F., Strom, R.G., 2013. Global resurfacing of Mercury 4.0-4.1 billion years ago by heavy bombardment and volcanism. Nature 499, 59–61. https://doi.org/10.1038/nature12280

Marchi, S., Massironi, M., Cremonese, G., Martellato, E., Giacomini, L., Prockter, L., 2011. The effects of the target material properties and layering on the crater chronology: The case of Raditladi and Rachmaninoff basins on Mercury. Planetary and Space Science 59, 1968–1980. https://doi.org/10.1016/j.pss.2011.06.007

Marchi, S., Mottola, S., Cremonese, G., Massironi, M., Martellato, E., 2009. A NEW CHRONOLOGY FOR THE MOON AND MERCURY. The Astronomical Journal 137, 4936–4948. https://doi.org/10.1088/0004-6256/137/6/4936

Matsuyama, I., Nimmo, F., 2009. Gravity and tectonic patterns of Mercury: Effect of tidal deformation, spin-orbit resonance, nonzero eccentricity, despinning, and reorientation. Journal of Geophysical Research 114, E01010. https://doi.org/10.1029/2008JE003252

McCauley, J.F., Guest, J.E., Schaber, G.G., Trask, N.J., Greeley, R., 1981. Stratigraphy of the Caloris basin, Mercury. Icarus 47, 184–202. https://doi.org/10.1016/0019-1035(81)90166-4

McClintock, W.E., Lankton, M.R., 2007. The Mercury atmospheric and surface

composition spectrometer for the MESSENGER mission. Space Science Reviews 131, 481–521. https://doi.org/10.1007/s11214-007-9264-5

McGill, G.E., King, E.A., 1983. Geologic map of the Victoria (H-2) quadrangle of Mercury. United States Geological Survey, Miscellaneous Investigations Series, Map I-1409.

Melosh, H.J., 1977. Global tectonics of a despun planet. Icarus 31, 221–243. https://doi.org/10.1016/0019-1035(77)90035-5

Michel, N.C., Hauck, S.A., Solomon, S.C., Phillips, R.J., Roberts, J.H., Zuber, M.T., 2013. Thermal evolution of Mercury as constrained by MESSENGER observations. Journal of Geophysical Research E: Planets 118, 1033–1044. https://doi.org/10.1002/jgre.20049

Mitrofanov, I.G., Kozyrev, A.S., Konovalov, A., Litvak, M.L., Malakhov, A.A., Mokrousov, M.I., Sanin, A.B., Tret'ykov, V.I., Vostrukhin, A. V., Bobrovnitskij, Y.I., Tomilina, T.M., Gurvits, L., Owens, A., 2010. The Mercury Gamma and Neutron Spectrometer (MGNS) on board the Planetary Orbiter of the BepiColombo mission. Planetary and Space Science 58, 116–124. https://doi.org/10.1016/j.pss.2009.01.005

Murakami, G., Hayakawa, H., Ogawa, H., Matsuda, S., Seki, T., Kasaba, Y., Saito, Y., Yoshikawa, I., Kobayashi, M., Baumjohann, W., Matsuoka, A., Kojima, H., Yagitani, S., Moncuquet, M., Wahlund, J.-E., Delcourt, D., Hirahara, M., Barabash, S., Korablev, O., Fujimoto, M., 2020. Mio—First Comprehensive Exploration of Mercury's Space Environment: Mission Overview. Space Science Reviews 216, 113. https://doi.org/10.1007/s11214-020-00733-3

Murchie, S.L., Klima, R.L., Denevi, B.W., Ernst, C.M., Keller, M.R., Domingue, D.L., Blewett, D.T., Chabot, N.L., Hash, C.D., Malaret, E., Izenberg, N.R., Vilas, F., Nittler, L.R., Gillis-Davis, J.J., Head, J.W., Solomon, S.C., 2015. Orbital multispectral mapping of Mercury with the MESSENGER Mercury

Dual Imaging System: Evidence for the origins of plains units and low-reflectance material. Icarus 254, 287–305. https://doi.org/10.1016/j.icarus.2015.03.027

Murchie, S.L., Watters, T.R., Robinson, M.S., Head, J.W., Strom, R.G., Chapman, C.R., Solomon, S.C., McClintock, W.E., Prockter, L.M., Domingue, D.L., Blewett, D.T., 2008. Geology of the Caloris Basin, Mercury: A View from MESSENGER. Science 321, 73–76. https://doi.org/10.1126/science.1159261

Murray, B.C., Strom, R.G., Trask, N.J., Gault, D.E., 1975. Surface history of Mercury; implications for terrestrial planets. Journal of Geophysical Research 80, 2508–2514. https://doi.org/10.1029/JB080i017p02508

Namur, O., Charlier, B., 2017. Silicate mineralogy at the surface of Mercury. Nature Geoscience 10, 9–13. https://doi.org/10.1038/ngeo2860

Ness, N.F., Behannon, K.W., Lepping, R.P., Whang, Y.C., 1975. Magnetic field of Mercury confirmed. Nature 255, 204–205. https://doi.org/10.1038/255204a0

Neuffer, D.P., Schultz, R.A., 2006. Mechanisms of slope failure in Valles Marineris, Mars. Quarterly Journal of Engineering Geology and Hydrogeology 39, 227–240. https://doi.org/10.1144/1470-9236/05-042

Neumann, G.A., Cavanaugh, J.F., Sun, X., Mazarico, E.M., Smith, D.E., Zuber, M.T., Mao, D., Paige, D.A., Solomon, S.C., Ernst, C.M., Barnouin, O.S., 2013a. Bright and dark polar deposits on Mercury: Evidence for surface volatiles. Science 339, 296–300. https://doi.org/10.1126/science.1229764

Neumann, G.A., Cavanaugh, J.F., Sun, X., Mazarico, E.M., Smith, D.E., Zuber, M.T., Mao, D., Paige, D.A., Solomon, S.C., Ernst, C.M., Barnouin, O.S., 2013b. Bright and dark polar deposits on Mercury: Evidence for surface volatiles. Science 339, 296–300. https://doi.org/10.1126/science.1229764

Neumann, W., Breuer, D., Spohn, T., 2014. Differentiation of Vesta: Implications for a shallow magma ocean. Earth and Planetary Science Letters 395, 267–280. https://doi.org/10.1016/j.epsl.2014.03.033

Nittler, L.R., Starr, R.D., Weider, S.Z., McCoy, T.J., Boynton, W. V., Ebel, D.S., Ernst, C.M., Evans, L.G., Goldsten, J.O., Hamara, D.K., Lawrence, D.J., McNutt, R.L., Schlemm, C.E., Solomon, S.C., Sprague, A.L., 2011. The major-element composition of Mercury's surface from MESSENGER X-ray spectrometry. Science 333, 1847–1850. https://doi.org/10.1126/science.1211567

Norman, M.D., Duncan, R.A., Huard, J.J., 2010. Imbrium provenance for the Apollo 16 Descartes terrain: Argon ages and geochemistry of lunar breccias 67016 and 67455. Geochimica et Cosmochimica Acta 74, 763–783. https://doi.org/10.1016/j.gca.2009.10.024

Oberbeck, V.R., 1975. The role of ballistic erosion and sedimentation in lunar stratigraphy. Reviews of Geophysics 13, 337. https://doi.org/10.1029/RG013i002p00337

Oberbeck, V.R., Horz, F., Morrison, R.H., Quaide, W.L., 1973. EMPLACEMENT OF THE CAYLEY FORMATION, NASA Technical Memorandum X-62,302.

Ogawa, M., 2016. Evolution of the interior of Mercury influenced by coupled magmatism-mantle convection system and heat flux from the core. Journal of Geophysical Research: Planets 121, 118–136. https://doi.org/10.1002/2015JE004832

Öhman, T., Aittola, M., Kostama, V.P., Hyvärinen, M., Raitala, J., 2006. Polygonal impact craters in the Argyre region, Mars: Evidence for influence of target structure on the final crater morphology. Meteoritics and Planetary Science 41, 1163-1173. https://doi.org/10.1111/j.1945-5100.2006.tb00513.x

Orgel, C., Fassett, C.I., Michael, G., Riedel, C., Bogert, C.H., Hiesinger, H., 2020. Re-examination of the Population, Stratigraphy, and Sequence of Mercurian Basins: Implications for Mercury's Early Impact History and Comparison With the Moon. Journal of Geophysical Research: Planets 125. https://doi.org/10.1029/2019JE006212

Osinski, G.R., Tornabene, L.L., Grieve, R.A.F., 2011. Impact ejecta emplacement on terrestrial planets. Earth and Planetary Science Letters 310, 167–181. https://doi.org/10.1016/j.epsl.2011.08.012

Ostrach, L.R., Mest, S.C., Prockter, L.M., Petro, N.E., Byrne, P.K., 2019. 2019 Update on the geologic map of the Borealis quadrangle (H-1) on Mercury. Planetary Geologic Mappers Meeting, Ab. #7027.

Ostrach, L.R., Robinson, M.S., Whitten, J.L., Fassett, C.I., Strom, R.G., Head, J.W., Solomon, S.C., 2015. Extent, age, and resurfacing history of the northern smooth plains on Mercury from MESSENGER observations. Icarus 250, 602–622. https://doi.org/10.1016/j.icarus.2014.11.010

Otto, K.A., Jaumann, R., Krohn, K., Matz, K.-D., Preusker, F., Roatsch, T., Schenk, P., Scholten, F., Stephan, K., Raymond, C.A., Russell, C.T., 2013. Mass-wasting features and processes in Vesta's south polar basin Rheasilvia. Journal of Geophysical Research: Planets 118, 2279–2294. https://doi.org/10.1002/2013JE004333

Paige, D.A., Siegler, M.A., Harmon, J.K., Neumann, G.A., Mazarico, E.M., Smith, D.E., Zuber, M.T., Harju, E., Delitsky, M.L., Solomon, S.C., 2013. Thermal stability of volatiles in the north polar region of Mercury. Science 339, 300–303. https://doi.org/10.1126/science.1231106

Pasquon, K., Gargani, J., Massé, M., Vincendon, M., Conway, S.J., Séjourné, A., Jomelli, V., Balme, M.R., Lopez, S., Guimpier, A., 2019. Present-day development of gully-channel sinuosity by carbon dioxide gas supported

flows on Mars. Icarus 329, 296–313. https://doi.org/10.1016/j.icarus.2019.03.034

Pegg, R.D.L., Rothery, D.A., Balme, M.R., Conway, S.J., 2019a. Explosive Vents on Mercury: Commonplace Multiple Eruptions and Their Implications, in: 50th Lunar and Planetary Science Conference. The Woodlands, Houston, Texas, p. LPIContrib.No.2132, Ab. #1273.

Pegg, R.D.L., Rothery, D.A., Balme, M.R., Conway, S.J., 2019b. Geological Mapping of the Debussy Quadrangle (H-14) of Mercury, Preliminary Results, 50th Lunar and Planetary Science Conference. The Woodlands, Houston, Texas, Ab. #1271.

Peplowski, P.N., Evans, L.G., Hauck, S.A., McCoy, T.J., Boynton, W. V., Gillis-Davis, J.J., Ebel, D.S., Goldsten, J.O., Hamara, D.K., Lawrence, D.J., McNutt, R.L., Nittler, L.R., Solomon, S.C., Rhodes, E.A., Sprague, A.L., Starr, R.D., Stockstill-Cahill, K.R., Hurwitz, D.M., 2011. Radioactive elements on Mercury's surface from MESSENGER: Implications for the planet's formation and evolution. Science 333, 1850–2. https://doi.org/10.1126/science.1211576

Peplowski, P.N., Klima, R.L., Lawrence, D.J., Ernst, C.M., Denevi, B.W., Frank, E.A., Goldsten, J.O., Murchie, S.L., Nittler, L.R., Solomon, S.C., 2016. Remote sensing evidence for an ancient carbon-bearing crust on Mercury. Nature Geoscience 9, 273–276. https://doi.org/10.1038/ngeo2669

Peplowski, P.N., Lawrence, D.J., Evans, L.G., Klima, R.L., Blewett, D.T., Goldsten, J.O., Murchie, S.L., Mccoy, T.J., Nittler, L.R., Solomon, S.C., Starr, R.D., Weider, S.Z., 2015a. Constraints on the abundance of carbon in near-surface materials on Mercury: Results from the MESSENGER Gamma-Ray Spectrometer. Planetary and Space Science 108, 98-107. https://doi.org/10.1016/j.pss.2015.01.008

Peplowski, P.N., Lawrence, D.J., Feldman, W.C., Goldsten, J.O., Bazell, D., Evans, L.G., Head, J.W., Nittler, L.R., Solomon, S.C., Weider, S.Z., 2015b. Geochemical terranes of Mercury's northern hemisphere as revealed by MESSENGER neutron measurements. Icarus 253, 346–363. https://doi.org/10.1016/j.icarus.2015.02.002

Peplowski, P.N., Lawrence, D.J., Rhodes, E.A., Sprague, A.L., McCoy, T.J., Denevi, B.W., Evans, L.G., Head, J.W., Nittler, L.R., Solomon, S.C., Stockstill-Cahill, K.R., Weider, S.Z., 2012. Variations in the abundances of potassium and thorium on the surface of Mercury: Results from the MESSENGER Gamma-Ray Spectrometer. Journal of Geophysical Research: Planets 117, E00L04. https://doi.org/10.1029/2012JE004141

Peterson, G.A., Johnson, C.L., Byrne, P.K., Phillips, R.J., 2020. Fault Structure and Origin of Compressional Tectonic Features Within the Smooth Plains on Mercury. Journal of Geophysical Research: Planets 125, e2019JE006183. https://doi.org/10.1029/2019JE006183

Peterson, G.A., Johnson, C.L., Byrne, P.K., Phillips, R.J., 2019. Distribution of Areal Strain on Mercury: Insights Into the Interaction of Volcanism and Global Contraction. Geophysical Research Letters 46, 608–615. https://doi.org/10.1029/2018GL080749

Pettengill, G.H., Dyce, R.B., 1965. A radar determination of the rotation of the planet Mercury. Nature, 206, 1240. https://doi.org/10.1038/2061240a0

Peulvast, J.-P., Mège, D., Chiciak, J., Costard, F., Masson, P.L., 2001. Morphology, evolution and tectonics of Valles Marineris wallslopes (Mars). Geomorphology 37, 329–352. https://doi.org/10.1016/S0169-555X(00)00085-4

Pike, R.J., 1988. Geomorphology of impact craters on Mercury,. In: Vilas, F., Chapman, C.R., Matthews, M.S. (Eds.), Mercury. Univ. Arizona Press, Tucson, AZ,

pp. 165–173.

Pike, R.J., 1977. Size-dependence in the shape of fresh impact craters on the moon, in: Impact and Explosion Cratering: Planetary and Terrestrial Implications; Proceedings of the Symposium on Planetary Cratering Mechanics, September 13-17, 1976.

Preusker, F., Stark, A., Oberst, J., Matz, K.-D., Gwinner, K., Roatsch, T., Watters, T.R., 2017. Toward high-resolution global topography of Mercury from MESSENGER orbital stereo imaging: A prototype model for the H6 (Kuiper) quadrangle. Planetary and Space Science 142, 26–37. https://doi.org/10.1016/J.PSS.2017.04.012

Prockter, L.M., Ernst, C.M., Denevi, B.W., Chapman, C.R., Head, J.W., Fassett, C.I., Merline, W.J., Solomon, S.C., Watters, T.R., Strom, R.G., Cremonese, G., Marchi, S., Massironi, M., 2010. Evidence for young volcanism on Mercury from the third MESSENGER flyby. Science 329, 668–671. https://doi.org/10.1126/science.1188186

Prockter, L.M., Kinczyk, M.J., Byrne, P.K., Denevi, B.W., Head III, J.W., Fassett, C.I., Whitten, J.L., Thomas, R.J., Buczkowski, D.L., Hynek, B.M., Ostrach, L.R., Blewett, D.T., Ernst, C.M., 2016. The First Global Geological Map of Mercury, in: Lunar and Planetary Science Conference. p. Ab. #1245. https://doi.org/10.1029/2012JE004154.

Rava, B., Hapke, B., 1987. An analysis of the Mariner 10 color ratio map of Mercury. Icarus 71, 397–429. https://doi.org/10.1016/0019-1035(87)90037-6

Riner, M.A., Lucey, P.G., Desch, S.J., McCubbin, F.M., 2009. Nature of opaque components on Mercury: Insights into a Mercurian magma ocean. Geophysical Research Letters 36, L02201. https://doi.org/10.1029/2008GL036128

Robinson, M.S., Lucey, P.G., 1997. Recalibrated mariner 10 color mosaics: Implications for mercurian volcanism. Science 275, 197–200. https://doi.org/10.1126/science.275.5297.197

Robinson, M.S., Murchie, S.L., Blewett, D.T., Domingue, D.L., Hawkins, S.E., Head, J.W., Holsclaw, G.M., McClintock, W.E., McCoy, T.J., McNutt, R.L., Prockter, L.M., Solomon, S.C., Watters, T.R., 2008. Reflectance and Color Variations on Mercury: Regolith Processes and Compositional Heterogeneity. Science 321, 66–69. https://doi.org/10.1126/science.1160080

Rothery, D., Altieri, F., Le Mouelic, S., Mangold, N., Massironi, M., Penasa, L., Pozzobon, R., Pio Rossi, A., Van Der Bogert, C., 2017. Planmap Mapping Standard Definition (https://wiki.planmap.eu/display/public/Deliverables?preview=/8193472/8193931/776276-planmap_D2.1.pdf).

Rothery, D.A., Massironi, M., 2010. Beagle Rupes – Evidence for a basal decollement of regional extent in Mercury's lithosphere. Icarus 209, 256–261. https://doi.org/10.1016/j.icarus.2009.12.009

Rothery, D.A., Massironi, M., Alemanno, G., Barraud, O., Besse, S., Bott, N., Brunetto, R., Bunce, E., Byrne, P., Capaccioni, F., Capria, M.T., Carli, C., Charlier, B., Cornet, T., Cremonese, G., D'Amore, M., De Sanctis, M.C., Doressoundiram, A., Ferranti, L., Filacchione, G., Galluzzi, V., Giacomini, L., Grande, M., Guzzetta, L.G., Helbert, J., Heyner, D., Hiesinger, H., Hussmann, H., Hyodo, R., Kohout, T., Kozyrev, A., Litvak, M., Lucchetti, A., Malakhov, A., Malliband, C., Mancinelli, P., Martikainen, J., Martindale, A., Maturilli, A., Milillo, A., Mitrofanov, I., Mokrousov, M., Morlok, A., Muinonen, K., Namur, O., Owens, A., Nittler, L.R., Oliveira, J.S., Palumbo, P., Pajola, M., Pegg, D.L., Penttilä, A., Politi, R., Quarati, F., Re, C., Sanin, A., Schulz, R., Stangarone, C., Stojic, A., Tretiyakov, V., Väisänen, T.,

Varatharajan, I., Weber, I., Wright, J., Wurz, P., Zambon, F., 2020. Rationale for BepiColombo Studies of Mercury's Surface and Composition. Space Science Reviews 216, 66. https://doi.org/10.1007/s11214-020-00694-7

Rothery, D.A., Thomas, R.J., Kerber, L., 2014. Prolonged eruptive history of a compound volcano on Mercury: Volcanic and tectonic implications. Earth and Planetary Science Letters 385, 59–67. https://doi.org/10.1016/j.epsl.2013.10.023

Ruiz, J., López, V., Dohm, J.M., Fernández, C., 2012. Structural control of scarps in the Rembrandt region of Mercury. Icarus 219, 511–514. https://doi.org/10.1016/j.icarus.2012.03.030

Schaber, G.G., McCauley, J.F., 1980. Geologic map of the Tolstoj quadrangle of Mercury (H-8). Map I-1199. USGS Miscellaneous investigations series Map I--1199 1980.

Schlemm, C.E., Starr, R.D., Ho, G.C., Bechtold, K.E., Hamilton, S.A., Boldt, J.D., Boynton, W. V., Bradley, W., Fraeman, M.E., Gold, R.E., Goldsten, J.O., Hayes, J.R., Jaskulek, S.E., Rossano, E., Rumpf, R.A., Schaefer, E.D., Strohbehn, K., Shelton, R.G., Thompson, R.E., Trombka, J.I., Williams, B.D., 2007. The X-ray spectrometer on the MESSENGER spacecraft. Space Science Reviews 131, 393–415. https://doi.org/10.1007/s11214-007-9248-5

Scully, J.E.C., Russell, C.T., Yin, A., Jaumann, R., Carey, E., Castillo-Rogez, J., McSween, H.Y., Raymond, C.A., Reddy, V., Le Corre, L., 2015. Geomorphological evidence for transient water flow on Vesta. Earth and Planetary Science Letters 411, 151–163. https://doi.org/10.1016/j.epsl.2014.12.004

Semenzato, A., Massironi, M., Ferrari, S., Galluzzi, V., Rothery, D.A., Pegg, D.L., Pozzobon, R., Marchi, S., 2020. An integrated geologic map of the

rembrandt basin, on Mercury, as a starting point for stratigraphic analysis. Remote Sensing, 12(19), 321. https://doi.org/10.3390/rs12193213

Semenzato, A., Massironi, M., Pozzobon, R., Galluzzi, V., Rothery, D.A., Ferrari, S., 2018. Discovering Rembrandt basin's subsurface and Enterprise Rupes: 3D-model based on stratigraphic mapping and structural analysis. European Planetary Science Congress 2018 12, 450–462. https://doi.org/10.1002/9781405164535.ch35

Senthil Kumar, P., Keerthi, V., Senthil Kumar, A., Mustard, J., Gopala Krishna, B., Amitabh, Ostrach, L.R., Kring, D.A., Kiran Kumar, A.S., Goswami, J.N., 2013. Gullies and landslides on the Moon: Evidence for dry-granular flows. Journal of Geophysical Research E: Planets 118, 206–223. https://doi.org/10.1002/jgre.20043

Shinbrot, T., Duong, N.H., Kwan, L., Alvarez, M.M., 2004. Dry granular flows can generate surface features resembling those seen in Martian gullies. Proceedings of the National Academy of Sciences of the United States of America 101, 8542–8546. https://doi.org/10.1073/pnas.0308251101

Shoemaker, E.M., Hackman, R.J., 1962. Stratigraphic Basis for a Lunar Time Scale. Symposium - International Astronomical Union 14, 289–300. https://doi.org/10.1017/S007418090017826X

Sibson, R.H., 1992. Implications of fault-valve behaviour for rupture nucleation and recurrence. Tectonophysics 211, 283–293. https://doi.org/10.1016/0040-1951(92)90065-E

Slade, M.A., Butler, B.J., Muhleman, D.O., 1992. Mercury radar imaging: Evidence for polar ice. Science 258, 635–640. https://doi.org/10.1126/science.258.5082.635

Soderblom, L.A., 1970. A model for small-impact erosion applied to the lunar

surface. Journal of Geophysical Research 75, 2655–2661. https://doi.org/10.1029/JB075i014p02655

Solomon, S.C., 1976. Some aspects of core formation in Mercury. Icarus 28, 509–521. https://doi.org/10.1016/0019-1035(76)90124-X

Solomon, S.C., Anderson, B.J., 2018. The MESSENGER Mission: Science and Implementation Overview, in: Mercury: The View after MESSENGER. Cambridge University Press, p. 21.

Solomon, S.C., McNutt, R.L., Gold, R.E., Acuña, M.H., Baker, D.N., Boynton, W. V., Chapman, C.R., Cheng, A.F., Gloeckler, G., Head, J.W., Krimigis, S.M., McClintock, W.E., Murchie, S.L., Peale, S.J., Phillips, R.J., Robinson, M.S., Slavin, J.A., Smith, D.E., Strom, R.G., Trombka, J.I., Zuber, M.T., 2001. The MESSENGER mission to Mercury: Scientific objectives and implementation. Planetary and Space Science 49. https://doi.org/10.1016/S0032-0633(01)00085-X

Soter, S., Ulrichs, J., 1967. Rotation and Heating of the Planet Mercury. Nature 214, 1315–1316. https://doi.org/10.1038/2141315a0

Spudis, P.D., Guest, J.E., 1988. Stratigraphy and geologic history of Mercury, Mercury. University of Arizona Press, Tucson, AZ.

Spudis, P.D., Prosser, J.G., 1984. Geologic map of the Michelangelo Quadrangle of Mercury. USGS 1659.

Stark, A., Preusker, F., Oberst, J., Matz, K.-D., Gwinner, K., Roatsch, T., 2017. High-Resolution Topography from MESSENGER Orbital Stereo Imaging — The H5 Quadrangle 'Hokusai' in: 48th Lunar and Planetary Science Conference. The Woodlands, Houston, Texas, p. Ab. #2287.

Steinbrügge, G., Stark, A., Hussmann, H., Wickhusen, K., Oberst, J., 2018. The performance of the BepiColombo Laser Altimeter (BELA) prior launch and prospects for Mercury orbit operations. Planetary and Space Science

159, 84–92. https://doi.org/10.1016/j.pss.2018.04.017

Stockstill-Cahill, K.R., McCoy, T.J., Nittler, L.R., Weider, S.Z., Hauck, S.A., 2012. Magnesium-rich crustal compositions on Mercury: Implications for magmatism from petrologic modeling. Journal of Geophysical Research: Planets 117, E00L15. https://doi.org/10.1029/2012JE004140

Strom, R.G., Banks, M.E., Chapman, C.R., Fassett, C.I., Forde, J.A., Head, J.W., Merline, W.J., Prockter, L.M., Solomon, S.C., 2011. Mercury crater statistics from MESSENGER flybys: Implications for stratigraphy and resurfacing history. Planetary and Space Science 59, 1960–1967. https://doi.org/10.1016/j.pss.2011.03.018

Strom, R.G., Chapman, C.R., Merline, W.J., Solomon, S.C., Head, J.W., 2008. Mercury Cratering Record Viewed from MESSENGER's First Flyby. Science 321, 79–81. https://doi.org/10.1126/science.1159317

Strom, R.G., Malin, M.C., Leake, M.A., Kozak, R., 1990. GEOLOGIC MAP OF THE BACH (H-15) QUADRANGLE. United States Geological Survey, Miscellaneous Investigations Series , Map: I2015.

Strom, R.G., Trask, N.J., Guest, J.E., 1975. Tectonism and volcanism on Mercury. Journal of Geophysical Research 80, 2478–2507. https://doi.org/10.1029/JB080i017p02478

Tanaka, K.L., Skinner, J.A., Hare, T.M., Kelley, M.S., Bleamaster Iii, L.F., Crown, D.A., Gregg, T.K.P., Mest, S.C., Williams, D.A., 2011. Planetary Geologic Mapping Handbook - 2011.

Thomas, R.J., 2015. Planet Mercury : volatile release on a contracting world. PhD Thesis, The Open University.

Thomas, R.J., Hynek, B.M., Rothery, D.A., Conway, S.J., 2016. Mercury's low-reflectance material: Constraints from hollows. Icarus 277, 455–465. https://doi.org/10.1016/j.icarus.2016.05.036

Thomas, R.J., Rothery, D.A., Conway, S.J., Anand, M., 2014a. Hollows on Mercury: Materials and mechanisms involved in their formation. Icarus 229, 221–235. https://doi.org/10.1016/j.icarus.2013.11.018

Thomas, R.J., Rothery, D.A., Conway, S.J., Anand, M., 2014b. Long-lived explosive volcanism on Mercury. Geophysical Research Letters 41, 6084–6092. https://doi.org/10.1002/2014GL061224

Thomas, R.J., Rothery, D.A., Conway, S.J., Anand, M., 2014c. Mechanisms of explosive volcanism on Mercury: Implications from its global distribution and morphology. Journal of Geophysical Research E: Planets 119, 2239–2254. https://doi.org/10.1002/2014JE004692

Trask, N.J., Dzurisin, D., 1984. Geologic map of the Discovery (H-11) quadrangle of Mercury. USGS Miscellaneous investigations series Map I--1658 1659.

Trask, N.J., Guest, J.E., 1975. Preliminary geologic terrain map of Mercury. Journal of Geophysical Research 80, 2461–2477. https://doi.org/10.1029/JB080i017p02461

Trask, N.J., Strom, R.G., 1976. Additional evidence of Mercurian volcanism. Icarus 28, 559–563. https://doi.org/10.1016/0019-1035(76)90129-9

Uno, H., Johnson, C.L., Anderson, B.J., Korth, H., Solomon, S.C., 2009. Modeling Mercury's internal magnetic field with smooth inversions. Earth and Planetary Science Letters 285, 328–339. https://doi.org/10.1016/j.epsl.2009.02.032

Vander Kaaden, K., McCubbin, F., Nittler, L., Peplowski, P., Weider, S., Frank, E., McCoy, T., 2017. Geochemistry, mineralogy, and petrology of boninitic and komatiitic rocks on the mercurian surface: Insights into the mercurian mantle. Icarus 285, 155–168. https://doi.org/10.1016/j.icarus.2016.11.041

Vander Kaaden, K.E., McCubbin, F.M., 2015. Exotic crust formation on Mercury: Consequences of a shallow, FeO-poor mantle. Journal of Geophysical Research: Planets 120, 195–209. https://doi.org/10.1002/2014JE004733

Vilas, F., Domingue, D.L., Helbert, J., D'Amore, M., Maturilli, A., Klima, R.L., Stockstill-Cahill, K.R., Murchie, S.L., Izenberg, N.R., Blewett, D.T., Vaughan, W.M., Head, J.W., 2016. Mineralogical indicators of Mercury's hollows composition in MESSENGER color observations. Geophysical Research Letters 43, 1450–1456. https://doi.org/10.1002/2015GL067515

Watters, T.R., Daud, K., Banks, M.E., Selvans, M.M., Chapman, C.R., Ernst, C.M., 2016. Recent tectonic activity on Mercury revealed by small thrust fault scarps. Nature Geoscience 9, 743–747. https://doi.org/10.1038/ngeo2814

Watters, T.R., Head, J.W., Solomon, S.C., Robinson, M.S., Chapman, C.R., Denevi, B.W., Fassett, C.I., Murchie, S.L., Strom, R.G., 2009. Evolution of the Rembrandt impact basin on Mercury. Science 324, 618–621. https://doi.org/10.1126/science.1172109

Watters, T.R., Nimmo, F., 2010. The tectonics of Mercury, in: Planetary Tectonics. Cambridge University Press, pp. 15–80. https://doi.org/10.1017/cbo9780511691645.003

Watters, T.R., Robinson, M.S., Banks, M.E., Tran, T., Denevi, B.W., 2012. Recent extensional tectonics on the Moon revealed by the Lunar Reconnaissance Orbiter Camera. Nature Geoscience 5, 181–185. https://doi.org/10.1038/ngeo1387

Watters, T.R., Selvans, M.M., Banks, M.E., Hauck, S.A., Becker, K.J., Robinson, M.S., 2015. Distribution of large-scale contractional tectonic landforms on Mercury: Implications for the origin of global stresses. Geophysical

Research Letters 42, 3755–3763. https://doi.org/10.1002/2015GL063570

Watters, T.R., Weber, R.C., Collins, G.C., Howley, I.J., Schmerr, N.C., Johnson, C.L., 2019. Shallow seismic activity and young thrust faults on the Moon. Nature Geoscience 12, 411–417. https://doi.org/10.1038/s41561-019-0362-2

Weidenschilling, S.J., 1978. Iron/silicate fractionation and the origin of Mercury. Icarus 35, 99–111. https://doi.org/10.1016/0019-1035(78)90064-7

Weider, S.Z., Nittler, L.R., Murchie, S.L., Peplowski, P.N., McCoy, T.J., Kerber, L., Klimczak, C., Ernst, C.M., Goudge, T.A., Starr, R.D., Izenberg, N.R., Klima, R.L., Solomon, S.C., 2016. Evidence from MESSENGER for sulfur- and carbon-driven explosive volcanism on Mercury. Geophysical Research Letters 43, 3653–3661. https://doi.org/10.1002/2016GL068325

Weider, S.Z., Nittler, L.R., Starr, R.D., Crapster-Pregont, E.J., Peplowski, P.N., Denevi, B.W., Head, J.W., Byrne, P.K., Hauck, S.A., Ebel, D.S., Solomon, S.C., 2015. Evidence for geochemical terranes on Mercury: Global mapping of major elements with MESSENGER's X-Ray Spectrometer. Earth and Planetary Science Letters 416, 109–120. https://doi.org/10.1016/j.epsl.2015.01.023

Weider, S.Z., Nittler, L.R., Starr, R.D., McCoy, T.J., Stockstill-Cahill, K.R., Byrne, P.K., Denevi, B.W., Head, J.W., Solomon, S.C., 2012. Chemical heterogeneity on Mercury's surface revealed by the MESSENGER X-Ray Spectrometer. Journal of Geophysical Research: Planets 117, E00L05. https://doi.org/10.1029/2012JE004153

Weihs, G.T., Leitner, J.J., Firneis, M.G., 2015. Polygonal impact craters on Mercury. Planetary and Space Science 111, 77–82. https://doi.org/10.1016/j.pss.2015.03.014

Wetherill, G.W., 1975. Late heavy bombardment of the moon and terrestrial planets., In: Lunar Science Conference, 6th, Houston, Tex., March 17-21, 1975, Proceedings. Volume 2. (A78-46668 21-91) New York, Pergamon Press, Inc., 1975, p. 1539-1561.

Whitten, J.L., Fassett, C.I., Ostrach, L.R., 2019. Can the Intercrater Plains Unit on Mercury be Meaningfully Subdivided?: Characterization of the Derain (H-10) Quadrangle Intercrater Plains. LPICo 2154, 7016.

Whitten, J.L., Fassett, C.I., Ostrach, L.R., Whitten, J.L., Fassett, C.I., Ostrach, L.R., 2018. Geologic Map of the Derain (H-10) Quadrangle on Mercury: The Challenges of Consistently Mapping the Intercrater Plains Unit, in: Planetary Geologic Mappers Annual Meeting. p. 7027.

Whitten, J.L., Head, J.W., 2015. Rembrandt impact basin: Distinguishing between volcanic and impact-produced plains on Mercury. Icarus 258, 350–365. https://doi.org/10.1016/j.icarus.2015.06.022

Whitten, J.L., Head, J.W., Denevi, B.W., Solomon, S.C., 2014. Intercrater plains on Mercury: Insights into unit definition, characterization, and origin from MESSENGER datasets. Icarus 241, 97–113. https://doi.org/10.1016/j.icarus.2014.06.013

Wilhelms, D.E., 1987. The geologic history of the Moon. U.S. Geological Survey Professional Paper. https://doi.org/10.3133/pp1348

Wilhelms, D.E., 1976. Mercurian volcanism questioned. Icarus 28, 551–558. https://doi.org/10.1016/0019-1035(76)90128-7

Wilson, L., Head, J.W., 2008. Volcanism on Mercury: A new model for the history of magma ascent and eruption. Geophysical Research Letters 35, L23205. https://doi.org/10.1029/2008GL035620

Wilson, L., Head, J.W., 1981. Ascent and eruption of basaltic magma on the Earth and moon. Journal of Geophysical Research 86, 2971–3001.

https://doi.org/10.1029/JB086iB04p02971

Wise, D., 1963. Keystone Faulting and Gravity Sliding Driven by Basement Uplift of Owl Creek Mountains, Wyoming. AAPG Bulletin 47, 586–598. https://doi.org/10.1306/bc743a67-16be-11d7-8645000102c1865d

Wright, J., 2019a. MESSENGER Observations of Volcanism on Mercury: From Hokusai Quadrangle Down to Small Cones. PhD Thesis, The Open University. https://doi.org/10.21954/ou.ro.0000f075

Wright, J., Rothery, D.A., Balme, M.R., Conway, S.J., 2019b. Geology of the Hokusai quadrangle (H05), Mercury. Journal of Maps 15, 509–520. https://doi.org/10.1080/17445647.2019.1625821

Wright, J., Rothery, D.A., Balme, M.R., Conway, S.J., 2018. Constructional Volcanic Edifices on Mercury: Candidates and Hypotheses of Formation. Journal of Geophysical Research: Planets 123, 952–971. https://doi.org/10.1002/2017JE005450

Wright, J., Rothery, D.A., Balme, M.R., Conway, S.J., 2017. Late-stage effusive volcanism on Mercury: Evidence from Mansurian impact basins, in: 48th Lunar and Planetary Science Conference. The Woodlands, Houston, Texas, p. ab. #2239.

Xiao, Z., Komatsu, G., 2014. Reprint of: Impact craters with ejecta flows and central pits on Mercury. Planetary and Space Science 95, 103–119. https://doi.org/10.1016/j.pss.2013.07.001

Xiao, Z., Strom, R.G., Blewett, D.T., Byrne, P.K., Solomon, S.C., Murchie, S.L., Sprague, A.L., Domingue, D.L., Helbert, J., 2013a. Dark spots on Mercury: A distinctive low-reflectance material and its relation to hollows. Journal of Geophysical Research: Planets 118, 1752–1765. https://doi.org/10.1002/jgre.20115

Xiao, Z., Zeng, Z., Ding, N., Molaro, J., 2013b. Mass wasting features on the

Moon – how active is the lunar surface? Earth and Planetary Science Letters 376, 1–11. https://doi.org/10.1016/J.EPSL.2013.06.015

Zambon, F., Galluzzi, V., Carli, C., Capaccioni,) F, Wright, J., Rothery, D.A., 2017. Spectral variations on H-2 Victoria quadrangle on Mercury: the case of Hokusai rays. EPSC EPSC2017-903. https://doi.org/10.1002/2016GL069868

Zharkova, A.Y., Kreslavsky, M.A., Head, J.W., 2019. RARITY OF BOULDERS ON MERCURY: COMPARISON WITH THE MOON, in: 50th Lunar and Planetary Science Conference, Held 18-22 March, 2019 at The Woodlands, Texas. LPI Contribution No. 2132, Id.1162. p. 1162.

Zhou, Y.C., Xu, B.H., Yu, A.B., Zulli, P., 2002. An experimental and numerical study of the angle of repose of coarse spheres. Powder Technology 125, 45–54. https://doi.org/10.1016/S0032-5910(01)00520-4